UNIVERSITY of TASMANIA
AUSTRALIA

STRUCTURAL BEHAVIOUR OF THIN-WALLED STEEL ELEMENTS WITH GEOMETRIC AND SECTIONAL NON-UNIFORMITIES

by

Tohid Ghanbari Ghazijahani

Submitted in fulfilment of the requirements for the degree of

Doctor of Philosophy

at the

UNIVERSITY OF TASMANIA

February 2017

In the name of the most compassionate

To my wife who never stopped her heartfelt supports and my lovely daughter.

STATEMENT OF ORIGINALITY AND AUTHORITY OF ACCESS

I hereby declare that, except where a reference is included, this PhD thesis is original and no material has been submitted to or published by any university for a degree or diploma, nor does the thesis contain previously published or written material by another person except where due acknowledgement is made. The thesis may be available for loan and limited access in accordance with the Copyright Act 1968.

Tohid Ghanbari Ghazijahani

ABSTRACT

This PhD program proposes innovative ideas within a comprehensive and yet umbrella definition as indicated through the title. Above all, this thesis provides a comprehensive compendium of experimental results on a variety of aspects of buckling of thin walled steel elements and an invaluable resource of experimental data for the later studies of such structural elements.

This thesis experimentally investigates the structural stability of thin-walled steel members with different geometrical and material specifications. For tubular circular members made exclusively from steel, large imperfections in the form of dents were examined under axial loading, bending and external pressure. As another form of geometrical irregularity, different shapes and geometries of cutouts were considered in order to investigate the effect of these imperfections on the structural behaviour of the steel members. Circular shell elements with normal fabrication-related imperfections were investigated under external pressure. Reinforcement of the shell members with additional elements (stiffeners/thickeners) and without additional material (corrugation) was also undertaken.

Large imperfections such as dents and cutouts with different sizes were then examined for circular tubes under cyclic loading. Rehabilitation of members with cutouts (using Carbon Fibre Reinforced Polymer, CFRP), fully recovered the reduced capacity resulted from the existence of the cutouts; yet, employed reinforcements manifested capacities well above the intact models.

Sectional irregularity was also of a great interest in this PhD thesis, which was adopted for composite members. Composite elements such as CFRP and timber were combined with thin-walled steel members to produce light-weight elements with great *structural efficiency*. Timber cores with different cross sections were utilised for timber filled CHS steel tubular sections. CFRP reinforced the timber-filled CHS members from outside the steel so that both inward and outward buckling was restricted. The same scenario was used for

the CHS members with timber and concrete cores, in which the timber blocks were employed to act as compressive members, alongside their key role to form (cast) the concrete inside the tubes. Bending members including timber, reinforced by U-shape steel members were designed in order to make a light-weight flexural element. The effect of such strengthening on the capacity as well as the ductility of the beams in question was evaluated.

Keywords: Thin-walled steel elements; Buckling; Hollow sections; Geometric and sectional non-uniformities; Composite elements; Reinforcement; CFRP and timber;

ACKNOWLEDGEMENTS

This thesis was undertaken under supervision of Dr. Hui Jiao and Dr. Damien Holloway. I would like to express my sincere gratitude to Dr. Jiao who greatly supported me especially whilst conducting tests and also great discussions throughout analysing data. My special thanks go to Dr. Holloway for his great patience, understanding and invaluable and constructive comments whilst preparation of the papers and the thesis. Also, the support of the School of Engineering and ICT, and the technicians of the Mechanical Workshop of the School, Mr. Andrew Bylett, Mr. Peter Seward, Mr. David Morley and especially Mr. Calverly Gerard is greatly appreciated.

Finally, I must warmly appreciate my family, my wonderful wife for her significant role in providing me with sincere and endless support during this PhD program, my lovely daughter for bringing happiness to our life while in Australia, and my parents and parents in law for their support and patience.

AWARD ACHIEVEMENT OF THE THESIS

Fifteen quality papers were organised out of this thesis, amongst which 14 papers were accepted/published in top-tier journals of Civil and Structural Engineering, e.g. two papers by American Society of Civil Engineers (ASCE) and several papers by Elsevier. The output of the research carried out throughout this PhD program was well recognised by the Dean of Faculty of Science, Engineering and Technology at the University of Tasmania. Tohid Ghanbari Ghazijahani received the following competitive award for which the applicants were from five different schools of the University:

Exceptional Performance by Current Higher Degree by Research Candidates, Dean of Faculty of Science, Engineering and Technology, August 2016.

Tohid Ghanbari Ghazijahani and Professor Brian Yates, Dean of the Faculty of Science, Engineering and Technology.

PUBLICATION OUTPUT OF THE THESIS

- Tohid Ghanbari Ghazijahani, Hui Jiao, Damien Holloway, "Composite Timber Beams Strengthened by Steel and CFRP" Journal of Composites for Construction (ASCE), 21 (1) 2017.
- Tohid Ghanbari Ghazijahani, Hui Jiao, Damien Holloway, "Concrete-Filled Circular Steel Tubes with a Timber Infill under Axial Compression", Journal of Structural Engineering (ASCE), 143 (7) 2017.
- Tohid Ghanbari Ghazijahani, Hui Jiao, Damien Holloway, "Timber filled CFRP Jacketed Circular Steel Tubes under Axial Compression" Construction and Building Materials (Elsevier), 94 (2015) 791–799.
- Tohid Ghanbari Ghazijahani, Hui Jiao, Damien Holloway, "Plastic Buckling of Dented Steel Circular Tubes under Axial Compression: An Experimental Study" Thin-Walled Structures (Elsevier), 92 (2015) 48–54.
- Tohid Ghanbari Ghazijahani, Hui Jiao, Damien Holloway, "Structural Behavior of Shells with Different Cutouts under Compression: An Experimental Study" Journal of Constructional Steel Research (Elsevier), 105 (2015) 129–137.
- Tohid Ghanbari Ghazijahani, Hui Jiao, Damien Holloway, "Longitudinally Stiffened Corrugated Cylindrical Shells under Uniform External Pressure" Journal of Constructional Steel Research (Elsevier), 110 (2015) 191–199.
- Tohid Ghanbari Ghazijahani, Hui Jiao, Damien Holloway, "Fatigue Experiments on Circular Hollow Sections with CFRP Reinforced Cutouts" Journal of Constructional Steel Research (Elsevier), 106 (2015) 322–328.
- Tohid Ghanbari Ghazijahani, Hui Jiao, Damien Holloway, "Fatigue Tests of Damaged Tubes under Flexural Loading" Steel & Composite Structures, An International Journal (Techno Press), Vol. 19, No. 1 (2015) 223-236.
- Tohid Ghanbari Ghazijahani, Hui Jiao, Damien Holloway, "An Experimental Study on Externally Pressurized Stiffened and Thickened Cylindrical Shells" Thin-Walled Structures (Elsevier), 85 (2014) 359–366.

- Tohid Ghanbari Ghazijahani, Hui Jiao, Damien Holloway, "Influence of a Cutout on Circular Steel Hollow Sections under Cyclic Loading" Journal of Constructional Steel Research (Elsevier), 100 (2014) 12–20.
- Tohid Ghanbari Ghazijahani, Hui Jiao, Damien Holloway, "Experiments on Dented Cylindrical Shells under Peripheral Pressure" Thin-Walled Structures (Elsevier), 84 (2014) 50-58.
- Tohid Ghanbari Ghazijahani, Hui Jiao, Damien Holloway, "Rectangular Steel Tubes with Timber Infill and CFRP Confinement under Compression: Experiments" Journal of Constructional Steel Research (Elsevier), 114 (2015) 196–203.
- Tohid Ghanbari Ghazijahani, Hui Jiao, Damien Holloway, "Experiments on Locally Dented Conical Shells under Axial Compression", Steel & Composite Structures, An International Journal (Techno Press), 19 (6) 1355-1367 (2015).
- Tohid Ghanbari Ghazijahani, Hui Jiao, Damien Holloway, "Experiments on Dented Steel Tubes under Bending" Advances in Structural Engineering (Multi-Science, UK), Vol. 18, No. 11 (2015) 1807–1817.
- Tohid Ghanbari Ghazijahani, Hui Jiao, Damien Holloway, "CFRP Confined Circular Steel Tubes under Axial Compression", submitted – under review.
- Tohid Ghanbari Ghazijahani, Hui Jiao, Damien Holloway, "Recent Advances on the Behavior of Locally Damaged Circular Steel Hollow Sections", Proceeding of the International Conference: Performance-based and Life-cycle Structural Engineering (PLSE 2015), edited by: Dilum Fernando, Jin-Guang Teng and Jose L. Torero, ISBN: 978-1-74272-147-7, published by: School of Civil Engineering, The University of Queensland, Brisbane, Australia, December 2015;

TABLE OF CONTENTS

TABLE OF FIGURES

Note: *Figures of this thesis should be considered in colour.*

LIST OF TABLES

Chapter 1

Introduction

Thin walled steel structural elements have long been widely used in Civil and Structural Engineering. These elements are quite vulnerable to the buckling instability when exposed to compressive stresses, which can most commonly occur for elements under pure axial compression and under bending. Buckling of thin walled structures can be also seen in pressurised shells. The instability of such structures highly depends on the geometry of the cross section, which is oftentimes called slenderness. Aside from the slenderness of thin walled sections, the perfectness of the geometry is also significant. In one respect, the former parameter, slenderness, may lead to different types of failure in such elements. As an example, bifurcation type of instability generally takes place for thinner members wherein the failure is accompanied by a relatively abrupt reduction of the load, which usually appears as a critical load. Limit point instability, in contrast, occurs for thicker elements in which the nonlinear stage of the load displacement curve is maintained in a more gradual fashion. The latter parameter may affect the ultimate load carrying capacity.

Geometric uniformity is a significant parameter for thin walled steel members. Generally speaking, the more precise the fabrication and/or construction of thin steel sections is, the higher the structural capacity may be. As such, sensitivity of thin walled structures to a variety of imperfections has been the focus of many investigators. Some examples with the tendency towards thin *shell* structures can be found as Refs. [1-7]. One of the main areas that has been looked into is that imperfection sensitivity of an element under various loads differs from one another [3]. As an example, capacity of thin walled structures under pure axial compression is believed to be more significantly affected by the imperfection phenomenon relative to other loading conditions. Thus, this thesis investigates many elements with imperfections under different loads.

Normal fabrication-related imperfections have been studied in many references, wherein the effects of such imperfections, appearing with various distribution and diversity, were examined on the structural capacity. Apart from the normal imperfections though, development of large imperfections is seen in real structures during service. In offshore structures as an instance the collision of different moving objects (e.g. utilised for transportation and so forth) can cause damage to the elements during their service life. It is quite evident that the collision is not limited to the offshore structures. In fact, in general it could occur for any structural elements. Cutouts are often also introduced to a structural element as an afterthought, and so form another type of large imperfection not present initially. Thus, the presence of such local large geometric imperfections inspired a substantial part of this PhD program, as seen in the first main chapter to examine the effects of such non-uniformities (dents and cutouts) on the capacity of circular thin steel sections. Apart from the relevant publication output out of this thesis about large imperfections, Refs. [8-16] provided input into the effect of large local imperfections, as a few examples in the literature.

Due to the significance of large local imperfections (dents and cutouts), and as this thesis aims to extensively study the effect of large local imperfections under different loading conditions, these geometric irregularities were also investigated in a chapter on tubular steel shell structures under *cyclic loading*. Note that CHS (Circular Hollow Section) members appear in many structural applications, some cases of which are under bending moment [17, 18]. Unreinforced CHS tubes with non-uniformities and under cyclic bending were undertaken. Cutouts have been used in a few published studies to reduce the stress concentration in critical areas of specimens such as Refs. [19-21]. Although in some of these references relief holes were used to stop development of a crack after creation, the same concept was considered in part of this thesis as the hole near the end helped deflect the stress flow lines from the most critical area to less critical zones. Furthermore, with a view to recover the lost fatigue life resulted from large cutouts, as the main non-uniformities of this series of tests, reinforcing the area around the cutouts with CFRP (Carbon Fibre Reinforced Polymer) was studied.

Stiffening of the thin walled steel structures is extensively used to reinforce, and accordingly enhance the load carrying capacity. Although different kinds of stiffeners make the geometry of thin walled steel sections non-uniform, they can reinforce steel shells against normal fabrication related imperfections. Stiffening is known to improve the transverse strength of thin pressurised shells [22-25]. Challenges of stiffening always necessitate evaluation of different options in various projects against stiffening. One of the challenges of stiffening is the residual stresses resulting from different methods of connection of stiffeners such as welding. This challenge becomes more crucial especially when the elements are thinner as thinner elements cannot absorb the residual stresses across the thickness so that a residual stress propagates into a larger area in comparison to thicker elements. A chapter of this thesis introduces a method of epoxy connection in lieu of welding or soldering in which the heat produces a great deal of residual stress. The topic of reinforcement of such structures with fabrication imperfections was followed by the idea of even eliminating the additional material (stiffeners) yet changing the geometry and the material of a cylindrical shell in order to achieve a higher capacity. To this end, longitudinal corrugation of the surface was proposed and tested. The results demonstrated a noticeable rise in the buckling capacity, which is comparable to the use of stiffeners, given that usage of corrugation is believed to be quite cost effective.

An alternative way to address weaknesses against buckling is to employ different materials working in synergy with the parent section, which leads to the idea of composite materials. In line with the topic of the thesis, it was hypothesised that sectional non-uniformity developed through composite materials may help decrease the sensitivity of thin-walled steel tubular elements to normal fabrication-related geometrical non-uniformities. Over the past two decades, there has been significant interest in research relating to tubes with different infills, which led to penetration of this technology into practice (see Refs. [26-33]). The last main chapter of the thesis aims to discuss the effect of timber and/or concrete filled and CFRP reinforced tubes on the structural response of tubes under compression. The composite materials of timber, CFRP and concrete were employed so as to synergise with the base element (steel) to reach a great capacity whilst maintaining a light weight for the current composites. The last part of the thesis discusses that this combination, as composite elements, not only yields reliable results for structural members under axial compression but also flexural members may greatly benefit from the present composite functionality.

Overall, the main chapters this thesis are organised as:

- Thin walled cylindrical shells with large imperfections;
- Thin cylindrical shells with fabrication-related imperfections reinforced with and without additional materials;
- Cylindrical shells with large imperfections under cyclic bending; and
- Thin walled steel elements and sectional non-uniformities (composite functionality).

Chapter 2

Thin Walled Cylindrical Shells with Large Imperfections

Publication output of Chapter 2

This chapter consists of five journal papers published in international journals as follows:

- "Plastic Buckling of Dented Steel Circular Tubes under Axial Compression: An Experimental Study" **Thin-Walled Structures** (Elsevier), 92 (2015) 48–54.
- "Experiments on Dented Cylindrical Shells under Peripheral Pressure" **Thin-Walled Structures** (Elsevier), 84 (2014) 50-58.
- "Experiments on Locally Dented Conical Shells under Axial Compression", **Steel & Composite Structures, An International Journal** (Techno Press)**,** 19 (6) 1355-1367 (2015).
- "Experiments on Dented Steel Tubes under Bending" **Advances in Structural Engineering** (Multi-Science), Vol. 18, No. 11 (2015) 1807–1817.

- "Structural Behavior of Shells with Different Cutouts under Compression: An Experimental Study" **Journal of Constructional Steel Research** (Elsevier), 105 (2015) 129–137.

2.1 Introduction

Steel shells have long been used in various parts of different structures. Sensitivity to the initial geometrical imperfection has been one of the most significant issues on the stability of these structures, which has made them vulnerable to the buckling [3]. Most attention has been devoted to structures under normal fabrication related imperfections [23, 34-36]. Notwithstanding, the challenges of large local imperfections – presented in this work as dent-shaped imperfections or cutouts – have not been fully studied for these structures under different loading conditions (see Refs. [8-16, 37-42] as examples in which large imperfections were discussed). This chapter investigates the effect of large imperfection on the structural behaviour of thin-walled shells under different loading and geometric conditions.

Firstly, the effect of large local imperfections, *dents*, on the plastic buckling capacity of short steel tubes under axial compression was examined. Following that the buckling and post-buckling response of thin cylindrical shells with local dent imperfections under uniform external pressure was experimentally investigated. Through a separate series of experiments, locally dented conical shells were studied under axial compression. In all these tests, the specimens were indented through a process such that dent imperfections with various depths were introduced to different locations on the body of the specimens. Buckling modes as well as the capacity of the specimens were thoroughly investigated. The adverse effect of such a local damage on the load carrying capacity was quantified for different values and types of imperfections.

A considerable volume of literature is found regarding the effect of an opening in thin cylindrical shells under different loading (e.g. Ref. [38-40, 42-44]). Among these, quite a few references are directly related to the cutouts along the length of the shells in the form of entrance doors. Following the above-mentioned tests on the effect of geometric damage to the body of the shell elements, this section investigates the effect of cutout – as another type of geometric non-uniformity – on circular steel shells. Different buckling modes as well as the effect of geometric parameters of a cutout were examined in this section. A stiffening method was also used to decrease the effect of the cutout on the capacity of such structures.

Due to the extensive usage of steel tubular sections in many kinds of Civil and Mechanical Engineering structures, such as in offshore industry, bridge elements, etc., the last section of this chapter examines the effect of the dent imperfection on bending of tubes with the same geometry as for the previous section in which the effect of cutouts was discussed. It is worth mentioning that although many studies focused on the bending stability of steel members (e.g. [45-48]), very little research can be found on the effect of surface defects, such as dent imperfection, on the bending behaviour of such tubular members. After evaluating the effect of dents for different shells under compression, and due to the fact the bending comprises compression and tension stresses, this section of this chapter aimed to evaluate the effect of dent-shaped defects on the flexural capacity of CHS members, particularly for the compression side of the shells.

In all tests conducted in this chapter, for shell structures under different loading and geometric conditions, a relation between the capacity and large imperfections was seen. This chapter chiefly aimed to quantify the effect of different dents and cutouts on the structural capacity and deformational modes of shells of revolutions. Evaluation of the results against previous tests, existing theoretical equations and codes verified the obtained experimental data, indicating that test data can be reliably used to validate future numerical and analytical modelling. Above all, the results of this chapter may be regarded as an experimental database for dent and cutout studies to provide researchers with insight into the response of steel shell structures with such geometric non-uniformities.

2.2 Plastic buckling of dented steel circular tubes under axial compression

2.2.1 Introduction

The very common usage of CHS members as structural elements has stimulated many researchers to investigate their structural behaviour. Many researches have focused on these elements under compression. Copious papers have also looked into the sensitivity of such structures to geometrical irregularities, also known as geometric imperfections. In some cases these elements are prone to physical contacts caused by collisions such as columns in car parks, tubular members in offshore structures collided by supply boats and so forth.

A limited number of papers have, however, studied the dent imperfections in hollow sections. Most recently, Ghanbari Ghazijahani studied the buckling behaviour of very thin cylindrical shells subject to axial stresses [49]. 27 specimens were tested in this study with different dents. It appeared that the capacity of such structures decreased due to the effect of the damaged areas. Buckling of dented short carbon steel cylindrical shells under axial loading were studied parametrically by Prabu et al. [13]. Angle, size and inclination of the local dent imperfection were investigated in this research. The effect of dent imperfections was examined by Ghanbari Ghazijahani et al. for slender shell specimens under pressure loading, which similarly led to the capacity reduction [14, 50]. Bending capacity of dented CHS tubes was investigated through two respective studies [51, 52], and the failure modes as well as the ultimate capacity was thoroughly assessed for locally imperfect specimens. Indentation of ring-stiffened cylinders using wedge-shaped indenters was studied by Karroum et al. through both FE and an experimental research [9]. The failure location for all specimens was identified to be at a bulkhead of the specimens, where the plastic strain values were also evaluated.

Eyvazinejad Firouzsalari and Showkati studied steel dented tubes with *D/t* (diameter to thickness) ratio of around 55 [8, 53]. It was found that axial compression had a significant effect in some tests on the behaviour of pipes against local lateral loading. Residual strength of dented structures was studied by Paik [10], which addressed the mechanics of dented members based on test observations and FE computations. An indentation process employing wedge-shaped indenters and a single spherical indenter was adopted to investigate tubular members [54]. The conducted tests were presented along with simplified analytical models, which yielded closed-form expressions.

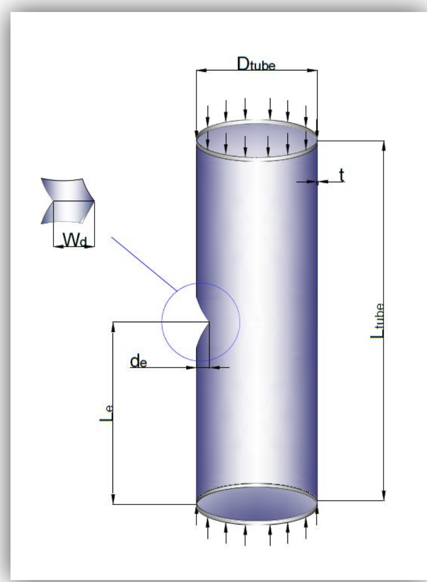

Figure 2-1: Geometry of the dented specimens.

Despite the mentioned studies, relevant papers on local large imperfections seem insufficient to cover all aspects of structural behaviour of shells with damaged geometries. To that end, this section aims to address the plastic buckling of steel CHS tubes under pure compression. The key aims of this section are: (i) to conduct consistent indentation by a suitable V-shaped indenter, (ii) to perform tests on the tubes under axial compression, (iii) evaluate the failure modes considering the presence of dent shape pre-deformation, (iv) to discuss the load carrying capacity of the dented tubes considering different local imperfections, and (v) to evaluate the results against previously published data.

2.2.2 Experimental procedure

Specimens

Specimens were all cold formed mild steel CHS tubes. The geometry of the specimens and the properties of the material used for fabrication of the tubes are given in Figure 2-1 and Table 2-1.

Table 2-1: Geometry of the specimens and material properties.

Specimen	L_{tube} (mm)	D_{tube} (mm)	D_{tube}/t
TUD.1-11	220	76.2	47.6
Yield stress (MPa)	**Ultimate stress (MPa)**	**Young's modulus (GPa)**	
307	360.2	216.3	

The material properties were obtained from tensile coupon tests and a stress strain curve obtained from this test is available in Ref. [55] (also seen in Figure 2-52). In Table 2-1 and Table 2-2, L_{tube} and D_{tube} are the length and the diameter of the tubes. Additionally, d_e, L_e and W_d are the depth of the dent, distance of the dent from the bottom end and width of the dent respectively, discussed in the next section.

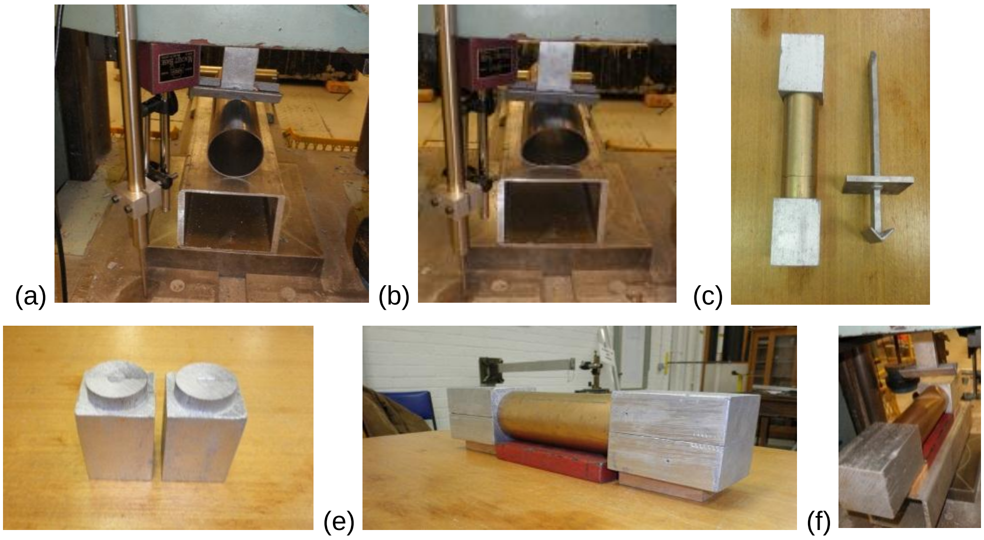

(a) (b) (c) (d) (e) (f)

Figure 2-2: (a),(b) Indentation of an unsupported specimen, (c) Supported specimen and indenter (d) end support fittings, (e) supported aligned specimen and (f) Indentation of a supported specimen.

Indentation

As seen in Figure 2-2, indentation was conducted using a V-shape 90° angled indenter. Figure 2-2 (a) and (b) show the indentation process of an unsupported specimen, wherein the ovalisation of cross sections occurred along the whole length. Figure 2-2 (c) shows a tube specimen before indentation, with end supports inserted into both ends to prevent the ovalisation of the end sections.

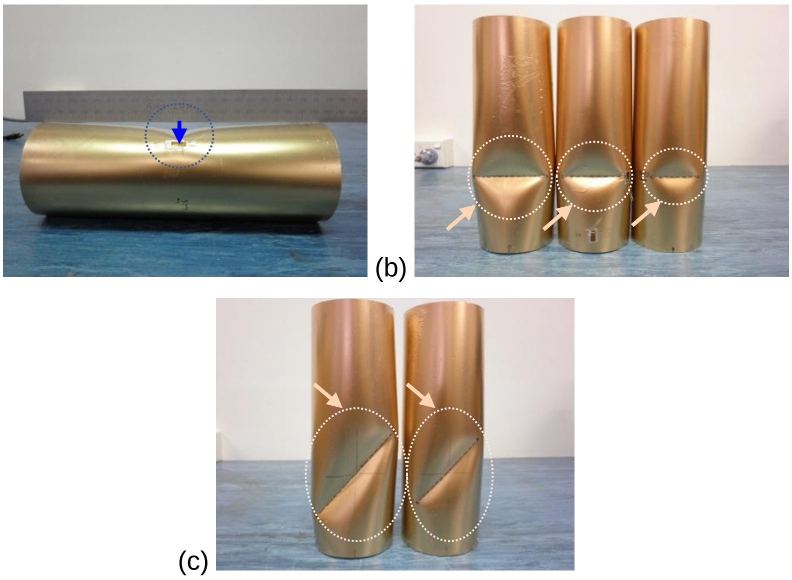

(a) (b) (c)

Figure 2-3: (a), (b) and (c) Different dents with various sizes and orientations.

Figure 2-3 displays different specimens with horizontal and inclined dents. The load displacement behaviour of the specimens under concentrated indenting loads was recorded throughout the indentation. The curves out of this process are presented in Figure 2-4. It is plainly seen that a nonlinear trend dominated the deformations from the initial stages of loading.

Table 2-2: Specimens and dent specifications.

Specimen	**d_e (mm)**	**L_e (mm)**	**W_d (mm)**	**Orientation**
TUD.1	0	0	0	-
TUD.2	4	45	37	Horizontal
TUD.3	8.5	45	56	Horizontal
TUD.4	19	45	85	Horizontal
TUD.5	5.7	73.3	46	Horizontal
TUD.6	11.5	73.3	62	Horizontal
TUD.7	16	73.3	71	Horizontal
TUD.8	9.5	110	53	Horizontal
TUD.9	18.3	110	77	Horizontal
TUD.10	9	73.3	79	Diagonal (45°)
TUD.11	17	73.3	105	Diagonal (45°)

Experimentation

An Avery Universal Testing Machine with the loading capacity of 1000 kN was utilised to apply the axial loading. The boundary condition of the specimens was adopted as a simple contact of the two edges of the specimens with the rigid plates of the loading machine. Loading was applied slowly (around 0.1kN/s) so as to apply a quasi-static loading. Loading was initiated and monotonically increased until final failure of the specimens took place.

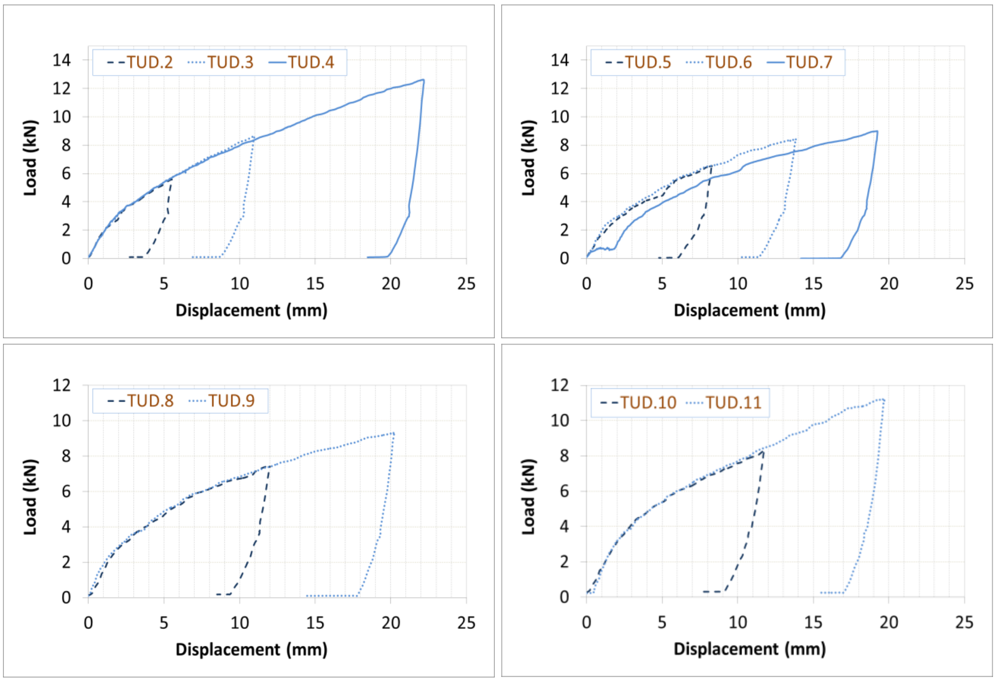

Figure 2-4: Load-displacement of the dented location for different specimens (see Table 2-2 for dent specifications).

2.2.3 Results and discussions

Observation of the test

The intact specimen (TUD.1), as expected, failed with the so-called *elephant foot* plastic buckling. The buckling bulge occurred approximately 15 mm (D/5) from one end in a ring shape as an outward deformation. This end of the tubes deformed quite symmetrically.

Deformations for the dented specimens were initiated from the dented area such that the dents predominantly extended at the both ends towards the sides. This was further accompanied by the deepening of the dents. As deformations developed further, a U-shaped wave started in the end opposite the dent until it encompassed approximately half the circumference approaching the dent. Likewise, the same phenomenon, i.e. bulge, was seen at the top end of the specimens for some specimens. Deformations at the end opposite the dent occurred exactly at the same location at which the intact specimen buckled.

However, the area underneath the dented zone remained unbuckled as seen in Figure 2-5 (c) and (d).

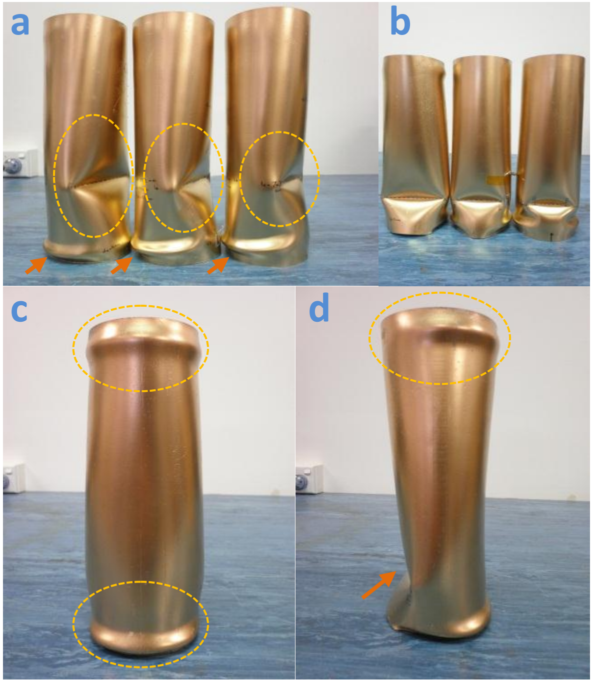

Figure 2-5: (a), (b) Different specimens with various dent sizes after failure, and (c), (d) *elephant foot* bulge at the opposite end to the dent.

The same behaviour was seen for CHS tubes with different shapes of cutout presented in Ref. [56], where the authors hypothesised that the axial stress flow lines deflected to the sides upon approaching the cutout. The same response is verified for the present dented specimens through this study.

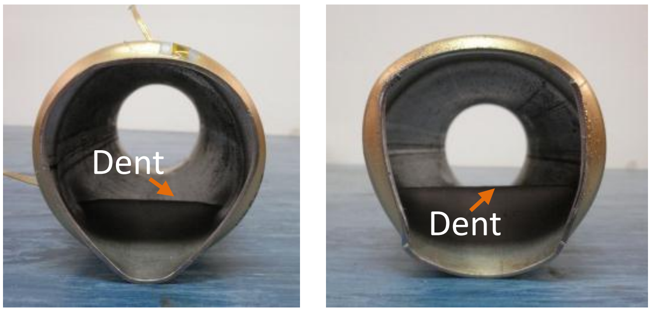

Figure 2-6: Inside view of the dent and end section shape after failure: triangular for a medium size dent (left), quadrangular for a deeper dent (right).

Figure 2-6 shows the dent and the end section after failure. The end section was triangular which was rather closer to a round shape in the specimen with a medium size dent, whereas as the dent became deeper the end section approached a quadrangular which was certainly a consequence of the depth of the dent. This demonstrates that for deeper dents the final failure mode changed compared with the intact specimen. Figure 2-7 shows the typical buckling progress in a dented specimen, through which the development of buckling around the dent and on the opposite side is schematically illustrated. The same phenomenon was observed for TUD.5 and TUD.2 as given through Figure 2-8 and Figure 2-9.

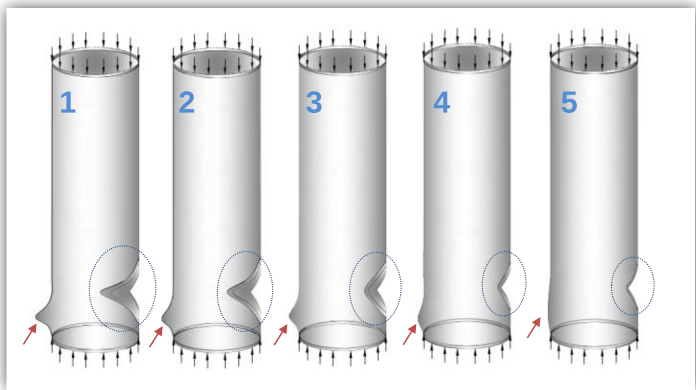

Figure 2-7: Schematic illustration for a dented specimen, progress of deformations at the dented area as well as bulge at the opposite side of the dent (deformations are rather magnified to show a clear progress).

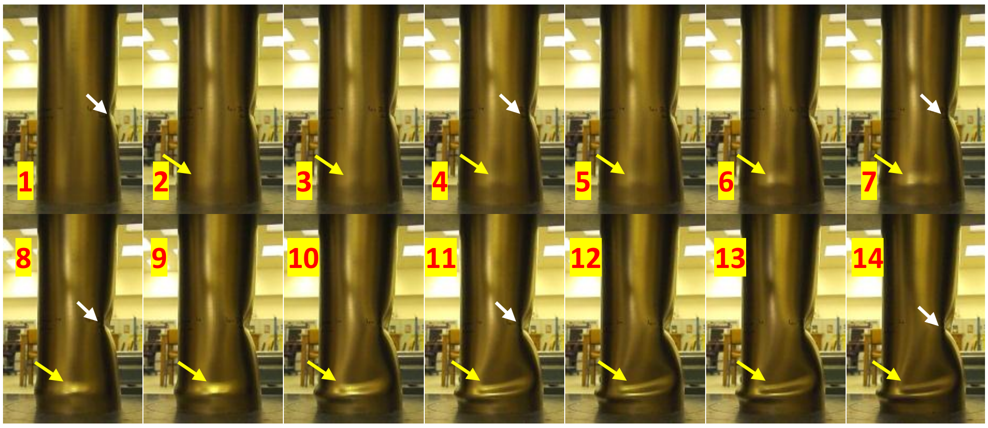

Figure 2-8: Buckling progress for the specimen TUD.5 with the salient deformations marked.

Displacement and strain behaviour

Figure 2-10 shows end shortening of different specimens versus the axial load. It is apparent that TUD.1 (intact specimen) had a more stable behaviour under axial load. The load displacement behaviour of this specimen consisted of two almost linear parts with a deflection region on the curve in between, which accounted for the yield. For the dented specimens, TUD.2, TUD.3 and TUD.4 nonlinear response started progressively sooner in comparison with TUD.1, which clearly illustrates the effect of increasingly large dent imperfections. The same observation is seen for the rest of the specimens, among which TUD.4, TUD.6, TUD.9 and TUD.11, which had the deepest dents, displayed the most nonlinear load displacement curves. Furthermore, referring to the end shortening curves the ductility of the dented specimens was rather more than the intact specimen, as for a given load the displacement of the dented specimens was higher than that of the intact one.

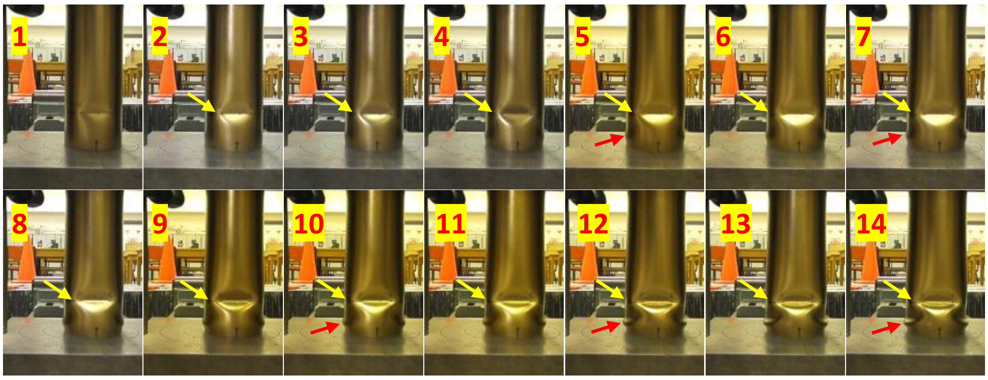

Figure 2-9: Buckling progress for the specimen TUD.2 with the salient deformations marked.

Figure 2-11 plots the strain at a few locations within the specimens versus the axial load. For the intact specimen three strain gauges designated as SG.1, SG.2 and SG.3 were attached to each quarter on the circumference in order to record the axial strain. They were all located 15 mm from one end of the specimens (the end close to the dent). As can be seen, a typical plastic trend was obtained with considerable plastic elongation. Moreover, all three SGs behaved approximately similar, in terms of value and trend.

As illustrated in Figure 2-11, SG.1 for the specimens TUD.6 and TUD.8 was located at a corner of the dent so as to track the development of deformations at the dented area, while SG.2 was underneath the centre of the dent, 15 mm from the end and SG.3 was equivalent to SG.2, but exactly on the opposite side of the tube, i.e. with a 180° circumferential interval. As expected, SG.1 and SG.2 recorded negative values indicating that the stresses were compressive, whereas SG.3 showed approximately zero for the axial stresses up until the plastic region governed. However, upon the initiation of the nonlinear trend in SG.1 and SG.2, SG.3 recorded small positive values, i.e. tensile stresses. The reason for this result is deemed to be that the deformations accumulated at the points corresponding to SG.1 and SG.2. As a result, very small tensile stresses at SG.3 occurred due to the expansion of the body of the tube at that point.

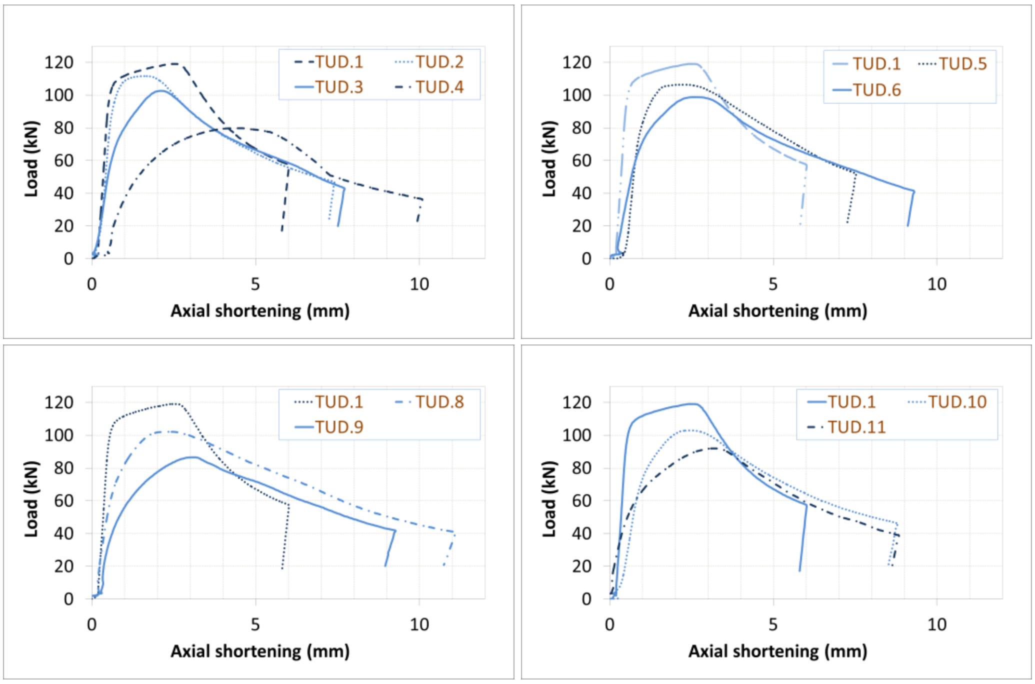

Figure 2-10: End-shortening versus load for different specimens.

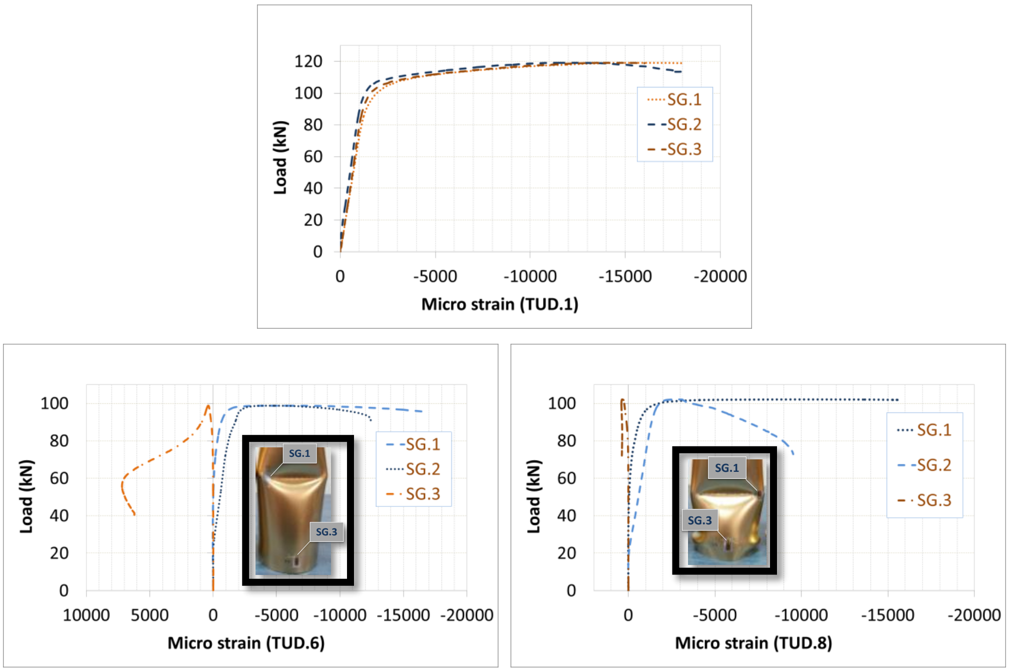

Figure 2-11: Strain values of different points for the specimens TUD.1, TUD.6 and TUD.8.

Load carrying capacity of the dented specimens

Figure 2-12 presents an overall trend of reduction in the capacity for locally imperfect specimens, which is plotted for different values of d_e (depth of the dent). Clearly the dent depth is the most important variable in determining the load capacity reduction. Table 2-3 lists the ultimate capacity of different specimens of TUD.2–11 with various dents along with their capacity reduction in percentage.

Table 2-3: Ultimate capacity of different specimens.

Specimen	P_{ult} (kN)	Capacity reduction (%)
TUD.1	119.08	0
TUD.2	111.63	6.3
TUD.3	102.64	13.8
TUD.4	79.79	33.0
TUD.5	106.40	10.7
TUD.6	98.79	17.0
TUD.7	94.14	20.9
TUD.8	102.14	14.2
TUD.9	86.57	27.3
TUD.10	102.95	13.5
TUD.11	91.98	22.8

For the dent imperfections located only 45 mm from the bottom end, 6–33% reduction was achieved. This decrease for the dented specimens with L_e = 73.3 mm was almost 10.5–21%, for the specimens horizontally indented at the mid-length the tube around 14 and 27%, and for the specimens with diagonal dents 13.5 and 23%.

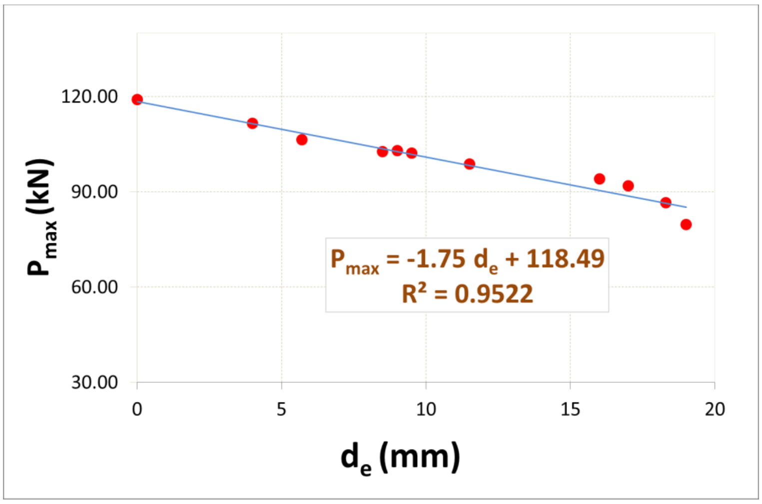

Figure 2-12: Decreasing trend of the ultimate load carrying capacity for different specimens with various values of d_e.

Figure 2-13 (a) shows the ultimate load for different specimens with horizontal dents, where results are given for three different values of L_e in different colours. One may observe that the closer the dent is to one end of the specimens the less the ultimate capacity. Furthermore, as d_e increased the ultimate load dropped for a certain value of L_e. Figure 2-13 (b) compares three specimens with horizontal and two specimens with diagonal dents with the same L_e, which indicates that the capacity decrease is proportional to the depth of the dent and the orientation of the dent seems not to have a marked effect.

2.2.4 Evaluations of the results against standards and other studies

A comparison of the results was drawn in this section on the basis of three parameters, viz. full-section strength, $P_{section}$, and slenderness parameter, λ_e, and non-dimensional buckling parameter, α. Note that these parameters are used in different studies and standards, in which $P_{section}$ is obtained using the yield stress (f_y = 0.2% proof stress). In Figure 2-14, dimensionless strength ($P_{ult}/P_{section}$) is plotted versus λ_e. Buckling and slenderness parameters are defined as Eq. (2.1) and Eq. (2.2):

$$\alpha = \frac{\mathrm{E\,t}}{\mathrm{f}_y\ \mathrm{D}_{tube}} \tag{2.1}$$

$$\lambda_e = \frac{\mathrm{E}}{250\ \alpha} \tag{2.2}$$

In these equations, E denotes the Young's modulus, D_{tube} denotes the diameter of the tubes and t is the thickness of the tubes. It is found that, for the present specimens with D/t ratio of around 48, $P_{ult}/P_{section}$ is very close to unity for the intact specimen indicating that the full capacity of the section is reached under compression as the whole section yields. It further appears that the data for the intact specimen consistently lies close to the results of the other studies [57-59] particularly Ref. [58], which demonstrates the consistency of the experimental data of the current study. Furthermore, the decreasing effect due to dent imperfections in the specimens is clearly seen through Figure 2-14.

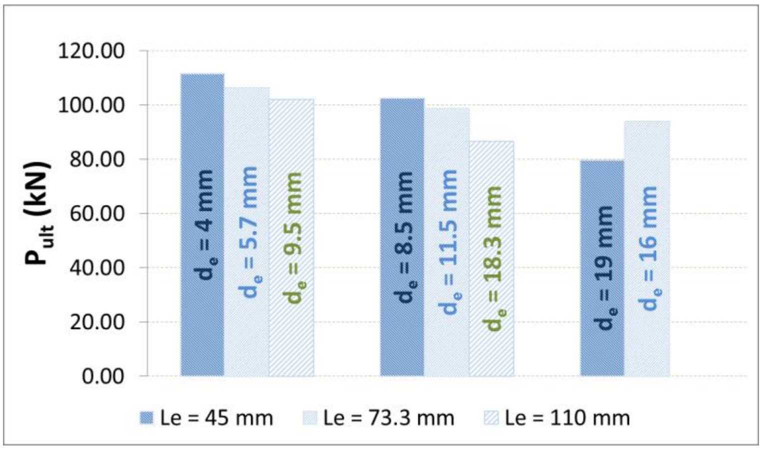

(a)

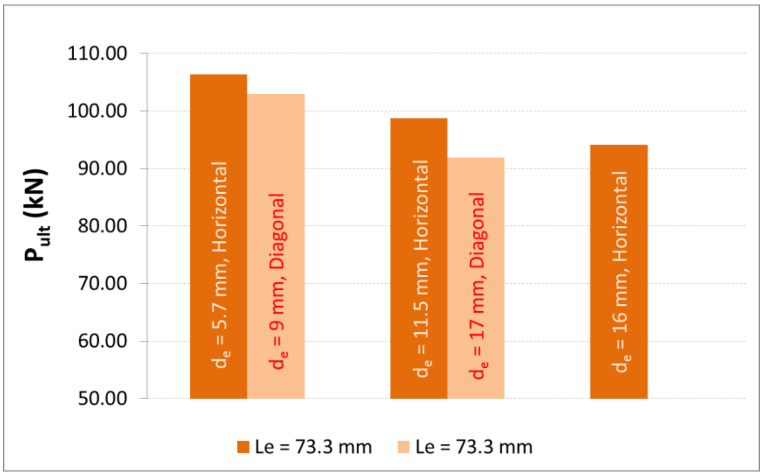

(b)

Figure 2-13: (a) Ultimate load for different specimens with horizontal dent, (b) comparison of load carrying capacity for the specimens with diagonal and horizontal dents with the same value of W_d.

2.2.5 Summary and conclusion

Plastic buckling of dented CHS tubes under axial compression was investigated through an experimental study. In total, 11 tests on short columns were carried out. Dent imperfections with various depths were introduced to different locations on the body of the specimens and ultimate axial strength was evaluated. The intact specimen TUD.1, as expected failed in *elephant foot* plastic buckling. The buckling bulge occurred approximately 15 mm from one end in a symmetric ring shape wave. Deformations for the dented specimens were initiated from the dented area such that the dents predominantly extended at both ends towards the tube ends, but the area underneath the dented zone remained unbuckled.

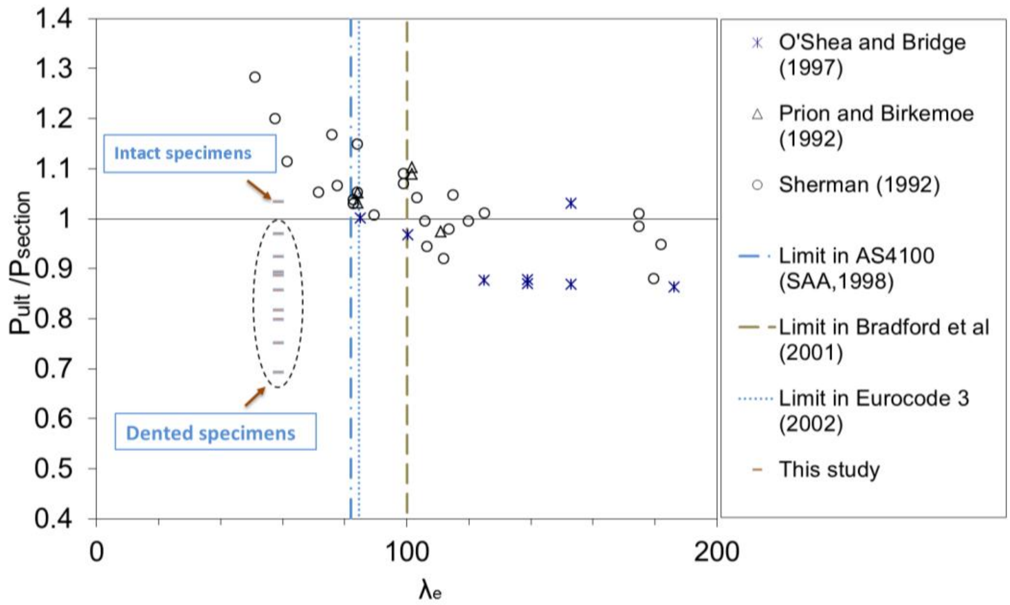

Figure 2-14: Evaluation of the results against the data of the previous references and standards, [1, 57-61]

It is believed that the axial stress flow lines deflected to the sides upon approaching the dent. TUD.1 (intact specimen) had a more stable response under axial load than the dented specimens. However, the nonlinear response started sooner after loading for the dented specimens. According to the load displacement curves, the dented specimens were more ductile than the intact specimen. SG.1 and SG.2 recorded negative values as expected, whereas SG.3 showed approximately zero for the axial stresses up until the inelastic region commenced.

Clearly the dent depth was the most important variable in determining the load capacity reduction. On the other hand for the dent imperfections located only 45 mm from the bottom end, 6–33% reduction was achieved. This range of decrease for the dented specimens with L_e= 73.3 mm was almost 10.5–21%. The closer the dent was to one end of the specimens the less the ultimate capacity. The capacity decrease was proportional to the depth of the dent, and yet the orientation of the dent seemed not to have a marked effect. It was found that the present data consistently lie close to the results of the other studies, which demonstrates the consistency of the experimental data of the current study.

2.3 Dented cylindrical shells under peripheral pressure

2.3.1 Introduction

Steel shells are commonly used as structural members. These structures are vulnerable to buckling when they are subjected to compressive stresses. Such structures are sometimes subject to external pressure, which is applied from outside the surface such as submarine pressure hulls. In some cases, an internal vacuum occurs due to discharge of a liquid so that atmospheric pressure acts as uniform external pressure.

Many researchers have investigated steel shells under different loading conditions to assess the buckling capacity. During the past fifteen years, Showkati and his co-authors extensively investigated such structures under vacuum. These experiments were mostly performed on structures with normal fabrication-related geometric imperfections. Showkati and Ansourian investigated the buckling behaviour of thin cylindrical shells under external pressure. They thoroughly assessed the effect of boundary conditions on the buckling behaviour of such structures [36]. Buckling of thin shells under atmospheric peripheral pressure was investigated by Showkati and Golzan and the effect of small amplitude imperfections was examined in this research [35]. Aghajari et al. conducted experiments on cylindrical shells with varying thickness [34]. They advised the usage of shells with less thickness variation subjected to external pressure. In recent years, Ghanbari Ghazijahani et al. investigated thin-walled steel structures with high *D/t* ratio [23, 46, 62-65]. It was found that even very small amplitude geometric irregularities may lead to big differences between experiments and theoretical predictions as these structures are highly sensitive to the geometrical features. Buckling behaviour of cylindrical shells with longitudinal joints was studied by Wang and Loizumi through both numerical and experimental modelling [66]. It was found that regardless of the geometric dimensions of the models buckling was strongly affected by features of the longitudinal joint, which can be rigid or flexible. Vacuum-induced buckling capacity of shells with *D/t* ratio of around 800 was investigated by De Paor et al. [67] and the effect of precisely measured imperfections was evaluated.

Weld-induced local imperfections were studied by Showkati and his co-researchers on cylindrical and conical shells [68-70]. Despite large local imperfections, such structures showed a stable post-buckling behaviour regardless of initial imperfections. In some cases weld-induced imperfections even had a strengthening effect on these structures.

Rathinam and Prabu, and Ghanbari Ghazijahani and Showkati numerically investigated thin structures with dent imperfections [14, 15, 71]. They showed the effect of location and depth of the dent on the critical buckling load of such structures. Despite these studies, no experimental data is found in the literature investigating the effect of dent imperfection on thin cylindrical shells under external pressure. To this end, the present section aims to explore the real behaviour of dented shells under uniform peripheral pressure. 14 specimens were tested which were indented to different depths. The results are compared with the available data in standards and design codes and some recommendations are made for real structures based on the presented results. Two instances of local dent-shaped irregularities on steel shell structures are shown in Figure 2-15.

Figure 2-15: Two instances of local dent-shaped irregularities on steel shell structures (courtesy of jenike.com).

2.3.2 Experimental modelling

Test rig

In the present experimental work, a MTS machine was employed in order to constrain the boundary regions of the pressure chamber, i.e. cylindrical shells (see Figure 2-16). Two plates were placed as top and bottom end plates so as to create a circumferential restraint all around the edges of the specimens. A circular groove was machined in each end plate to properly fix the specimens. The grooves were designed with a small tolerance in diameter which allowed the shell specimen to be conveniently installed. The plates were gripped by the MTS machine so that the vertical separation of the plates could be readily controlled. The grooves were fully sealed with a flexible sealant in order to avoid air leakage during the tests.

Table 2-4: Specimens and dent specifications.

Geometry	Specimen	Orientation of the dent	d (mm)	HD (mm)	HD/H	WD (mm)
D/t=758.85 t=0.2 (mm) H/D=1.45	EXCC.1	-	-	-	-	-
	EXCC.2	-	-	-	-	-
	EXCC.3	Horizontal	0.9	110	0.5	19
	EXCC.4	Horizontal	1.5	110	0.5	31
	EXCC.5	Horizontal	2.3	110	0.5	50
	EXCC.6	Horizontal	5	110	0.5	68
	EXCC.7	Vertical	0.7	110	0.5	21
	EXCC.8	Vertical	1.2	110	0.5	31
	EXCC.9	Vertical	1.8	110	0.5	54
	EXCC.10	Vertical	3	110	0.5	80
	EXCC.11	Diagonal (45°)	0.6	110	0.5	20
	EXCC.12	Diagonal (45°)	1.6	110	0.5	36
	EXCC.13	Diagonal (45°)	2.2	110	0.5	55
	EXCC.14	Diagonal (45°)	4.3	110	0.5	78

Specimens

Precisely fabricated thin specimens with *D/t* of around 759 (*D*=151.77) and *H/D* of 1.44 were used (see Figure 2-17 and Table 2-4). In Figure 2-17, *H,D* and *t* are the height, diameter and thickness of the specimens, *p* is the pressure, *d*, *LD* and *WD* are depth, height and width of the dent and *HD* is the distance of the centre of the dent from top edge of the shells. The material of the specimens was mild steel. Material properties were obtained from tensile coupon test conducted on the specimens showing a Young's modulus of 210 GPa and v=0.3 as the main material properties. The specimens had two sealed flat end caps attached, made from the same material as the shell specimens, which provided axial as well as radial loading.

Measurements

Five digital spring-loaded LVDTs with a maximum measuring capacity of 140 mm were used to measure the displacement at critical points on the specimens. “Micro-Measurements” strain gauges (CEA-06-240UZ-120) were utilised to record the strain during the application of the pressure. A digital pressure gauge was attached to the inside of the specimens which recorded pressure at very short intervals (see Figure 2-18).

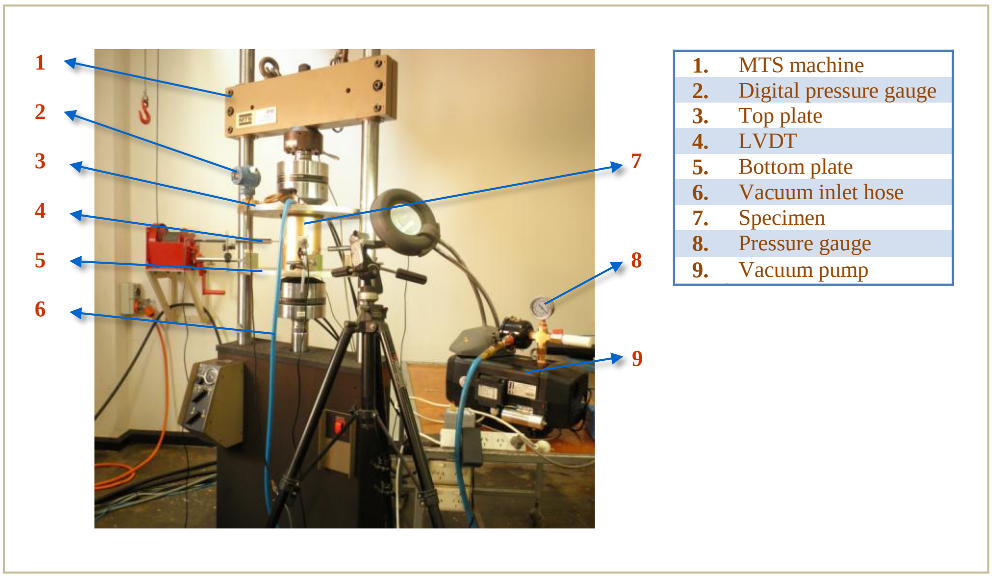

Figure 2-16: Overall view of the test apparatus.

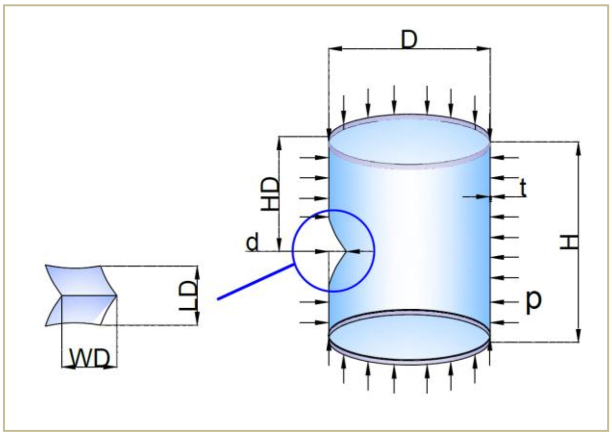

Figure 2-17: Schematic geometry of dented shells under external pressure.

Indentation process

Indentation was performed by a round-shaped indenter shown in Figure 2-19 made form a hard material. This indenter allowed the introduction of controllable dents on the body of the shells. Indentation was implemented by carefully moving the indenter over the surface of the shell and measuring to see if the created dent was desirable in terms of its depth and amplitude, i.e. height and width (see Figure 2-20).

Figure 2-18: (a) Digital pressure gauge, (b) sealed groove as boundary condition of the specimens.

Figure 2-19: (a) Finger LVDT, (b) indenter.

Figure 2-20: Dent imperfections with different depths and orientations (top row, specimens EXCC.7–10; middle row, specimens EXCC.3–6; bottom row, specimens EXCC.11–13).

2.3.3 Experimental results and discussions

Observations

Intact specimen

The intact specimen was used as a *control specimen*, and two replicates were tested in order to obtain a precise critical buckling load. These behaved very similarly with only a 2% difference in the critical load. At the initial stages of buckling there was no visible indication of displacements except a slight axial movement which is believed to have been the end plate attaching to the specimens, putting the whole specimen under axial stresses during loading. As the load increased, immediately prior to the buckling a very slight movement appeared on the surface of the specimens indicating the initiation of buckling. This was immediately followed by initial buckling with a pop sound indicating the creation of the first lobe(s) of buckling. This phenomenon was reported in Ref. [72] that for precisely fabricated specimens the initiation of buckling would be accompanied by the formation of more than one buckling waves. The initial buckling was followed by overall buckling in which the buckling waves encompassed the entire circumference one after another. After overall buckling, the load increased and the buckling waves deepened, at the same time the axial displacement considerably increased.

Dented specimens

The effect of the dent imperfections on the buckling mode depended on the depth of the dents. For the smallest horizontal dent, i.e. specimen EXCC.3, the yield line crossed the dent. However, for the medium and large horizontal dents (EXCC.4–EXCC.6) the dented area was placed between two longitudinal yield lines. This can be attributed to the fact that for specimens with larger dents, the dented area was strengthened as the material of the dented area was entered the inelastic zone or strain hardening region. This was due to the impact of the local load on the dented zone during the indentation process, which caused undulation of the body so that the second moment of inertia of the folded surface increases resulting in a stronger zone. Thus, the area adjacent to the dent was relatively more vulnerable to the buckling initiation. For vertically dented specimens, the dented area was always between the two yield lines such that one of the yield lines was very close and essentially parallel to the vertical dent (see Figure 2-21). In diagonally dented specimens, the dented area was similarly always completely between two longitudinal yield lines, and for the specimen with the largest diagonal dent the dented zone was placed exactly at the centre of the corresponding buckling lobe.

Figure 2-22, Figure 2-23 and Figure 2-24 show the progress of the buckling in three different specimens (EXCC.3, EXCC.6 and EXCC.14). In a similar way to the intact specimens, two phases of initial and overall buckling occurred in the dented specimens. Note that for specimens with large dents the buckling was initiated at the dented area such that the initial buckling lobe fully encompassed the dented zone. However, in some of the cases with the smaller dents, regardless of the orientation of the dent, the buckling was not always initiated exactly at the dented region. However, initial buckling mostly occurred at or very close to the dented area.

Figure 2-21: Dent imperfection's position in different specimens after buckling.

Figure 2-25 shows variation of radial displacements with pressure for different specimens measured at four different circumferential positions by means of the mentioned LVDTs. Note that the four LVDTs, i.e. T.1 through T.4, were placed at 90° intervals around the circumference at mid-height of the specimens, with T.3 corresponding to the centre of the dented zone. As can be seen, displacements were mostly linear prior to buckling. After the initial buckling, a significant jump was detected in the load-displacement curves followed by development of the buckling around the whole circumference.

Table 2-5: Experimental buckling load for the present specimens.

Specimens	**Initial buckling (kPa)**	**Overall buckling (kPa)**	P_{dented}/P_{intact}	**Difference (%)**
EXCC.1	-12.6	-12.6	-	-
EXCC.2	-12.33	-14.6	-	-
EXCC.3	-8.6	-15.22	0.69	31.0
EXCC.4	-11.5	-13.9	0.92	7.7
EXCC.5	-9.84	-10.6	0.79	21.1
EXCC.6	-10.9	-13.42	0.87	12.6
EXCC.7	-11.35	-12.64	0.91	8.9
EXCC.8	-11.56	-13.19	0.93	7.3
EXCC.9	-9	-10.2	0.72	27.8
EXCC.10	-9.91	-9.91	0.80	20.5
EXCC.11	-12.7	-13.9	1.02	-1.9
EXCC.12	-9.81	-9.81	0.79	21.3
EXCC.13	-10.84	-13.99	0.87	13.0
EXCC.14	-11.2	-13.07	0.90	10.1

Thus, each jump on the curves represents a formation of a buckling lobe until overall buckling covered the specimens. After the overall buckling, a steady post-buckling stage was detected in all specimens, accompanied by deepening of the buckling waves and axial shrinkage of the specimens. Strain values for the three different specimens with largest dents are plotted in Figure 2-26, in which S.1 was located at the dented area and S.2 on the intact zone on the next quarter at the mid-height of the specimens.

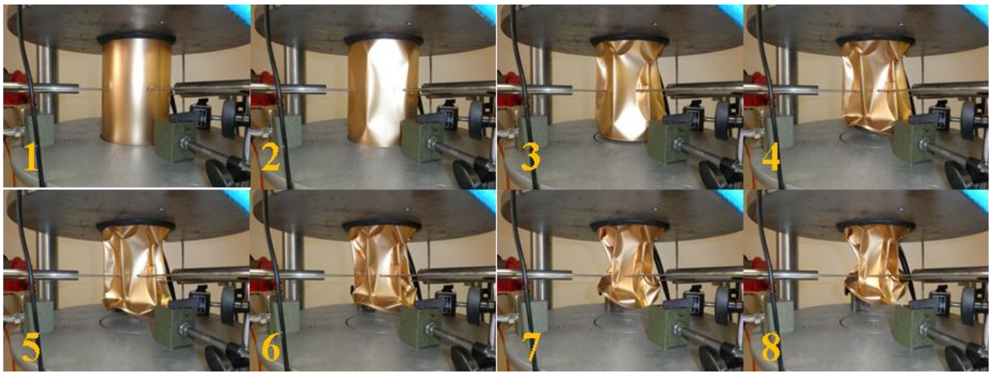

Figure 2-22: Progress of buckling in EXCC.3 from initial buckling to collapse.

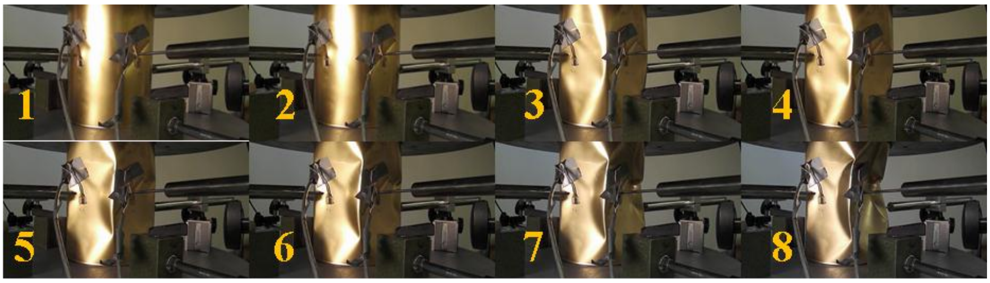

Figure 2-23: Progress of buckling in the specimen with the largest diagonal dent (EXCC.14).

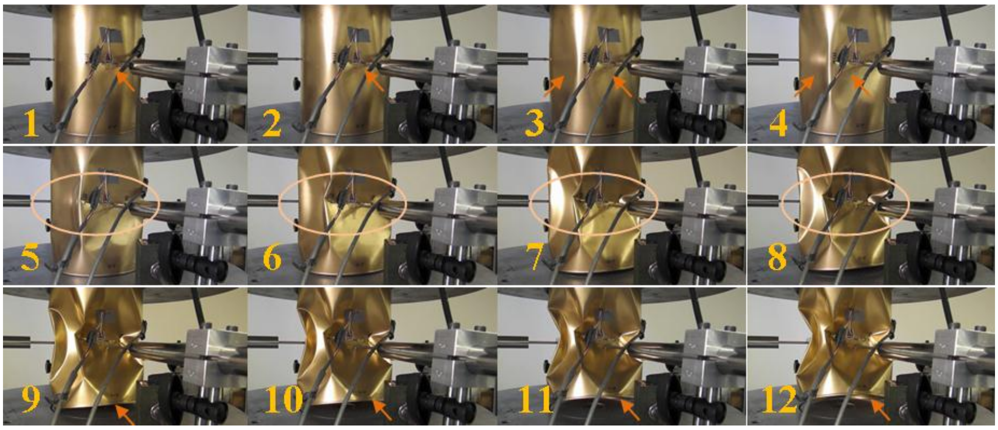

Figure 2-24: Development of buckling in EXCC.6 with the pressure increase (progress of deformations marked).

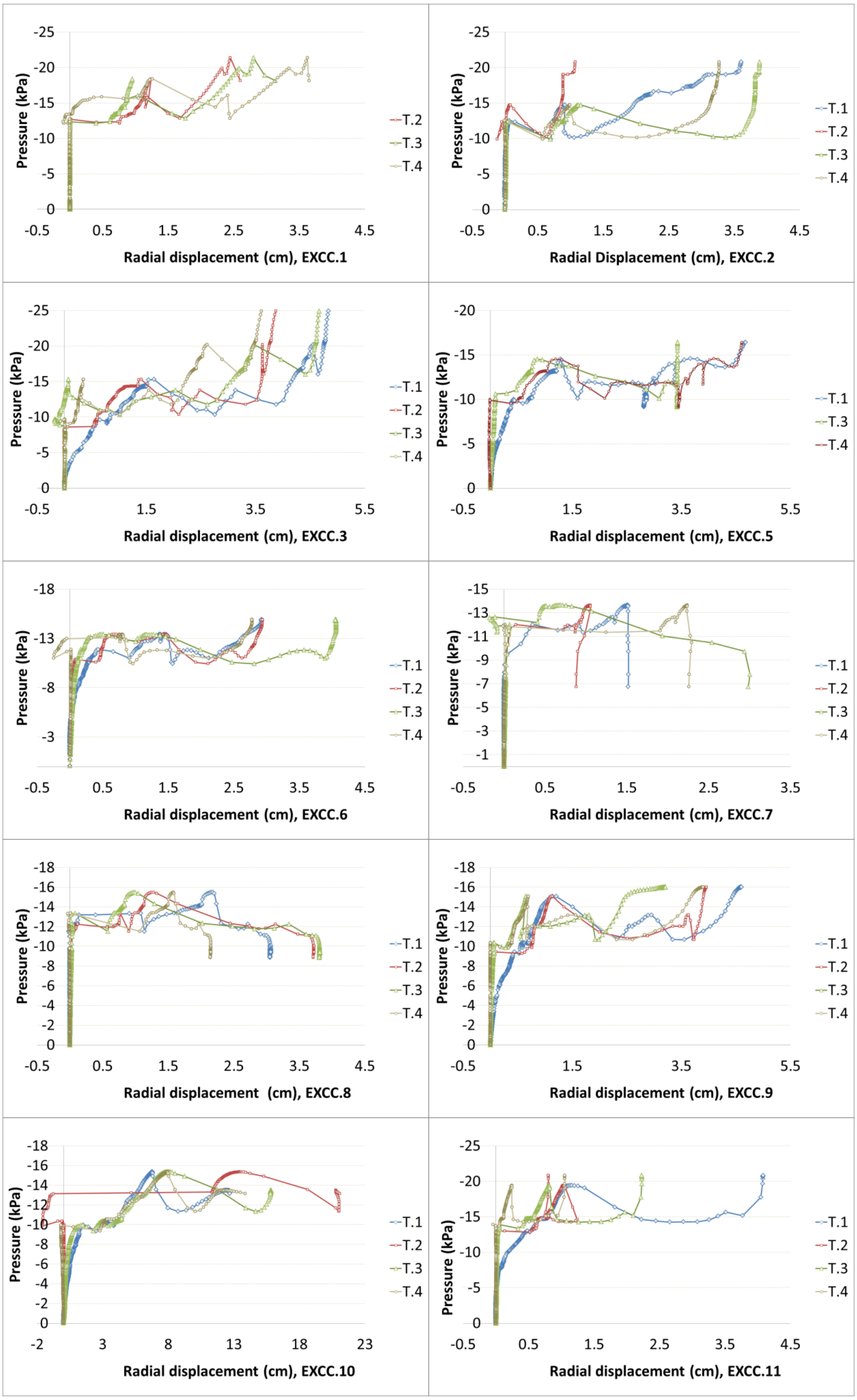

Continued in the next page.

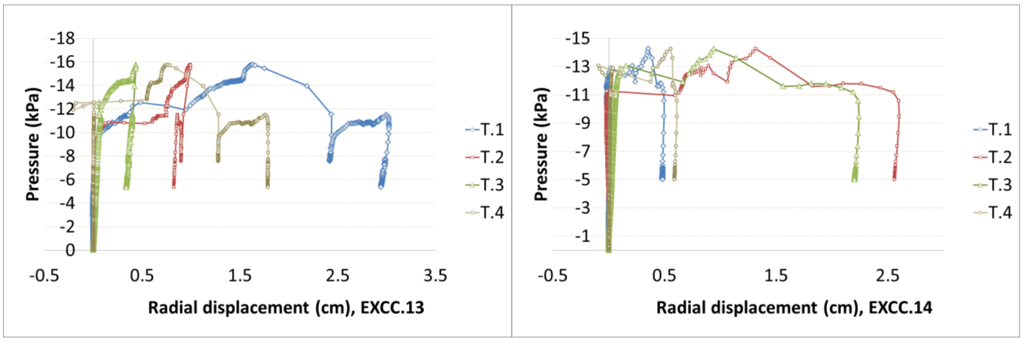

Figure 2-25: Radial displacement and development of the buckling lobes in different specimens.

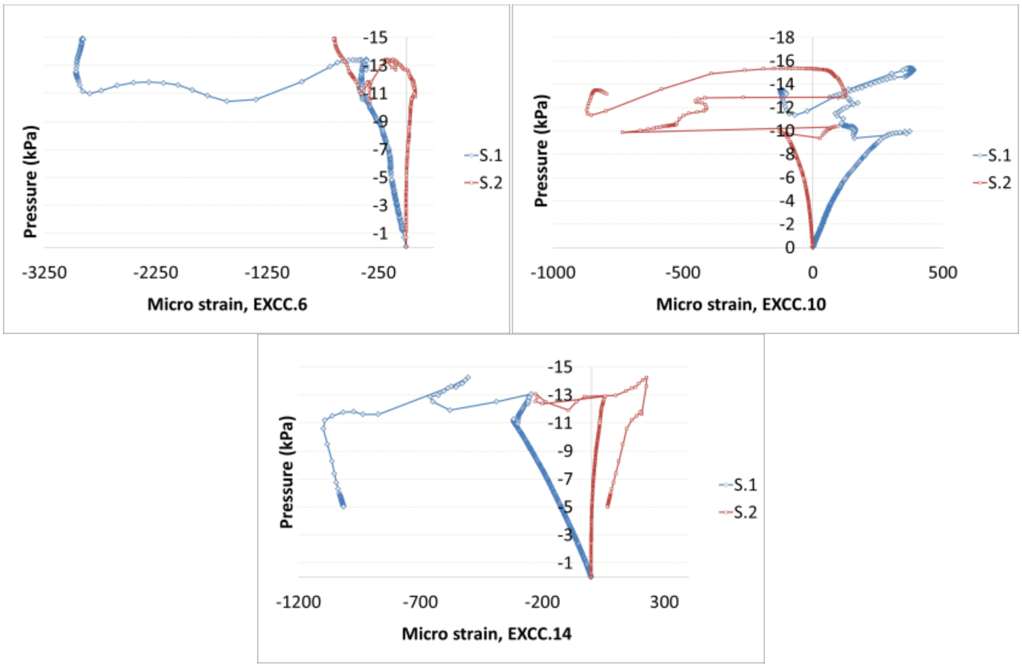

Figure 2-26: Strain data on the three different specimens with largest dents.

Axial movement of the specimen and yield lines

As mentioned earlier, the present specimens had end caps attached to them so that axial stresses occured during loading. This phenomenon was quite clear throughout the load application. For lower values of load a uniform axial shrinkage of the specimens was observed in close review of recorded videos. Overall buckling was accompanied by around 10 mm of axial displacement detected at the bottom of the specimens. As the load was increased the buckling lobes deepened and the axial displacement developed up to approximately 1/3 of the initial height of the specimens (Figure 2-27).

Figure 2-27: (a) Different specimens after collapse, (b) axial displacement after collapse.

It was of interest that very small-angled V-shaped yield lines occurred between each pair of buckling lobes, which became severely distorted as the load grew after the overall buckling. These yield lines were mostly zigzagged near both ends of the specimens so that the whole specimen was tilted towards the side in which greatest twisting of the yield lines occurred (randomly in each specimen). It is noteworthy that the bottom end of the specimens developed a curved shape after collapse of the specimens (see Figure 2-28).

Figure 2-28: Buckling and curved shape of the bottom end of the specimens.

Buckling capacity of the present specimens

Figure 2-29 shows the buckling load of the specimens plotted against the depth of the dent (d) and against the parameter $\zeta = d\ WD$, which includes two main geometric parameters of the dent imperfection (depth and width). The decreasing trend is clearly seen in Figure 2-29, which shows that the specimens were affected by the dent imperfection. Note that the trendlines can definitely be updated if and when further experimental data is obtained in the future. The maximum effect of the dent imperfection occurred in EXCC.3 with 31% decrease in capacity (see Table 2-5). Following that, EXCC.9, EXCC.12, EXCC.5 and EXCC.10 experienced the capacity reduction of around 28%, 21%, 21% and 21% respectively. The capacity decrease in the other specimens was less than 20% if compared with the intact specimens. The buckling capacity of the specimens considering various orientations is shown in Figure 2-30. The average difference for the specimens with horizontal dents was around 18% in comparison with the intact specimens. For the specimens with vertical and diagonal dents the average difference was 16% and 11% respectively, indicating that the horizontal dent had more effect indeed, on the buckling capacity of the current shell specimens. This effect was followed by vertical and inclined dents respectively.

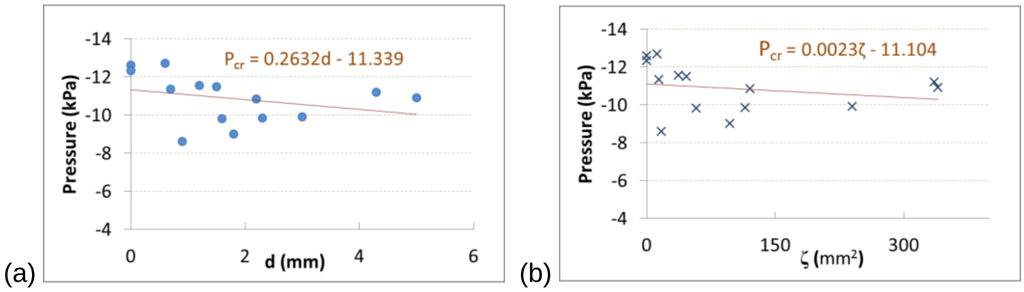

Figure 2-29: Buckling load versus: (a) the depth of the dents, (b) different orientations.

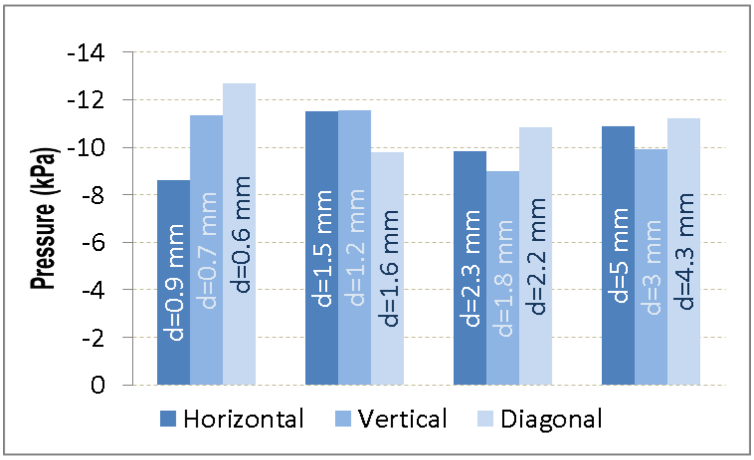

Figure 2-30: Buckling load of the specimens considering different orientations.

2.3.4 Comparisons and evaluations

The results of the current experimental work were evaluated against existing estimations available as design codes and other recommendations (see Table 2-6). Jawad proposed an equation for the buckling of shells structures [73]. Another estimation, known as David Taylor Model Basin (DTMB) formula was proposed for the buckling load of a cylindrical shell [74]. British Standards Institution (BSI) proposed a design chart by which a parameter ε can be obtained [75], which is a function of $2R/t$ and $H/2R$ and can be used to calculate the elastic instability pressure of cylindrical shells of revolution. European Convention for Constructional Steelwork (ECCS) also proposed a formula in terms of β_{min}, a function of t/R and H/R, the main geometric ratios of a cylindrical shell [76]. Using design charts for different geometries of cylindrical shells, the value of β_{min} can be extracted and the buckling pressure of different cylindrical shells can be calculated. These formulas are given in

Table 2-6 in which t is the thickness, R is the radius, E is the Young's modulus, H is the height, D is the diameter, ε is a function of $2R/t$ and $H/2R$.

Table 2-6: Theoretical predictions of codes and other studies.

Equation	**Code/Reference**
$P_{cr} = \dfrac{0.92E\,(t/R)^{2.5}}{H/R}$	Jawad, 1994
$P_{cr} = \dfrac{2.6E\,(t/D)^{2.5}}{H/D - 0.45\,(t/D)^{0.5}}$	DTMB, Ross, 2007
$P_{mc} = \dfrac{Et\varepsilon}{R}$	BSI, 2009
$P_{cr} = E\dfrac{t}{R}\beta_{\min}$	ECCS, 1988

Figure 2-31 shows the comparison of the critical buckling load of the current specimens with the above-mentioned design codes and theoretical predictions. As can be seen, theoretical estimations overestimate the buckling load of the specimens in a similar way that other studies reported. For example, for similar specimens under vacuum Niloufari et al. reported a difference of more than two times compared with Jawad's equation [70]. A similar range of discrepancy was also obtained for the specimens tested by Fatemi et al. in which 12 imperfect cylindrical shells were tested under vacuum [69].

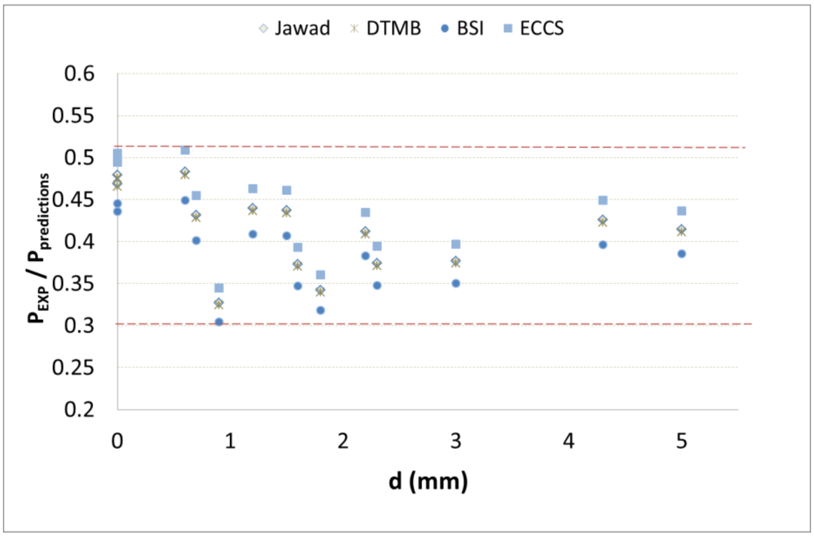

Figure 2-31: Comparison of the critical buckling load with available design codes and theoretical predictions.

The differences between the theoretical estimations and experiments could be, in essence, due to (i) geometrical imperfections or out-of-roundness arising from the fabrication process, as such specimens possessed very low transverse strength, and are accordingly more vulnerable to local effects, (ii) different assumed boundary conditions, which can vary from theory to different experimental circumstances, (iii) material non-homogeneity, and (iv) as mentioned earlier, current specimens possessed end plates so that additional axial stresses were developed. As a consequence of the latter, the buckling load can be considerably affected by the axial load imposed by the end plates. Therefore, the comparisons suggest acceptable consistency considering the above-mentioned points, although future FE modelling would result in more consistency of the results.

2.3.5 Imperfection tolerance in design codes and present tests

A few design codes and standards have defined tolerance values for depth and amplitude of the imperfections in shells of revolution. Figure 2-32 shows ECCS, EN and DIN limit bounds for local imperfections respectively, in which allowable values have been proposed mostly based on the thickness of the shell structures [77-79]. It was pointed out that shells with local imperfections of larger than a certain fraction of the thickness must not be used as a structural member.

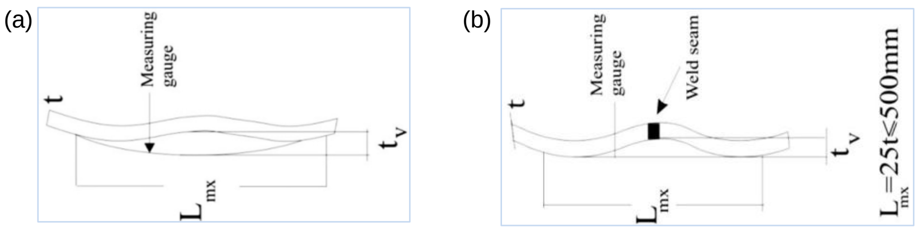

ESSCRec, 2008	ENV 1993-1-6, 2007	DIN 18800-4
L=Ir:t_r=W t_r<1% of L_{mx}	$L_{mx}=L_g$:$t_r=\Delta w_0$ $t_r \leq 0.006L_{mx}$ OR (0.01 L_{mx}, 0.016 L_{mx} for different classes)	t_r<1% of L_{mx}

Figure 2-32: Initial dimple tolerated in existing codes, (a) in longitudinal direction, (b) in hoop direction [69, 70].

However, Showkati and his co-researchers in three respective experimental programs conducted on different shells with weld-induced local imperfections showed that the recommendations of the mentioned standards are not necessarily and always applicable for all kinds of local imperfections [68-70]. They drew a different conclusion regarding the local imperfections because their experiments showed that some types of local imperfections even had a slightly positive effect on the buckling load. A similar phenomenon was observed in the most recent experimental study of Ghanbari Ghazijahani et al. on similar specimens, in which especially severely dented specimens experienced a locally stiffened area against axial loading [49].

Table 2-7 shows the geometric values of the dent imperfections in the current study, which all exceed the magnitudes tolerated by the standards. Nonetheless, in some specimens the effect of the local dent is not significant enough to be differentiated from normal fabrication-related imperfections, which are allowed in the mentioned design codes. In view of all these, it seems that standards need to be reconsidered, especially when it comes to damaged or dented areas on the shells structures.

Table 2-7: Geometric parameters of the dents considering the mentioned design standards.

Specimen	**d/t**	**d/WD (%)**	**WD/t**
EXCC.3	4.5	21.11	95
EXCC.4	7.5	20.67	155.0
EXCC.5	11.5	21.74	250
EXCC.6	25	13.60	340
EXCC.7	3.5	30.00	105
EXCC.8	6	25.83	155
EXCC.9	9	30.00	270
EXCC.10	15	26.67	400
EXCC.11	3	33.33	100
EXCC.12	8	22.50	180
EXCC.13	11	25.00	275
EXCC.14	21.5	18.14	390

Perhaps it would be advisable to categorise the geometrical imperfections in design codes into normal imperfections and large imperfections, e.g. dent or gouges caused by physical contacts. To put it in a nutshell, further studies might still be required to thoroughly clarify the effect of different shapes and amplitude of local imperfections on shell structures.

2.3.6 Conclusion

In the present section, 14 thin-walled intact and dented cylindrical shells were tested under external pressure. The key findings are in summary:

- At the initial stages of buckling there was no visible indication of displacements except a slight axial movement, which occurred due to the attached end plate to the specimens. The commencement of the buckling occurred by development of one or more lobes.
- Dent imperfection affected buckling mode of the present specimens depending on the depth of the dents such that for the smallest horizontal dent yield line crossed the horizontal dent and for the medium and large horizontal dents the dented area was placed within the two longitudinal yield lines. For vertically and diagonally dented specimens the dented area was always within the two nearby yield lines.
- When dent imperfection had a strengthening effect, the area adjacent to the dent was more vulnerable to the buckling initiation.
- For specimens with large dents, buckling was initiated from the dented area. In cases of the smaller dents, and regardless of the orientation of the dent, buckling was not always initiated exactly at the dented region. However, buckling mostly occurred very close to the dented area.
- Throughout the loading application, a uniform axial shrinkage of the specimens was observed at lower loads when recorded videos were closely reviewed after the tests. As the load was increased the buckling lobes deepened and the axial displacement developed up to approximately 1/3 of the initial height of the specimens.
- Some small-angled V-shaped yield lines occurred between each pair of the buckling lobes. These were mostly zigzagged near both ends of the specimens so that the whole specimens were tilted towards the side on which the severest twisting of the yield lines had occurred.
- The maximum effect of the dent imperfection occurred in EXCC.3 with a 31% decrease in capacity. Following that, EXCC.9, EXCC.12, EXCC.5 and EXCC.10 experienced capacity reductions of 28%, 21%, 21% and 21% respectively.

- The average difference between the specimens with horizontal dents and the intact specimen was 18%. For the specimens with vertical and diagonal dents the average difference was 16% and 11% respectively, which indicates that the horizontal dent had more effect on the buckling capacity of the current shell specimens.
- Perhaps, it would be advisable to categorise the geometrical imperfections in design codes into normal imperfections and large imperfections, e.g. dent or gouges caused by physical contacts. Further studies might be still required to thoroughly clarify the effect of different shapes and amplitude of local imperfections on the shell structures.

Section 2.4 has been removed for copyright or proprietary reasons.

It has been published as: Ghanbari Ghazijahani, T., Jiao, H., Holloway, D., 2015. Experiments on locally dented conical shells under axial compression, Steel & composite structures, 19(6) 1355-1367

2.5 Cylindrical shells with cutout imperfections under axial compression

2.5.1 Introduction

Cylindrical shells as important structural elements are often found with various local geometric non-uniformities, among which are different forms of openings. Such openings are widely used as the entrances of the steel towers for maintenance and any other accessibility purposes. These cutouts are also employed for the attachment of electrical devices to such structures.

Figure 2-49: Entrance door of a wind turbine tower (courtesy of ramblingsdc.net).

Many researchers have investigated the structural behaviour of such structures with various openings. Tennyson [42] investigated the effects of unreinforced circular cutouts on the buckling behaviour of circular cylindrical shells subjected to axial compression. A membrane stress distribution and isoclinic patterns were defined around the edge of the opening in this research. Numerical and experimental methods were used by Jullien and Limam to investigate the stability of cylindrical shells with openings [44]. The analysis showed that the buckling load was quite sensitive to the opening angle or circumferential size of a cutout. An Area Replacement Method (ARM) of strengthening the circular cutouts in a cylindrical shell on the buckling strength of such shell was studied analytically and experimentally by Bennett et al. [37]. Buckling of steel cylindrical shells with elliptical cutouts was studied by Shariati and Rokhi [41]. It appeared that the buckling load decreased when the width of cutouts was constant and height increased. Simple design rules were proposed by Eggwertz and Samuelson considering theoretical analyses and experimental data for shells with rectangular cutouts [43]. Aluminium cylindrical shells with rectangular cutouts in different locations along the specimens were studied by Han et al. [39] who showed that the location and the size of an opening significantly affected the buckling load of such structures. Steel shells with elliptical cutout under axial compression were studied numerically and experimentally by Shariati and Rokhi [40]. They showed that longer shells were much more sensitive to the position of a cutout.

This section investigates the effect of different longitudinally located cutouts at the end zone of the shells, which may represent different entrances or doors in steel hollow section, e.g. towers (see Figure 2-49). The main objectives of this section are to address: (i) experimental modelling of the entrance-shaped cutouts, (ii) compression tests of different shapes of such perforated shells, (iv) evaluation of the effect of different shapes of the cutout and, (iii) comparison of the results with the available data.

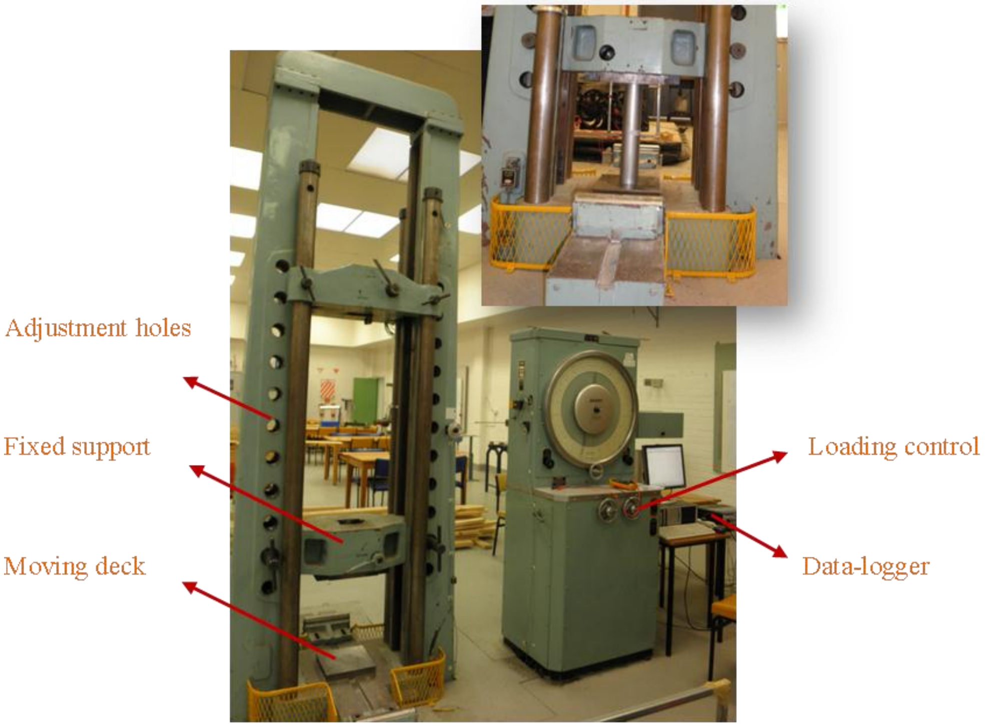

Figure 2-50: Overall view of the test rig.

2.5.2 Experimentation

Test rig

An AVERY machine was employed for the experimental program of this section (Figure 2-50). The machine was calibrated by Australian Calibration Service (ACS) to ensure the accuracy of the function of the machine. The AVERY machine was capable of applying a static loading with a controllable loading rate.

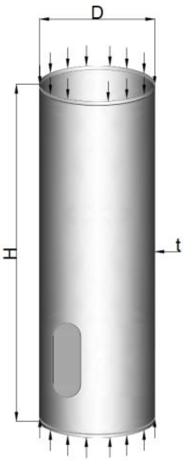

Figure 2-51: A cylindrical shell with cutout under axial compression.

Test specimens were mild steel tubes with *D/t* ratio of 47.6 (*D*=76.2 mm, *t* =1.6 mm and *H*=400 mm, see Figure 2-51). Both ends of the specimens were machined to allow the top and bottom plates to contact the specimens uniformly. A CHEVALIER 2040 VMC, three axis CNC cutting machine was utilised to cut the cutouts in different shapes. As mentioned earlier, the main objective of selection of such cutouts are to assess the structural behaviour of the shells when they act as entrance-shaped cutouts. Cutouts in five different forms were adopted: (i) rectangular cutouts with two semi-circular ends (RCSC), (ii) semi-RCSC cutouts with the same top shape as RCSC yet half height and a flat bottom (SRCSC), (iii) elliptic shapes (FOVA), (iv) semi-oval shaped openings (SOVA) and (v) rectangular cutouts with filleted corners (RECT). These shapes are all illustrated in Figure 2-54. An intact specimen was also included as a control specimen. Stress-strain relationship and the material properties of the specimens were obtained through tensile coupon tests, as presented in Table 2-1 (yield and ultimate stresses and Young's modulus) and Figure 2-52.

Geometric features of the cutouts are seen in Figure 2-53 and Figure 2-54. A constant ratio of b/a=0.4 was applied for all full cutout specimens and b/a=0.8 for all semi cutouts so that different specimens could be compared directly. For all of the specimens, a distance of 50 mm from the bottom end was taken as the lower boundary limit of the cutout.

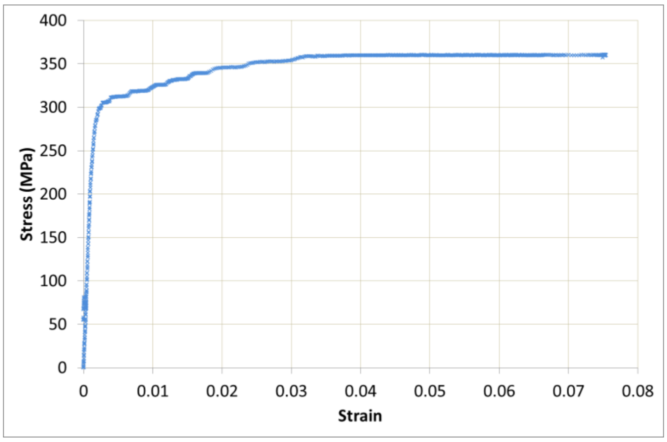

Figure 2-52: Stress-strain curve of the material.

Note that the cutout was made at the area opposite to the seam weld of the specimens to avoid any possible influence of the residual stresses caused by the welding. Three different values for a were considered representing small, medium and large cutouts (see Table 2-12). Sharp corners were avoided in all cutout designs to minimise/limit stress concentration.

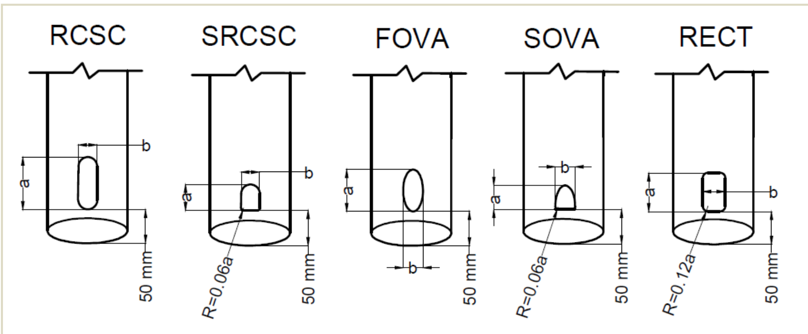

Figure 2-53: Schematic illustration of the cutout shapes and geometric parameters (dimensions a and b are given in Table 2-12).

End-shortening of the specimens while loading was accurately recorded by the AVERY machine. CEA-06-240UZ-120 Micro-Measurements strain gauges were used and attached to the most critical points (side edge of the cutout and near the bottom edge – further details are given later in this section) to record the strain values and evaluate the load-strain behaviour of such areas.

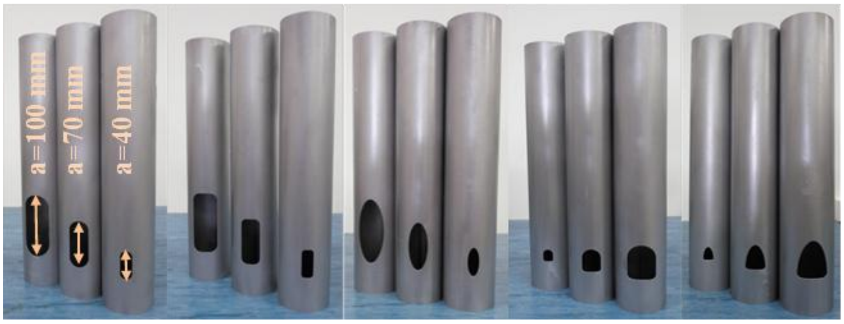

Figure 2-54: Different shapes of cutouts, full shaped cututs and half shaped holes.

2.5.3 Results and discussions

Observations

Intact specimen

Figure 2-55 shows the intact specimen after the buckling, displaying a symmetric ring-shaped bulging wave near the base commonly referred to as *elephant foot* buckling.

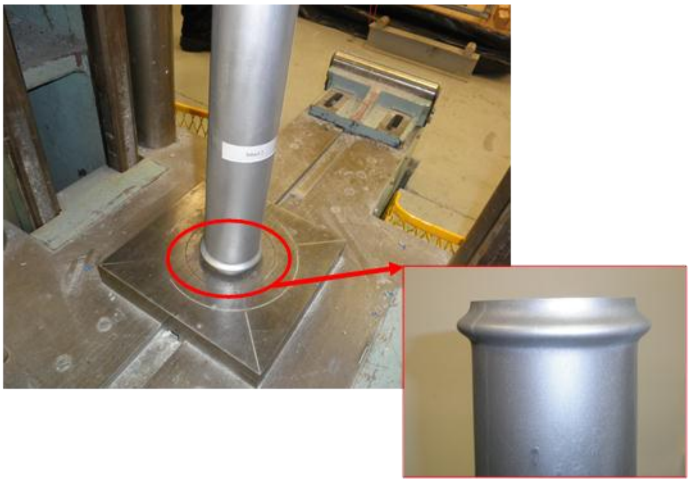

Figure 2-55: *Elephant foot* mode of buckling in the intact specimen.

This mode of buckling occurred at around 15 mm from one end of the intact specimens and encompassed the whole circumference of the buckled section. A gradual decrease of the axial load was seen after initiation of the buckling. Loading was continued until the buckling wave covered the whole hoop direction of the tube which was eventually accompanied by a significant drop in the loading.

Specimens with cutout

The specimens with a cutout showed a unique buckling mode in which the edge area of the tubes together with the cutout were influenced by the buckling phenomenon. Presumably this mode of buckling has not been reported by other investigators. In this mode, buckling was initiated at the edge of the cutouts with outward sine-waves in a symmetric arrangement. As the load increased, the waves deepened and developed to the adjacent area while at the same time buckling of the opposite side of the tubes was detected in an *elephant foot* mode (see Figure 2-56). It should be mentioned that the *elephant foot* mode of buckling developed only nearly up to the half of the section (see Figure 2-57) such that the area below the cutout was not affected whatsoever. Figure 2-57 also shows the buckling in RCSC.3 specimen around the cutout and the edge area.

Table 2-12: Specifications of the cutouts (see Figure 2-53 and Figure 2-54 for the details of "*a*" and "*b*").

Specimens	**RCSC.1**	**RCSC.2**	**RCSC.3**
a (mm)	40	70	100
b (mm)	16	28	40
Specimens	**RECT.1**	**RECT.2**	**RECT.3**
a (mm)	40	70	100
b (mm)	16	28	40
Specimens	**FOVA.1**	**FOVA.2**	**FOVA.3**
a (mm)	40	70	100
b (mm)	16	28	40
Specimens	**SRCSC.1**	**SRCSC.2**	**SRCSC.3**
a (mm)	20	35	50
b (mm)	16	28	40
Specimens	**SOVA.1**	**SOVA.2**	**SOVA.3**
a (mm)	20	35	50
b (mm)	16	28	40
Specimens	**SRECT**	**-**	**-**
a (mm)	100	-	-
b (mm)	40	-	-

Note: All full cutouts (RCSC, FOVA and RECT) have a fixed ratio *a/b* = 2.5; semi cutouts (SRCSC and SOVA) have fixed ratio *a/b* = 1.25. In all cases *b* = 21%, 36.7% and 52.5% of the diameter for the three variations of each shape.

It is interesting to note that buckling in the specimens RCSC.3 and RECT.3, which had the largest cutout, was initiated near the top of the cutout whereas with the decrease in the size of the cutout the initial buckling wave approached the centre of the opening. Figure 2-58 shows the buckling waves occurring in the three different RECT and RCSC specimens in which RECT.3 experienced the buckling wave initiation at around 0.23*a* from the top of the cutout, RECT.2 at 0.32*a* and for the smallest cutout, the buckling wave initiated at the middle of the height of the hole.

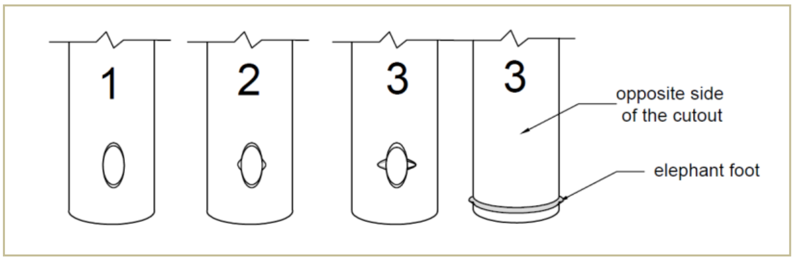

Figure 2-56: Deformation and buckling stages in a FOVA specimen.

Figure 2-57: Two forms of buckling in RCSC.3 specimen.

Figure 2-59 shows FOVA, SRCSC and SOVA specimens after buckling, in which for FOVA and SRCSC the buckling waves occurred in the mid-height of the cutout. In Figure 2-59, the compressive areas of the buckling waves showed a kind of paint-flaking over the surface of the tubes. Progress of buckling is seen in Figure 2-60 for the specimens RECT, RCSC and FOVA at three different stages of loading.

Capacity of the specimens

Table 2-13 shows the ultimate capacity and the ratio of the capacity of the specimens with cutouts to the ultimate load of the intact specimen. The decreasing trend of the capacity was plotted in Figure 2-61 and Figure 2-62 for the present specimens. Parameter *b* is the width of the cutout which is the most important geometric parameter of the cutout area since for high values of *b* the cross section has lost more material so that the tubes were weaker against the buckling. A parameter μ was also defined as $\mu=Dab/t$ in which the D/t ratio was included as well as the two major geometric parameters of the cutout, *a* and *b*.

Figure 2-58: RECT and RCSC specimens after buckling.

Figure 2-59: FOVA, SRCSC and SOVA specimens after buckling.

Figure 2-62 shows that the cutout had less effect on SOVA and SRCSC specimens (semi-height cutouts) in comparison with the full-shaped cutouts. The smallest cutouts (SOVA.1 and SRCSC.1) had a capacity loss of around

12% and 10% relative to the intact specimen, while the capacity was decreased by 24% in SOVA.3 and SRCSC.3, i.e. the largest cutouts.

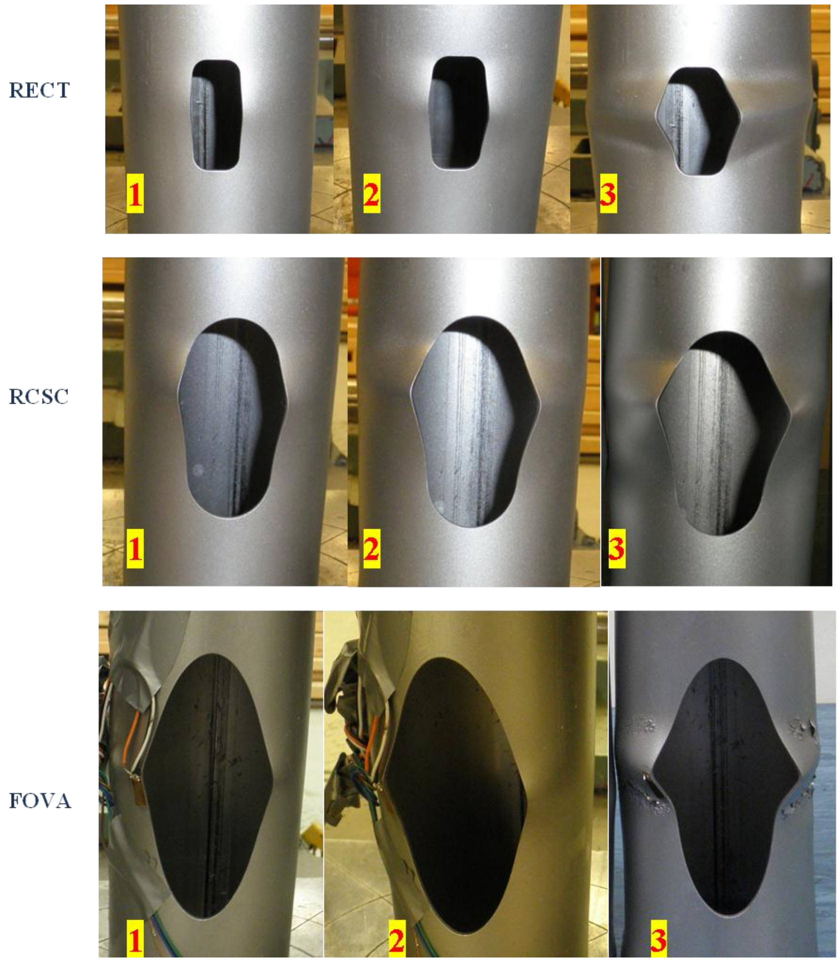

Figure 2-60: Buckling progress in different specimens.

Moreover, Table 2-14 lists the average capacity reduction of five different specimens with various shapes of the cutouts. The full-shaped openings (RCSC, RECT and FOVA specimens) decreased the capacity by around 20%, whereas this reduction was 17.5% for the semi-shaped cutouts. This table also shows the average ratio of P_{ult}/P_{intact} for small, medium and large cutouts with different shapes which are obtained as 0.87, 0.81 and 0.74 respectively indicating the effect of shape on the buckling capacity of these structural elements.

The effect of the height of a cutout can be clearly seen in Figure 2-63, in which the capacity was plotted versus the height of the specimens with the same widths. The height of the cutout had a slight effect on the capacity which was always less than 5% in different specimens with same widths. Moreover, the effect of the shape of the cutouts can be seen in Figure 2-63 as the bar charts show the results of different specimens with same widths and heights.

Table 2-13: Capacity of the specimens.

Specimen	**P_{ult} (kN)**	**μ (mm^2) × 10^3**
Intact	117.50	0.00
RCSC.1	99.27	30.60
RCSC.2	94.59	93.71
RCSC.3	85.43	191.25
SRCSC.1	103.56	15.30
SRCSC.2	94.13	46.86
SRCSC.3	88.94	95.63
FOVA.1	103.52	30.60
FOVA.2	95.41	93.71
FOVA.3	85.16	191.25
SOVA.1	105.62	15.30
SOVA.2	97.03	46.86
SOVA.3	89.07	95.63
RECT.1	100.72	30.60
RECT.2	93.60	93.71
RECT.3	84.2	191.25
SRECT	93.5	191.25

As an additional test, specimen SRECT was strengthened by two stiffeners (2PL: 140 × 9 × 3.2) covering the longitudinal edges of the specimen with the largest rectangular cutout (RECT.3), as seen in Figure 2-64. Welding was performed only on the one side of the stiffener opposite to the cutout to ensure that the edge area of the cutout was minimally affected by adverse effects of the welding. Buckling of this specimen commenced by tilting of the stiffener and simultaneously buckling of the tube adjacent to the stiffener at the top end of the cutout in a similar location to the RECT.3 specimen. Buckling deepened accordingly and developed to form the *elephant foot* buckling at the base on the opposite side of the cutout. Progress of the deformations is seen in Figure 2-65. It is noteworthy that the stiffener recovered almost 33% of the lost capacity which had occurred due to the cutout.

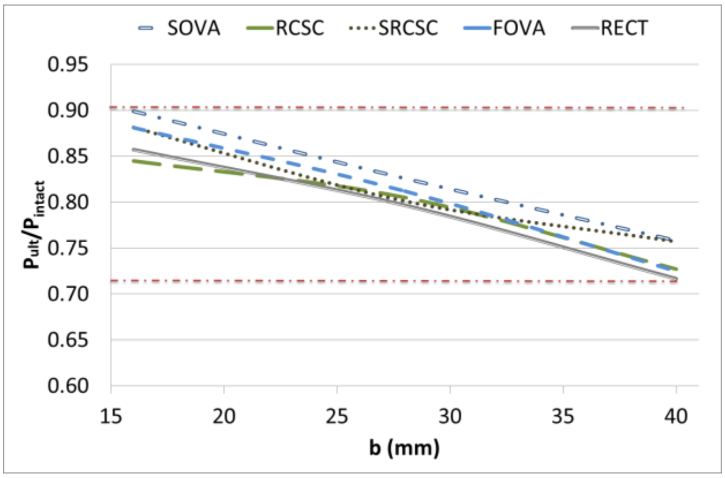

Figure 2-61: Capacity of the specimens with different cutouts versus the width of the cutouts.

(a)

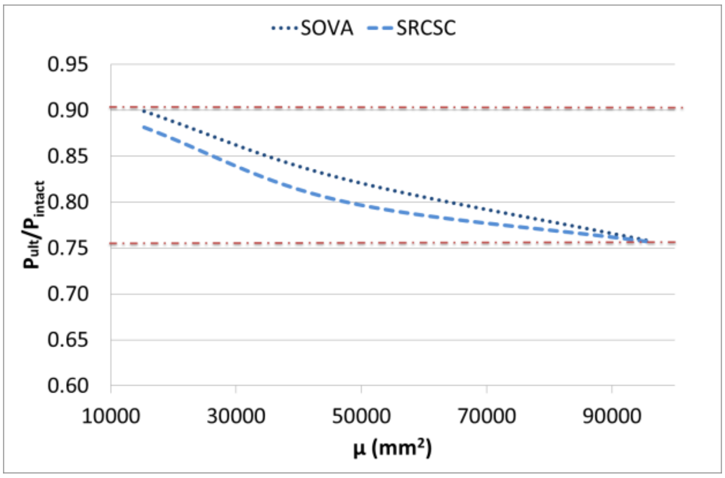

(b)

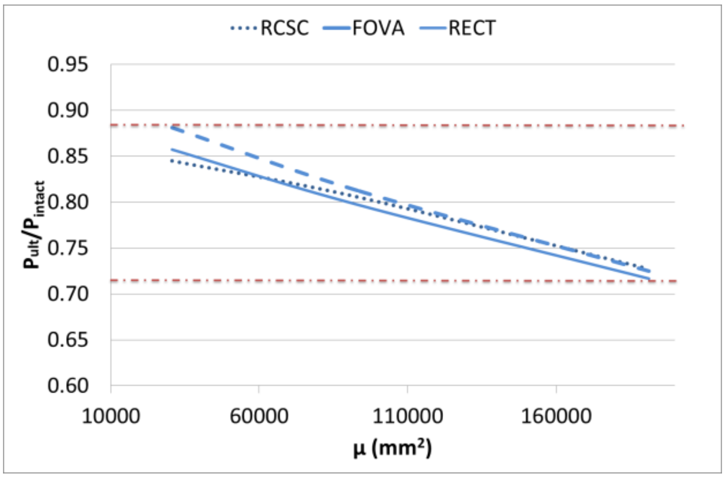

Figure 2-62: (a) Capacity the specimens with semi-shaped cutouts, (b) Capacity the specimens with full shaped cutouts.

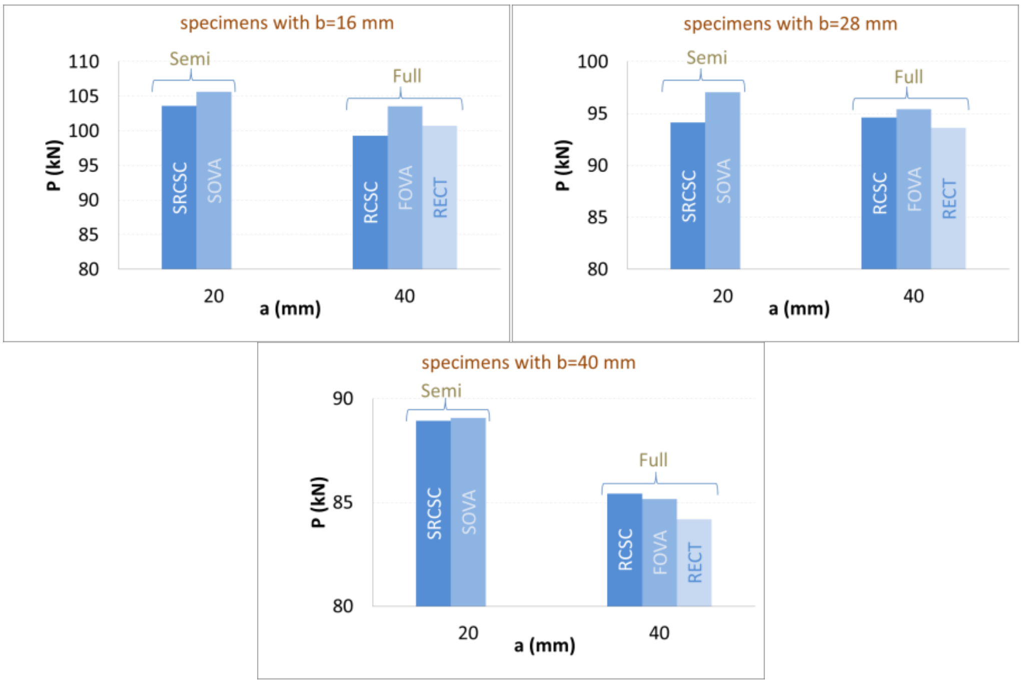

Figure 2-63: Capacity the specimens with semi and full shaped cutouts.

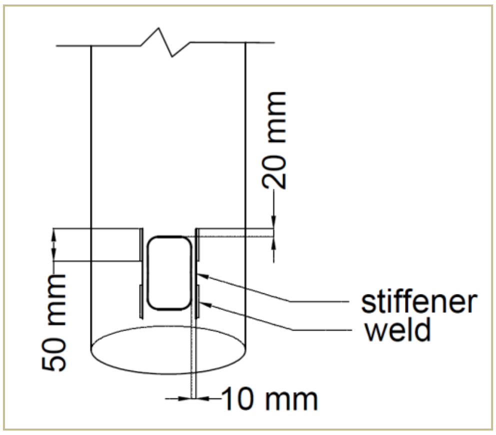

Figure 2-64: Stiffeners around the cutout.

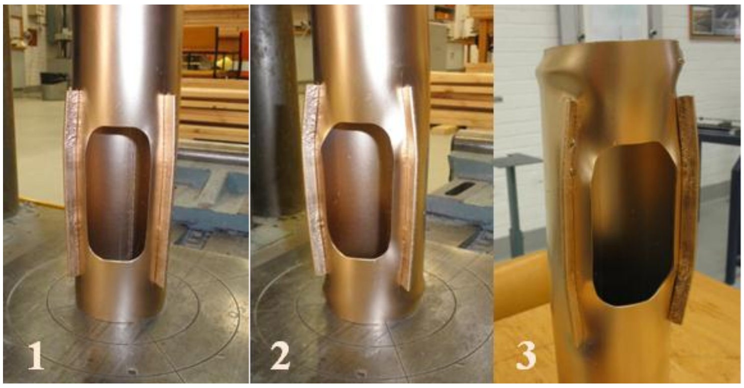

Figure 2-65: Development of deformations in the stiffened cutout.

2.5.4 Displacement and strain behaviour

Current specimens

End shortening of the present specimens was plotted versus the axial load in Figure 2-66, in which limit-load instability is seen for the present specimens. As a typical load-displacement trend, the displacement was quite proportional to the loading at the initial stages of loading. The initiation of the buckling near the cutout was accompanied by a gradual and steady reduction in the load carrying capacity for the current specimens until buckling developed near the cutout. This was followed by the *elephant foot* mode of deformation at the opposite edge of the specimens. As expected, this phenomenon was accompanied by the yield of the material in the form of buckling waves. It appeared that the present tubes, even with large cutouts, were capable of carrying a considerable proportion of the peak axial load after initiation of buckling, indicating significant post-buckling strength.

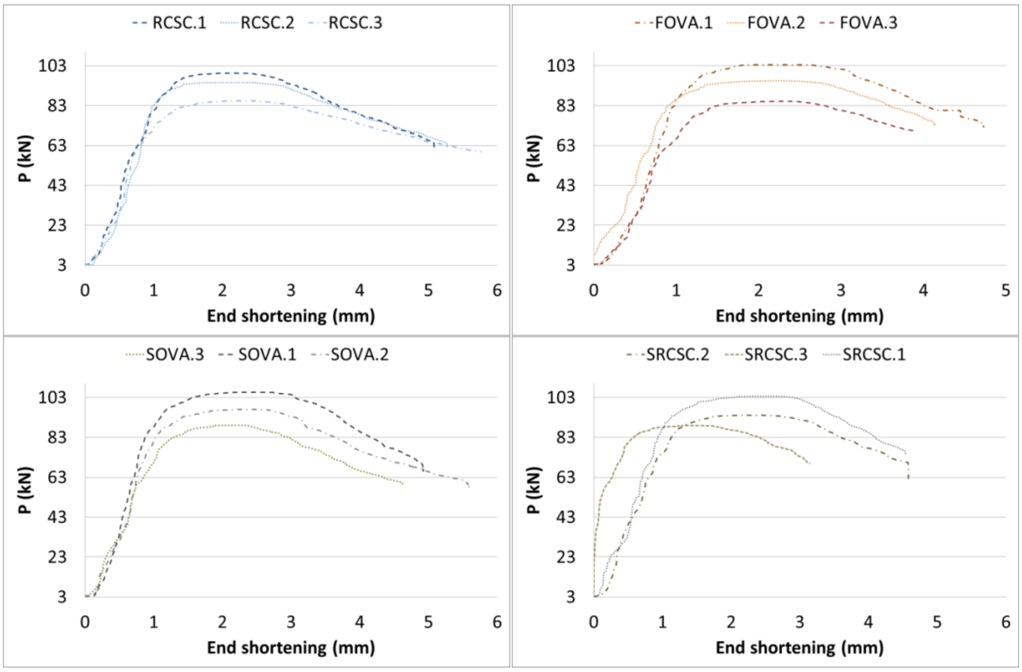

Figure 2-66: End shortening of the specimens with four different cutout shapes.

Figure 2-67 shows strain gauge locations. As seen in this figure, S.1 corresponds to the axial strain measured at the mid-height of the cutout side edge (immediately attached to the edge) and S.2 was measured also in the axial direction near the end edge of the specimens directly below the cutouts (at 10 mm from the bottom). Strain values for two specimens were potted in

Figure 2-68. Note that strain gauges were attached to the outside surface of the tubes. It is interesting to mention that initially the values of the two strain gauges increased almost proportionally to the loading and had similar values, indicating shortening without bending.

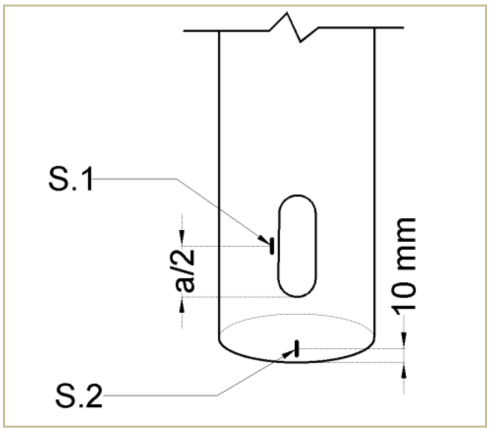

Figure 2-67: Typical layout of the strain gauges.

However, with the load being increased more stresses were concentrated in S.1 and the axial strain value was decreased in S.2. As a result, once nonlinear behaviour commenced in S.1, the values corresponding to S.2 dramatically decreased.

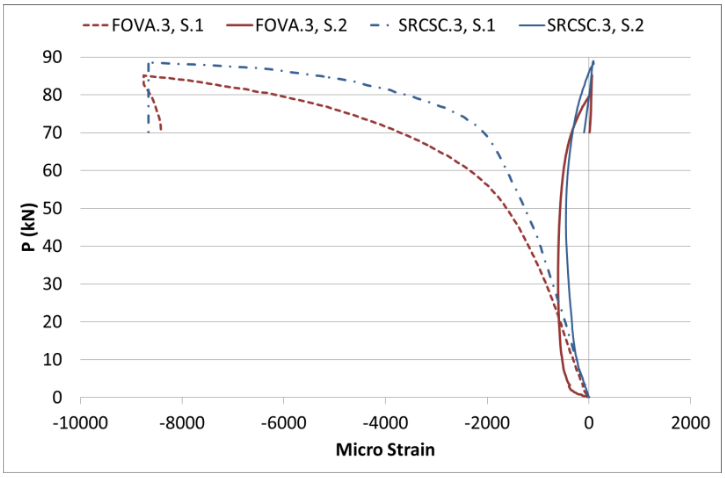

Figure 2-68: S.1 and S.2 values for two different specimens.

This phenomenon was also reported in Ref. [95]. The reason why this phenomenon occurred might be the stress flow lines that deflected when they met the cutout. After buckling in the cutout, the effective cutout area became wider so that the stress flow lines deflected further to the sides – more obviously a slight lift off occurred at the bottom edge underneath the cutout –

and the strain values below the cutout decreased with the development of the buckling (see Figure 2-69). As a consequence, compressive stresses concentrated more on the surface opposite to the cutout so that the *elephant foot* occurred in the opposite side of the cutout.

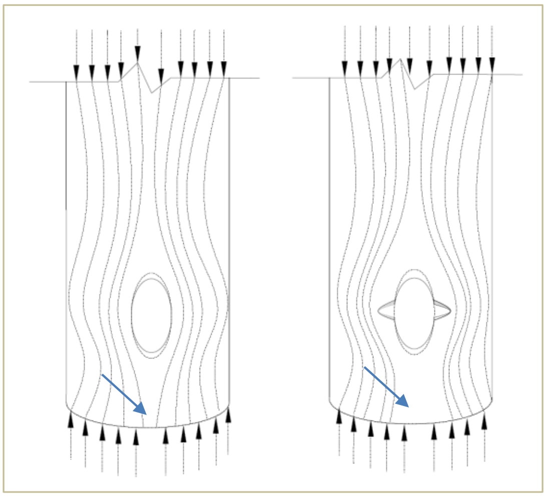

Figure 2-69: Illustration of force flow lines (blue arrows illustrate the density of the force flow lines as buckling progresses).

2.5.5 Comparison with VHS tubes

For intact very high strength (VHS) steel tubes, Jiao et al. [1] reported an *elephant foot* buckling with a sharp decrease occurring after initial buckling for specimens with almost the same *D/t* ratio as in the current study. Despite the same buckling mode, the difference of the load displacement response of the present set of experiments and Ref. [1] can be due to the material property difference between VHS and the mild steel CHS specimens of the present study.

2.5.6 Comparison of the results with the previous studies

Different studies as standards and design codes, reported estimates of ultimate load based on the slenderness of the CHS sections. The ratio of ultimate load of the current tube specimens to $P_{section}$ is plotted in Figure 2-70 versus the slenderness and buckling parameters. In this figure, $P_{section}$ is the full-section strength considering yield of the material (0.2% proof stress), and α and λ_e are respectively dimensionless buckling and slenderness parameters which are defined in Eq. (2.1) and Eq. (2.2) as discussed in some references, e.g. [96].

The intact specimen is marked with an arrow in these figures. It is quite evident that the result for the intact specimen agrees well with the results of the other studies presented in Figure 2-70, Refs. [41, 57-59] especially with the data presented in Ref. [41], as the marked point lies just slightly below the data from other experimenters. The samples with cutouts on the other hand lie well below this point.

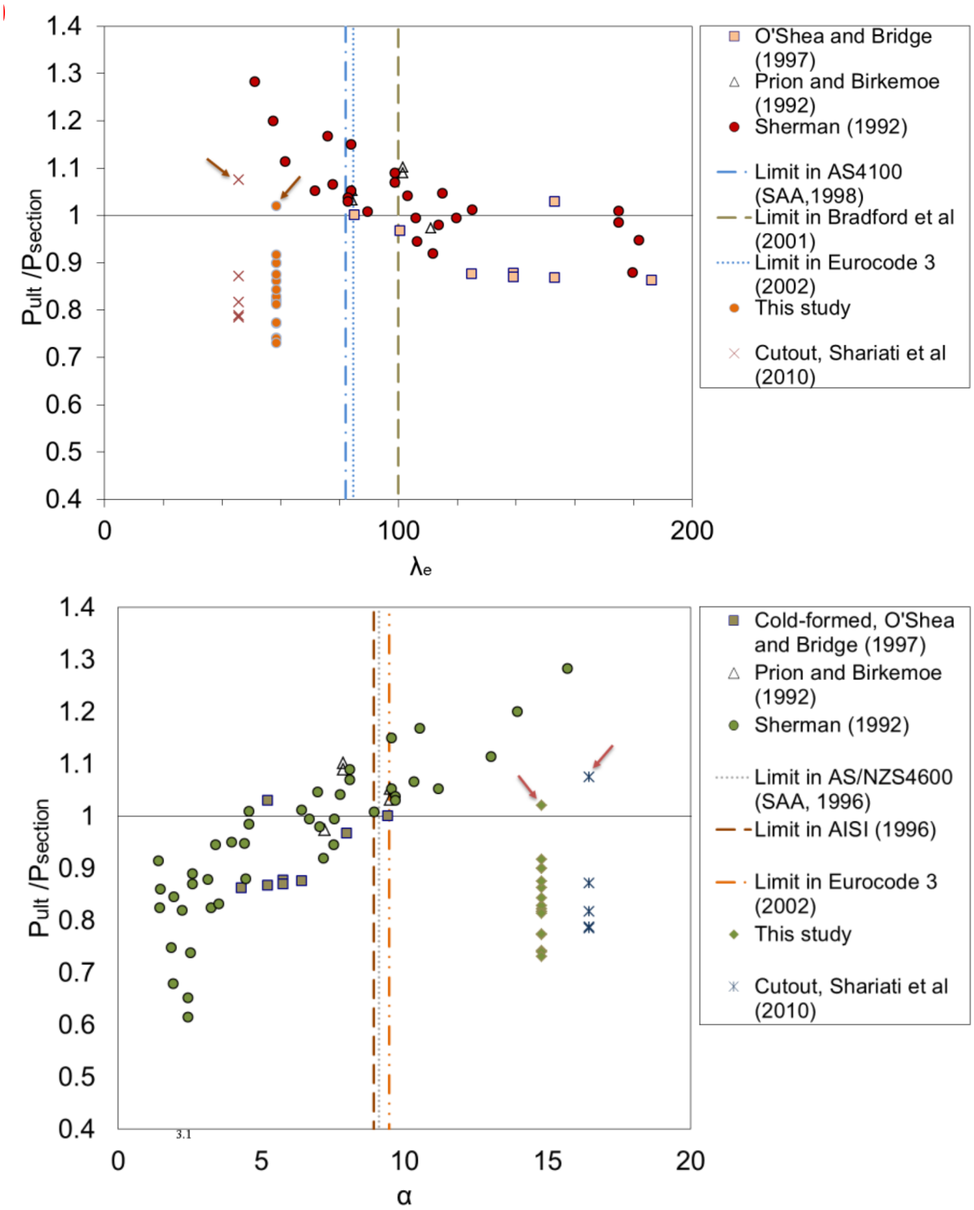

Figure 2-70: Comparison of the results with standards and other studies: (top) versus slenderness, (bottom) versus buckling parameter (intact specimen marked) [1, 41, 57-61].

Moreover, the ultimate load of the intact specimen was very close to $P_{section}$ indicating that yield is the influencing parameter in the instability of the present specimens. The other specimens with different shapes of cutouts are also seen in the Figure 2-70 in which the decreasing trend due to the cutout is clearly observed. Furthermore, the results for the specimens with horizontally located elliptical cutouts reported in Ref. [41] (Shariati et al. in this figure) were evaluated against the cutout specimens of the present research and are also included in these figures. As can be seen, good consistency of the results was observed for the specimens with cutouts from the two studies in terms of the decrease in the capacity as the specimens of the two studies with similar values of slenderness parameter (λ_e) and/or buckling parameter (α) experienced consistence rate of capacity reduction.

Table 2-14: P_{ult}/P_{intact} for different specimen along with the average values.

Specimen		**Small cutout**	**Medium cutout**	**Large cutout**	**Average capacity decrease**
Full cutouts	RCSC	0.84	0.81	0.73	20.8%
	RECT	0.86	0.796	0.72	21.0%
	FOVA	0.88	0.81	0.72	19.4%
Semi cutouts	SOVA	0.90	0.83	0.76	17.2%
	SRCSC	0.88	0.80	0.76	18.7%
Average		0.87	0.81	0.74	-

2.5.7 Conclusion

Tube specimens with different shapes of cutouts were studied experimentally in this research. The salient points from this section are summarised as follows:

- A symmetric ring-shaped bulging wave occurred in the intact specimen with a gradual decrease of the axial load which was seen after initiation of the buckling.
- Specimens with different shapes of cutout near one end showed a unique buckling mode in which the edge area of the tubes together with the cutout were influenced by the buckling phenomenon.
- In the specimens RCSC and RECT with the largest cutout, buckling was initiated near the top zone of the cutout, whereas with the decrease in the

size of the cutout the buckling wave approached the centre of the opening. However, buckling waves occurred in the mid-height of the cutout for FOVA and SRCSC specimens.

- The cutout had slightly less effect in the half-cutouts (SOVA and SRCSC specimens) in comparison with the other specimens for the same width. However, the height of the cutout had only a slight effect on the capacity which was always less than 5% in different specimens.
- In certain shapes of opening, the difference in the capacity reduction between the specimens with large and small cutouts was around 15% if compared to the intact specimen.
- Limit-load instability was seen in the specimens as the initiation of the buckling near the cutout for the CHS specimens was accompanied by a gradual and steady reduction in the load carrying capacity.
- The present tubes, even with the large cutouts, were capable of carrying a considerable proportion of the peak axial load after initiation of buckling so that a significant post-buckling strength was maintained for the present specimens.
- Due to the stress flow lines deflection or more obviously a slight lift off, *elephant foot* buckling occurred opposite the cutout.
- The ultimate load for the intact specimen was very close to $P_{section}$ indicating that yield is the influencing parameter in the instability of the present specimens.
- Good consistency of the results was observed for the specimens with cutouts compared to other studies in terms of reduction in the load carrying capacity.

2.6 Dented steel tubes under bending

2.6.1 Introduction

Tubular hollow sections are extensively used in industrial structures. These structures are often under imposed bending stresses during their service life. These elements sometimes contain surface defects, such as a dent, which may be caused due to a collision or during the transportation of the products. Very limited research has been conducted to evaluate the effect of surface defects on the loading capacity of such structures. As a result, very limited recommendation can be found in design codes and guidelines to determine the tolerated size of large surface defects in tubular sections. To this end, this section assesses the post-collision integrity of such structures under bending.

The applicability of tubular members as industrial structures with different geometries, i.e. considering various *D/t* ratios, was thoroughly discussed [97]. A literature review on the dented shell structures shows that previous studies have been carried out on various kinds of thin-walled structures under different loading conditions. Prabu, et al. examined shells exposed to dent imperfection and subjected to compressive loads [12]. It was found that buckling capacity dramatically decreased for the shells with both short and long dents. Raviprakash, et al. studied the effect of the size and orientation of a centrally located dent on the ultimate capacity of a thin steel plate under axial compressive loading [16]. They mentioned that the load carrying capacity of the dented plate largely depended on the area of the dented plate excluding the area of DAR (dent affected region). In addition, it was pointed out that plates with a longitudinal dent had either equal or higher ultimate strength than the dented plates with a transverse dent of the same size. Theoretical and experimental investigation of damaged tubular members in offshore structures was studied by Taby et al. [98]. Ellinas studied the ultimate capacity of damaged tubular bracing elements [99]. The mechanics of damage was examined as a parametric study, which eventually led to design recommendations as well as a quick and accurate means to identify the integrity of the structure.

Smith et al. investigated the buckling capacity and post-collapse response of bracing elements including damage effects [100]. The conservative prescribed tolerance of the design codes for damages were concluded based on the analysis conducted through this study. Smith et al. studied the stiffness and residual strength of damaged steel bracing members as well as a respective study [101]. The relationship between collision load and value of damage deformations was obtained in this study. Initiation of buckling propagation in pipes under denting loads was studied [102]. It was found that the diameter of a point and/or knife indenter had no significant effect on the initiation of the buckling. Behaviour of cylindrical shells under external pressure as well as the reducing effect of the dent on such structures was explored [11]. Bending behaviour of cylindrical shells was recently investigated [45, 46]. Experimental results in these studies showed that buckling happened in the compression side of these shells depending on the location of geometrical imperfections. Furthermore, the most relevant papers showing the dented shells as in the experimental models are found in the most recent works of Refs. [49, 50, 64] presenting the decreasing effect of the dent imperfection depending on the geometry of such a local imperfection. Nevertheless, it appeared that tubes with an initial dent subject to bending have not been investigated. The following aspects are taken into account in this section:

- experimental modelling of cantilever CHS sections;
- indentation on the surface of the tubes with specific geometric features of the dented area;
- strain development exploration on the dented zone;
- comparison between the intact tubes and locally dented ones;
- failure modes and deformations, and
- capacity assessment and general guidelines.

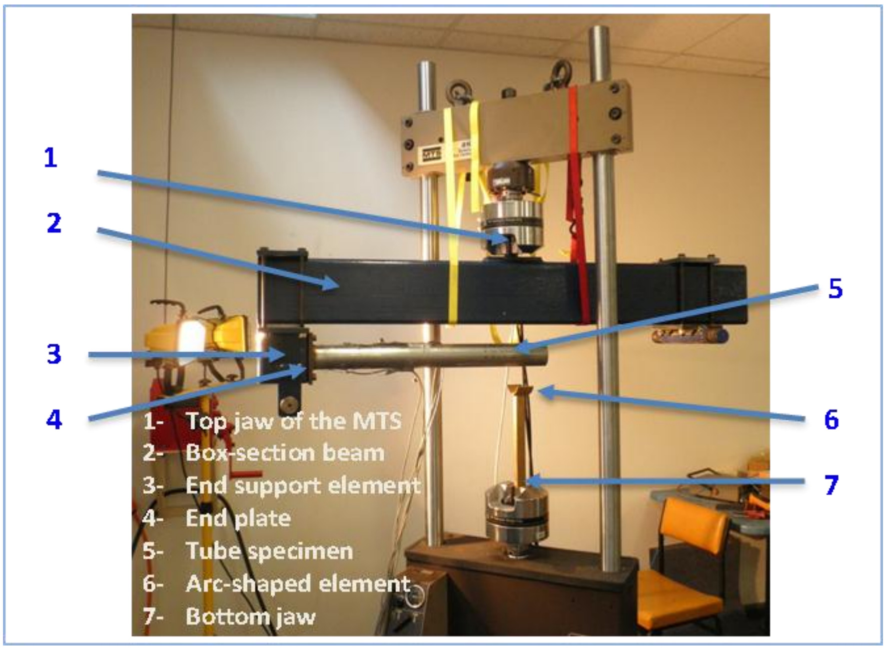

Figure 2-71: Overall views of the test program.

2.6.2 Testing program

Apparatus set-up

Testing Machine

A MTS-810 testing machine with a loading capacity of 100 kN was used for this set of experiments. This machine had been calibrated by the Australian Calibrating Services (ACS) to ensure the accuracy of the applied loads. An overall view of the testing machine is presented in Figure 2-71.

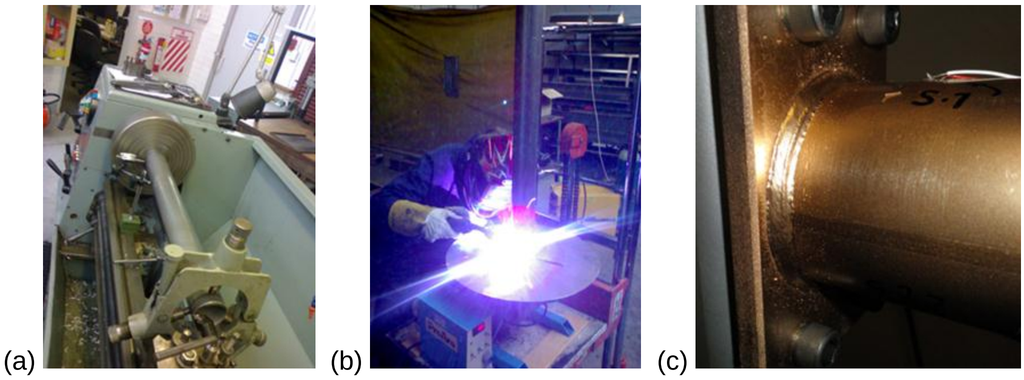

Figure 2-72: (a) Machining of the end of the specimen, (b) rotating set up for accurate welding, (c) welded end of the specimen.

As can be seen, it consisted of a loading frame with a RHS (300 × 150 × 5) being welded to a plate that was gripped to the top jaw of the machine. Another short RHS (300 × 150 × 5) section was fixed vertically to one end of the loading frame to hold the cantilever beam specimen. Screwed holes were drilled on one side of the vertical short RHS section for the connection of the cantilever specimens. The CHS sections used in this research program were mild-steel tubes made by Specialist Australian Manufacturer of Precision. A total of eight specimens were cut into lengths of 620 mm as listed in Table 2-15. One end of each specimen was machined by means of a lathe to reach a precise finish before welding to the end plate as shown in Figure 2-72.

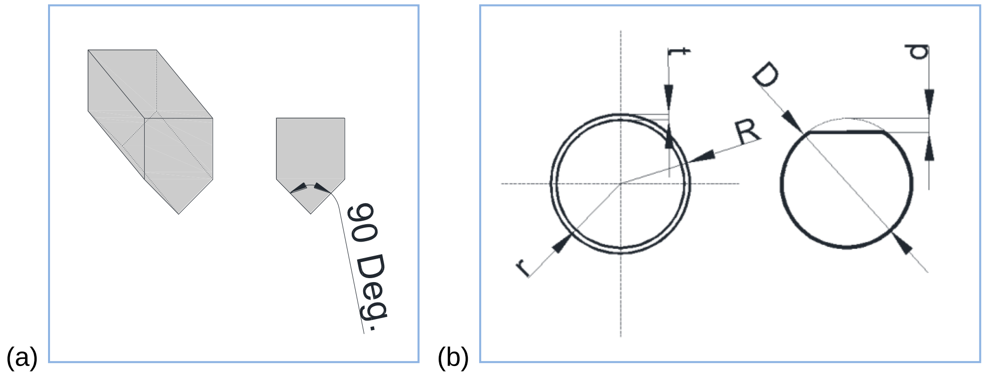

Figure 2-73: (a) overall view of the indenter (b) Tube cross-section and indentation illustration.

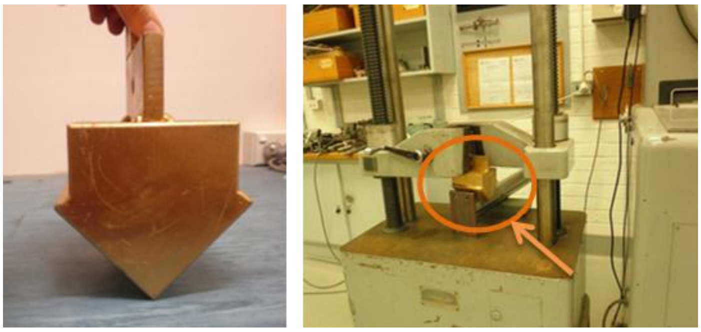

Figure 2-74: Indenter and indentation.

High strength bolts were used to avoid any unfavourable deflections and displacements. An arc-shaped steel element was welded to a steel plate that was gripped in the bottom jaw of the MTS machine to apply a concentrated load to one end of the specimen. The arc-shape helped to uniformly transfer the load and to avoid any stress concentration in the loading zone.

Specimen fabrication

To make cantilever beam specimens, each tube was welded to the end plates with the seam weld of each CHS tube placed at the neutral axis zone. Hence, the effect of the seam weld on the test results as well as the Heat Affected Zone (HAZ) for the welded areas were excluded. In order to ensure the quality of the weld, a rotating machine with an adjustable rotation speed was employed to achieve an accurate, uniform and penetrated weld. Figure 2-72 (c) shows a welded specimen.

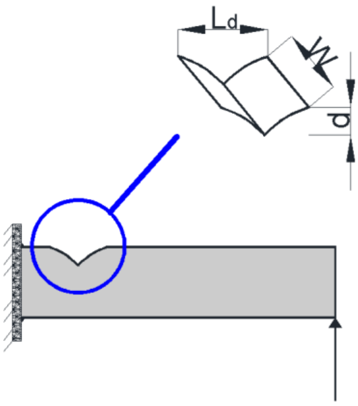

Figure 2-75: Position and geometry of the dent on the compression side of the specimens.

Figure 2-76: Tensile coupon test specimens.

Indentation

Indentation on the tube surface was made by a 90° angled round tipped indenter as shown in Figure 2-73. An indentation was performed by compressing the indenter into the tube surface through a compression machine as shown in Figure 2-74. The load was applied gradually and in a step-by-step manner until the required depth was reached. The depth of the dents was measured using a digital calliper vernier. The dent dimensions are illustrated in Figure 2-75 and tabulated in Table 2-16.

Table 2-15: Geometric Specifications of the specimens.

Specimen label	Length (mm)	D/t	D (mm)
TS1–TS8	620	47.6	76.2

Measuring devices

Micro Measurements CEA-06240UZ120 strain gauges were applied on each specimen to record the strain near the weld and around the dented areas. The load, displacement and strain data were obtained through a National Instruments data acquisition system. A LabVIEW program was used to acquire the data and to show the load versus strain curves during each test.

Table 2-16: Geometry of the dented area.

Specimens	d (mm)	Dent location	W (mm)	L_d (mm)
TS1	–	no dent	–	–
TS2	1.6	in the middle of the tube	21	20.2
TS3	2	50 mm from the weld end, in the compression side	26	20.4
TS4	4	50 mm from the weld end, in the compression side	37.1	35
TS5	9.5	50 mm from the weld end, in the compression side	60.7	55.3
TS6	22	50 mm from the weld end, in the compression side	91.8	86.5
TS7	19.2	50 mm from the weld end, in the tension side	90.6	81.6
TS8	24.7	50 mm from the weld end, on the side of the tube	127	95.3

Material properties

Tensile tests were conducted to obtain material properties of the current specimens. Figure 2-76 shows six coupons that were prepared in accordance with Australian Standard AS 1391 [91]. A typical stress strain curve is plotted in Figure 2-52. The yield-stress, the ultimate tensile strength and Young's modulus of the steel tube are listed in Table 2-1 (yield and ultimate stresses and Young's modulus).

2.6.3 Results and discussion

Failure modes

Specimen without any dent

In order to compare the behaviour of the specimens with and without a dent, a specimen without a dent was tested under the same testing condition as the dented ones. It was observed that as the load increased, the specimen initially showed a linear behaviour on the load-strain curves.

(a) 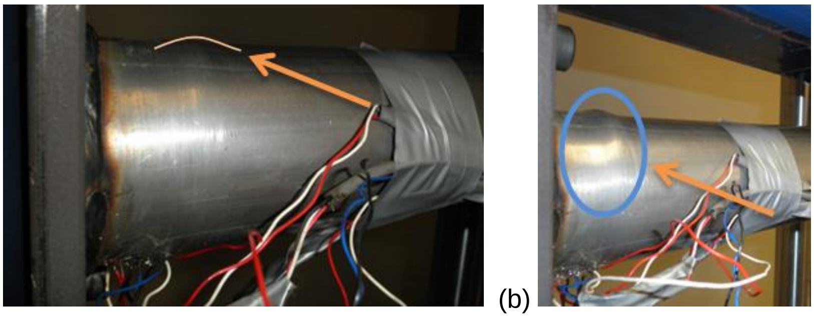 (b)

Figure 2-77: (a) Initiation of a bulge, (b) developed local deformation.

With further increasing of the load a non-linear stress-strain relationship was initiated in the tension side of the specimen followed by the yielding on the compression side. A bulge-shaped deformation eventually formed on the compression side at the position of 30 mm measured from the end plate (see Figure 2-77).

(a) 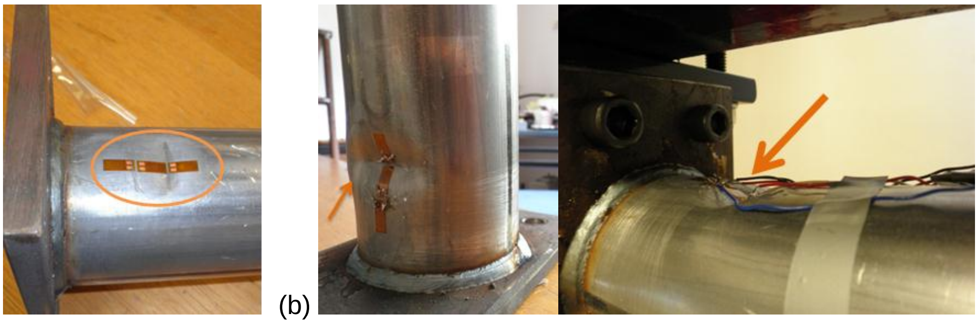 (b)

Figure 2-78: (a) TS3 before testing, (b) after the test.

In sample TS1, the bulge had quite a symmetric shape indicating that the loading was accurately applied in the vertical direction. Note that no crack was observed near the welding on the tension side of the specimen.

Dented specimens

Specimen TS2 was prepared with a dent equal to the thickness of the tube at the mid-length of the specimen. During testing, a bulge shaped yielding occurred at about 30 mm from the base. This was accompanied by the yielding on the tension side of the tube at the weld-toe of the end plate. A bending capacity of 2.82 kN.m was obtained for TS2, which was nearly the same as the capacity of TS1 (2.83 kN.m). It appeared that this dent did not affect the bending capacity of the tube as the position of the dent was away from the area of the maximum bending stress.

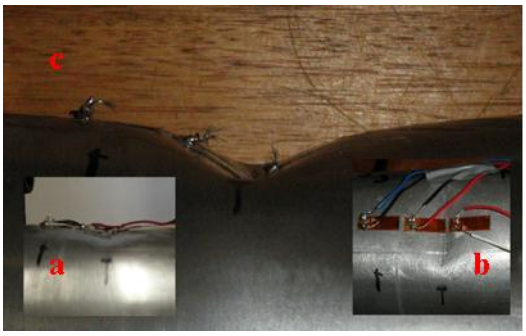

Figure 2-79: (a) and (b) dented area in TS4 before testing, (c) after the test (TS4).

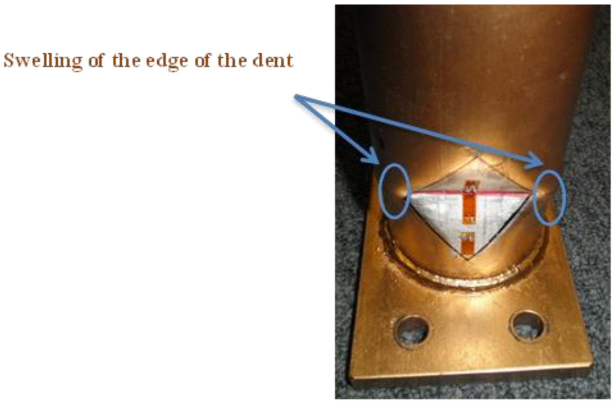

Figure 2-80: Failure of TS5 (area in silver was marked before testing).

The failure mode of the specimens TS3 to TS6 was local deformation at the dented area with the deformations increasing proportionally to the dent depth. This failure mode was different from that of the specimens TS1 and TS2 such that the inward deformations were developed at the dented zone rather than the bulge-shaped yielding of the first two specimens (Figure 2-78 and Figure 2-79). Moreover, not only the dent deepened in specimens with larger dents, but also the dent developed outwards on both sides of the centre line of the dent as shown in Figure 2-80. Considering the results of specimen TS1, it was decided to make a dent at the most critical area of the specimens, thus a position on the compression side near the end plate was adopted. Dent imperfections with the depth ranging from 2 mm to 22 mm were made at that position on different specimens.

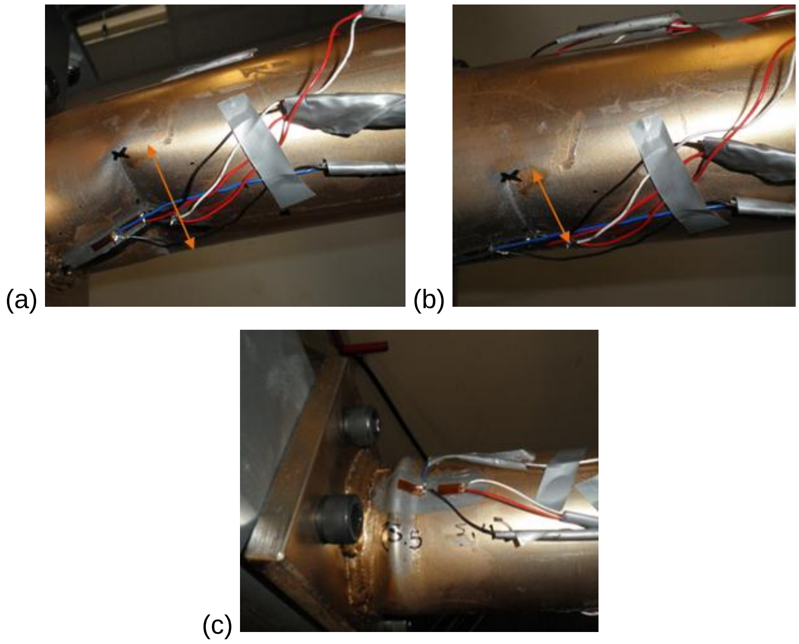

Figure 2-81: (a) Dent before loading in TS7, (b) recovery of the dent after loading, and (c) bulge form wave on the compression side.

The two last specimens were tested by making the dent in different positions in consideration of the fact that in real applications a dent may be made on any position in relation to the loading direction. As seen in Figure 2-81, specimen TS7 was tested with the dent located in the tensile region. It is interesting to note that the dent gradually recovered as the load increased, accordingly the dent depth notably decreased. As the load further increased, the tube's material in the proximity of the end plate yielded on both tension and compression sides. This was accompanied by a bulge shaped deformation on the compression side at a distance of about 50 mm from the end plate. Although this failure mode was similar to that of the specimens TS1 and TS2, much lower load carrying capacity was recorded for TS7 as presented in Table 2-17. It is quite evident that this was due to the geometric irregularity of the tube in the dented section, which led to the onset of the deformations.

It is clear in Figure 2-82 that the dent was made in a position parallel to the loading direction for TS8. As observed in TS7, the dent location affected the bending behaviour of the tube. It can be seen from Figure 2-82 that TS8 failed by yielding with an inward localised deformation formed in the compression zone immediately adjacent to the initial dent. Moreover, a lower load carrying capacity was obtained for TS8 that has been discussed thoroughly in the next section.

(a)

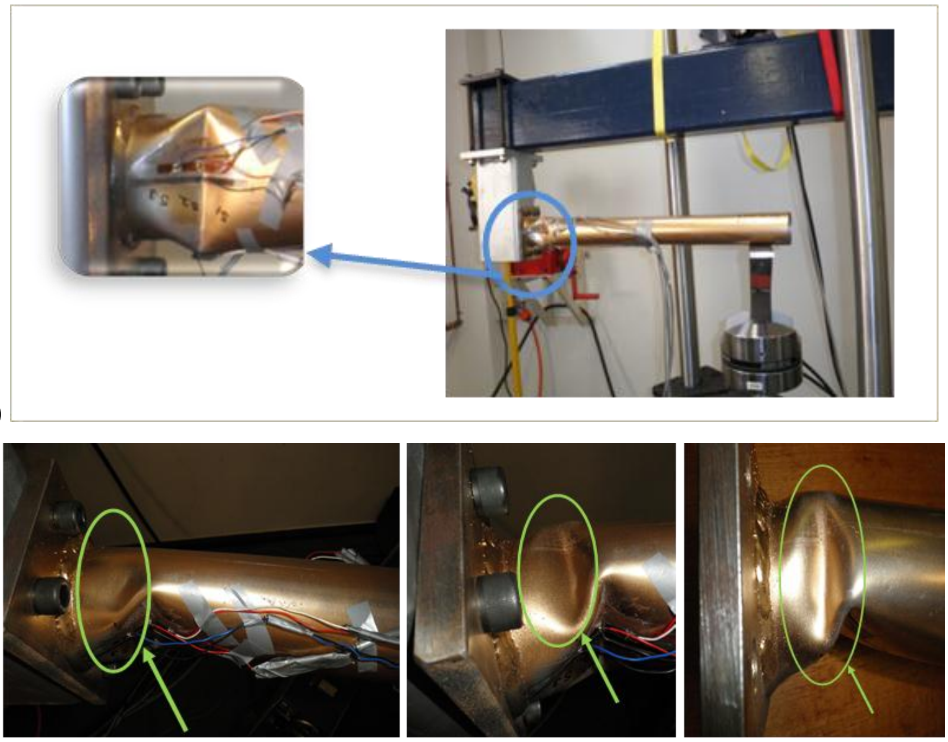

(b)

Figure 2-82: (a) Dent before loading in TS8, (b) inward wave progress on the compression side after loading.

Bending capacity of the tubes

The ultimate bending capacity and the differences of the dented specimens' capacity from the intact specimen are tabulated in Table 2-17. It can be seen from Table 2-17 that the bending capacity of TS2 was similar to that of TS1. As already noted, this can be due to the position and/or the depth of the dent created in the mid-span of the tube which did not have any appreciable effect on the failure of the tube.

It was also found that for the dents in the compression region near the end plate the reduction in the bending capacity was mostly related to the depth of the dent as the deeper the dent, the higher the reduction in the bending capacity of the tube. For instance, specimen TS4 had a dent with the depth equal to 2.5*t*. This tube lost around 13.6% of its bending capacity compared with the intact specimen. When the depth of the dent was increased to 6.25*t* (in TS5), the capacity reduction was around 25.4%.

(a)
(b)

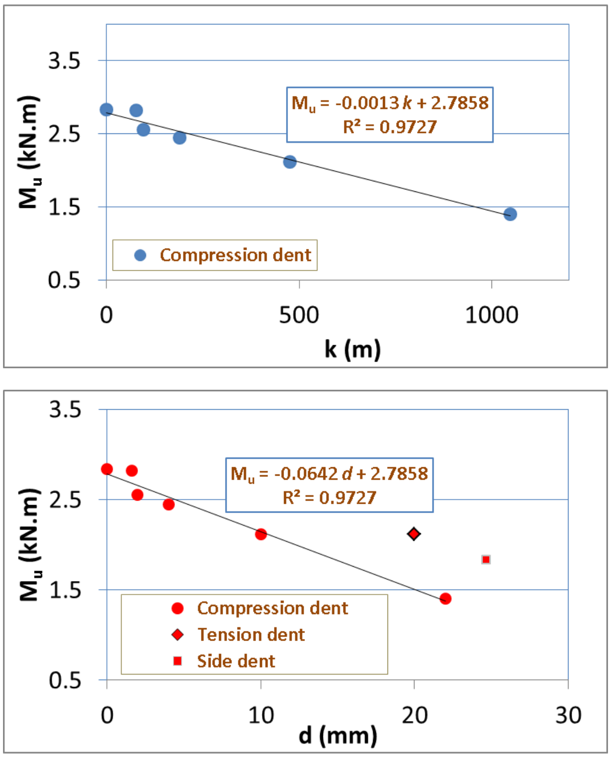

Figure 2-83: (a) Ultimate bending capacity of the tube specimens, (b) bending moment versus k ($k = \frac{Dd}{t}$)

A dramatic decrease in the bending capacity was recorded when the depth of the dent was further increased in TS6. For this specimen dented with the depth of 13.75*t*, the capacity decreased by around 51% which is considered a substantial decrease in the ultimate load capacity.

Table 2-17: Bending capacity of the specimens and the failure modes.

Test	d/t	M_u (kN.m)	Difference from TS1 (%)	Failure mode
TS1	0	2.83	0	bulge-wave at compression
TS2	1.00	2.82	0.4%	bulge-wave at compression
TS3	1.25	2.55	9.9%	deepening of the dent
TS4	2.50	2.45	13.6%	deepening of the dent
TS5	6.25	2.11	25.4%	deepening of the dent
TS6	13.75	1.40	50.6%	deepening of the dent
TS7	12.50	2.11	25.4%	bulge-wave at compression
TS8	15.44	1.83	35.5%	inward deformation of compression

On the other hand relatively less reduction was relatively recorded when the dent was formed on the tension side of the tubes. For the specimen TS7 with d =12.5t the reduction in the bending capacity was about 25%. This decrease was less than that of TS6 which was around 51% with d =13.75t.

The ultimate bending capacity of each specimen versus *d* is plotted in Figure 2-83. Here the parameter *k* is defined as *k=Dd/t* to determine the bending behaviour versus a parameter including both *D/t* ratio and *d* as the depth of the dent [49]. A similar phenomenon was observed when a dent was formed on a position parallel to the loading direction (TS8), in which the influence of the dent was not as significant as in the case of the corresponding compression side. In summary, the most critical position for a dent to affect the bending capacity of a tube occurred when the dent was located in the compression area of a tube.

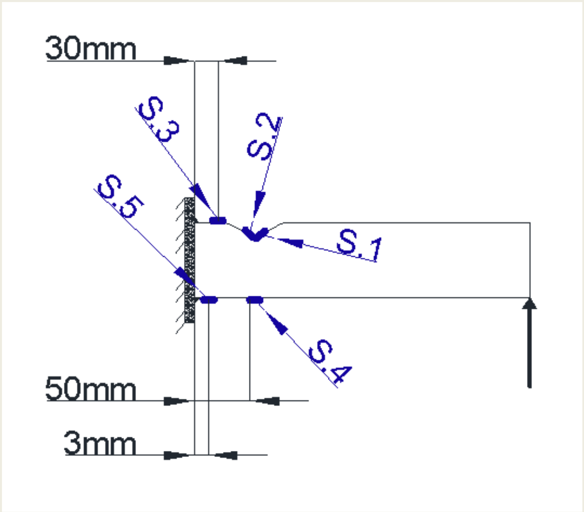

Figure 2-84: Strain gauges positions (S.1 and S.2 start immediately from through of the dent towards top zones of the tube).

Strain behaviour of dented specimens

Five strain gauges were applied over each specimen with three of them on the compression side and the other two on the tension side as shown in Figure 2-84. The measured strains are plotted against the bending moment in Figure 2-85 for the dented specimens at S.1 and S.3. Complicated strain behaviour was recorded in the dented region on the compressive side. It can be seen in Figure 2-85 that all the curves were initially in the compression area. However, the strain changed from compression to tension as the applied load approached the ultimate bending moment of each tube. Similar strain behaviour was observed in the position between the dent and the end plate in the compression side for the position of S.3. This phenomenon of change in the strain from compression to tension in the dent area could be due to the plastic deformation caused by the deepening of the dented region or local bending of the plate due to the buckling wave.

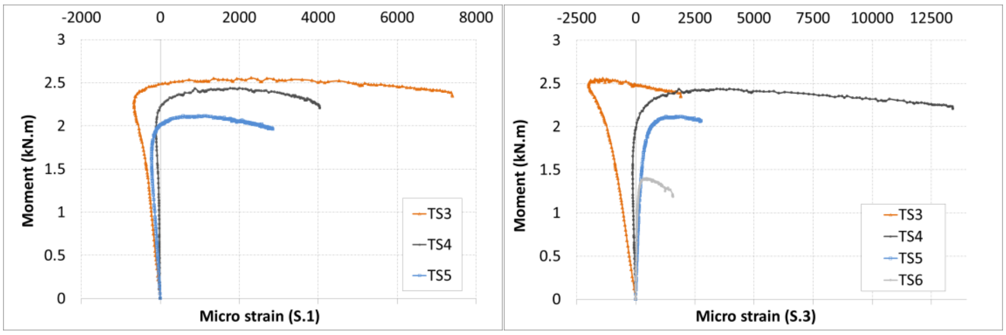

Figure 2-85: Strain versus moment curves measured at strain gauge S.1 and S.3.

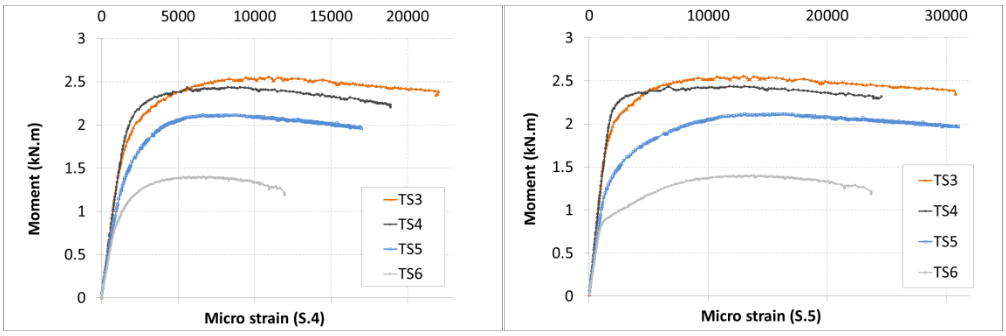

Figure 2-86: Strain at S.4 and S.5 versus the moment for the dented specimens.

The strain data at the positions of S.4 and S.5 are plotted against the moment in Figure 2-86. It can be seen that the strain at the bottom of the tubes remained consistently in tension during loading. Note that displacement data at the loading point for the specimens TS3 to TS6 were recorded by the MTS machine itself, which is plotted in Figure 2-87. One may recall that the post-yielding range of the end displacement in the current specimens was approximately between 12-50 mm.

2.6.4 Comparison of results with previous studies

In this section, the results obtained from the experimental study are compared with the available theoretical predictions and recommendations (Figure 2-88). The ultimate capacity of the tubes was studied theoretically by a number of researchers as outlined herein. A simplified formula was proposed [48] as Eq. (2.7) in which σ_u is the ultimate stress of the material. An equation was also proposed considering *D/t* ratio which is considered herein as Eq. (2.8) [47].

$$M_{u1} = 3\sigma_u \, t \, R^2 \tag{2.7}$$

$$M_{u2} = (1.05 - 0.0015\, D/t).\, \sigma_Y . D^2 .\, t \tag{2.8}$$

In addition, RAM Pipe Requal Project [103] reported a formula including the plastic moment of the tubes as Eq. (2.9). The plastic bending moment M_p, which provides a good estimation of strength of thick and nearly perfect tubes is given by Eq. (2.10), (see e.g. [38]). The bending moments obtained in a set of tests are compared with the values calculated using Eq. (2.7) to Eq. (2.10). The results are tabulated in Table 2-18 where M_e is the elastic moment of an intact section.

$$M_{u3} = 1.13\, M_p .\, \exp(-X),\ X = \sigma_Y D/E\, t \tag{2.9}$$

$$M_p = 4\, \sigma_y/3\, ((R+t/2)^3 - (R - t/2)^3) \tag{2.10}$$

As mentioned earlier, EN 1993-1-6 standard [77] categorised shell elements to three different fabrication tolerance quality classes in which excellent, high and normal classes are seen with the recommended values of eccentricity tolerances. In this reference, χ is the buckling reduction factor for elastic-plastic effects which is given for different values of slenderness as:

$$\chi = 1 \qquad (if\ \ \bar{\lambda} \le \bar{\lambda}_0) \tag{2.11}$$

$$\chi = 1 - \beta \left(\frac{\bar{\lambda} - \bar{\lambda}_0}{\bar{\lambda}_p - \bar{\lambda}_0}\right)^{\eta} \qquad (if\ \ \bar{\lambda}_0 \le \bar{\lambda} \le \bar{\lambda}_p) \tag{2.12}$$

$$\chi = \frac{\alpha}{\bar{\lambda}^2} \qquad (if\ \ \bar{\lambda}_p \le \bar{\lambda}) \tag{2.13}$$

In these equations, $\bar{\lambda}$ is the relative slenderness, $\bar{\lambda}_0$ is squash limit relative slenderness and $\bar{\lambda}_p$ is the plastic limit relative slenderness, β and η are plastic range factor and interaction exponent respectively. Different values for α are obtained from EN 1993-1-6 based on three different fabrication quality classes. Furthermore, a dimple tolerance parameter for different quality classes (U_{0max}) is presented in this reference. Nonetheless, as the fabrication related imperfections are different from damage induced large local imperfections, further studies are still required to cover the dented imperfections.

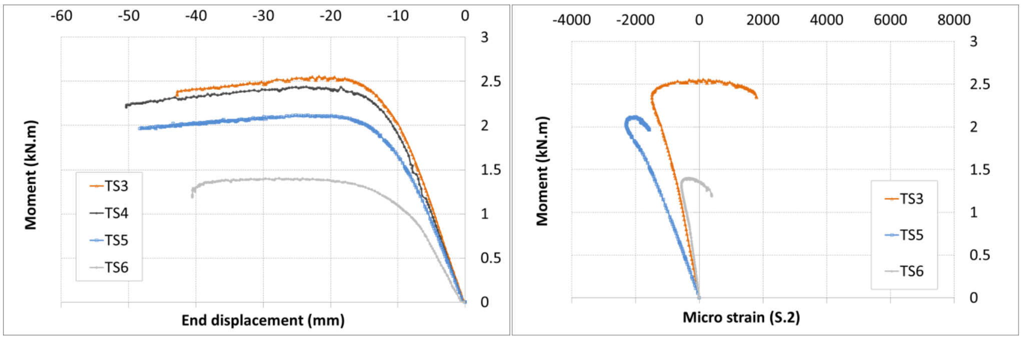

Figure 2-87: End displacement of the specimens and strain values at S.2.

It can be seen from Figure 2-88 that Eq. (2.7) properly predicts the ultimate capacity of such structures. For the intact specimen it overestimates the maximum capacity by about 13%, which is quite consistent due to the pre-existing fabrication-related geometric imperfections of the specimens and/or testing apparatus [23, 104]. Eq. (2.8), on the other hand, reveals a very close agreement for the intact specimens with a discrepancy of around 2%.

Table 2-18: Comparison of the test results of the intact specimen with the previous studies.

Test	M_{test}/M_e	M_{test}/M_{u1}	M_{test}/M_{u2}	M_{test}/M_{u3}	M_{test}/M_p
TS1	1.347	1.129	1.015	0.941	0.993

Likewise, Eq. (2.9) agrees well with the experimental results and eventually similar consistency is also achieved for Eq. (2.10), in which the difference between the prediction and the test result is less than 1%. Perhaps the reason why Eq. (2.8), Eq. (2.9) and Eq. (2.10) are more consistent with the results of this section is that the yield and plastic moments were considered in these equations. Needless to say, based on the moderate *D/t* ratio of the current specimens the failure of the specimens was accompanied by yield than premature buckling. Overall, considering the results of the analytical estimations, the accuracy of the test results is clearly verified; hence the negative effect of the dent imperfection can be obtained comparing the results of the dented specimens with the intact one.

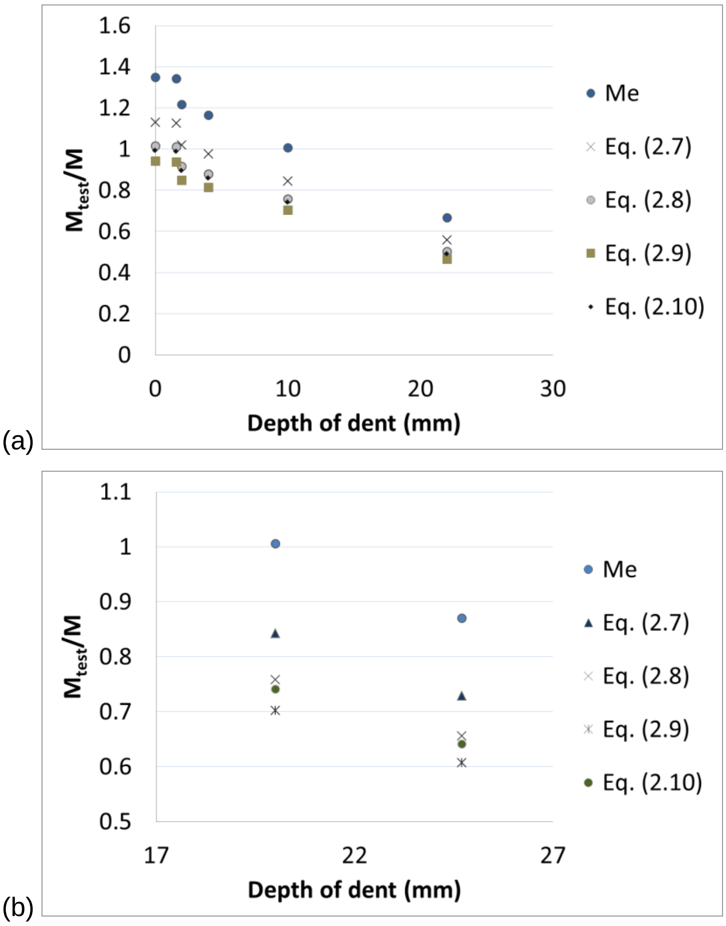

Figure 2-88: Comparison of dimensionless bending moment for tubes with other equations: (a) dent in the compression side and (b) dent in the tension and side dent (M_e is the elastic moment of the present intact specimen).

2.6.5 Concluding remarks

An experimental study on the damaged tubular members was conducted in this section. Eight specimens were tested to explore the ultimate load carrying capacity of dented structures. The following concluding remarks are gained from this section:

(a) Different failure modes were observed for intact and dented specimens. Intact specimen failed by yielding with a local bulge on the compression side of the tube, whereas dented specimens failed by the deepening in the dented region when the dent was located in the compression-side in a “diamond-like” shape.

(b) When a dent was located on the tension side of the tube, the dent was largely recovered under a bending moment in terms of the shape of the dent. However, the load carrying capacity was reduced owing to the dented area.

(c) When a dent was located in a position parallel to the loading direction, the tube failed by yielding with an inward localised deformation formed in the compression zone between the end plate and the initial dent, which was accompanied by a reduction in the load carrying capacity.

(d) The load carrying capacity of a tube was strongly related to the size and the position of a dent created on the tubes. A dent with a depth equal to the thickness of the pipe and created in the mid-length had no effect on the pipe's capacity nor on the deformational behaviour. However, when a dent was located in a position of higher stresses, i.e. near the end plate, the effect was significant as the larger the imperfection amplitude of the dent, the greater the reduction in the load carrying capacity.

(e) For a certain cross section of the current tube specimens, the most critical position of a dent imperfection is the compression side. Dents located at side and tension zones are less significant relative to the compression ones.

(f) Complicated strain distribution in the dented region was observed, which was attributed to the plastic deformations of the damaged area. The strain on the dent changed from compression to tension when the dent was located in the compression side of the tubes.

(g) The capacity of the specimens can be well compared with a number of theoretical equations presented in this section leading to quite acceptable consistency and agreement.

2.7 Conclusions of Chapter 2

Clearly the dent depth and cutout's geometry and location were the most important variables in determining the load capacity reduction of such structures with these types of non-uniformities. Under different loading conditions dented shells behaved in a variety of manners in terms of the buckling mode and ultimate capacity. The capacity decrease was proportional to the depth of the dent, while the orientation of the dent seemed to have different effects under different loads. Elephant foot and diamond mode of buckling were generally dominant for all intact and dented specimens under axial compression, while lobar buckling was obtained for the pressurised shells. For all samples under axial compression the dent – albeit depending upon the depth and location – affected the stability of the structure as evident in the load displacement curves. A bifurcation type of load-displacement was observed for intact and dented thinner shells under axial loading, whilst a limit load type of failure was obtained for the thicker shells. Tested specimens of this chapter, regardless of loading conditions, geometric non-uniformities and cross sections, even with the large dents or cutouts, were capable of carrying a considerable proportion of the peak axial load after initiation of buckling so that a significant post-buckling strength was maintained for the present specimens.

There seems to be an interrelation between the geometrical irregularity (surface undulation) and the material properties of the dented zone. The former may result in an adverse effect (due to non-uniformity) and an strengthening effect (due to undulation and increase of second moment of inertia) on the capacity whereas the latter appeared to have a positive effect, which is why the areas adjacent to the dented zones were more sensitive to the buckling. The reason is that the dented area is believed to have reached a hardened material in comparison to the intact areas, whilst the area adjacent to the dent was affected by the geometric non-uniformity of the large imperfection, the material of which not as hardened as the dented zone.

For all types of dented shells under different loading conditions the decreasing trend was generalised through a regression equation in this chapter which can provide an insight into future numerical and experimental studies on the basis of this extensive experimental data. Based on the results of this section though, designers of similar tubular members may gain general insight to decide whether they have to change a dented element, strengthen or keep it, if they encounter similar damage. This decision, indeed, may be made considering the rate and the type of service loads, the position and the depth of the damage and the significance of the damaged member in different structures.

Perhaps, it would be advisable to categorise the geometrical imperfections in design codes into normal imperfections and large imperfections, e.g. dent or gouges caused by physical contacts. Future studies are still required to thoroughly clarify the effect of different shapes and amplitude of local imperfections on the shell structures with different geometric, loading and boundary conditions.

Chapter 3

Thin Cylindrical Shells with Fabrication-Related Imperfections Reinforced with and without Additional Materials

Publication output of Chapter 3

This chapter consists of two journal papers published in international journals as follows:

- "An Experimental Study on Externally Pressurized Stiffened and Thickened Cylindrical Shells" **Thin-Walled Structures** (Elsevier), 85 (2014) 359–366.
- "Longitudinally Stiffened Corrugated Cylindrical Shells under Uniform External Pressure" **Journal of Constructional Steel Research** (Elsevier), 110 (2015) 191–199.

3.1 Introduction

As described in the previous chapter, thin walled cylindrical shells may be highly susceptible to the buckling phenomenon. The previous chapter sought to describe the buckling of these shells under a variety of geometry and loading conditions, to quantify the buckling loads, and to investigate the capacity reduction caused by dents or cutouts. In some circumstances it may be important to recover some or all of this lost capacity, which can be achieved through the use of stiffeners or other forms of reinforcement. This chapter, therefore, sets out to investigate the effect of reinforcement on the capacity of pressurised shells with fabrication-related non-uniformities.

Many strengthening methods have been utilised in order to increase the buckling capacity of such structures (e.g. see [22-25]). It has long been identified that stiffening of steel shells is one of the most effective ways of enhancing the capacity of these structures. Stiffeners, largely in the form of welded elements, have been employed to strengthen shell structures, which generally cover the whole length of the structure.

The first section of the chapter studies the effect of partial and full length stiffening of shells in which the stiffeners were attached without welding to avoid the adverse effects of the residual stresses. Furthermore, local thickening of the shells by the same stiffening strips was investigated and the results were evaluated against the plain specimen. The effect of strengthening provided by local thickening was slightly less but comparable to that provided by the stiffeners.

The second section of this chapter aimed at a new approach for strengthening such structures that reinforced without additional material as used in the first section. Corrugation of the body of the shells was introduced for these structures and the performance of vertical corrugations was tested on cylindrical shell specimens under uniform external pressure. The results showed a considerable increase in the buckling capacity of such structures with an optimum configuration.

3.2 Reinforcement of pressurised shells with additional material (stiffeners/thickeners)

3.2.1 Introduction

Cylindrical shells are seen in a vast range of structural elements of different industrial applications. Such structures sometimes resist external pressure, particularly in the offshore industry. In some cases, in contrast, internal evacuation of pressure takes place due to discharge of liquid inside these structures.

A great deal of research has been conducted in regard to thin shells under external pressure. In some cases, modelled structures were directly subjected to external pressure imposed from outside the surface of these structures whereas in some cases a vacuum was applied such that the atmospheric pressure plays the role of the peripheral pressure. Since 1996, Showkati and his research colleagues have conducted many studies in which a uniform external pressure was imposed through an internal vacuum. Some of these investigations are outlined herein: The effect of boundary condition on shell structures was studied in Ref. [36], in which different buckling modes were exhaustively discussed. Buckling and post-buckling of imperfect thin shells [35, 62], and the effect of thickness variation on the buckling response of such structures under vacuum [34] were also explored. In addition, the effect of load combination in the presence of the vacuum in long cylindrical shells [63] and the effect of various types of geometric imperfections for the shells with similar *D/t* ratios were thoroughly investigated [49, 63, 65, 68-71].

The effect of stiffeners in thin structures under uniform vacuum was studied in two respective studies [22, 23]. In Ref. [23], the effect of stiffeners was evaluated against thickening of the steel specimens. The capacity increase was determined for each strengthening method. The effect of rings or ring-beams on the buckling behaviour of tanks and silos were studied by Chen and Rotter [24]. The effective length of shells with stiffeners was calculated theoretically in this research.

It should be mentioned that in most cases welding was utilised to connect the stiffening elements. However, Barkey et al. performed some tests on conical shell specimens in which epoxy adhesive was employed to connect the stiffeners to the surface of the shells [25]. In fact, this connection method helped the structures to have uniform material properties in comparison with the welded or soldered connections, in which considerable residual stress can affect the buckling behaviour. Proper facilities should be developed if the usage of epoxy is adopted in practice for real structures.

In this section, same method of connection was employed using epoxy in the present thin shells, which resulted in a highly satisfactory connection both for longitudinal stiffeners (known as stringers), and thickeners. It is of interest that this geometry leads to a different collapse mode in these structures, which has not been reported yet. Note that stiffened shells with an end plate are quite widespread in many applications in which the end plate takes the role of a cap in such cylindrical shell structures.

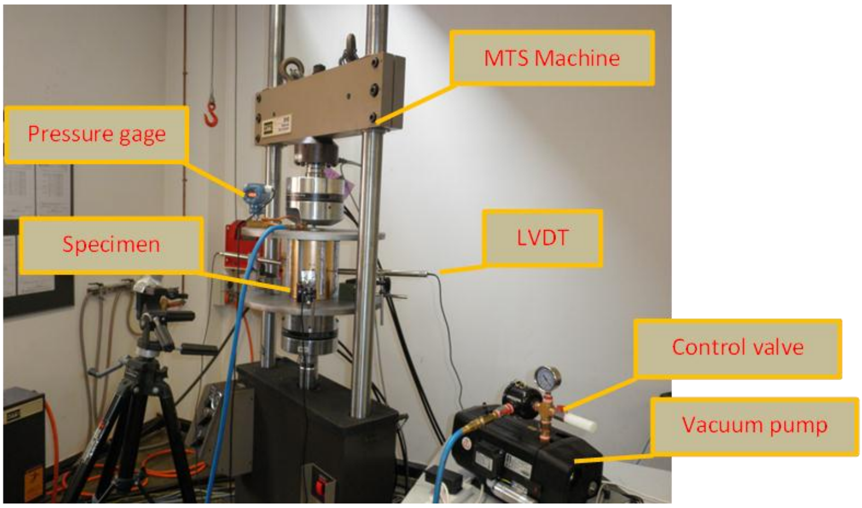

Figure 3-1: Main features of the test rig.

3.2.2 Details of the test rig

Apparatus and specimens

Figure 3-1 and Figure 3-2 illustrate the main features of the test apparatus and specimens used in this set of experiments. Two grooved end plates were made in order to apply the boundary conditions in these specimens. These plates were installed on a test machine known as MTS such that the distance between the plates was easily adjustable in the axial direction. The end edges of the specimens were covered by the grooves such that a rotational restriction was applied to the boundary regions. Accurately fabricated mild-steel specimens and stiffeners were used in these tests (see Table 3-1, in which n is the number of stiffeners, L_s, b_s and t_s are the length height and thickness of the stiffeners respectively). A structural epoxy adhesive "Spabond 345" was employed to connect the stiffeners. The area to be stiffened was carefully degreased and cleaned prior to the connection of the stiffeners to reach a perfect connection (see Figure 3-3, Figure 3-4 and Figure 3-5).

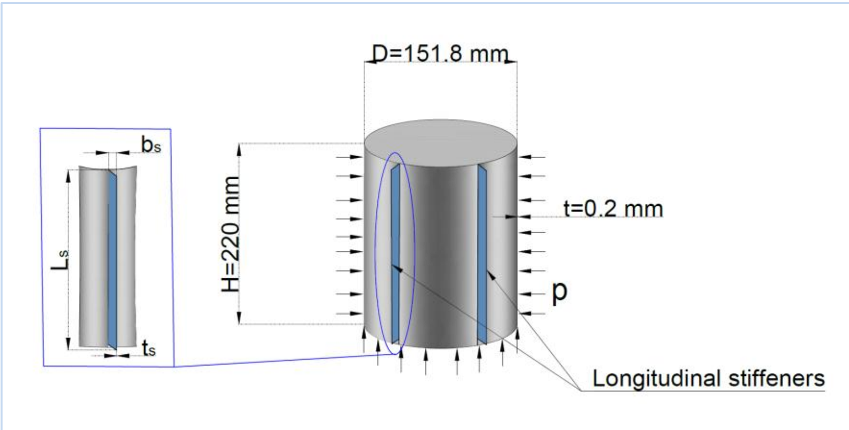

(a)

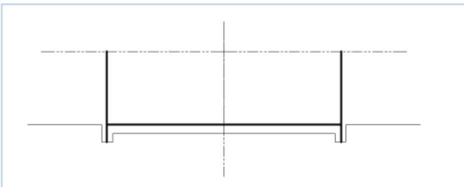

(b)

Figure 3-2: (a) Schematic illustration of the specimens and stiffeners and (b) radial boundary condition of the end edge of the shells located to be in the groove of the end plate.

(a) (b) (c)

Figure 3-3: (a) and (b) Full length stiffeners and (c) partial stiffeners connected to the specimen.

Loading

A vacuum pump was utilised to apply the loading. A control release valve was used to control the rate of the loading to ensure a uniform pressure with a monotonic and low rate of increase. A digital pressure gauge measured and reported the pressure throughout the tests. This gauge was connected to the pressure chamber by means of a flexible copper hose through a hole in the top plate to reach the chamber. The inlet hose to the pressure pump was connected to the pressure chamber by the same means.

Table 3-1: Specimens and stiffeners geometric specifications.

Geometry	Specimen	Strengthening	n	L_s (mm)	t_s (mm)	b_s (mm)
D/t=758.85	ECS.1	–	–	–	–	–
	ECS.2	Stiffener, partial	4	100	0.5	16
	ECS.3	Stiffener, partial	6	100	0.5	16
t=0.2 (mm)	ECS.4	Stiffener, partial	8	100	0.5	16
	ECS.5	Stiffener, partial	10	100	0.5	16
	ECS.6	Stiffener, full	6	198	0.5	16
H/D=1.45	ECS.7	Stiffener, full	8	198	0.5	16
	ECS.8	Thickener, full	6	198	0.5	16
	ECS.9	Thickener, full	8	198	0.5	16

Figure 3-4: Strengthened specimens with *n*=6 (left) and *n*=8 (right).

Measurements

Four LVDTs were used to measure the radial displacement of four points on the specimens. These devices were placed at mid-height of each specimen at each quarter of the circumference in a symmetrical manner between stiffeners. CEA-06-240UZ-120 strain gauges (Micro-Measurements, Vishay Precision Group, Inc. USA) were attached midway between the stiffeners to record the micro-strain of the specimens. The orientation of the strain gauges is given in the later sections.

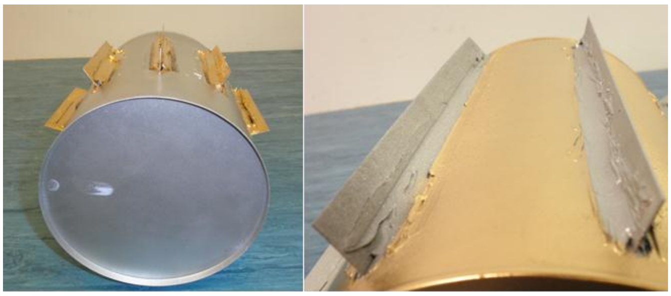

Figure 3-5: Partial (left) and full stiffeners (right).

3.2.3 Results and discussions

Test observations

The buckling response of the plain shell (ECS.1, without reinforcement) was discussed in detail in the previous chapter, where dented shells were described. Since the specimens and the loading condition were the same for two sets of experiments the buckling behaviour was obtained similar for the plain specimens, which is not included here to avoid repetition.

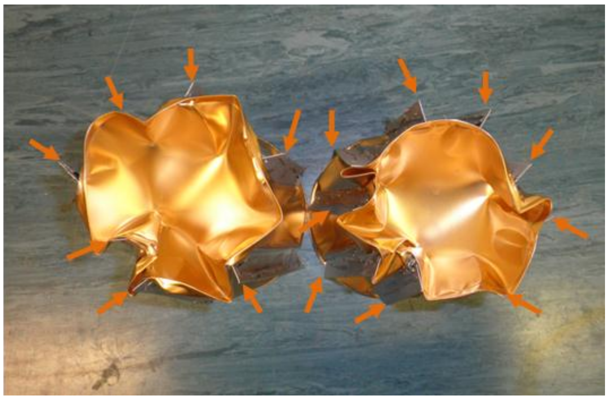

Figure 3-6: Specimens with stiffeners after collapse (stiffeners marked).

Partially stiffened shells

Initial buckling in the form of lobed buckling midway between the stringers was observed in this set of tests. The top and bottom portions of the surface were not stiffened so the buckling propagated to those zones. For ECS.2 specimen the circumferential unstiffened area between the stringers was large so V-shaped yield lines appeared midway between the stringers. These became zigzagged at the post-buckling stages of loading (see Figure 3-7). Axial shortening was quite obvious in this type of specimens as the top and bottom unstiffened regions were fairly crumpled at the collapse stage.

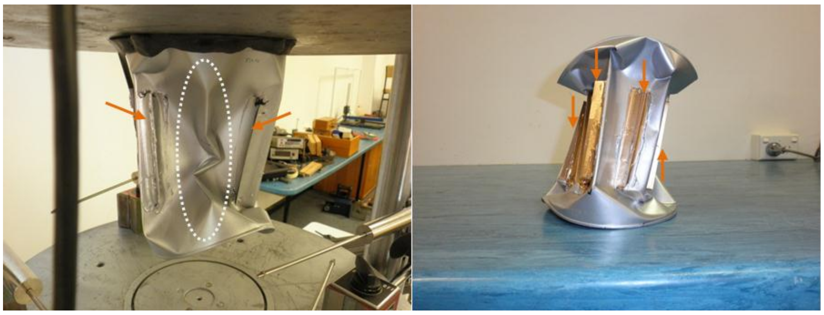

Figure 3-7: Buckled mode of two specimens with partial stiffeners, *n*=4 (left) and *n*=8 (right).

Fully stiffened shells

Fully stiffened specimens were quite stable relative to the partially stiffened ones so that the initial buckling occurred in a relatively more brittle manner. U-shaped yield lines were observed as the full length stiffeners (stringers) caused these specimens to be less able to shrink circumferentially than the partially stiffened ones. Nonetheless, a truncated conical shape was eventually seen for the collapsed specimens (see Figure 3-8 and Figure 3-9). The reason why this shape was observed is that the bottom plate connected to the specimens – which was made of the same material – allowed the specimens to be dislocated from the groove due to the existence of an axial loading imposed to the bottom plate. Thus, as the pressure increased, the plate was deformed circumferentially towards the centre of the specimens. As a result, the whole specimen eventually took the form of a frustum cone in the collapse phase. Buckling progress of a typical section for a fully stiffened specimen with 8 stiffeners is shown in Figure 3-10.

Thickened shells

Figure 3-11 shows the buckling progress of the thickened specimens with 8 stiffeners. Note that these figures were extracted after a close review of a video taken from the whole experimentation for that specimen. Initial buckling was lobar, and progressed with deepening of the buckling lobes and ultimately local dislocation of the bottom edge as seen in Figure 3-11. As the buckling waves deepened they encompassed some thickeners in the post-buckling phase of this specimen.

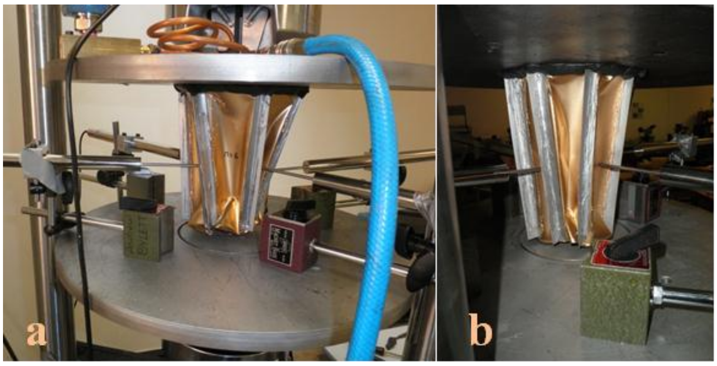

Figure 3-8: Fully stiffened specimens after collapse, (a) *n*=6, (b) *n*=8.

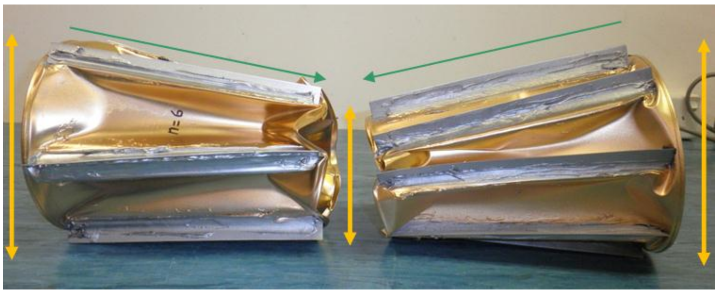

Figure 3-9: Fully stiffened specimens after collapse, *n*=6 (left) and *n*=8 (right).

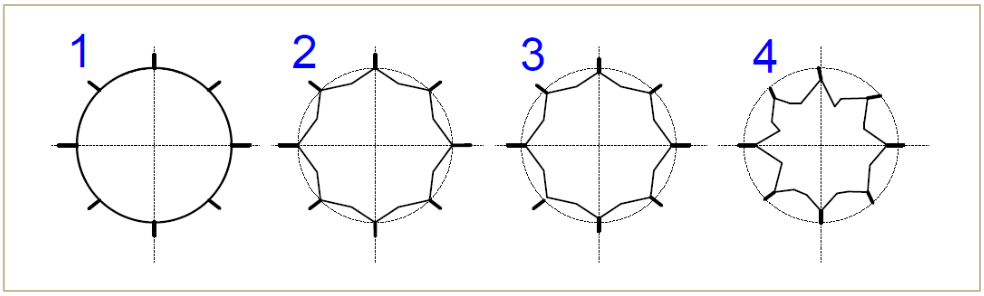

Figure 3-10: Buckling progress in a typical section for a fully stiffened specimen.

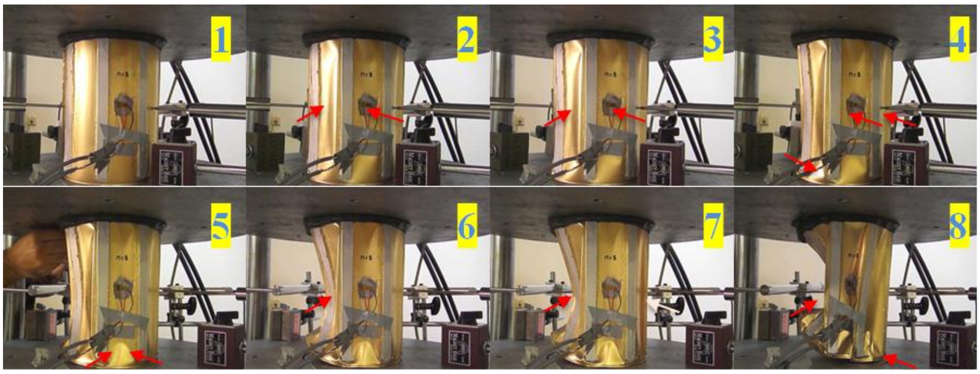

Figure 3-11: Buckling progress for the strengthened specimen with *n*=8 (arrows show the deformation progress).

Load displacement and strain curves

Figure 3-12 shows the radial displacement versus pressure for two partially stiffened specimens. T1 through T4 specify the four aforementioned LVDTs. It can be seen that the loading was terminated after the formation of the entire lobes and collapse of the specimens. In these specimens the initial buckling and overall buckling occurred at the same time with the formation of the lobes simultaneously. The post-buckling stage of the tests exhibited deepening of the buckling waves accompanied by relevant jumps on the load displacement curves (see Figure 3-12).

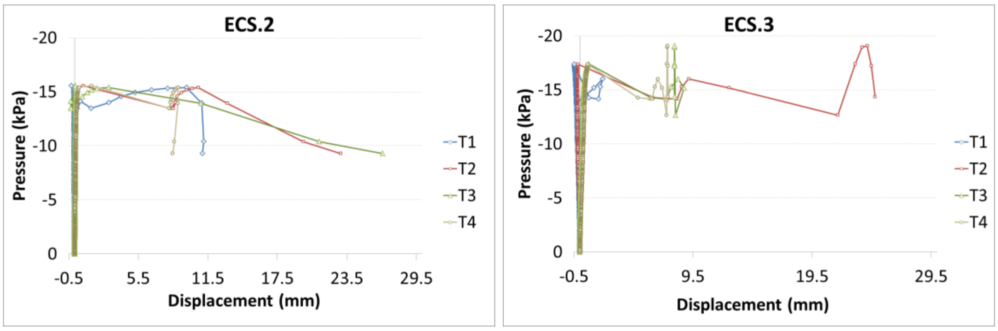

Figure 3-12: Load versus radial displacement curves for partially stiffened specimens with 4 (left) and 6 stiffeners (right).

For the fully stiffened specimens the post-buckling stage of loading was quite stable (see Figure 3-13). The pressure was increased further up to approximately 60 kPa after the buckling waves had covered the entire specimen. Although the pressure rate was rather high relative to the initial buckling capacity of the specimens, no air leakage took place; therefore, a stable post-buckling path is displayed in Figure 3-13 for these two specimens. It should be noted that as the fully stiffened specimens were more stable at the post-buckling stage in terms of deformations, the post-buckling path of the load-displacement curves for these specimens were more stable in comparison with the partially stiffened specimens (see Figure 3-12 and Figure 3-13).

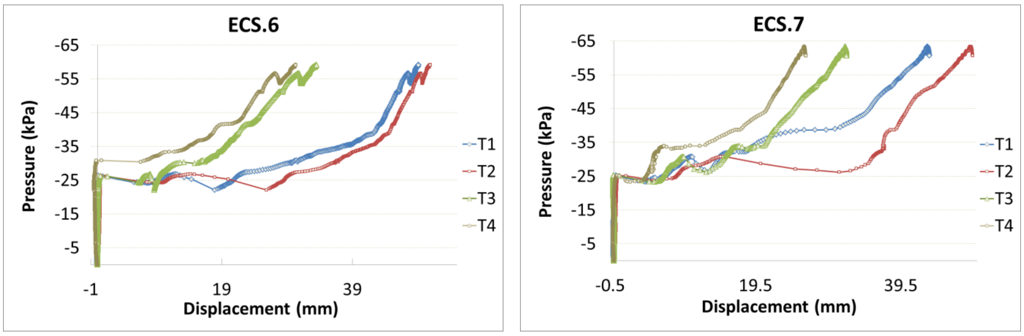

Figure 3-13: Load versus radial displacement for fully stiffened specimens with 6 (left) and 8 stiffeners (right).

For the thickened specimens, two strain gauges were attached with S1 connected in a longitudinal direction and S2 in the circumferential direction.

Figure 3-14 shows the radial displacement and the strain values for the two strengthened specimens with local thickening.

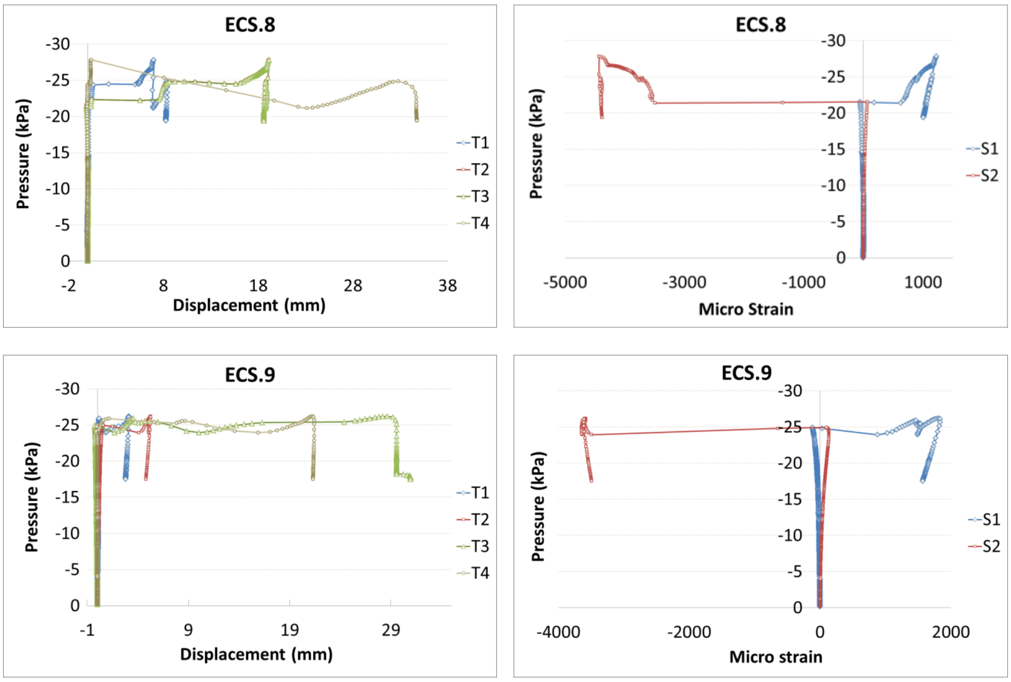

Figure 3-14: Load versus radial displacement (left) and micro-strain values (right) for the thickened specimens (ECS.8 and ECS.9).

3.2.4 Buckling capacity of the current shells

Table 3-2 shows the values of initial and overall buckling in these specimens. Additionally, the ratio of the initial buckling load of the stiffened specimens to the plain specimen was presented. As shown, for ECS.2–ECS.5 with between 4 and 10 partial stiffeners, the buckling capacity increased by 23.8%, 38.1%, 17.5% and 22.2%. Overall, there was an optimal improvement of around 38%, evidently therefore, 6 partial stiffeners were sufficient to bring about this improvement. However, the critical weakness was in the unstiffened end zones so that additional stiffeners gave no further improvement.

For ECS.6 and ECS.7 with 6 and 8 full-length stiffeners the buckling load was improved by 105% and 99% respectively, which was approximately two times more than the plain specimen. Again, 6 stiffeners were sufficient to bring about this improvement and there was no evidence of benefit from using 8 stiffeners.

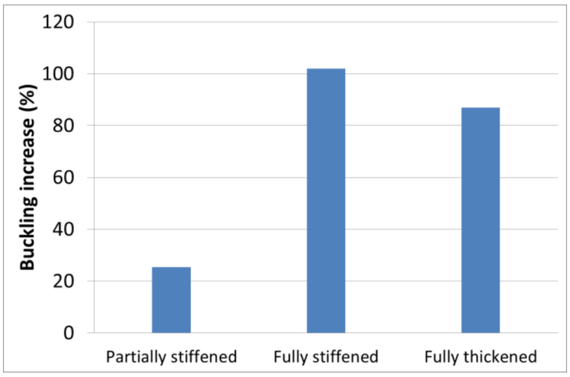

Figure 3-15: Average values for buckling load increase relative to unstiffened specimen for three different types of strengthening.

For thickened specimens, the increase in the capacity was also noticeable, although this rise was slightly milder than the fully stiffened specimens. The use of 8 thickeners had a comparable effect to 8 stiffeners. However, when only 6 were used the capacity improvement was not quite achieved. This may be due to the fact that the thickener, although it is identical in cross section to the stiffeners, was bent about its minor axis.

Table 3-2: Experimental buckling load for the present specimens.

Specimens	Initial buckling (kPa)	Overall buckling (kPa)	$P_{strengthened}/P_{plain}$	Difference (%)
ECS.1	-12.6	-12.6	1.00	0
ECS.2	-15.6	-15.6	1.24	24
ECS.3	-17.4	-17.4	1.38	38
ECS.4	-14.8	-17.6	1.17	18
ECS.5	-15.4	-16.8	1.22	22
ECS.6	-25.8	-30.5	2.05	105
ECS.7	-25.1	-25.1	1.99	99
ECS.8	-22.3	-27.8	1.77	77
ECS.9	-24.8	-25.9	1.97	97

Note that the installation arrangement for the thickeners is likely to be generally more convenient in practice. Where the minor increase in performance achieved by the stiffener configuration is not required we would therefore recommend using the added plates as thickeners. The average values of the capacity increase for three types of strengthening are presented in a bar chart respectively as seen in Figure 3-15.

3.2.5 Evaluation of the results against the design codes and studies

Theoretical predictions that are available in various studies and recommendations in standards were presented in the previous chapter.

European Convention for Constructional Steel-work [76], Jawad and Ross [73, 74] and British Standards Institution (BSI) proposed expressions for the critical load of the shells [75] (see the previous chapter for the equations). Figure 3-16 shows the results of this section compared to the mentioned predictions, in which the plain specimen's data is marked on the graph. The increasing effect of the stiffening with different numbers of stiffeners can be seen in this figure and Figure 3-17 with different specified strengthening methods and corresponding critical buckling loads.

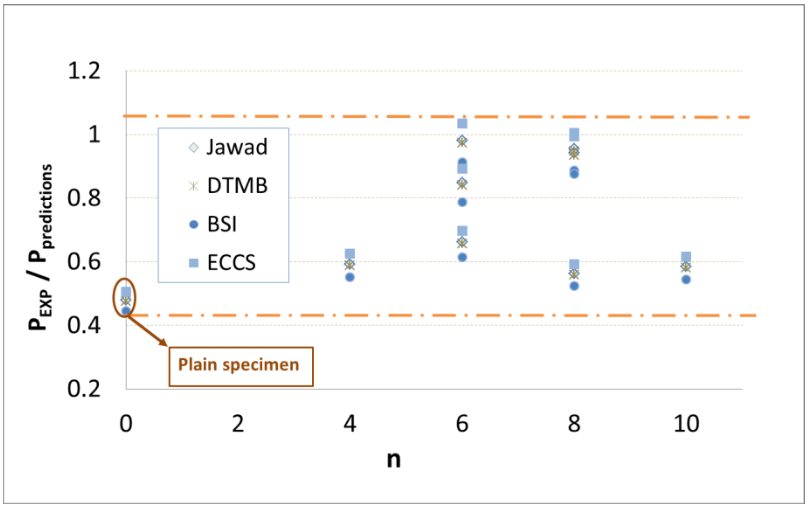

Figure 3-16: Comparison of the results with [73-76].

As can be seen, the equation presented by ECCS shows the closest agreement with the test results, which can be more reliable for the estimation purposes in comparison with the other studies. On the other hand conducted studies under vacuum over the last 15 years showed that theoretical predictions overestimate the experimental results. This is believed to be largely attributed to the geometrical imperfections found in fabrication of specimens and test set up, which are inevitable [46, 105]. In light of this, the results of the present study can be considered to be acceptably consistent with the predictions. One may note that in theoretical estimations, apart from neglecting the real geometrical imperfections, some assumptions such as boundary conditions might be different from what is seen in the real experiments so that the results are by-and-large overestimated.

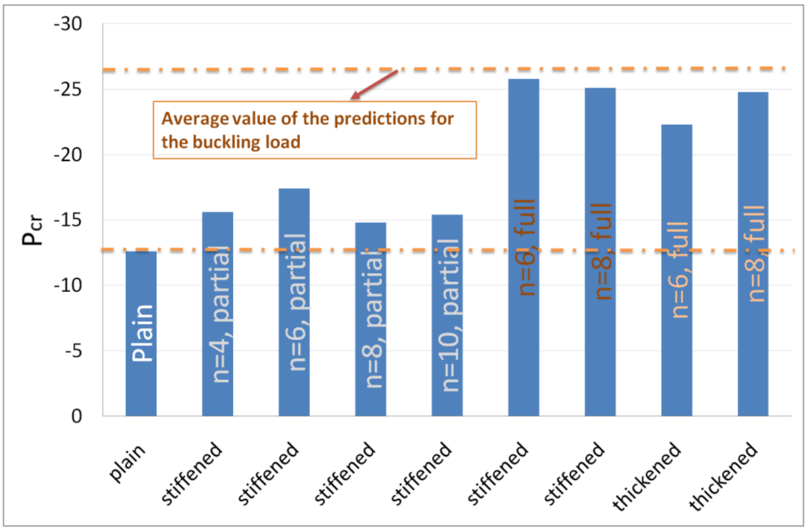

Figure 3-17: Different strengthening methods and critical buckling loads.

3.2.6 Concluding remarks

Nine specimens were tested under uniform external pressure applied through vacuum. The specimens were mild steel thin-walled cylindrical shells with end caps. Partial and full length stiffeners (stringers) and also full length thickeners were applied in this set of specimens with varying number of strengtheners.

For partly stiffened specimens, as the end portions of the cylindrical surface were not stiffened the buckling propagated to those zones. Fully stiffened specimens were quite stable relative to the partially stiffened ones. A truncated conical shape was ultimately seen for the collapsed specimens in the fully stiffened specimens. For specimens with 4, 6, 8 and 10 partial stiffeners the buckling capacity increased between around 20-40% respectively. For ECS.6 and ECS.7 with 6 and 8 full-length stiffeners the buckling load increased by approximately 105% and 99%, i.e. nearly two times more than the plain specimen. For thickened specimens the increase in the capacity was noticeable, although this rise was milder than the fully stiffened specimens. It is noteworthy that if not much increase in capacity is required by the designers, the thickening cases would be preferable as the installation of this type of strengthening is more convenient. Thickening resulted in only slightly less capacity compared with the stiffening method.

3.3 Reinforcement of pressurised shells without additional materials (corrugation)

3.3.1 Introduction

The usage of thin pressurised shells was discussed earlier in this section as well as the previous chapter of the thesis. The introduction of this section sets out to briefly present a few references on the background work, as well as the corrugation method of reinforcement as the main idea of this section.

Externally pressurised shells and buckling

Ghanbari Ghazijahani and Showkati conducted a few experimental studies in which various shells with high *D/t* ratios were tested and the buckling behaviour of these structures was examined [45]. In this investigation the effect of geometrical imperfection was considered. Cylindrical shells reinforced by stiffeners were recently investigated in Ref. [106], and through another study by Shahandeh and Showkati [22]. It was found that both ring stiffeners and stringers considerably enhanced the ultimate capacity of the mentioned structures. Ghanbari Ghazijahani et al. investigated the effect of local dent-shaped imperfection in shells structures in three respective studies [65, 71, 106]. It should be mentioned that the geometric form of a dent imperfection was quite similar to the present corrugations, but the corrugations were applied to the overall length and circumference, while dents affected a local area on the surface of shell structures. A kind of strengthening effect of the local dent imperfection on the capacity was identified in some cases for shells under external pressure in the mentioned studies. As mentioned before, this behaviour was verified by the recent studies of Showkati et al. who concluded a sort of stiffening effect of weld-induced longitudinal imperfections in thin cylindrical and conical shell structures [68-70]. The stiffening effect of some specimens of the aforementioned studies motivated this research to consider an approach through which the local effect on the geometry of these structures could be used as a stiffening method. In this method, no additional stiffeners would have been required to increase the buckling capacity of such structures.

Corrugated shells and this study

A theoretical study was performed on a number of tin cans with different geometric features [107]. This paper showed that the wall thickness of thin specimens can be reduced by around 57% leading to a significant weight decrease and accordingly total costs can be considerably reduced. Ross studied ring stiffened and corrugated cylinders through a FE modelling program [108]. It appeared that the corrugation idea was structurally more efficient than the conventional stiffening method. Corrugated carbon fibre pressure vessels under external hydrostatic pressure were studied by Ross and Little [109]. It was found that buckling took place when the vibration eigenmode was similar to the buckling eigenmode.

A few further studies were conducted by Ross et al. [109-113] on corrugated shells, which have mostly focused on circumferential corrugation of the shells. Apart from the mentioned studies on corrugation, no other relevant study has sufficiently covered the stability of longitudinally corrugated structures under external pressure. To this end, the experimental program of this section of the thesis was conducted and both vertical and diagonal corrugations were used to enhance the buckling capacity. The main objectives of this section are in summary:

- experimental modelling of longitudinal corrugation on shell specimens;
- buckling assessment and evaluation of the current longitudinally corrugated shells;
- optimal design of the number of stiffeners and their geometric orientations, and,
- comparison of the results with the existing design codes and theoretical recommendations.

3.3.2 Experimental set-up

In this set of the tests two plates were utilised as boundary conditions which had annular grooves. A MTS machine was used for testing the present specimens (item 1 in Figure 3-18). Shell specimens were placed within the grooves in order to rotationally restrain both ends of the specimens. An overall view of the test rig is presented in Figure 3-20. The top and bottom plates (items 3 and 5 in Figure 3-20) were gripped by the top and bottom jaws of the MTS machine to allow them to be adjusted vertically in a proper position. Accurately fabricated shell specimens (item 7) with the geometric features given in Figure 3-18 and Figure 3-19 and Table 3-3 were employed in this experimental investigation. Due to rings at top and bottom of the specimens the corrugations were developed as close as possible, but not right up to the ends with the similar depth.

Table 3-3: Geometric specifications of the specimens.

Geometry	Specimen	Length of corrugations (mm)	Orientation of corrugations	Number of corrugations (n)
D/t=758.85 t=0.2 (mm) H/D=1.44	SDF.1	-	-	-
	SDF.2	Full length	Vertical	4
	SDF.3	Full length	Vertical	6
	SDF.4	Full length	Vertical	8
	SDF.5	Full length	Vertical	10
	SDF.6	Full length	Vertical	12
	SDF.7	Full length	Vertical	16
	SDF.8	Full length	Diagonal $\alpha=75^{\circ}$	8
	SDF.9	Partial (98 mm)	Vertical	6
	SDF.10	Partial (98 mm)	Vertical	8
	SDF.11	Partial (101.5 mm)	Diagonal, $\alpha=75^{\circ}$	8

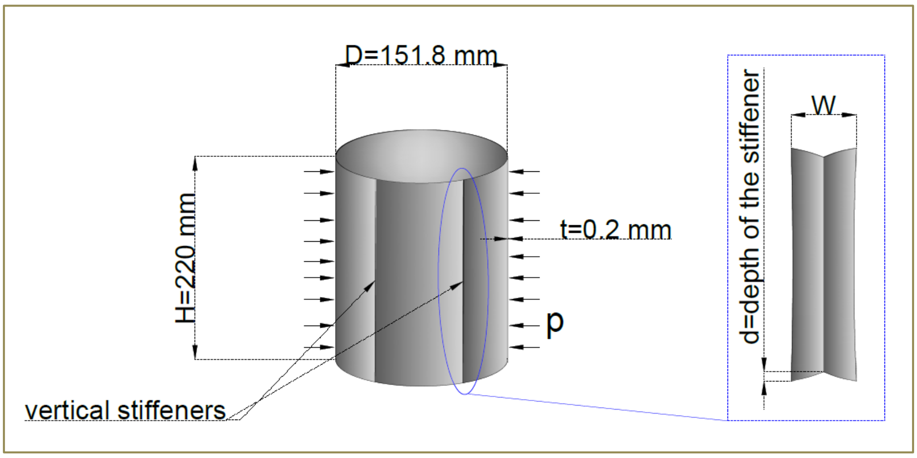

Figure 3-18: Overall configuration of a typically stiffened specimen.

Properties of the present mild steel material were obtained from a conducted coupon test as reported in Ref. [49]. Top and bottom edges of the specimens were enclosed with two circular caps. Four Linear Variable Differential Transformers (LVDTs) were utilised (4) to monitor and record the displacement of different points on the surface of the shells throughout loading.

A vacuum pump (10) was used to apply the loading. An inlet hose (6) connected the pump to the inside chamber of the specimens.

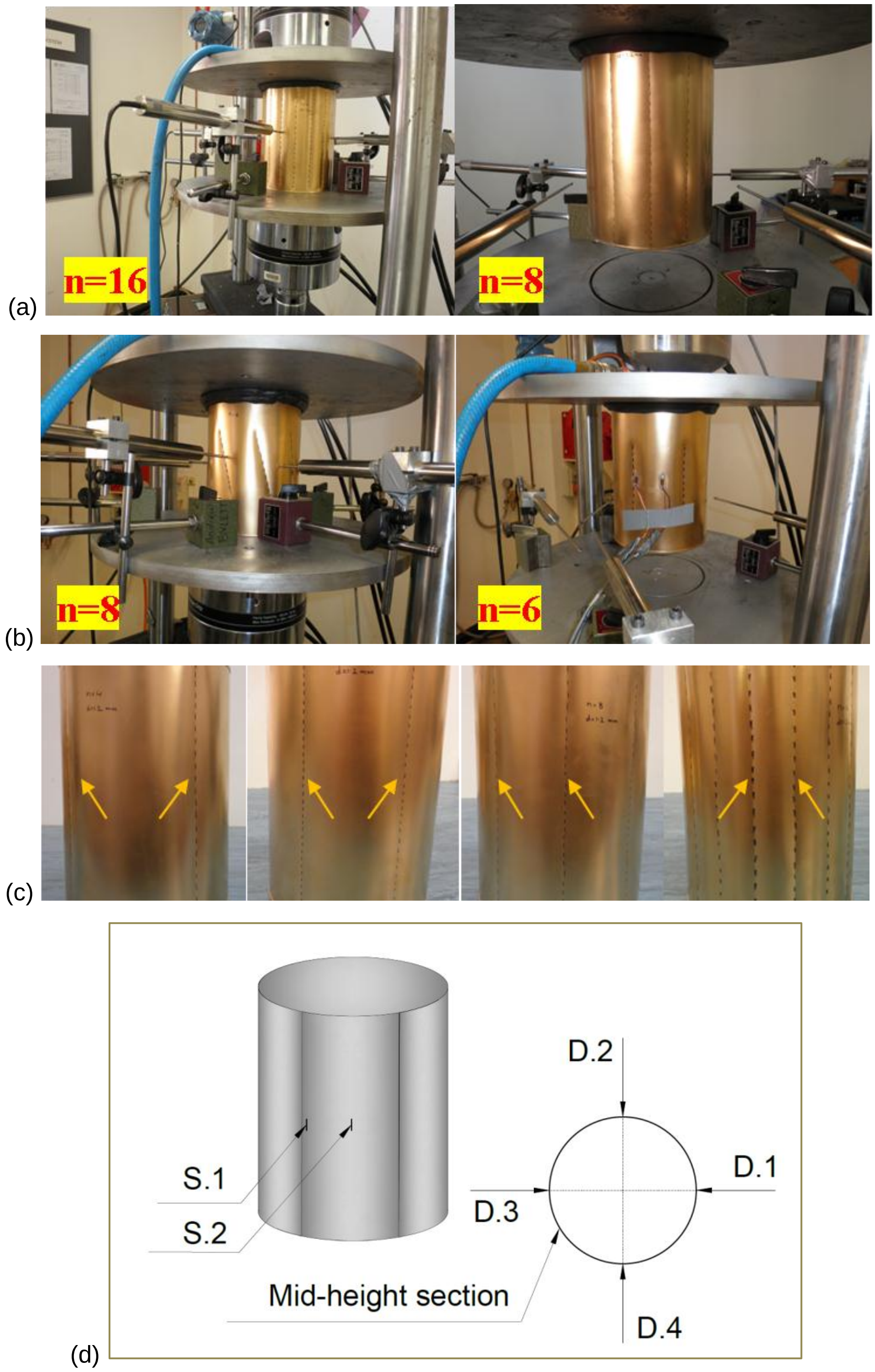

Figure 3-19: (a) Fully vertically stiffened specimens before testing with different number of stiffeners marked, (b) different partially stiffened specimens (vertically and diagonally), (c) fully stiffened specimens with different number of stiffeners (stiffeners marked with arrows), (d) details of LVDTs and strain gauges.

Two control valves (9) were installed through the evacuation canal through which the air flowed (vacuum) and accordingly loading speed was precisely controlled to reach quasi-static loading during the tests. CEA-06-240UZ-120 strain gauges were attached on the surface of the shells to record the strain magnitude during the loading.

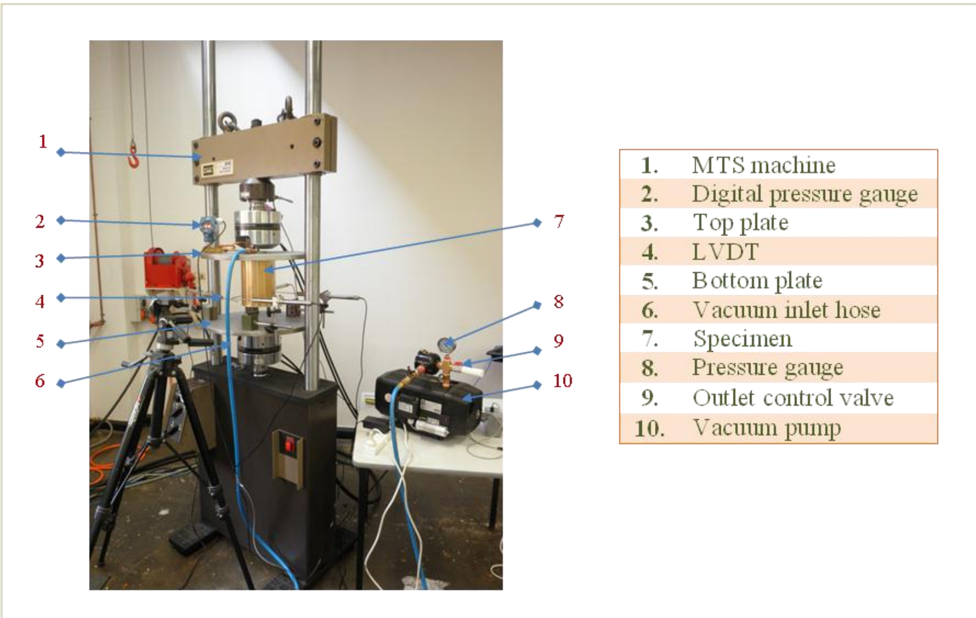

Figure 3-20: Experimental set-up for cylindrical shell specimens under external pressure.

Specimens were completely sealed by a reliable flexible sealant both at the groove and around the top and bottom edges of the specimens. A digital pressure gauge (2), and a gauge attached to the pump (8) were connected to the pressure chamber of the specimens in order to measure the pressure precisely during the tests.

3.3.3 Test results and discussions

General observations

In the present experimental program the plain specimen (SDF.1) was quite vulnerable to buckling as after increasing the load up to the critical point buckling waves occurred one after another or in pairs in a very short interval. The asymmetrical buckling lobes quickly covered the whole circumference such that, as expected, the inward deformations were quite dominant relative to outward ones. Inward deformations took place at the depression areas of the buckling lobes which were deformed in a U-shaped form towards the centre of the specimen. Outward deformations appeared in the form of V-shaped yield lines, which were severely affected by the plastic deformations in the post-buckling stage of the loading. As the pressure increased the specimen shrank circumferentially and the outward deformations, i.e. yield-lines, also deformed towards the centre of the specimen. It is noted that torsion of the whole specimen was observed once the yield-lines were randomly broken. This phenomenon occurred together with the formation of the V-shaped and/or U-shaped inflection points along the yield-lines.

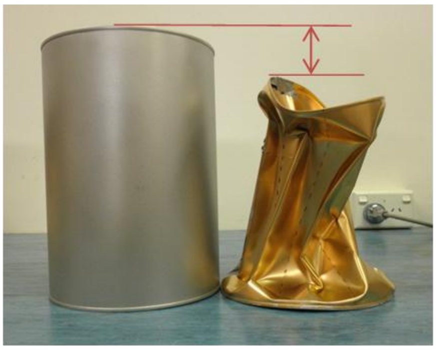

Figure 3-21: Axial displacement after collapse.

As for the corrugated shell specimens (SDF.2–11), the buckling waves were regularly oriented and geometrically shaped owing to the existing of the corrugations such that the corrugation lines were placed exactly at the centre of each buckling wave. In other words, the longitudinal yield-lines encompassed the corrugation lines from both sides once overall buckling occurred.

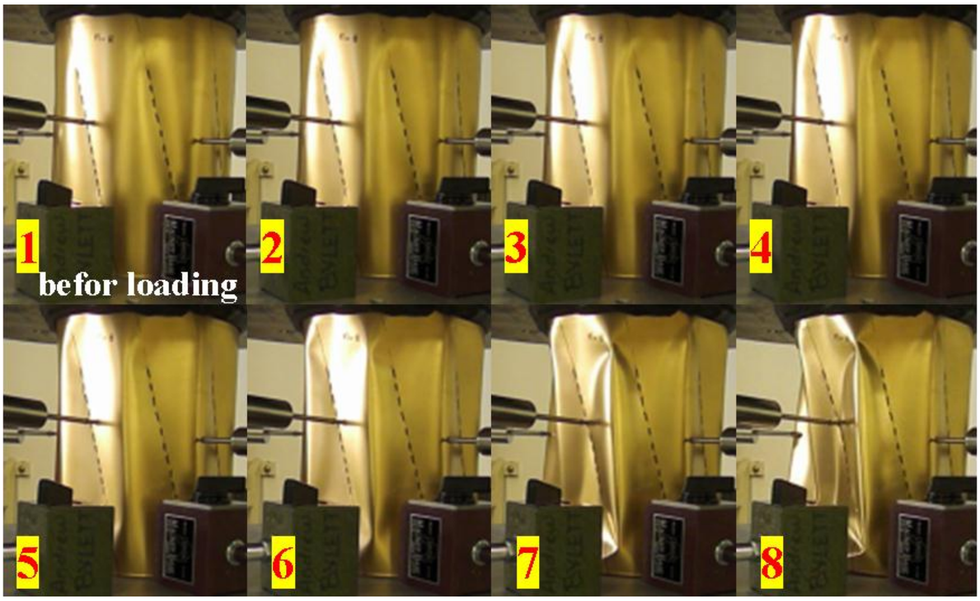

Figure 3-22: Buckling progress during loading for the specimen SDF.11.

Furthermore, buckling waves were initiated at the mid-height and accordingly developed along the whole length of the specimens. It is noteworthy that the number of the buckling waves depended on the number of the stiffeners, i.e. corrugations. For SDF.2, more than one buckling waves occurred between each pair of stiffeners, whereas each stiffener was placed at the centre of a single buckling lobe for the specimen SDF.3 and SDF.4.

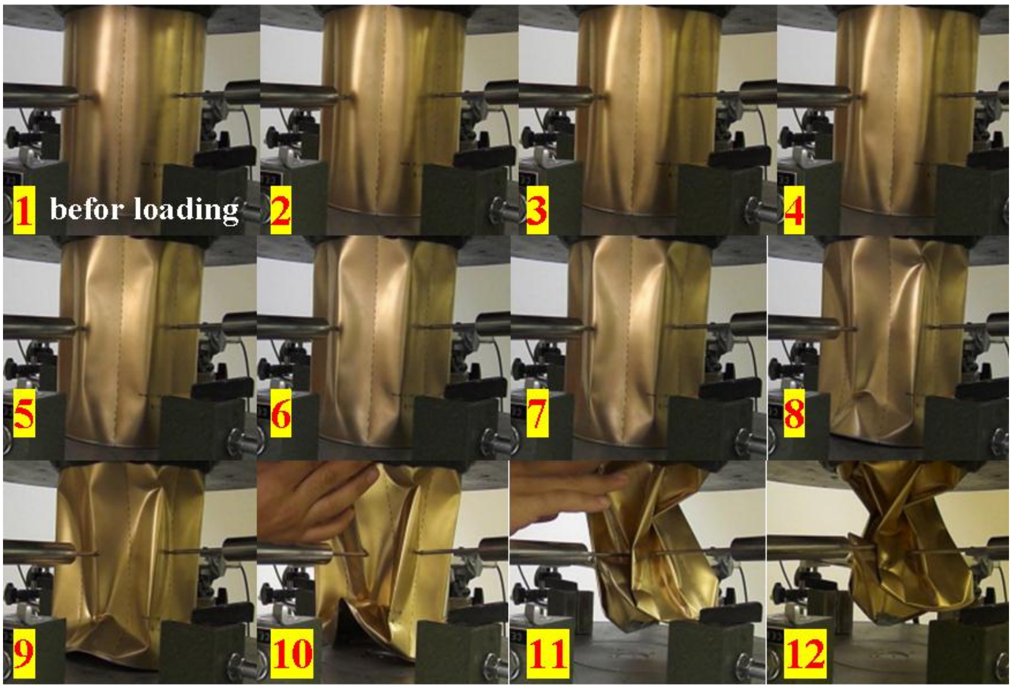

Figure 3-23: Deformational stages for the specimen SDF.3.

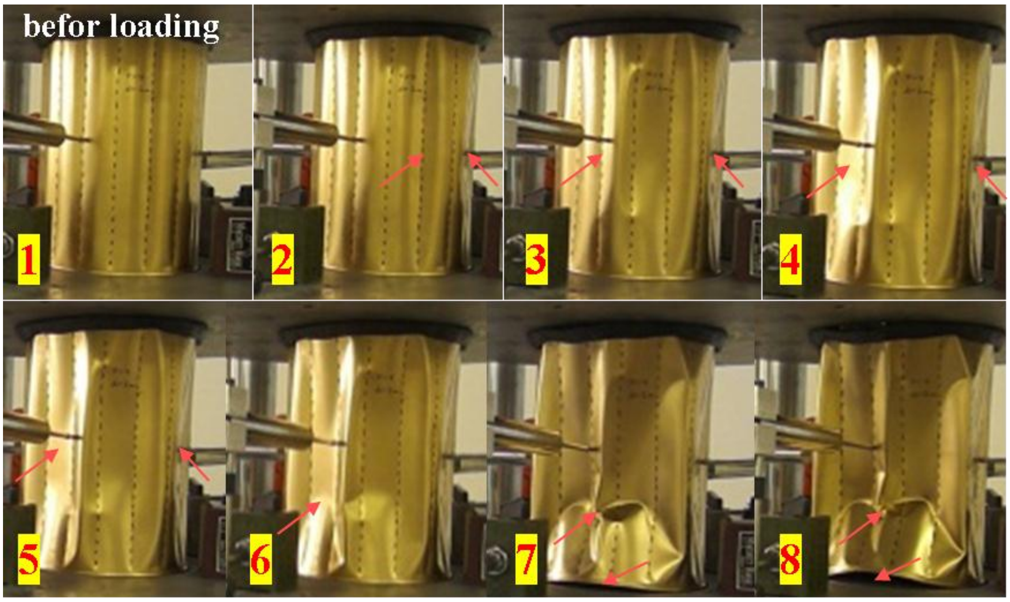

Figure 3-24: Development of the buckling during loading for the specimen SDF.7 (salient areas marked).

Torsion of the specimens in the post-buckling phase of the deformations occurred for the corrugated specimens in a similar way to the plain specimen. This phenomenon was accompanied by the axial deformation, developed due to the end caps, of the specimens which can be plainly seen in Figure 3-21. Axial deformation occurred in corrugated specimens affecting approximately a quarter of the whole height as can be seen in Figure 3-21.

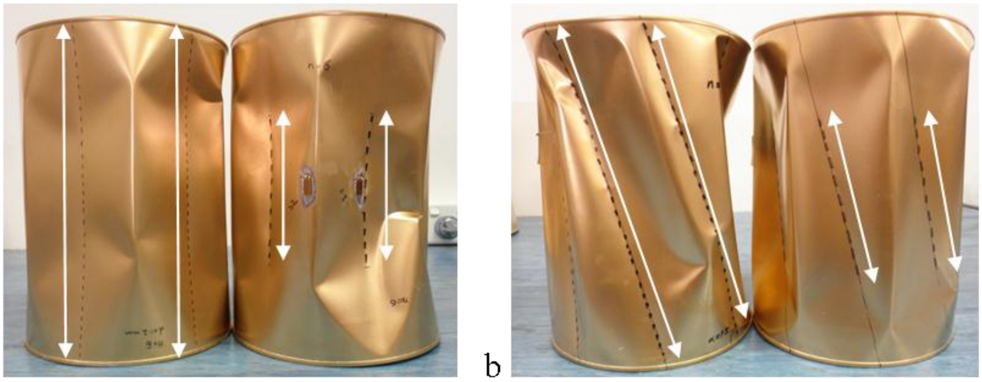

a b

Figure 3-25: Specimens with partial and corresponding full stiffeners with n=6: (a) vertical corrugation, (b) diagonal corrugation.

Progress of buckling is shown in Figure 3-22, Figure 3-23 and Figure 3-24 with the salient deformed points marked in Figure 3-24. As can be seen in Figure 3-22, diagonal partial corrugation was applied to the specimen SDF.11. As discussed earlier, buckling was initiated in the corrugated lines and developed towards the sides nearby. Figure 3-23 and Figure 3-24 show the buckling progress in the specimens SDF.3 and SDF.7 with fully corrugated stiffeners. In the case of SDF.3 the pressure rose up to more than 50 kPa, which geometrically led to an extremely crumpled specimen after collapse.

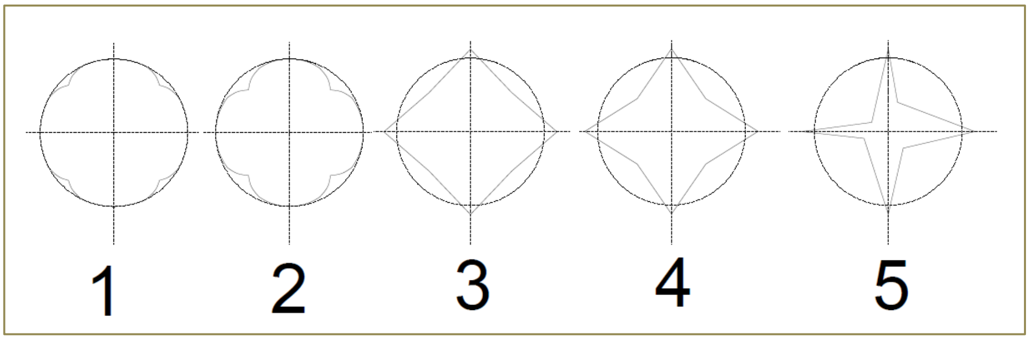

Figure 3-26: Buckling progress for a typical section of the specimen with four stiffeners.

Figure 3-25 shows four specimens with partial and corresponding full stiffeners with n=6 in the form of vertical and diagonal corrugations after testing. It is quite obvious that the corrugations resulted in a regular and harmonic shape of overall buckling in these specimens in which the yield lines appeared between the corrugation lines. Buckling progress for a typical section of the specimen with four stiffeners is also illustrated in Figure 3-26. Torsion of the collapse lines (yield lines) in two different specimens is also presented in Figure 3-27.

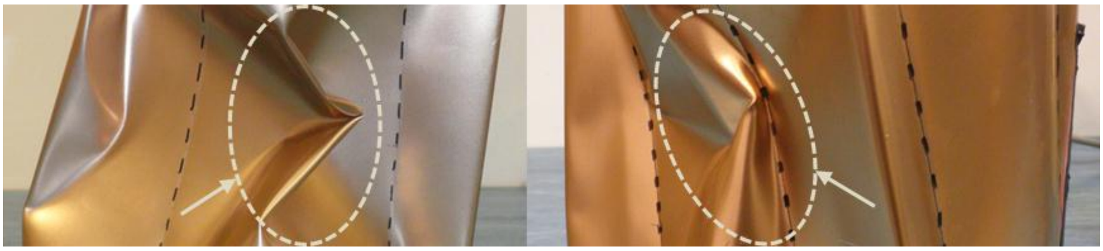

Figure 3-27: Torsion of the collapse lines in two different specimens.

Load displacement and strain curves and buckling

Pressure against radial displacement is presented in Figure 3-28 and Figure 3-29 for different specimens. In these figures, labels D.1–D.4 represent four different LVDTs. D.1 and D.3 were located in points at the trough point of the corrugation while D.2 and D.4 were placed midway between two stiffeners. Each LVDT was located on each quarter of the circumference at the mid-height of the specimens.

As is seen in Figure 3-28, the specimen SDF.2 with the minimum number of stiffeners showed an unstable load displacement behaviour in comparison with the other specimens especially in the post-buckling stage of the deformations. Each jump on the load displacement curves represented an abrupt local and/or global deformation which can be considered to be a formation of the buckling lobe(s) until the overall buckling had occurred. In some specimens all inflection points on the curves occurred at or very close to a certain pressure indicating that those specimens were geometrically perfect in terms of fabrication of both specimens and stiffeners so that all the buckling lobes tended to occur concurrently. In other words, the initial and overall buckling occurred simultaneously in these specimens.

A salient point is that total values of the radial displacement for the specimens with fewer corrugated lines were rather less than those with more stiffeners, which is another indication of the efficiency of the corrugation in improving the structural stability of the present specimens.

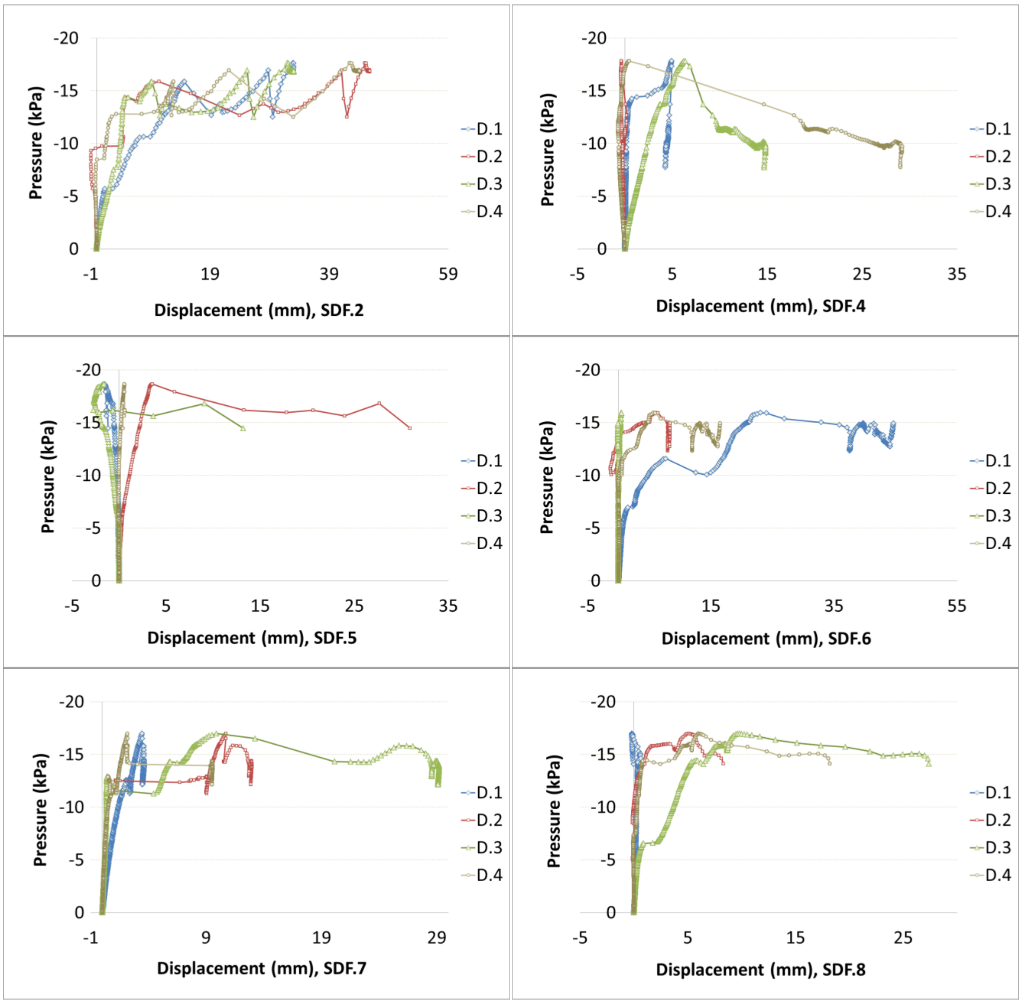

Figure 3-28: Pressure-radial displacement for the specimens fully stiffened longitudinally.

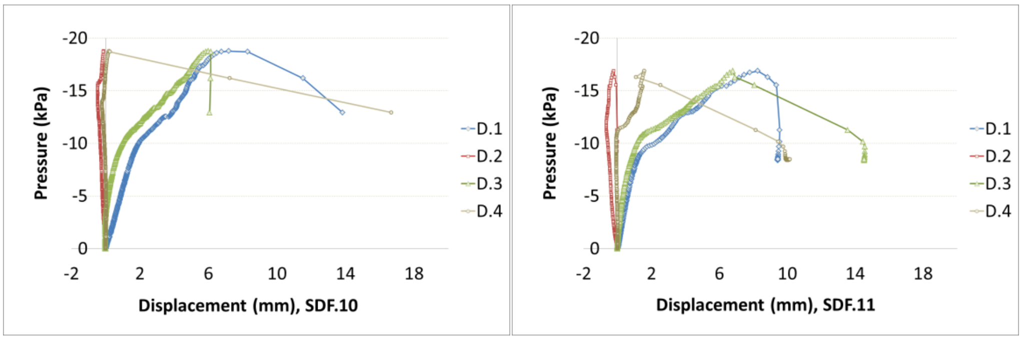

Figure 3-29: Radial displacement for the specimens partially stiffened.

In addition, one may detect negative values in some of the curves for the LVDTs especially for D.2 and D.4, which indicate outward deformations as these LVDTs were placed on the predicted yield line positions. However, all data changed to positive values after further development of the displacement, demonstrating the overall circumferential shrinkage of the specimens. Strain data of two specimens, SDF.9 and SDF.10, are presented in Figure 3-30 in which S.1 was located on the trough point at the corrugation area at mid-height and S.2 was correspondingly placed on the equivalent intact (non-corrugated) zone. Both strain gauges were recording the longitudinal strain of the present specimens.

(a) (b)

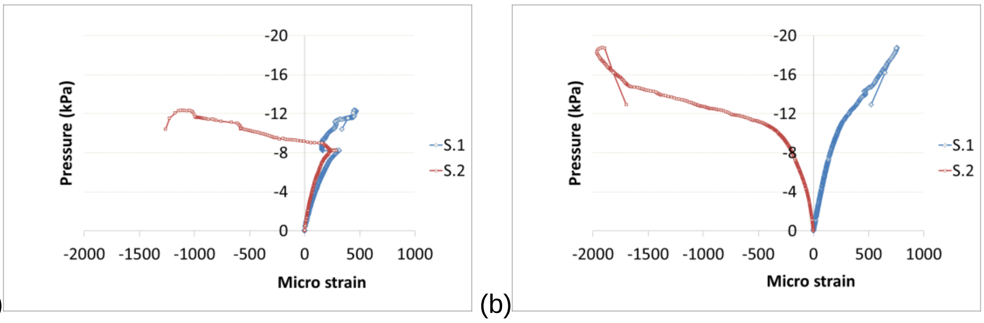

Figure 3-30: Strain values in the specimens: (a) SDF.9 and (b) SDF.10.

3.3.4 Longitudinal corrugation and buckling load of the present specimens

Table 3-4 shows the buckling load of the present specimens. For the fully corrugated specimens with 4, 6, 8, 10 and 12 vertical corrugations the buckling load increased by 2.4%, 16.2%, 42.4%, 48.5% and 27.5% respectively. These values demonstrate that the maximum magnitudes of the buckling load occurred in SDF.4 and SDF.5, with the optimum number of corrugation, of which SDF.5 showed a capacity growth of around 50% (see Figure 3-31). This growth was particularly noteworthy considering that no additional material has been used to strengthen the specimens. This increase can be attributed to the material property of the stiffened area which is believed to be changed due to the application of local load, i.e. indentation. Indenting as mentioned resulted in the material entering the inelastic range so that the strain hardening of the material caused a stronger area for the dented zone. As a consequence, the indented area acted as a stiffener. The other reason for the capacity increase is the undulation of the surface of the shells, which increases the second moment of inertia and the capacity of the shells accordingly.

As the number of corrugations increased, the buckling pressure increased up to the specimen SDF.5 where 10 corrugations were introduced. For SDF.6 and SDF.7, on the other hand, the buckling capacity decreased compared with the specimen SDF.5, and for the specimens SDF.7 the buckling load was nearly equal to the plain specimen, although 16 corrugations were applied. For the specimens with more corrugations than the optimum number, the lower capacity increase might be attributed to greater manipulation through corrugations which led to the circular section of the specimen to change excessively and accordingly have an adverse effect on the capacity. For the specimens with fewer corrugations than the optimum number, the strengthening effect did not appear to be as much as the specimen with the optimum number. Thus, there is an interrelation between the amount of manipulation of the geometry (non-uniformity) causing adverse effects on the capacity, and the strengthening effects. This interrelation for the specimens of this section led to the optimum number of 10 vertical corrugations.

Table 3-4: Critical buckling load of the specimens.

Specimens	**Initial buckling (kPa)**	**Overall buckling (kPa)**	**P/P_{intact}**	**Difference (%)**
SDF.1	-12.5	-12.6	1.00	0.0
SDF.2	-12.8	-15.9	1.02	2.4
SDF.3	-14.5	-14.5	1.16	16.2
SDF.4	-17.8	-17.8	1.42	42.4
SDF.5	-18.6	-18.6	1.48	48.5
SDF.6	-15.9	-15.9	1.27	27.4
SDF.7	-12.5	-17.0	1.00	0.3
SDF.8	-14.4	-16.9	1.16	15.5
SDF.9	-11.5	-12.3	0.92	-7.8
SDF.10	-12.5	-12.5	1.00	0.0
SDF.11	-13.0	-13.0	1.04	4.0

As regards the diagonally corrugated specimen, i.e. SDF.8, the buckling pressure rose by around 15.5% which was far less than the equivalent specimen with vertical corrugations (SDF.4). It should be mentioned that for the specimens with partial corrugations no considerable change in the buckling capacity was observed. This behaviour seems quite expected as the stiffeners were applied partially and the top and bottom portions were still unstiffened, which made the shell specimens fairly susceptible to the buckling in those regions. The partial stiffeners were not strong enough to affect the top and bottom unstiffened segment of the shells.

3.3.5 Shell buckling under external pressure in previous literature

Existing standards and design codes

As presented earlier in this Chapter as well as Chapter 2, ESSC, ENV 1993-1-6 and DIN 18800-4 define the allowable limits of geometric imperfections for shell structures. Notwithstanding these, Showkati et al. have lately conducted several experiments on thin shells indicating that stiffening effect can be obtained from some cases of local dent-shaped or gouge-shaped imperfections [68-70].

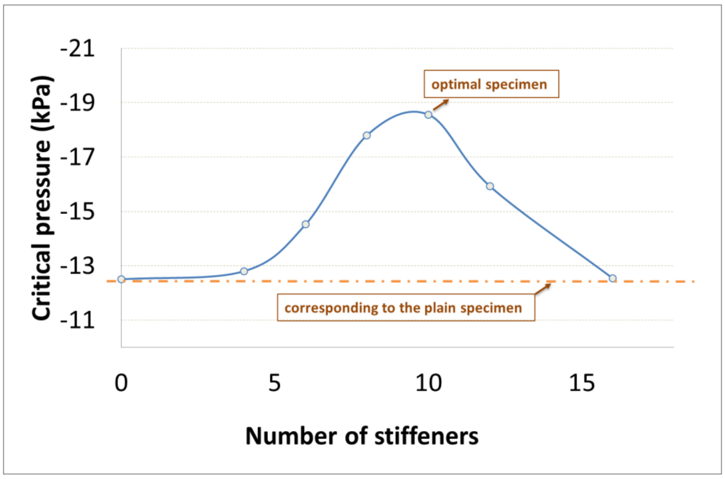

Figure 3-31: Critical buckling pressure versus the number of stiffeners.

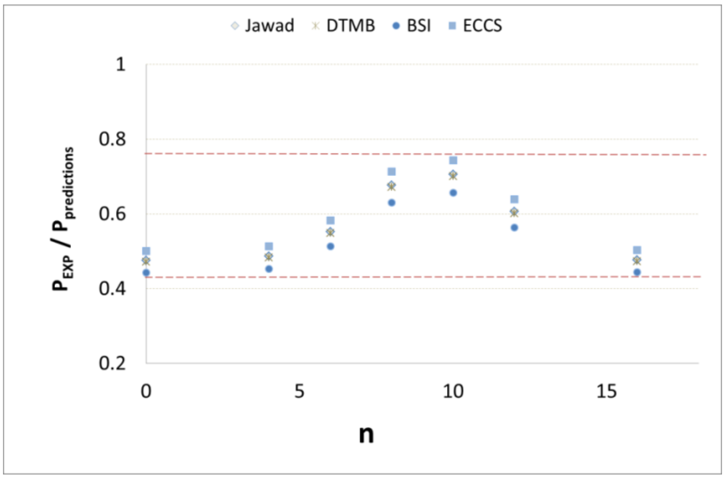

Figure 3-32: Comparison of the results with the design codes and standards [73-76].

In the light of the mentioned results, the research of this section was conducted so as to demonstrate that geometric irregularities in some special forms can be utilised as stiffeners. The present results conclusively prove this hypothesis. In short, it is believed that, to say the least, the existing recommendations in design codes could be subject to revision when it comes to local large imperfections.

Comparing the current results with the theoretical predictions

In this section, four theoretical predictions are presented, which are available in design standards in order to estimate the buckling load of the shell structures. Jawad equation [73], David Taylor Model Basin (DTMB) equation [74], BSI Standard equation [75] and ECCS recommendation for the buckling of shell structures [76] are presented herein and the results of the current tests are evaluated against these predictions. Figure 3-32 shows the ratio of the experimental buckling load of the current specimens to those of the mentioned predictions. It should be remembered that most of the experiments recently conducted on thin shells showed lower values comparing with the theoretical estimations, which is largely attributed to the existence of normal fabrication-related geometric imperfections [35, 68-70]. By the same token, since geometric imperfections are inevitable in all studies related to shells of revolution, the obtained results are reasonably verified considering the predictions.

3.3.6 Conclusion

Eleven thin-walled cylindrical shell specimens with different longitudinal corrugations subject to external pressure were tested in this section. The key findings and observations are presented as follows:

(i) Deformations and failure: Owing to the existing of the corrugations, the buckling waves were regularly oriented and geometrically shaped for the corrugated shell specimens such that the corrugation lines were placed exactly at the centre of each buckling wave. The number of the buckling waves depended on the number of the stiffeners. Axial deformation occurred in these specimens affecting approximately a quarter of the whole height. In case of SDF.3, the pressure magnitude rose to more than 50 kPa after buckling which led to an extremely crumpled specimen after collapse. Total values of the radial displacement for the specimens with fewer corrugated lines were rather less than those with more stiffeners which can be another indication to the efficiency of the corrugation in enhancing structural stability of the present specimens.

(ii) Buckling load: For the fully corrugated specimens with up to 10 vertical corrugations, the buckling load increased by around 50% which was particularly noteworthy considering that no additional material has been used to strengthen the specimens. However, further corrugations led to the circular section of the specimen to change more and accordingly have an adverse effect on the capacity in comparison to the specimens with fewer corrugations. It is worth mentioning that the optimum number of corrugations may depend upon global geometric parameters such as *D/t* ratio.

(iii) Contribution, design and practical considerations: The main contribution of this research is to introduce a method by which a specimen can be used with no additional material as stiffeners yet nearly 50% increase in the capacity is gained. Additionally, the corrugation is applied to the present specimens after rolling them to a cylindrical shape or indeed to a ready cylindrical specimen. This method can be applied to various shell structures if proper instrumentations are devised in this regard so that these structures can be *initially* designed with less thickness and *afterwards* the corrugation can rectify the buckling strength of them after fabrication. In a nutshell, the idea of employing corrugations on shell structures would be notably cost-effective if industry welcomes this idea and equips with proper devices through which the corrugations can be applied even after installation of the shells.

3.4 Conclusions of Chapter 3

This chapter studied the effect of reinforcement on pressurised thin cylindrical shells with normal fabrication-related non-uniformities. In the first section of the chapter partial and full length stiffeners (stringers) and also full length thickeners with varying number of strengtheners were applied (reinforcement with additional material). The main contributions of this set of experiments were the usage of partial reinforcement as well as introducing the connection method by which the reinforcing elements were applied. This method is believed to be preferable in many cases to the welding.

The second section of the chapter investigated longitudinal corrugations to enhance the structural stability such of structures (reinforcement without additional material). Reinforcement with additional material clearly led to more capacity rise in comparison to the specimens reinforced without additional material. However, the optimum number of corrugations resulted in a considerable capacity increase. As well, total cost of the shells reinforced with corrugation seems far less than reinforcement of the shells through additional material. On this basis, if and when appropriate equipment is provided, the corrugation idea seems to be generally preferable, although special consideration of each project must be taken into account before any decision is made regarding different methods of reinforcement.

Chapter 4

Cylindrical Shells with Large Imperfections under Cyclic Bending

Publication output of Chapter 4

This chapter consists of three journal papers published in international journals as follows:

- "Fatigue Tests of Damaged Tubes under Flexural Loading" **Steel & Composite Structures, An International Journal** (Techno Press), Vol. 19, No. 1 (2015) 223-236.
- "Influence of a Cutout on Circular Steel Hollow Sections under Cyclic Loading" **Journal of Constructional Steel Research** (Elsevier), 100 (2014) 12–20.
- "Fatigue Experiments on Circular Hollow Sections with CFRP Reinforced Cutouts" **Journal of Constructional Steel Research** (Elsevier), 106 (2015) 322–328.

4.1 Introduction

CHS members appear in many structural applications, some cases of which are under bending moment [17, 18, 46]. These elements are in some cases exposed to cyclic loading [114, 115]. Cyclic loading is taken into account as a significant loading scheme for Civil and Structural Engineering structures, which in steel structures often leads to fatigue of the material. This chapter investigates the effect of large geometric imperfections, appearing as dents and cutouts, on the fatigue strength of circular steel tubes.

The first two sections of the chapter examine the response of such elements with imperfections but with no reinforcement. In the first section, a dent imperfection, normally caused by a collision for different structures, was modelled, which was followed by fatigue tests. Fatigue life as well as the failure modes are thoroughly discussed. The next section of the chapter reports on the effect of circular openings on the fatigue behaviour of CHS members. Circular cutouts were made near the area of maximum tension stress of steel tube specimens. As with the first section of the chapter the failure of the specimens along with the fatigue response are extensively explored. It was interesting that, due to the distribution of the stress concentration, a cutout with an optimal diameter helped to extend the fatigue life of a tube compared to those without the cutout imperfections, which inspired extensive discussions in this section of the chapter. The key finding of this section that large cutouts significantly reduced the fatigue life while small cutouts provided stress relief to the base stimulated the idea of the next section of this chapter. With a view to recover the lost fatigue life resulted from large cutouts, as the main non-uniformities of this series of tests, the last section of this chapter focuses on reinforcing the area around the cutouts with CFRP. The first two sections of this chapter focus on unreinforced CHS tubes with non-uniformities and under cyclic bending, whilst the last section proposes a practical method to rehabilitate the non-uniform structures under such loading, quantifies and analyses the results of tubes with reinforcement and makes proper comparisons.

Section 4.2 has been removed for copyright or proprietary reasons.

It has been published as: Ghanbari Ghazijahani, T., Jiao, H., Holloway, D., 2015. Fatigue tests of damaged tubes under flexural loading, Steel & composite structures, 19(1) 223-236

4.3 Cylindrical shells with large imperfection (cutouts)

4.3.1 Introduction

For various applications, cutouts in the form of circular holes are sometimes found in circular hollow sections. Towers door openings (see Figure 4-23), cable entrance holes of overhead traffic signs or any transition or secondary element attachments can be instances of the application of the cutout in such structural elements. There are a multitude of papers in the literature regarding structural behaviour of cylindrical shells, among which only a few papers reflected the tubes with cutout under static bending. Based on the conducted literature review, there is no reference exploring tubes with circular opening under cyclic loading.

Figure 4-23: Entrance opening in a tower (courtesy of buildingcodedivision.umn.edu)

The plastic limit load of cylindrical shells with cutouts subject to a pure bending moment was investigated in [123]. In this research, analytical estimations of the lower bound limit load and finite element calculations of thin-walled cylindrical shells with a central circular opening of various geometric parameters were studied and the results were compared with experimental values. The elasto-plastic buckling of cylindrical shells with a cutout under pure bending was investigated analytically and experimentally [124]. It was found that the limiting buckling moment of a shell was smaller when a cutout was on the compression side of the shell than on the tension side. The buckling load of oblique loaded steel cylindrical shells with elliptical cutout was reported [125]. Results of this study showed that the critical load increased with the increase of deformations before the critical buckling load. The buckling load of mild steel cylindrical shells of various *D/t* and *L/D* ratios

(D, t and L are diameter, thickness and length respectively) with elliptical cutouts in different positions was determined [40]. Critical areas of the bulking of thin cylindrical shells under bending were determined [45, 46]. It was believed that any geometrical discontinuities such as cutouts should be avoided in the most critical areas. Analysis and design of a prototype of a steel 1-MW wind turbine tower with opening was evaluated considering different loadings [126]. The plastic behaviour of an elasto-plastic cylindrical shell with circular and rectangular cutouts under bending moment was investigated numerically and experimentally [127]. It was found that the limiting buckling moment of a shell with a cutout increased when the cutout was located toward one of the clamped ends.

In this section, tests were conducted to examine the fatigue life and the failure modes of the tubes with circular cutouts. The effects of the opening size on the fatigue life and the stress concentration were investigated in this research.

Table 4-4: Cutout specifications.

Specimen	Cutout's diameter (mm)	Centre of the hole
QWE.1	36	65 mm from end
QWE.2	36*	65 mm from end
QWE.3	23	65 mm from end
QWE.4	12	65 mm from end
QWE.5	0	-
QWE.6	14	65 mm from end
QWE.7	0	-
QWE.8	19	65 mm from end

*With top and bottom hole.

4.3.2 Experimental program

Features of test rig and loading condition

Eight cantilever beam specimens were tested by means of the MTS-810 machine under cyclic unidirectional loading. Different components of the test apparatus are shown in Figure 4-3. In this set of experiments, the loading was not a reversal loading and was applied as a maximum stress and unloaded up to a minimum stress. A stress ratio of 0.1 (minimum/maximum stress) was adopted for all specimens. The applied maximum stress was about 50% of the calculated yield limit of the intact tubes. Note that although the cutout diameter of each specimen was different from the others, the stress ratio was kept 0.1 for all specimens.

Specimen preparation and perforation process

Mild-steel tube specimens labelled as QWE.1 to QWE.8 with the geometrical features given in Figure 4-24, Figure 4-25, Table 4-1 and Table 4-4 were used in this section. These specimens were accurately prepared and cut into desired lengths. One end of each specimen was machined in a lathe to ensure that the specimen was welded quite perpendicular to the end plate. This was conducted to avoid the influence of non-alignment of a specimen on the fatigue life. The welding of the specimens was carried out using an automatic rotating machine, which allowed the welding to be conducted at a uniform speed.

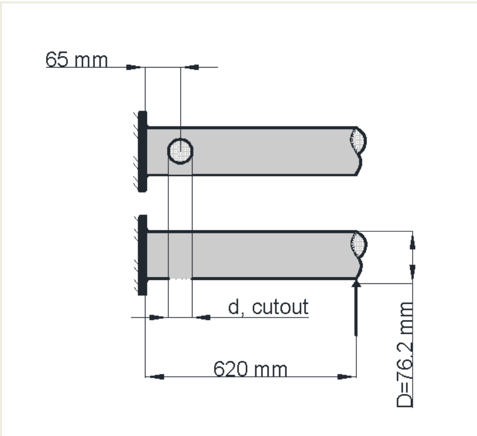

Figure 4-24: Cutouts position and the tubes specifications.

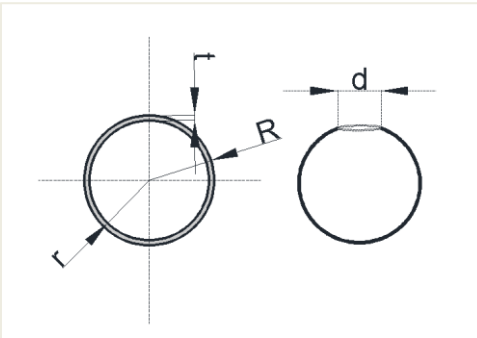

Figure 4-25: Cross-section geometry.

Figure 4-26 shows a welded specimen. Cutouts were made on the tension side using a precise drilling method by which an accurate circular opening was obtained. Two specimens after perforation as well as an overall view of a specimen with a cutout before test are shown in Figure 4-27.

Figure 4-26: Welding and connections of the tube specimen.

Material properties

The same material used in the first section of this chapter was used for the tube specimens of this chapter. The results were yield and ultimate stresses of 307 and 360.2 MPa respectively and a Young's modulus of 216.3 GPa.

(a) (b)

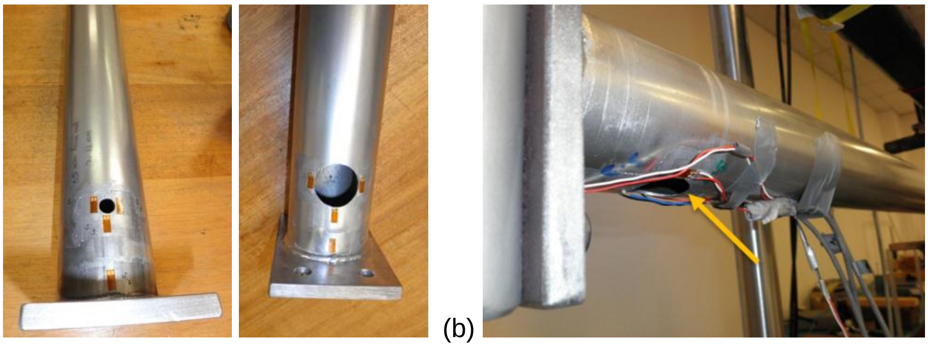

Figure 4-27: Specimens with small and large cutouts, (b) overall view of a specimen with a cutout before test.

4.3.3 Test observations

Failure modes

The two failure modes of *brace tension side* and *cutout crack failure (CCF)* were observed in this set of specimens.

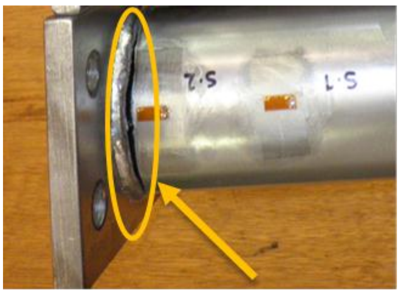

Figure 4-28: Fatigue crack, *brace tension side* failure in QWE.5.

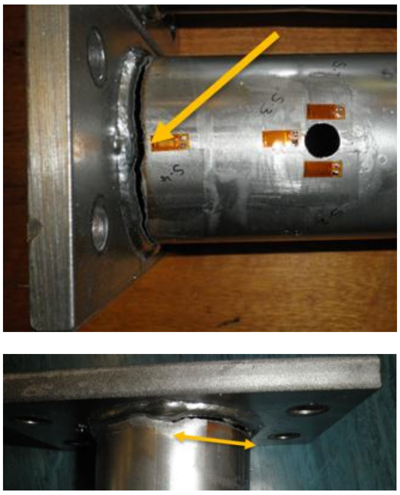

(a)

(b)

Figure 4-29 (a) Crack beside the welding for QWE.4, (b) propagation of the crack towards the nominal neutral axis.

Brace tension side failure

Failure occurred along the welding for specimens QWE.5 and QWE.7 (no holes). Figure 4-28 shows the development of the crack in these intact specimens. As reported by Jiao et al. [121], this mode of failure occurred at the zone of maximum tension stress in the form of a circumferential crack. In this failure mode, a crack was initiated in the extreme fibre in the tension side of the tube. The specimen failed when the crack developed towards the neutral axis. Similarly, this failure mode was observed for specimen QWE.4 as the diameter of the opening was relatively small in this specimen (see Figure 4-29 and Figure 4-30).

Figure 4-30: Crack near the welding.

Cutout-crack-failure (CCF) mode of failure

This mode of failure occurred in the section of the cutout with the minimum cross-sectional area. The crack was initiated at both edges of the cutout and propagated towards the neutral axis of the specimens (see Figure 4-31). Failure occurred when the specimen was unable to carry the applied load due to the development of the crack accompanied by a large deformation in the free end of the tubes. It is worth mentioning that the *CCF* mode was detected in specimens with medium and larger holes. Specimen QWE.2 with holes on both tension and compression sides also showed the *CCF* mode of failure as shown in Figure 4-32, Figure 4-33, Figure 4-34 and Figure 4-35. Figure 4-36 shows different specimens after failure with different failure modes.

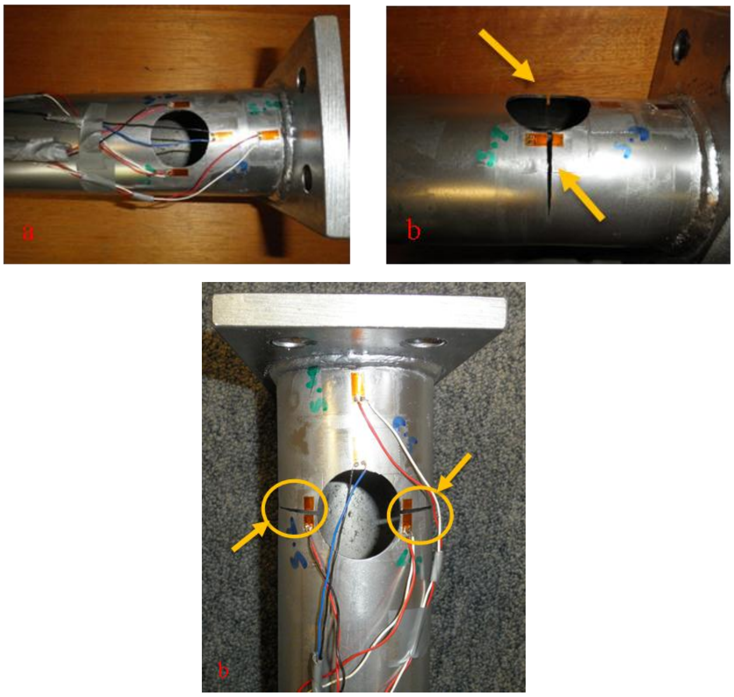

Figure 4-31: QWE.1 specimen before and after *CCF* failure.

4.3.4 Discussions

4.3.4.1 *Stress concentration relief-holes in previous studies*

It should be mentioned that holes were used in a few published studies to reduce the stress concentration in critical areas of specimens. In this section, a few references are discussed to show how the specimens of this study benefited from the same mechanism to reduce the stress concentration, which will be described later. It is believed that a counter intuitive approach of decreasing the stress concentration is to make a cutout at the end zone of a developing crack. This method was discussed in Ref. [19] in which the stop-drilling procedure improved the crack initiation and the total fatigue life in aluminium alloy specimens of 6061-T651 and AISI 304 stainless steel. The crack initiation life was the cycles initiating a 0.2 mm crack at a stop-hole edge. It was mentioned that the larger the stop-hole diameter the more cycles before crack initiation and the longer the total fatigue lives. A method of drilling crack-flank holes near to, but not at, the crack tip has been studied [20] and retardation of the crack was achieved. Moreover, if the holes were drilled at a small distance ahead of the tip, the crack was likely to grow into the hole, achieving a considerable amount of life extension.

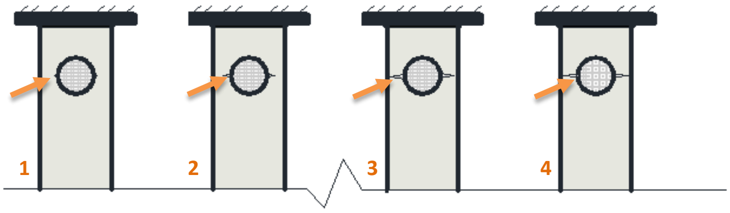

Figure 4-32: Failure stages of the specimens with the crack near the cutout area.

A new technical method for arresting crack initiation at stop-drilled holes by drilling ancillary holes was proposed in Ref. [21] followed by making the stop-drilled holes. The analyses showed that the existence of ancillary holes effectively reduced the stress concentration at the edges of the stop-drilled holes. Furthermore, it was shown that the limiting buckling moment of a shell with a cutout increased when the cutout was located toward one end of the clamped shell [124]. The stress concentration developed in the corners of a right angled indenter, which was designed to apply compression loads, was believed to be controlled by the relief-cuts as notches [128]. In some cases, the stress concentration at the notch root decreased to such a level that it could be negligible in the design of such structures. Although in some of the mentioned references relief holes were used to stop the development of the crack (after creation of the crack), the same concept was considered in this section before creation of the crack as the round shape of the hole near the end helped deflect the stress flow lines from the most critical area to less critical zones. Accordingly, stress concentration significantly decreased in the most critical area.

4.3.4.2 *Fatigue life and stress concentration*

The fatigue life of the present specimens is plotted against the hole diameter *d* in Figure 4-37. It should be noted that the intact specimen is considered as a *benchmark/control specimen* with which the other specimens are evaluated. Hence, in order to ensure that the number of cycles and the failure mode are reliable repetition of the fatigue test for the intact specimen was performed, giving a variation of around ±8% from the mean number of cycles for these two intact specimens.

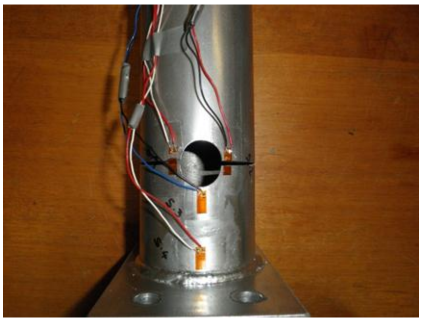

Figure 4-33: QWE.3 specimen after *CCF* mode of failure.

Table 4-5: Number of cycles, stress range and failure modes.

Specimen	d (mm)	Stress range (MPa)	Number of cycles	Failure mode
QWE.1	36	16.293–162.93	29769	CCF
QWE.2	36*	16.293–162.93	31685	CCF
QWE.3	23	16.293–162.93	71295	CCF
QWE.4	12	16.293–162.93	182889	BTS
QWE.5	0	16.293–162.93	110965	BTS
QWE.6	14	16.293–162.93	263473	BTS
QWE.7	0	16.293–162.93	130247	BTS
QWE.8	19	16.293–162.93	513576	CCF

*With top and bottom hole.

On the basis of the performed literature survey, no study has been conducted on the effect of a cutout on the fatigue behaviour of the CHS tubes. The results of this set of tests verified the effect of a small hole on decreasing the stress concentration and extending the fatigue life of a tube specimen. When a stress relieving hole with an optimal diameter was made near an area of high stress concentration the cutout significantly relieved the stress concentration and the fatigue life was dramatically increased. It was seen from Figure 4-37 that the fatigue life of QWE.8 specimen (with d = 19 mm) was nearly five times more than that of the intact specimens.

For the specimens with very large holes such as the specimens QWE.1 and QWE.2, the influence of the cutout on the fatigue life was quite negative. This can be attributed to a relatively high loss of the material in the cutout area which led to an increase in the stress concentration of the perforated zone compared with the welding region. No noticeable difference in the fatigue life was found between the specimens QWE.1 and QWE.2, although holes were made on both the tension and compression sides of specimen QWE.2.

(a) 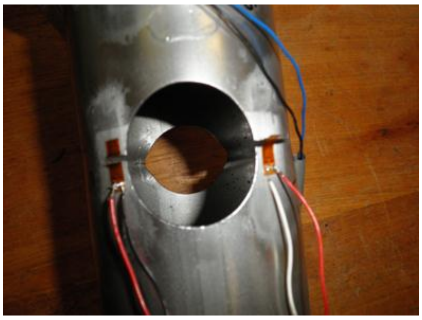 (b) 

(c) 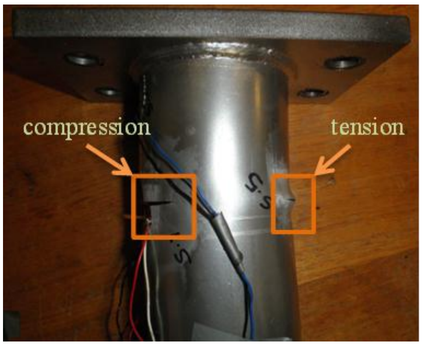

Figure 4-34: QWE.2 specimen with the holes on both tension and compressions sides, (a) tension side, (b) compression side, (c) side view of the specimen.

Figure 4-35: Crack at the cutout.

Table 4-5 shows the stress range applied to the specimens, mode of failure and number of cycles for each specimen. It can be seen from Figure 4-37 that an optimal diameter of the cutout around 19 mm gave maximum extension of the fatigue life of the current specimens. It is believed that these results cannot be generalised to the static loading as in static loading the larger the diameter of the hole, the less the capacity of the tubes.

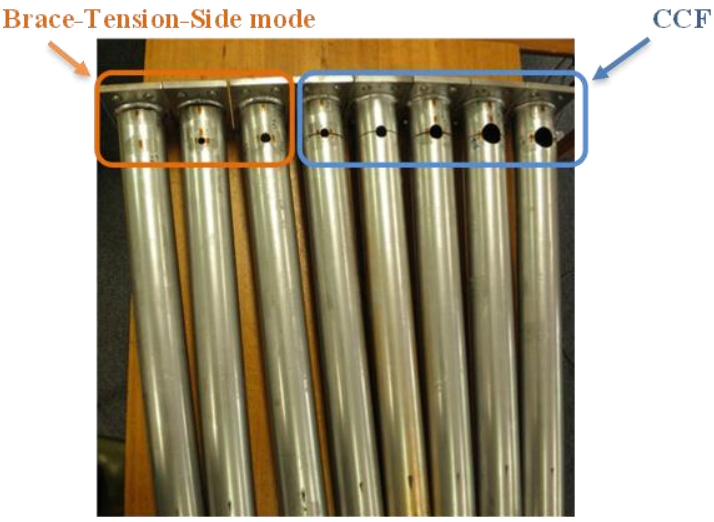

Figure 4-36: Overall view of different modes of failure.

4.3.4.3 *Strain values at the critical points*

Figure 4-38 shows the location of two strain gauges used in the most critical areas to assess the crack occurance and to evaluate the fatigue life of such tubes. One of the strain gauges was mounted near the support weld (S_{weld}) and the other one was on the edge of the cutout (S_{cutout}) in the tensile stress concentration zone. Figure 4-39 shows S_{cutout} versus the number of cycles for three specimens, in which the crack initiation is marked with an arrow. Since S_{cutout} was mounted on the zone of initiation of the crack, S_{cutout} indicated when the crack occurred (see Figure 4-39). In addition, after the initiation of the crack the specimens were still able to carry the cyclic loading until the crack was fully developed and the fatigue life was determined.

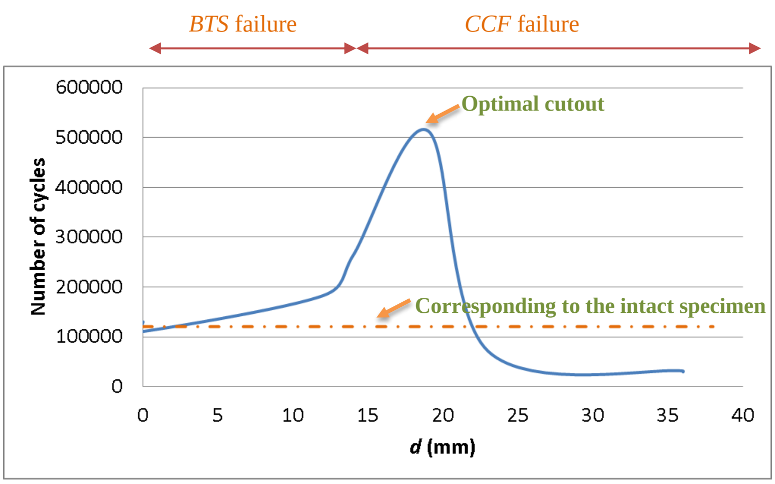

Figure 4-37: Number of cycles versus the diameter of the cutout.

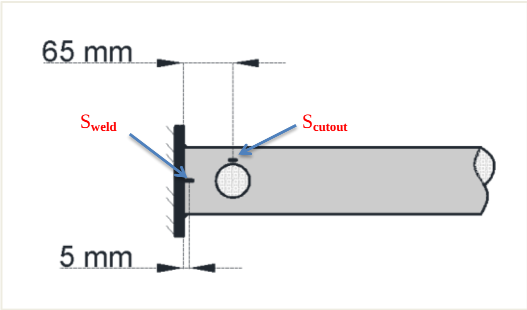

Figure 4-38: Strain gauges positions.

Figure 4-40 shows the strain values for the intact specimens in a position equivalent to the position of a cutout, and S_{cutout} of the specimen QWE.4. It is quite evident that for QWE.4 with a small cutout the magnitudes of the strain are considerably more than that of the intact specimens. The comparison of these values indicates that although the hole in QWE.4 was not ultimately affected by the fatigue crack, a significant amount of stress concentration was developed near such a small hole. Consequently, the stress concentration near the welding could be considerably relieved.

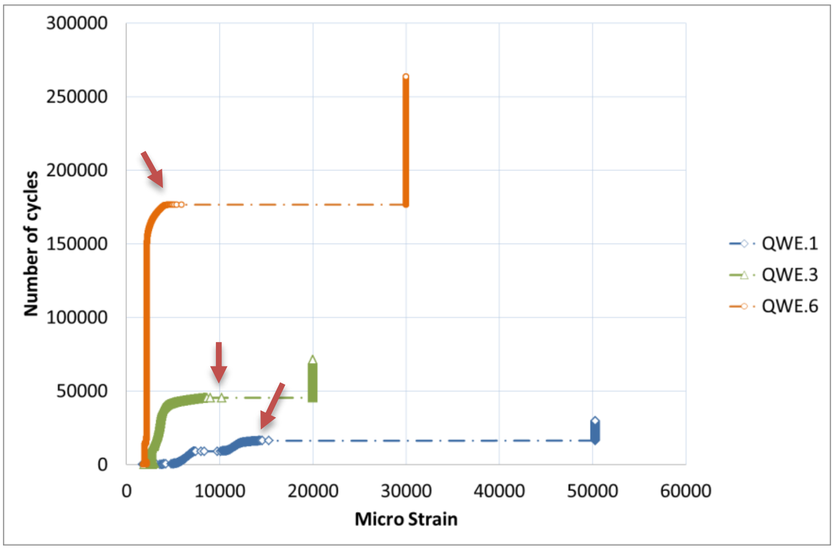

Figure 4-39: S_{cutout} for different specimens with large cutout, (crack initiation marked).

Figure 4-41 presents S_{cutout} and S_{weld} for the specimens QWE.3 and QWE.6. It is observed that when S_{cutout} starts to increase dramatically following crack initiation at the cutout, S_{weld} tends to decrease in value indicating that the deformational energy was mostly absorbed in the crack so that the rate of the stress concentration near the welding was reduced.

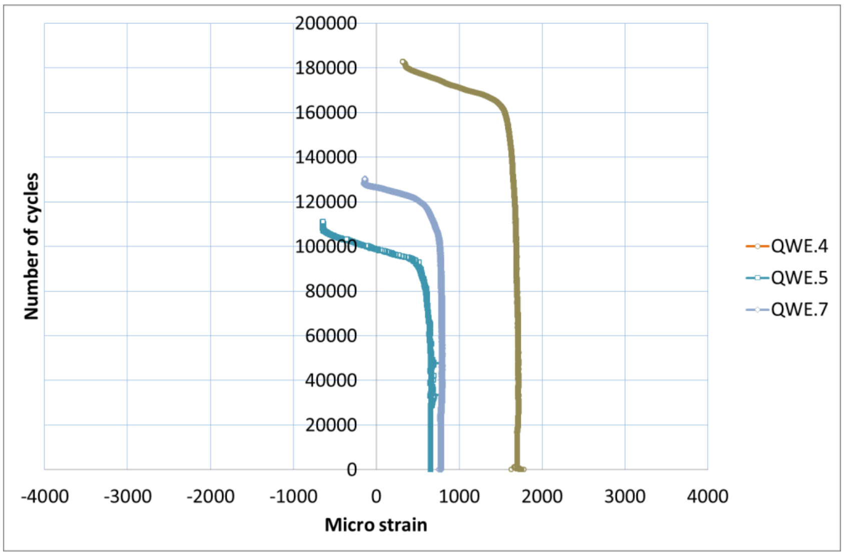

Figure 4-40: S_{cutout} for QWE.4, and the corresponding strain (at 65 mm from the support end, but the same longitudinal direction as S_{weld}) for intact specimens (QWE.5, QWE.7).

Figure 4-42 shows S_{cutout} and S_{weld} values in QWE.4 with a small cutout with d = 12 mm. Although S_{weld} is located in a point with higher bending moment, the strain values beside the cutout are more than those of S_{weld}. This can be largely due to the stress concentration at the cutout area and corresponding stress relief behind and in front of it. It can be seen that the strain value of S_{cutout} decreased when a crack occurred near the weld, as the deformations and the maximum stresses are significantly absorbed in the cracked region so that the strain magnitude around the hole is decreased.

In brief, one may observe an interaction between the strain values of S_{cutout} and S_{weld} which is strongly related to the diameter of the cutout created on the tension area of the tubes. For larger holes (d > 20 mm), the loss of material in the cutout-section is dominant so that the stress is predominantly concentrated at the cutout area, whereas for the medium sized holes (10 mm < d < 20 mm) a kind of stress concentration interrelation can be detected between S_{cutout} and S_{weld}. For very small holes (d < 10 mm) the stress concentration near the weld is dominant rather than near the hole, although small holes greatly help to relieve the stress concentration in the weld area.

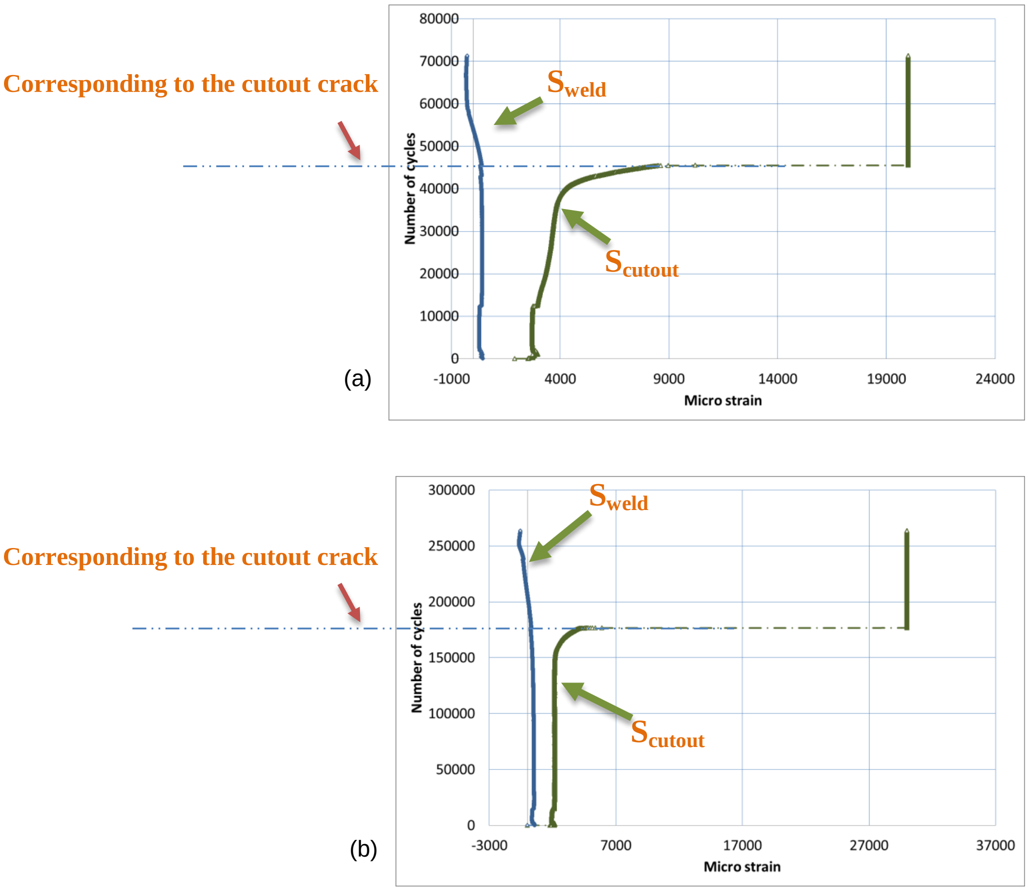

Figure 4-41: S_{weld} and S_{cutout} for the specimen: (a) QWE.3 and (b) QWE.6.

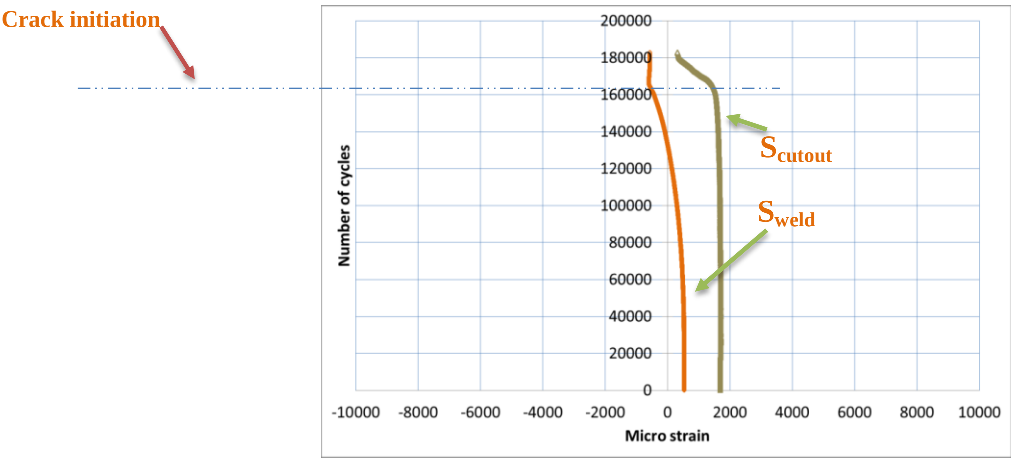

Figure 4-42: S_{weld} and S_{cutout} for the specimen QWE.4.

4.3.5 Comparison of the fatigue life with the S-N data of previous studies

Figure 4-43 shows a comparison of the fatigue life of the present specimens with the results of previous studies. The nominal stress range versus the number of cycles on a log scale is plotted for such a comparison. The fatigue life of VHS tubes with different thicknesses is included in the chart [121]. The results of the CHS tubes and the proposed design curve for such specimens is also taken into account [122]. As is seen in Figure 4-43, the fatigue life of the specimens in this study agrees well with the data of the aforementioned studies, especially with the results of the CHS tubes with $t < 4$ mm of Ref. [121]. Furthermore, the effect of the cutout can be observed within the data of the previous studies indicating the effect of the diameter of the cutout on the fatigue life of the tube specimens.

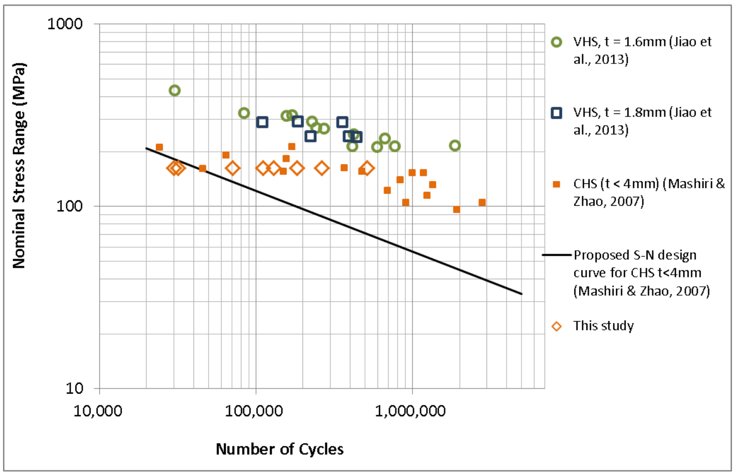

Figure 4-43: Fatigue life and the previous studies [121, 122].

4.3.6 Conclusions

A circular cutout was made on tubular structural elements to examine the fatigue behaviour of such CHS tubes. The salient points of the present section are summarised as follows:

- In general, two failure modes were observed in this research: (i) *brace tension side* failure occurred near the weld in the form of circumferential crack for intact specimens and the specimens with a small cutout. (ii) CCF mode was detected in medium and larger holes of the tested models such that failure occurred in the central cross-section of the cutout area and extended to the nominal neutral axis of an equivalent intact cross-section.

- Although a very small hole was not ultimately affected by the fatigue crack, a significant amount of stress concentration was developed near such a small hole. As a result, the stress concentration near the welding can be significantly relieved.
- With an optimal diameter of a cutout, the stress concentration at the end of the tube was significantly relieved and hence the fatigue life of the specimen dramatically increased.
- For very large holes the influence of the cutout on the fatigue life was quite negative which can be attributed to a relatively high loss of the material in the area of the cutout.
- No noticeable difference of the fatigue life was found between the single cutout in the tension zone and double cutouts both in the compression and the tension zones.
- It is believed that there is an interrelation between the strain values of S_{cutout} and S_{weld} which is strongly related to the diameter of the cutout created on the tension area. For larger holes ($d > 20$ mm) the loss of material in the central cross-section of the cutout was dominant so that the stress is predominantly concentrated at the cutout zone; whereas, for the medium-size holes (10 mm < d < 20 mm) a strong stress concentration interaction was detected between the two S_{cutout} and S_{weld} values.
- The fatigue lives of the specimens in this experimental program agree well with the data of previous studies.

4.4 Reinforcement of imperfect shells with composite materials

4.4.1 Introduction

Literature survey

As previously mentioned a proliferation of applications is found in industry for steel tubes due to the utility and aesthetic appearance of these structural elements and these elements frequently have perforations of different sizes and locations and in some cases these structures experience cyclic loadings. Moreover, a growing demand for the use of CFRP in steel structures has motivated much interest among researchers in strengthening steel elements with CFRP.

A considerable volume of research can be found on the load carrying capacity of steel tubes with cutouts. Tubes of various lengths and radiuses with cutouts located at different positions were investigated numerically and experimentally by Han et al. [129]. Equations for mean and peak crushing forces of tubes with a cutout were proposed in this research using regression methods applied to the results. Han et al. performed a series of nonlinear FE analyses to assess the effect of cutouts on thin cylindrical shells [39]. The results indicated that a cutout significantly reduced the buckling strength of the shells. Ghanbari Ghazijahani et al. investigated tubes with cutouts near the base and the stress concentration relief due to the existence of cutout was seen in this paper [56]. Shariati and Rokhi studied the effect of the location of various elliptical cutouts on the buckling of cylindrical shells [40]. In this study equations were proposed to find the buckling load of these structures. Thin-walled composite cylindrical shells with plain and reinforced cutouts under compression were investigated by Hilburger and Starnes Jr [130]. Yeh et al. studied the buckling response of elasto-plastic cylindrical shells with a cutout under bending [124]. The effects of the size and location of the cutout on the buckling capacity were examined in this research. As presented in the previous sections of this thesis the structural response of cantilever tubular CHS beams with geometrical imperfections under static and cyclic loading was studied [55, 119, 131].

Different failure modes were obtained through these experimental studies and the adverse effects of imperfections were demonstrated.

Fatigue behaviour of steel circular thin sections was considered in several studies. Fatigue failure and stress concentration factors for thin circular hollow-sections welded to end plates under in-plane bending were studied in experimental work of Mashiri and Zhao [132]. The relationship between a through-thickness crack and surface cracks of various lengths was examined in this research. A series of tests and design recommendations for thin CHS-plate T-joints under cyclic in-plane bending were conducted by Mashiri and Zhao [122]. Fatigue response of very thin-walled SHS tubes welded to plate joints was studied under in-plane bending by Mashiri el at. [133]. Test data was analysed with a least squares method in this research. Tong et al. studied the fatigue behaviour of thin-walled joints welded between circular and square hollow sections, and the influence of non-dimensional joint parameters on stress concentration factors was examined in this study [134].

Previous fatigue tests

Notwithstanding the vast volume of literature on fatigue behaviour of hollow sections, cyclic loading of tubular structures with cutouts has not been thoroughly investigated yet. In this light, a set of experiments was conducted on such structures, the result of which are presented in the previous section also published as Ref. [55]. In the mentioned study, cutouts were made close to the area of maximum tension stress in steel tube specimens. A total of eight beam specimens were studied under cyclic unidirectional loading and the fatigue life as well as the failure modes were examined. It was found that for larger holes the effect of cutouts on the fatigue life was quite detrimental. However, the stress concentration was significantly relieved when an optimal cutout was made near the base; as a consequence, fatigue life of the specimens was considerably enhanced.

In order to extend the previous study, the present section investigates reinforcement of the large holes of the previous specimens with CFRP, wherein fatigue life of the reinforced structures was considerably enhanced relative to the unreinforced cases.

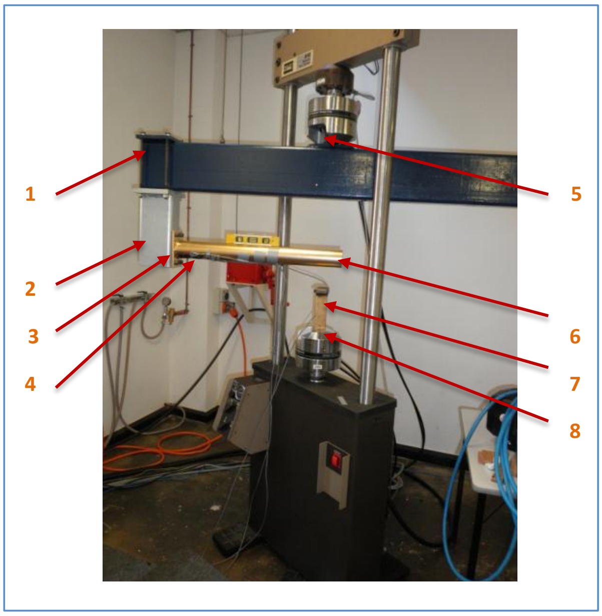

1- Box-section beam;
2- End box-section element;
3- Base plate;
4- CFRP and cutout;
5- Top jaw of the MTS;
6- Steel tube specimen;
7- Loading element;
8- Bottom jaw;

Figure 4-44: Test apparatus, overall view.

4.4.2 Test set-up and instrumentation

Test rig

As in the previous sections of this chapter, this set of tests was conducted using a Material Testing System 810 (MTS-810), which was capable of applying a cyclic loading at different frequencies (Figure 4-44). Load was applied by a T-shape plate (item 7 in Figure 4-44). This element was gripped by the bottom jaw of the MTS machine (item 8) while the top jaw (5) gripped a rigid box shape steel girder (1). A support arm (2) was manufactured for the cantilever tubes specimen (6). The specimen was welded to a thick end plate (3), which was connected to the box section and support arm by four high strength bolts. Meticulous attention was paid to install the specimens perfectly perpendicularly to the loading element. A load-control protocol was adopted in this set of experiments such that the maximum and minimum loads were ramped up over a few initial cycles and subsequently the machine was capable of maintaining the pre-set maximum and minimum loading in a steady and precise manner. High precision strain gages were used to record the strain values at selected critical spots on the specimens. A HBM data acquisition system with built-in amplifier and relevant software were used to record the test data.

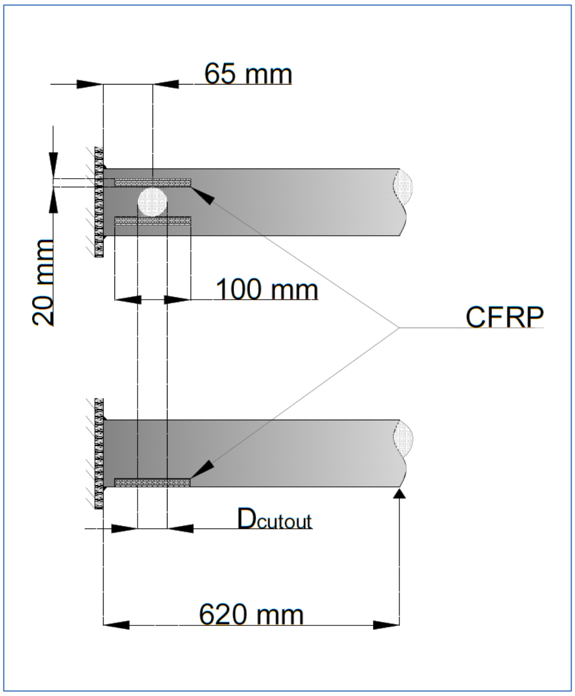

Figure 4-45: Tube specimens' geometric features.

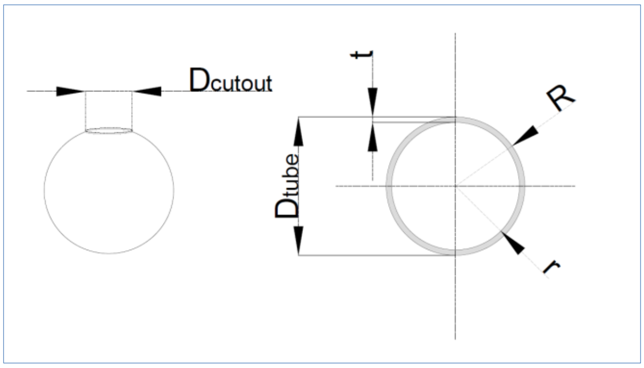

Figure 4-46: Cross section of the tubes and the cutout.

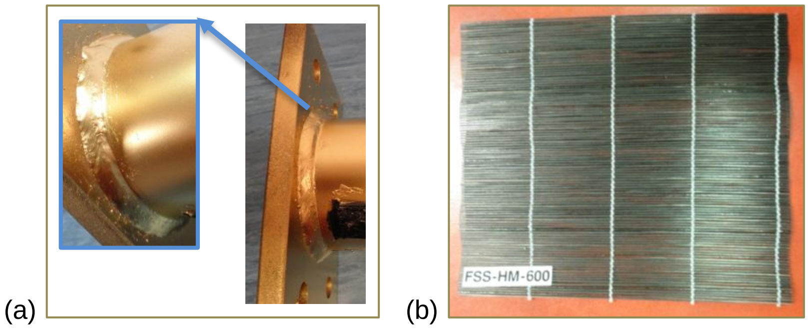

Figure 4-47: (a) Butt-weld of the tubes to the end plate, (b) CFRP.

Specimens and preparation

Highly precise cold rolled tube specimens (CUTFRP.1 to CUTFRP.10) were utilised for this series of tests. The specimens were supplied pre-cut into the desired lengths. The end of the tube to be welded to the end plate was accurately machined using a lathe. Perforations were made in a CNC machine. The specimen's geometry and the cutouts' specifications are presented in Figure 4-45 and Figure 4-46. Note that the geometry of the tubes was the same as in the previous section of this chapter, in which unreinforced specimens with different cutouts were tested. Welding was performed with the specimens held by a machine capable of rotating the specimens with a uniform and controllable speed. Through this technique an accurate and uniform weld was achieved (Figure 4-47).

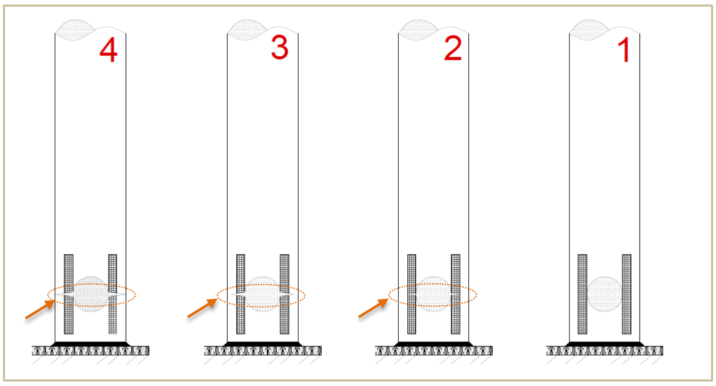

Figure 4-48: Crack initiation and development for the specimens with the crack at the cutout.

Strand Carbon Fibre–Reinforced Polymer sheets (CFRP, FSS–HM–600) was used to strengthen the tubes around the cutout area (Figure 4-47). The carbon fibre sheets were precisely cut into lengths (100 mm) and an epoxy adhesive "Spabond 345" was employed to attach these to the areas in the proximity of the cutout as shown in Figure 4-45. The applied carbon fibre sheets were in a single unidirectional ply, and the adhesive was able to properly absorb into the fibres which provided a very reliable reinforcement. Prior to application the surface of the steel was cleaned and degreased by recommended solvents after using fine sandpaper to remove any possible contaminating particles. In order to obtain the material properties of the tubes, tensile coupon tests were conducted, the results of which were outlined earlier in this chapter for the specimens with cutouts and without CFRP reinforcements.

4.4.3 Test results and observations

Mode of failure and overall observations

Based on the results presented in the previous section (also published in Ref. [55]), the failure mode of the present tubes under cyclic bending is highly dependent, above all else, on the diameter of the cutout, though also on the location. For large cutouts the *cutout crack failure mode* (*CCF*) dominated, in which the crack occurred at the mid-section of the cutout and subsequently developed circumferentially towards the nominal neutral axis of the cantilevered beam. Fatigue life was significantly reduced. On the other hand, for the optimal and smaller unreinforced cutouts as previously presented the fatigue life was significantly enhanced due to the stress concentration relief, and the *brace tension side* (*BTS*) failure mode was observed. In the *BTS mode* the base of the tubes cracked, which were not very amenable to CFRP reinforcement due to the challenges of applying the CFRP to such a small area.

Table 4-6: Diameter of the cutouts in different specimens and loading protocols.

Specimen	D_{cutout} (mm)	Ave. Min load (kN)	Ave. Max load (kN)
CUTFRP.1	40	0.30	1.82
CUTFRP.2	40	0.42	2.20
CUTFRP.3	36	0.15	1.87
CUTFRP.4	36	0.40	2.63
CUTFRP.5	30	0.65	1.83
CUTFRP.6	30	0.0	1.91
CUTFRP.7	30	0.50	2.84
CUTFRP.8	23	0.15	1.65
CUTFRP.9	23	0.61	2.42
CUTFRP.10	23	0.23	2.00

For these reasons the present study focuses on strengthening of the relatively larger cutouts. Thus, the diameters of the adopted cutouts range from 23–40 mm, and located in the same position as in the previous study, i.e. centred 65 mm from the base.

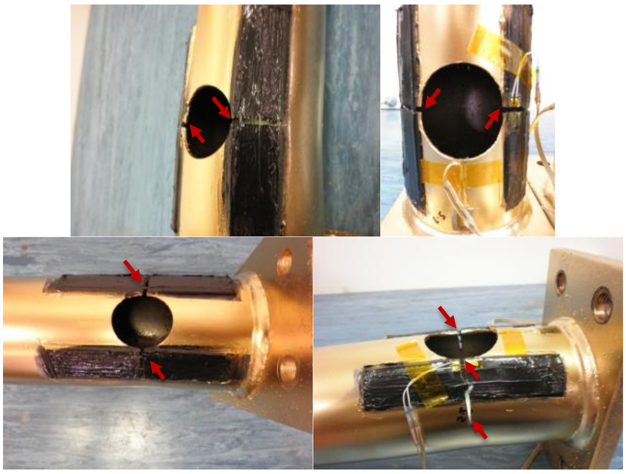

Figure 4-49: Fatigue failure at the cutout for different specimens.

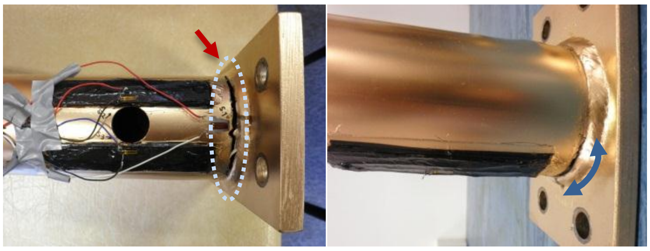

Figure 4-50: Fatigue failure at the base: top view (left), side view (right).

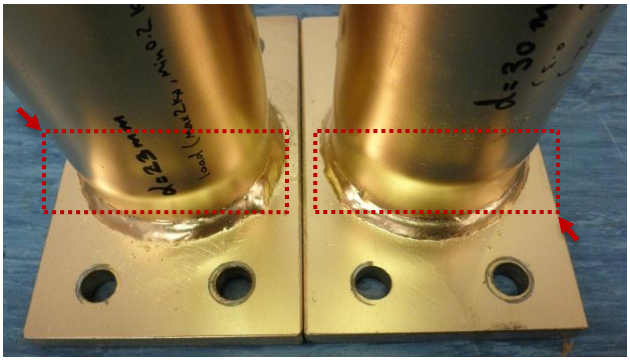

Figure 4-51: Plastic buckling of the compression side of the specimens after initiation and development of the fatigue crack.

Figure 4-48 schematically illustrates the crack initiation and development, in which a small crack occurred and developed further until full failure of the specimen by fatigue. A specimen was deemed failed as the testing stopped after a crack was initiated and propagated so that the specimen was unable to carry the applied load. Failure for all of the current reinforced specimens was in the *CCF mode* (Figure 4-49) except for CUTFRP.9 in which the cutout's diameter was 23 mm and the specimen failed in *BTS mode* (Figure 4-50).

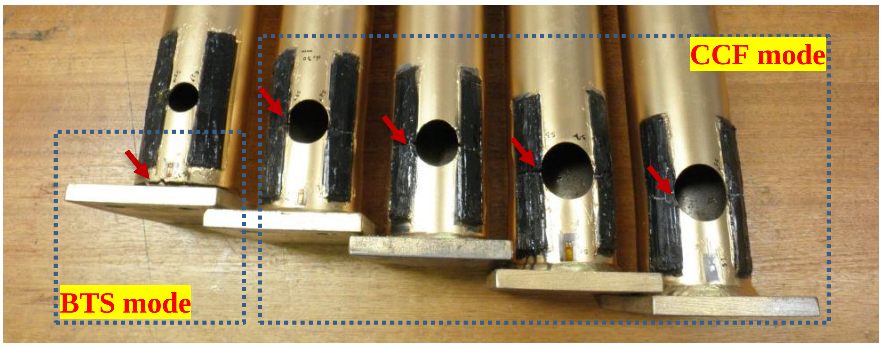

Figure 4-52: Two different fatigue failure modes.

It is believed that for this specimen the CFRP reinforced the cutout area sufficiently to prevent *CCF mode* failure, hence the stress was concentrated at the base of the tubes. For the remaining specimens – which failed in the *CCF mode* – the steel tube and CFRP reinforcement cracked at the same cross-section. It is noteworthy that there was no debonding whatsoever for the CFRP in this series of experiment. Hence, the CFRP with 100 mm bond length was adequate for strengthening the area around the cutout.

(a)
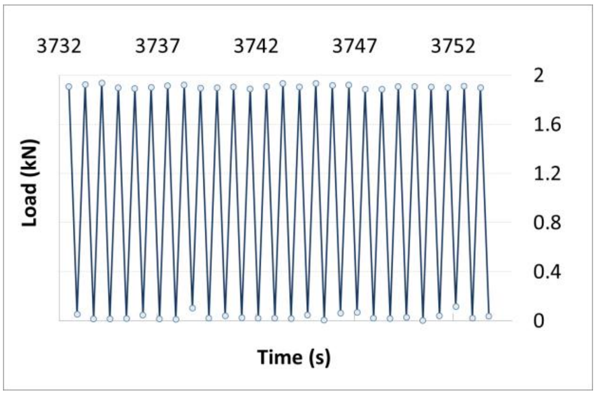

(b)
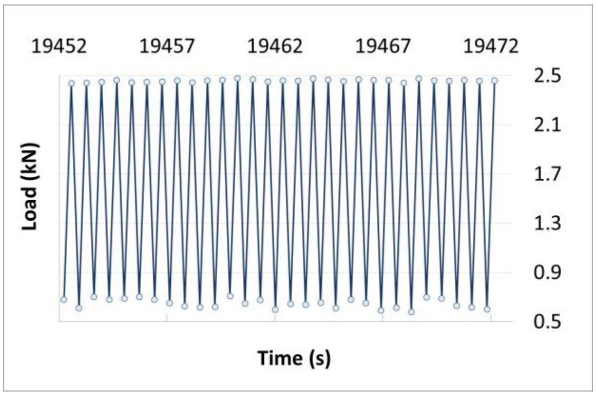

Figure 4-53: Typical loading protocol plotted for a limited period of time for: (a) CUTFRP.6, (b) CUTFRP.9.

Plastic buckling was detected in all of the specimens that failed in the *CCF mode*, manifest as a bulging shaped wave at the compression side immediately above the cutout (Figure 4-51). This phenomenon was seen throughout the final cycles as the final fatigue failure was being approached. Failure of several specimens with the fatigue crack is shown in Figure 4-52 and the cracks are marked with arrows in this figure. Figure 4-53 and Table 4-6 show typical loading protocol plotted for a limited period of time for CUTFRP.6 and CUTFRP.9.

4.4.4 Fatigue behaviour of the current specimens

4.4.4.1 *Fatigue life*

In general, the fatigue life was relatively low for the specimens with larger cutouts due to the high tensile stress at the section corresponding to the centre of the cutout, whereas for the specimens with smaller holes the fatigue life was greater. To illustrate, CUTFRP.2 with the largest hole of 40 mm and comprising a higher value of the stress range accounted for the lowest fatigue life, whereas CUTFRP.8 with a cutout of 23 mm was capable of carrying the cyclic loading up to more than 1,400,000 cycles without failure.

Table 4-7: Stress range and the number of cycles for different specimens.

Specimen	D_{cutout} (mm)	Stress range (MPa)	Number of cycles
CUTFRP.1	40	138	136108
CUTFRP.2	40	162	64011
CUTFRP.3	36	156	276585
CUTFRP.4	36	202	1696
CUTFRP.5	30	107	1048574
CUTFRP.6	30	174	131419
CUTFRP.7	30	212	17391
CUTFRP.8	23	136	1438160
CUTFRP.9	23	163	276894
CUTFRP.10	23	160	498307

Figure 4-54 shows the ultimate number of cycles for reinforced specimens with different cutouts. A nominal stress range (difference between maximum and minimum stresses) was calculated based on the actual loading applied to the equivalent plain tube without cutout. Specimens with a stress range less than 160 MPa were distinguished from the ones above 160 MPa in Figure 4-54. It is quite evident that the fatigue life was much higher for the specimens with the stress range less than 160 MPa. Figure 4-54 also shows a comparison between the ultimate number of cycles for the specimens with approximately similar stress range in the current tests and the specimens without reinforcement. A significant increase in total number of cycles is seen for the reinforced specimens in comparison with the equivalent unreinforced specimens.

(a)

(b)

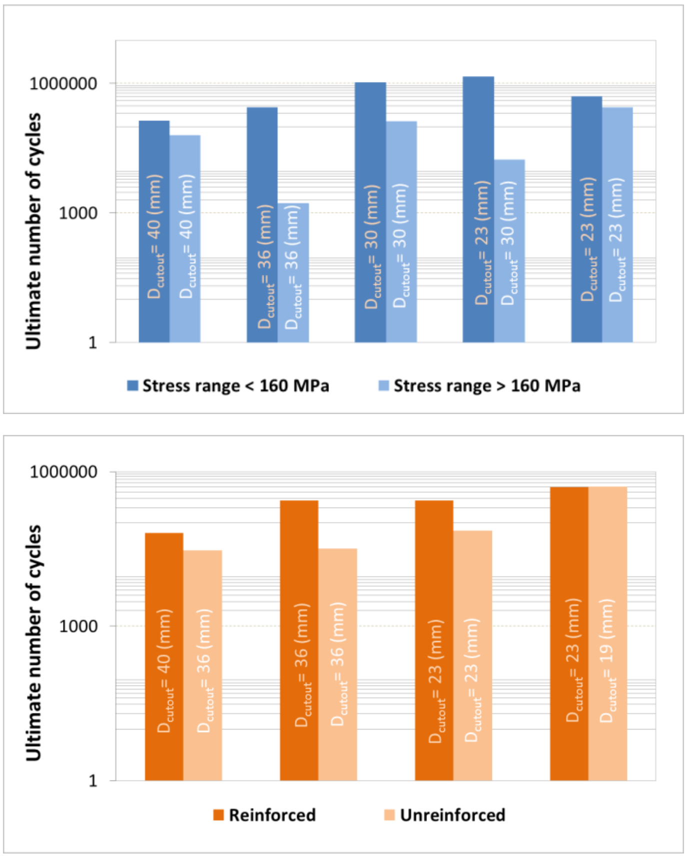

Figure 4-54: (a) Ultimate number of cycles for current specimens with different stress ranges and cutouts, (b) comparison of ultimate number of cycles for the specimens with approximately similar stress range of unreinforced specimens of the previous section or Ref. [55].

Table 4-7 gives the stress range together with the fatigue life of the specimens. As can be seen, two specimens with 40 mm diameter cutouts, two with 36 mm cutouts, and three each with 30 mm and 23 mm were tested under different loading ranges. This difference in the stress range resulted in a scattered, yet consistent number of fatigue cycles in which CUTFRP.5 and CUTFRP.8 attained more than one million cycles, accordingly these two tests were terminated with no failure. This is because the average number of cycles at failure for the specimens with no cutout – intact specimens QWE.5 and QWE.7 in Ref. [55] – was around 120,000 cycles. The number of cycles in reinforced specimens CUTFRP.5 and CUTFRP.8 exceeded the ultimate number of cycles of the unreinforced intact specimens QWE.5 and QWE.7 by more than 10 and

14 times respectively. This clearly signifies that specimens CUTFRP.5 and CUTFRP.8 were well strengthened against cyclic bending. It is, however, fitting to mention that, although the improvement brought about by CFRP was still highly significant, one should consider the stress range for the mentioned specimens in order to draw a meaningful comparison.

It is noted based on the previous section or Ref. [55] that the ultimate number of cycles for unreinforced specimens QWE.1 and QWE.2, with D_{cutout} = 36 mm (D_{cutout} is defined in Figure 4-45), was approximately 30,000. The CFRP reinforcement brought about a dramatic increase in capacity, as exemplified by CUTFRP.1 and CUTFRP.3 with D_{cutout} equal to 40 mm and 36 mm respectively, in which more than 130,000 and 270,000 cycles were achieved. In fact, the present CHS tubes with CFRP strengthened cutouts outperformed the tube with neither cutout nor strengthening (intact and bare specimen) under cyclic bending. Overall, comparing the fatigue life of the present study and the previous study with bare specimens and also considering the stress range applied to the specimens, the usage of CFRP for strengthening the cutout area is highly recommended, particularly for the case of the specimens with larger holes.

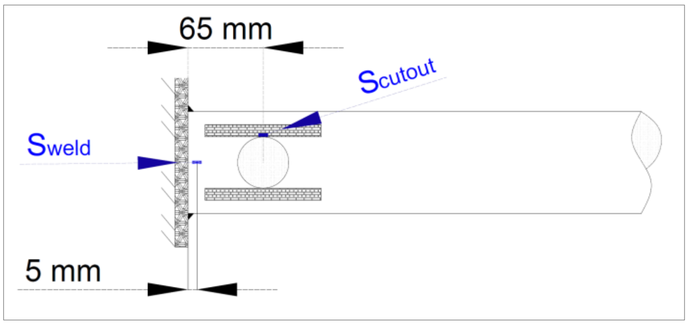

Figure 4-55: Layout of the strain gauges (S_{weld} and S_{cutout}).

4.4.4.2 *Strain behaviour*

Figure 4-55 shows a layout for the positions of the strain gauges. The two critical areas identified in previous studies were the stress concentration around the cutout, and the stress near the weld at the attachment to the base. These are labelled as S_{cutout} and S_{weld}, the location of which is shown in Figure 4-55.

(a)

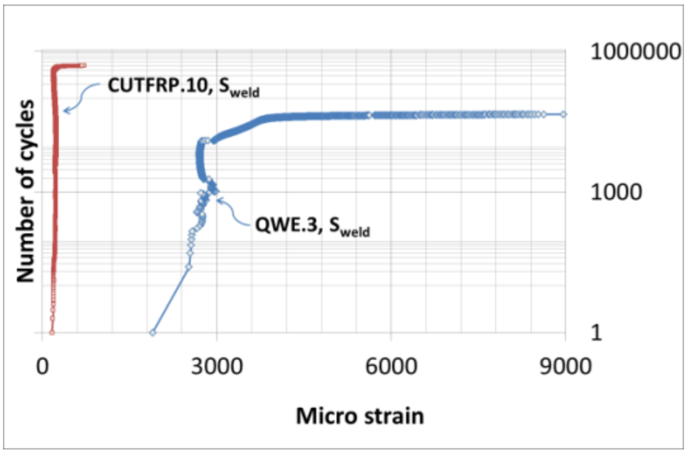

(b)

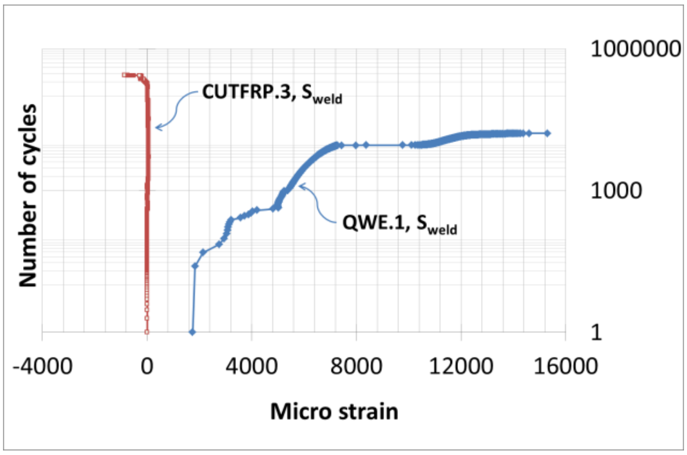

Figure 4-56: Strain magnitudes versus the number of cycles in specimens with a same cutout with CFRP (QWE), and without (CUTFRP): (a) D_{cutout} = 23 mm, (b) D_{cutout} = 36 mm.

Figure 4-56 plots the strain behaviour of four specimens against number of cycles on a log scale – QWE.1 and QWE.3 are bare specimens without any reinforcement [55], whereas CUTFRP.3 and CUTFRP.10 were CFRP reinforced but were respectively equivalent to the former specimens in terms of D_{cutout} and stress range. Figure 4-57 also shows the strain for the specimen with largest cutout (CUTFRP.1) but with the lower stress range than the similar specimens CUTFRP.2, CUTFRP.3 and CUTFRP.4.

It was found that for the specimens with CFRP the strain values were clearly far steadier prior to crack initiation relative to the specimens without CFRP. Furthermore, CFRP attached to the area near the cutout dramatically decreased the strain values of S_{cutout} and S_{weld} when the tubes were subjected to the cyclic bending.

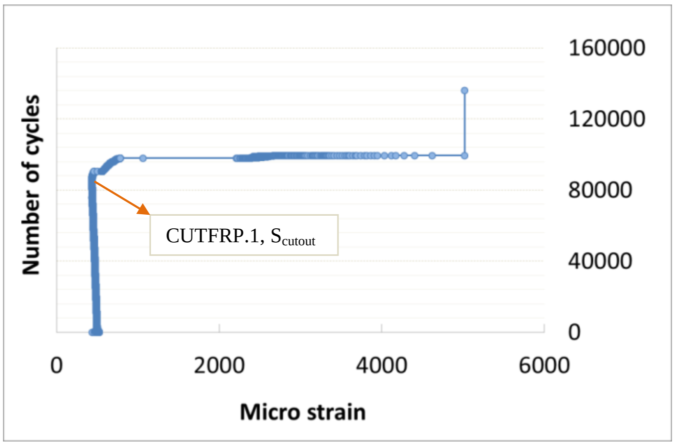

Figure 4-57: Strain values at the cutout area for the specimen CUTFRP.1.

4.4.5 Comparison with previous studies

Figure 4-58 shows a comparison of the results for the specimens with and without CFRP. Different specimens with different cutouts and stress ranges were plotted in this figure in order to demonstrate the effect of reinforcement. It is seen that specimens with larger cutouts were well reinforced against cyclic bending so that they experienced higher fatigue life. This figure also contains fatigue life of the unreinforced specimens of the previous section of this chapter with the same material and geometry. The closer the specimens were to the optimal cutout (D_{cutout} = 19 mm) the greater the number of cycles (over 513,000). As previously mentioned, this was attributed to relief of the stress concentration at the base.

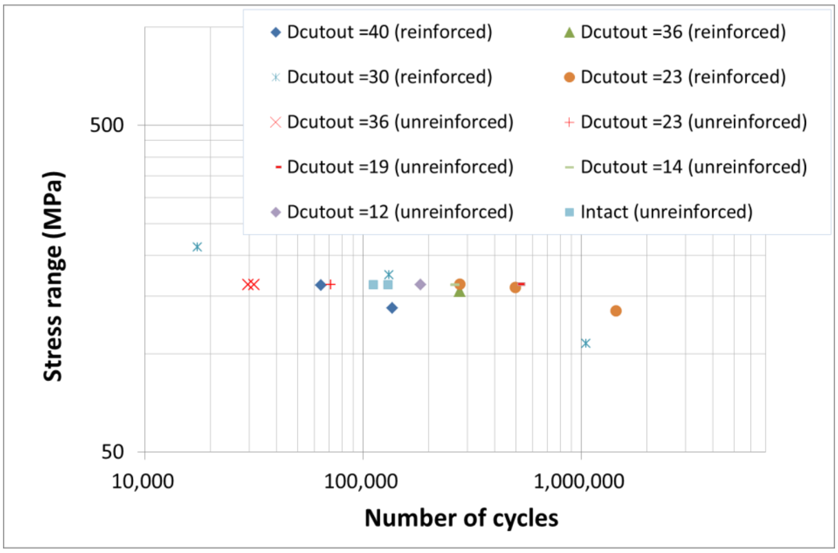

Figure 4-58: Comparison of the results for specimens with and without CFRP (unreinforced specimens are presented in the previous section of this chapter and reinforced specimens are presented in this section).

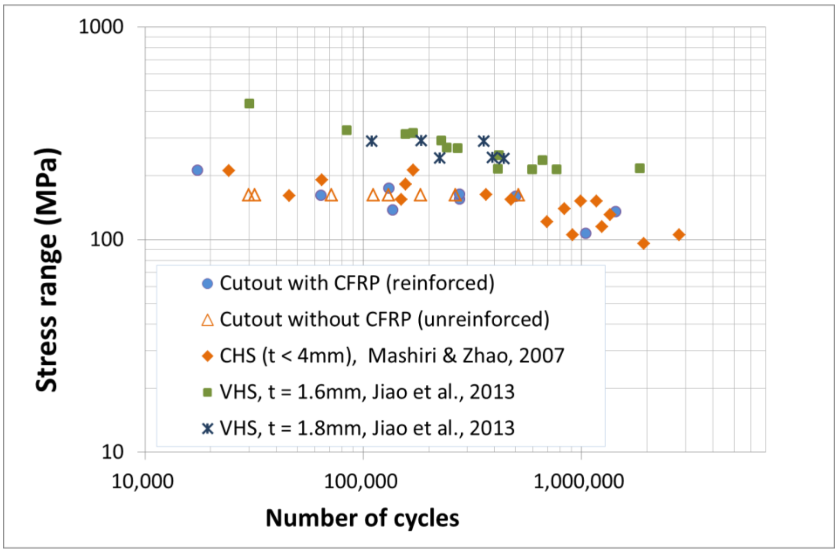

Figure 4-59: Evaluation of the results against previous studies [121, 122] (reinforced specimens are presented in this section and unreinforced specimens are presented in the previous section).

Figure 4-59 also compares the fatigue life of the specimens versus stress range with other published results without cutouts [121, 122]. This figure shows that the results of the current study consistently lie within the data of the previous studies, especially the CHS members of Ref. [122]. Considering Figure 4-59, the effect of the stress range applied to the specimens on the fatigue life can be also inferred. It further appears that there is an interrelation between the stress range and D_{cutout}.

4.4.6 Concluding remarks

This section aimed to reinforce large cutouts with CFRP and evaluate the results against existing data of previous studies. The cutout diameters ranged from about a third to slightly more than half the tube diameter, and they were in the same location as the previous section in which there was no CFRP strengthening. Failure for all of the specimens was in *CCF mode* except for CUTFRP.9, which had the smallest cutout diameter of 23 mm and failed in *BTS mode*. Plastic buckling was detected in all of the specimens that failed in *CCF mode*, evident as a bulge shaped wave at the compression side immediately above the cutout.

CFRP reinforcement significantly enhanced the fatigue life of the present specimens. The fatigue life was relatively lower for the specimens with larger cutouts due to high amount of tensile stress at the section corresponding to the centre of the cutout, whereas for the specimens with smaller holes the fatigue life was far greater. In two specimens the number of cycles exceeded by 10 and even 14 times the ultimate number of cycles of the intact specimen with no CFRP. It was found that with regard to fatigue life, the present CHS tubes with CFRP strengthened cutouts behaved even better than a tube with not cutout nor strengthening (intact and bare specimen). CFRP reinforcement significantly decreased the strains compared with the corresponding specimens with no reinforcement. Furthermore, for the specimens with CFRP the strain values were clearly far steadier prior to crack initiation relative to the specimens without CFRP. It further appeared that the results of the current study consistently lie within the data of the previous studies.

4.5 Conclusions of Chapter 4

This chapter investigates the fatigue response of tube CHS specimens with large non-uniformities. The first two sections of the chapter evaluate the effect of dent as well as cutout, as two major geometric non-uniformities, on the cyclic fatigue life and failure modes of such structures. The last section reports the effect of CFRP reinforcement on the cyclic behaviour of tubes with cutouts.

It was found that the failure mode was highly dependent upon the size of the large imperfections. For shells with relatively small dents or cutouts as well as the intact specimens, the BTS mode was seen, which occurred beside and along the welding. The DWF mode occurred both in the dented zone and near the welding for the specimens with medium sized dents. The DCF mode occurred in the trough zone of the dent for the most severe case of the dented specimens, while there was no crack seen in the tension side of the specimens. The CCF mode was detected in medium and larger holes of the tested models such that failure occurred in the central cross-section of the cutout area and extended to the nominal neutral axis of an equivalent intact cross-section. Failure for all CFRP reinforced specimens was in the CCF mode except for the specimen with smallest cutout, which failed in the BTS mode.

The fatigue life of the current specimens (including dented tubes, specimens with cutouts with and without reinforcement) was highly dependent upon the size of the non-uniformity. For dented tubes, the more the depth of the dent was, the shorter the fatigue life. Although a very small hole was not ultimately affected by the fatigue crack, a significant amount of stress concentration was developed near the hole. As a result, the stress concentration near the welding was significantly relieved. With an optimal diameter of a cutout, the stress concentration at the end of the tube was significantly relieved and hence the fatigue life of the specimen dramatically increased. For very large holes the influence of the cutout on the fatigue life was quite negative, which can be attributed to a relatively high loss of the material in the area of the cutout. Nonetheless, CFRP reinforcement dramatically enhanced the fatigue life of the specimens with cutouts such that in two specimens the number of cycles exceeded by 10 and even 14 times the ultimate number of cycles of the intact specimen with no CFRP. In other words, the tubes with cutouts strengthened with a small amount of CFRP significantly outperformed a tube with no cutout nor strengthening (intact and bare specimen).

Chapter 5

Thin Walled Steel Elements and Sectional Irregularities (Composite Functionality)

Publication output of Chapter 5

This chapter consists of five journal papers: four papers published in international journals (two papers by *American Society of Civil Engineers, ASCE*), and a paper under review:

- "Concrete Filled Circular Steel Tubes with a Timber Infill under Axial Compression" (accepted on 19 November 2016, in Journal of Structural Engineering (ASCE), 143 (7) 2017.
- "Timber filled CFRP Jacketed Circular Steel Tubes under Axial Compression" Construction and Building Materials (Elsevier), 94 (2015) 791–799.
- "Rectangular Steel Tubes with Timber Infill and CFRP Confinement under Compression: Experiments" Journal of Constructional Steel Research (Elsevier), 114 (2015) 196–203.
- "CFRP Confined Circular Steel Tubes under Axial Compression" (submitted – under review).

- "Composite Timber Beams Strengthened by Steel and CFRP" Journal of Composites for Construction (ASCE), Vol. 21, Issue 1 (February 2017).

5.1 Introduction

This chapter discusses the effect of composite functionality on the capacity of and structural response of members including thin-walled steel elements. The primary element is steel in most of the elements investigated in this chapter, and the composite elements consist of timber, concrete and CFRP. The aim is to exploit the full inherent strength of steel by preventing failure through buckling by composite action using a variety of complementary materials.

Timber-concrete filled tubes

Over the past two decades, there has been significant interest in research relating to concrete filled tubes, and a corresponding penetration of this technology into practice (see Refs. [135-139] as a few examples). This section of the current chapter aims to expound upon the effect of timber cores on the structural response of concrete filled circular tubes under compression. Infilling constrains inward deformation of the steel, while use of a concrete and timber combination significantly reduces weight compared to concrete alone. A timber infill with different shapes and geometries surrounded by concrete and encased in a steel tube was employed. The effects of the combination of infill elements on the failure, axial capacity, ductility and *structural efficiency* (weight versus capacity) are comprehensively set forth. Composite specimens including timber showed higher ductility among the other specimens. Greater ratios of energy absorption to the mass were obtained for the specimens with different timber cores in comparison to the equivalent values for fully concrete filled tubes, which is quite desirable in many practical scenarios. It is found that the use of timber as an inner core element in this new composite yields promising results in decreasing the weight and yet enhancing the capacity, ductility and energy absorption, and can be a good alternative to double skin concrete filled steel tubes.

CFRP confined hollow tubes

This section further develops the very limited experiments conducted by other researchers to date on CFRP confined circular tubes exposed to axial compression [140, 141], since the usage of CHS tubes is on the rise in Civil and Mechanical Engineering applications. The effect of length of CFRP-jacketed tubes as well as the direction of the confinement was examined through experiments. It was found that for shorter columns the effect of CFRP reinforcement around the periphery was more significant. The results were evaluated against the existing data in the literature and good consistency was found comparing the results.

Timber-filled, CFRP confined circular tubes

The structural behaviour of an innovative composite column through an experimental study was investigated in this section. The new composite comprised steel cylindrical hollow sections known as CHS, solid timber infill and CFRP confinements. Again the timber infill restricted inward buckling, while the external CFRP confinement restricted outward buckling with minimal added weight. The present stub columns were under pure axial compression. Plastic buckling, failure modes and deformational response of the mentioned elements were assessed. The ultimate capacity enhancement was evaluated for specimens with different conditions and discussions were made in order to clarify the effect of each material on the structural behaviour of different specimens.

Timber-filled, CFRP confined rectangular tubes

A new composite element comprising rectangular steel tubular sections filled with timber and confined with carbon fibre reinforced polymer (CFRP) was investigated in this section. Several tests were conducted on different specimens with varying geometrical conditions and the impact of each material was studied on the structural behaviour of these members under axial compression. The timber infill was found to significantly improve the capacity by preventing local inward buckling. This effect was further enhanced when the short columns were confined with sufficient layers of CFRP to prevent local outward buckling.

Composite beams comprising timber steel and CFRP

Following the study of composite functionality of the three materials, steel, timber and CFRP, which is described in this chapter, composite timber beams strengthened by U-shape steel sections and CFRP are studied experimentally in this section. Despite different reinforced beams seen in the literature (e.g. Refs. [142-147]), specimens with various composite combinations, i.e. steel only, CFRP only and a combination of the two, were considered under three-point flexural tests. Failure, displacement and strain response, ductility, bending capacity and *structural effici*ency were evaluated for the present tested models. Dramatic enhancement of the capacity as well as improved deflection and ductility were gained for the strengthened beams relative to the plain timber specimens, indicating the effectiveness of the reinforcement on the flexural strength of such composite beams.

5.2 Concrete filled circular steel tubes with a timber infill under axial compression

5.2.1 Introduction

Superiority of concrete in compressive strength and stiffness, alongside steel's great tensile capacity and ductility (to confine concrete) have made concrete filled tubes a popular structural member under compression. The topic of concrete filled tubes has clearly stimulated many researchers across the world, some instances of which are outlined in this section:

Li et al. [135] experimentally studied double skin concrete filled steel tubes under axial load. Axial capacity of such elements with preload was thoroughly considered and the effect of slenderness and preload ratio were discussed. Huang et al. [136] investigated the effect of some important parameters such as *hollow ratio* and *nominal steel ratio* on sectional capacities of double skin concrete filled tubular sections. A number of equations were proposed out of an experimental study by Uenaka et al. [137] to estimate the ultimate strength of double skin concrete filled stub tubular columns. Li et al. [138] investigated tapered concrete filled double skin tubular columns. The confinement effect was examined and some formulas were proposed in order to estimate the ultimate axial capacity of such structures.

Yang et al. [139] studied double skin concrete filled tubes under partial loading. A simplified model was put forward to predict the load carrying capacity of such elements. Han and Wei Li [148] experimentally determined the structural response of double-skin steel-concrete-carbon tubular sections. The slightly tapered and straight tubes were compared, wherein the results indicated a moderate effect of tapering on the ultimate capacity. Han et al. [149] studied double skin tubes with concrete infills under long-term axial loading. The effect of sustained loading was extensively discussed in this paper.

Apart from double skin tubes, many papers are seen in the literature investigating fully concrete filled steel tubes subject to compression. Squash (pure yield) axial loads of concrete filled tubes for a series of specimens with varying diameter to thickness (*D/t*) ratios were studied by Kwon et al. [26]. The results were evaluated against available design recommendations in this study. Rectangular concrete filled tubes exposed to axial loading and bending was theoretically studied by Kwon and Jeong [27]. The squash load was proposed and the results were compared with the existing codes. A few other researchers have also recently provided input into this field such as Dundu [28], Yang and Han [29, 30], Chitawadagi et al. [31], Tao et al. [32], and Teng et al. [33], where different aspects of the concrete filled tubes were explored. Most relevantly, steel circular and rectangular hollow sections (CHS and RHS) with solid timber infills and CFRP confinements, were tested throughout this PhD program, as described later in this chapter (see also Refs. [150, 151]). These two studies showed the significant effect of timber in enhancing the axial capacity of the new composite members.

The research of the present section was followed by and inspired through the last two mentioned references published earlier during this PhD program. The compressive capability of the timber was employed in the new composite, yet the addition of timber resulted in insignificant weight increase. Furthermore, the timber provided a space around which the concrete was readily shaped; thus the concrete was covered by the CHS from the outside while the inside was bounded by the timber. The results of the present timber-concrete filled specimens were compared with the fully concrete filled specimens of this study and fully timber filled specimens [151]. The comparisons provide remarkable insight into the topic as will be thoroughly discussed later in this section.

5.2.2 Experimental program

Test set up

The test set-up together with different constituting elements is shown in Figure 5-1. The Avery machine as detailed in the previous chapters was used to apply the loading. A LVDT was used to record the axial shortening of the specimens. As presented later, strain gauges were used to record the stain values of different points on the specimens. Further details of the test set-up and data acquisition system can be found in previous sections of the thesis as well as Refs. [150, 151].

Specimens

General information

Three materials, i.e. steel, concrete and timber were used in this set of tests. Table 5-1 lists the details of different specimens. Specimens 1–12 were all based on a steel CHS, with concrete and/or timber infills as indicated in columns 3 and 4 of this table. The reference specimens were named as CHS.1 and CHS.2, which were empty steel tubes with diameter to thickness (*D/t*) ratio of 47.6 (*D*=76.2 mm and *t*=1.6 mm).

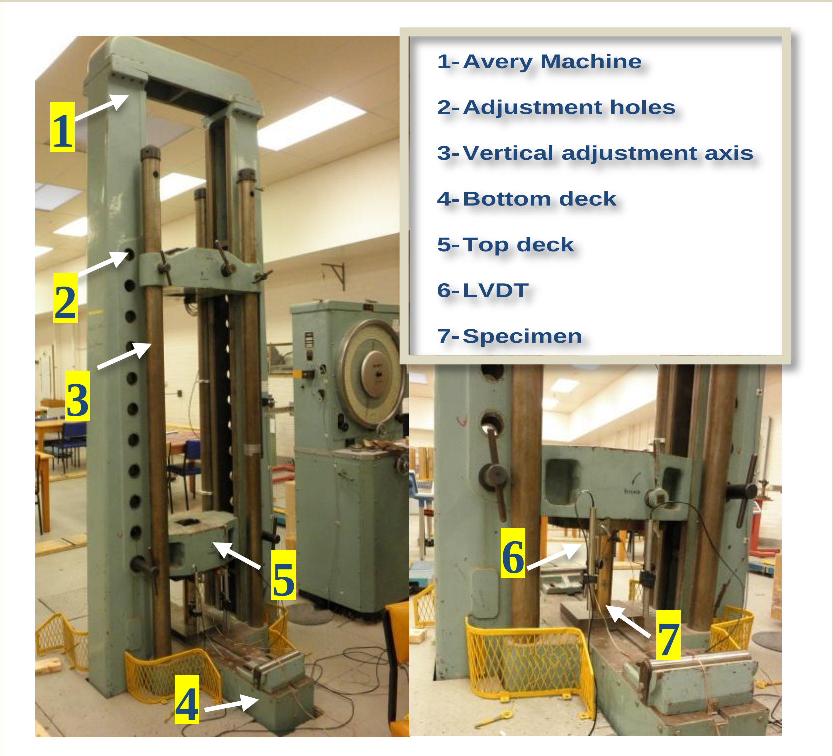

Figure 5-1: Test set up and components.

Two samples of each concrete and/or timber filled specimens were tested to ensure the repeatability and accuracy of the results. FFCHP.1 and 2 represented fully concrete filled specimens, while STCHP, RTCHP, CTCHP and RRTCHP comprised both concrete and timber cores (see Figure 5-2 for details). The specimens CSC.1–4 were cylindrical concrete samples with a diameter of 100 mm and height of 200 mm, compliant with AS 1012 [152], for the purpose of determining the concrete properties. These samples were properly cured and tested after 28 days. Amongst these samples, the maximum axial compression stress was found as 36.8 MPa.

Table 5-1: Specifications of the specimens.

No	Labels	Concrete infill	Timber infill	Remark
1	CHS.1	N/A	N/A	Empty CHS
2	CHS.2	N/A	N/A	Empty CHS
3	FFCHP.1	YES	N/A	Fully filled CHS
4	FFCHP.2	YES	N/A	Fully filled CHS
5	STCHP.1	YES	YES	Square timber
6	STCHP.2	YES	YES	Square timber
7	RTCHP.1	YES	YES	Rectangle timber
8	RTCHP.2	YES	YES	Rectangle timber
9	CTCHP.1	YES	YES	Circle timber
10	CTCHP.2	YES	YES	Circle timber
11	RRTCHP.1	YES	YES	Filleted rectangle timber
12	RRTCHP.2	YES	YES	Filleted rectangle timber
13	CSC.1	N/A	N/A	Concrete sample
14	CSC.2	N/A	N/A	Concrete sample
15	CSC.3	N/A	N/A	Concrete sample
16	CSC.4	N/A	N/A	Concrete sample

The material properties of the employed timber infill are shown in Table 5-2, which is based on the data provided by AS 1720.1 [153]. Moreover, conducted tensile coupon tests yielded the material properties of the utilised steel, which are also tabulated in Table 5-2.

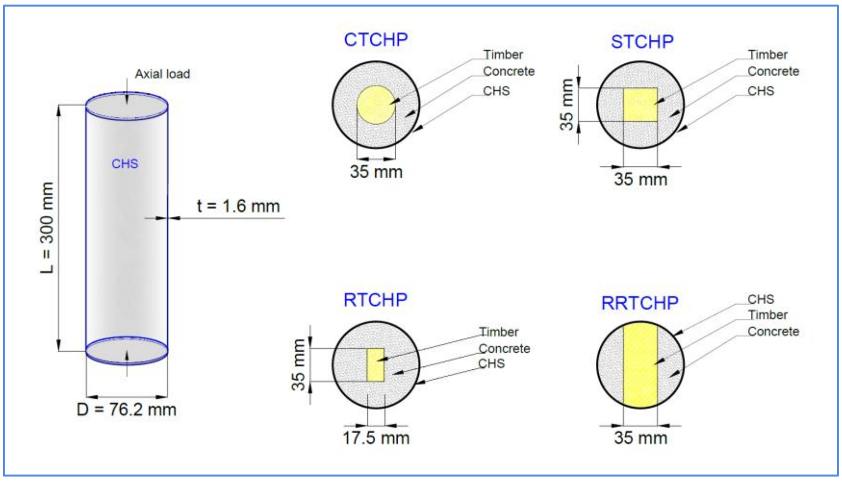

Figure 5-2: Geometric features of specimens.

Specimen preparation

CHS tubes were commercially available, supplied in larger lengths and cut into the designated lengths. Both ends were machined flat in order to have a uniform axial stress distribution on the end section. Timber blocks were prepared with different cross-sections as shown in Figure 5-3. Round surfaces were prepared, and flat edges were roughly overcut with a circular saw (if necessary) and finished with a planer thicknesser to have a uniform section all through the length. After preparation of the timbers – and to avoid the timber absorbing water from the concrete after casting – cling wrap was closely applied to the surface of the timbers in multiple layers. A concrete with a predesigned mixture (*Concrete Instant* as sand and aggregate with a separate sachet of cement, product code 2180578, supplied from K&D Warehouse, Australia) was utilised to fill inside the tubes.

Table 5-2: Material properties of the utilised steel (tested) and timber (AS 1720.1).

Materials and their properties	**Descriptions or Values**
Stress grade of timber	Radiata Pine – MGP10
Bearing of timber parallel to grain (MPa)	30
Ave. modulus of rigidity of timber (MPa)	670
Ave. modulus of elasticity of timber parallel to grain (MPa)	10000
Yield stress of steel (MPa)	307
Ultimate stress of steel (MPa)	360.2
Young's modulus of steel (GPa)	216.3

Timber blocks were placed, centralised and clamped inside the tubes. Throughout casting, a designated vibrator was employed to reach elimination of all voids within proper compaction of the concrete. Following the completion of the fabrication, the specimens were stored and covered with a damp cloth to prevent dehydration for 28 days, after which the specimens were ready for testing.

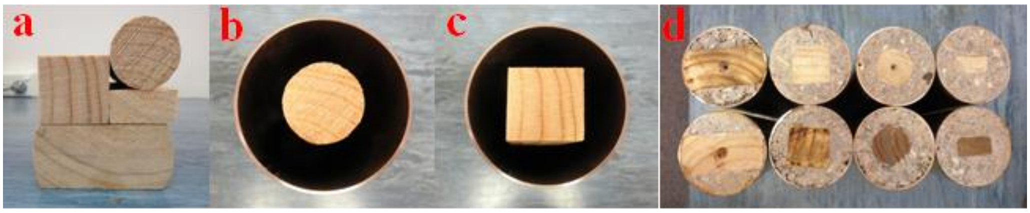

Figure 5-3: Specimens' components and concrete filled specimens.

In order to ensure smooth end surfaces before the tests, the top and bottom surfaces were carefully polished, removing a few millimetres such that the end surface of the concrete, timber and steel tubes were all coplanar and the axial load would be properly distributed (see Figure 5-3).

5.2.3 Experimental observations

Failure of the specimens

It is believed that the particular combination of materials for the new composite exploited their properties to reach highly ductile members. The confinement of the concrete provided by the CHS prevented spalling and prolonged its strength beyond the brittle failure point. The concrete in turn provided a solid core that delayed any buckling within the steel, and the timber reduces weight and cost while providing some additional rigidity and simplifying construction compared to the double skin arrangement.

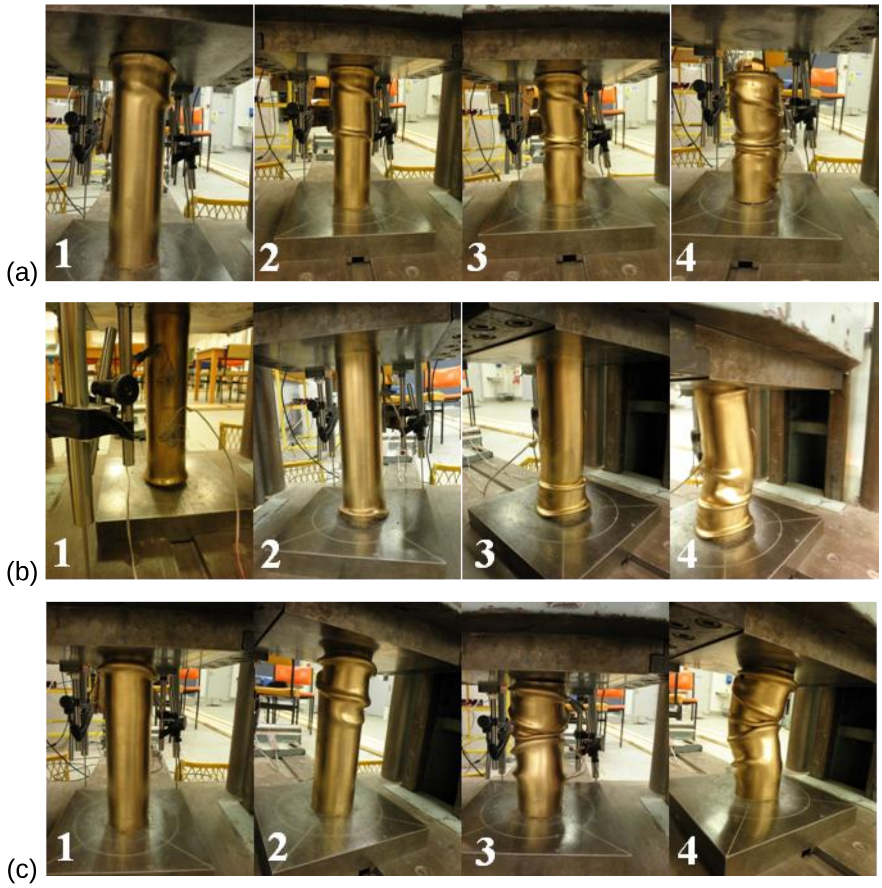

Figure 5-4: Crushing progress of three different specimens: (a) CTCHP.1, (b) RRTCHP.1 and (c) STCHP.1.

In order to investigate the ductility of the new composite elements the loading was continued after the initial peak load was obtained until the specimen approached around 33% shortening, although this large deformation may not be of interest for all practical structural applications. The reference specimens (CHS.1 and CHS.2) buckled in an elephant foot mode, well known to be a typical buckling mode for these elements. As the load progressed, the initial bulge sharpened and folded over the body of the tubes leading to the development of successive lobes.

The progress of the failure for three different specimens with both concrete and timber infills, CTCHP.1, RRTCHP.1 and STCHP.1, is shown in Figure 5-4. Similar to the reference specimens (albeit with more asymmetry of the geometry), bulge shape deformations appeared once the steel yielded. As the load grew further – in addition to the concrete-imposed outward deformations – bulges developed further and transformed to folds.

Figure 5-5: Sprung back timber after failure.

It is fitting to mention that in most of the specimens the failure manifested to some extent analogous to the column buckling as an overall deflection towards one side was observed along the length. Notwithstanding this though, the two end surfaces of the specimens were always parallel to the plane of the load application plates. Following unloading after the failure of the specimens with a timber infill, the timber sprang back out by less than 10 mm as can be seen in Figure 5-5. For timber-concrete filled specimens, the concrete after failure is deemed to be crushed after undergoing such a sizable axial deformation, while the steel was folded in lobes.

It appears that the timber's failure may partly depend upon the ratio of the timber's area to the area of the concrete as confining material. As an example, timber in RRTCHP comprises a higher area relative to the other specimens. Besides, timber in this specimen is confined with both concrete (straight sides) and steel (curved sides), while timber in other specimens is confined by concrete only. Figure 5-5 shows that failure of the timber in this specimen is different from RTCHP and CTCHP, as timber in RRTCHP turned out to undergo a more severe failure.

Load displacement behaviour and ductility

Axial shortening of different empty and filled specimens are shown in Figure 5-6. For the reference specimens the axial load dropped relatively sharply by around 80% once the initial peak load was reached.

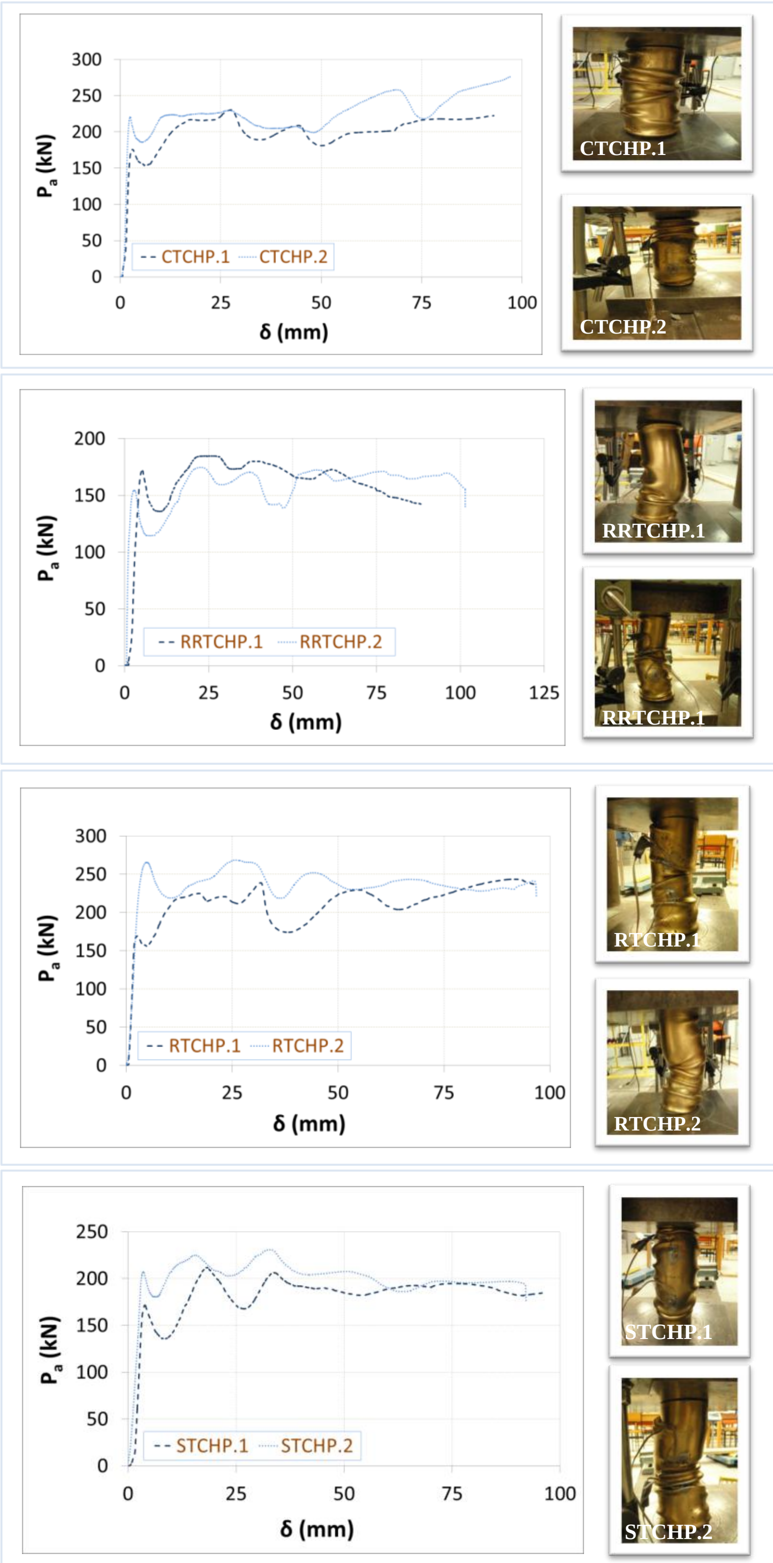

Continued in the next page.

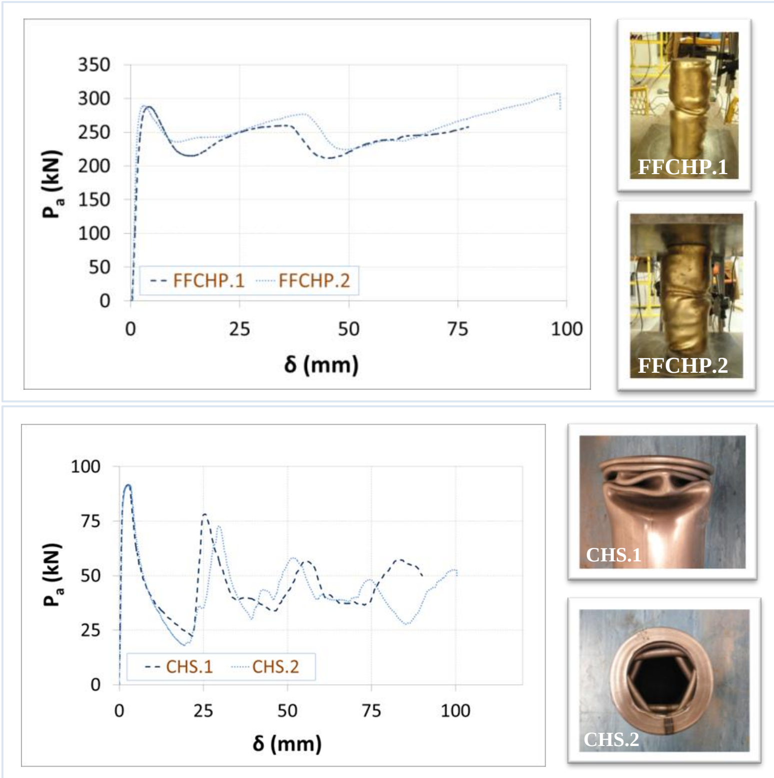

Figure 5-6: Axial shortening versus the axial load for different specimens, final failure modes of different specimens.

Nevertheless, an ebb and flow manner was observed by the progress of the axial loading, which was coupled with folding of plastic lobes in the steel. There was substantial load recovery after each fold had fully closed up, but substantial loss again as each new layer of folds started to form.

The load fluctuated in a more or less similar fashion for concrete and timber filled specimens, but over a significantly reduced range with only a minor loss of load following each peak. In all such cases, subsequent peak loads were formed in the plastic region.

In the fully concrete filled tubes, the post-yielding behaviour of the specimens on average achieved a load lower than the initial peak, whereas the concrete-timber-filled specimens generally experienced higher loads after the first peak was obtained. This definitely suggests the significant effect of the timber infill in providing a good deal of ductility for such composite elements. It is of interest that the specimens RRTCHP.1 and RRTCHP.2 – including the highest timber to concrete ratio – showed the highest ductility among the other specimens as a high load was maintained after the first drop occurred in the load displacement curve. Steel hollow tubes are made of a highly uniform material (steel), while fully concrete filled specimens comprise steel (highly uniform) and concrete (moderately uniform) material. Timber, however, is a natural material with ineluctable non-uniformities, which makes the nominally identical concrete-timber filled composites slightly different from one another, in contrast to the nominally identical fully concrete filled specimens or reference specimens. Yet, the overall trend of the nominally identical specimens shows a very consistent behaviour. The post yielding region undergoes an ebb and flow trend in which the waves of the two identical timber-filled specimens on the curves approach one another after the initial peak.

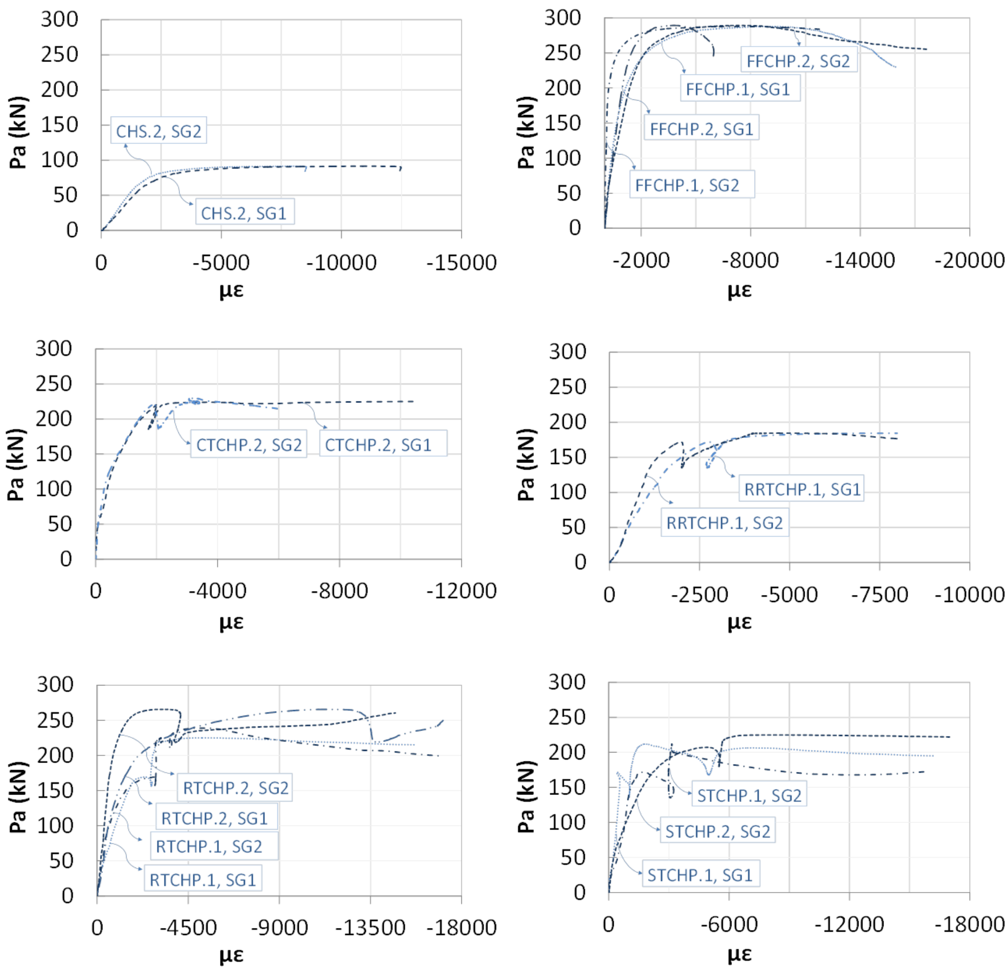

Figure 5-7: Micro strain values for different specimens.

Strain response of different specimens

Strain gauges *SG.1* and *SG.2* were attached at a distance of 100 mm (one third of the length) from each end of the specimens. Observing load strain graphs shown in Figure 5-7, it is found that the reference specimens (CHS.1 and CHS.2) as well as fully concrete-filled specimens (FFCHP.1 and 2) behaved more stably against the axial loading. However, when the timber took part as an infill the peak load in the load-strain graph was not reached as smoothly as the reference specimens or the fully concrete filled specimens. This can be, on the one hand, attributable to the interaction of the timber and the concrete, in which successive slippage and shear bonding occur, and the interaction forces required for these materials to act as a composite are alternately demobilised and mobilised. On the other hand, natural defects in the texture of the timber blocks, e.g. knots, can be a reason for this response. Despite these though, following a few small loops in the load strain curves, the strain values steadily increased to reach the ultimate load. In point of fact, the mentioned interaction of different materials is believed to be the inherent feature of the composite materials especially when the rigidity of various materials (concrete and timber) differs from one another. Nonetheless, this difference did not affect the significant contribution of the timber in the present composite, which will be further elaborated in the coming sections.

The folding and global (column) buckling observed above suggest that details of the strain behaviour would vary significantly along the length and around the perimeter at any given time in the tests. However, it is expected that the general features of the load versus strain curves would not qualitatively change. Indeed, in spite of only using two gauges very similar features are observed in the various graphs of nominally similar specimens.

5.2.4 Axial strength of specimens with different infills

Different infills and their effect on the capacity

The axial compression capacity of the present specimens is discussed in this section, where the effect of different materials on the strength is examined. A quantity *IPL*, or initial peak load, for the different specimens is plotted in a bar chart in Figure 5-8. Based upon the results, the two fully concrete filled tubes (FFCHP.1 and 2) accounted for the greatest *IPL* amongst the specimens, exceeding the axial capacity of the reference specimens by three times. This enhancement was closely followed by one of the concrete filled specimen with a rectangular timber core, whereby slightly less than three times increase was obtained.

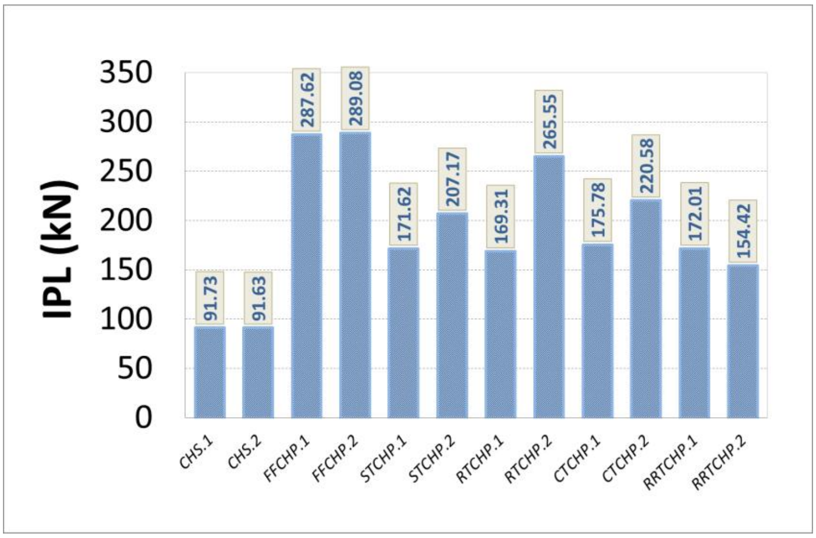

Figure 5-8: Initial peak load for different specimens.

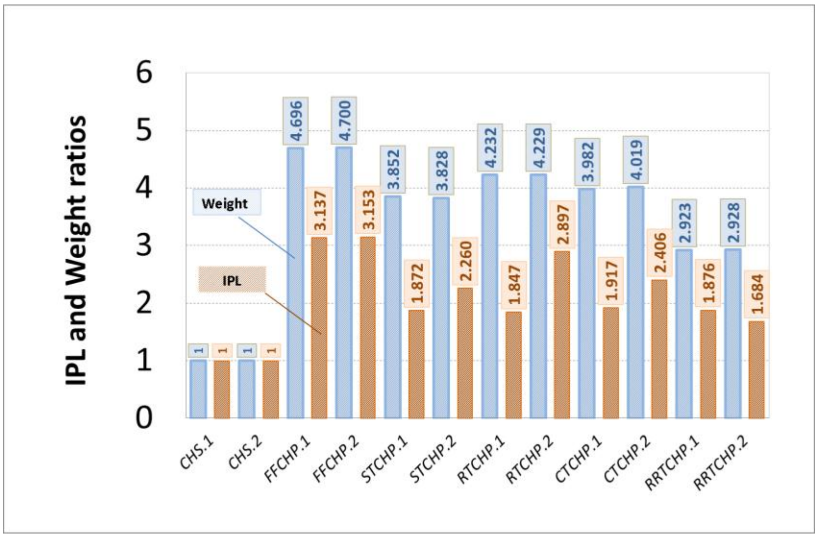

Figure 5-9: Ratios of *IPL* and weights of different specimens to the reference specimen.

The other such specimen reached and maintained a very similar load in the long yield plateau but possibly experienced some minor local buckling that produced a premature initial peak. Following the aforementioned specimens, the concrete filled tubes with a circular timber infill achieved relatively higher *IPL* as the concrete and timber infills enhanced the capacity by about 2.4 times. The capacity ratio of the concrete filled specimen with a square timber core (STCHP) to the reference specimen was about 2.3, which was quite close to the equivalent specimens with a circular timber infill. The lowest capacity enhancement was gained for the specimens RRTCHP, where the *IPL* augmented by approximately 1.9 times compared with the reference specimens. The abovementioned ratios were calculated based upon the highest capacity values obtained amongst the two replicas. Although these reasonably differed in some cases, there was still good consistency in all results presented. It should be noted that the specimens with more uniform materials yielded more consistency, when nominally identical specimens were compared. When a natural material takes part in a composite, the natural non-uniformities of the material – here knots of the timber as an example – may cause higher differences, which is why replicates were decided for this set of experiment.

Theoretical prediction and comparison with experimental results

A simplified theoretical prediction was made to compare the experimental results. The predicted load, P_{theory} in Eq. (5.1), is calculated based on the axial strength of each material's (steel, concrete and timber) individual axial stress (σ_i), and area of the cross section (A_i),

$$P_{\text{theory}} = \sum_{i=1}^{3} \sigma_{\text{i}} A_{\text{i}} \tag{5.1}$$

where subscript *i* refers to the three components. For the reference specimens made of steel only, the yield stress was taken into account in calculations, while for fully concrete filled steel tubes and concrete-timber filled specimens the concrete was assumed to have reached its ultimate stress (36.8 MPa) and a strain of 0.0012 was calculated as this stress divided by the elastic modulus (30.7 GPa, calculated in accordance with AS 3600 [154]).

Table 5-3: Timber and concrete infills ratio and strength comparisons.

Labels	A_c/A_t	I_t (%)	P_{exp} (kN)	P_{theory} (kN)	P_{exp} / P_{theory}
CHS	-	-	91.7	115.1	0.8
FFCHP	-	-	288.4	251.4	1.15
STCHP	2.42	0.29	189.4	221	0.86
RTCHP	5.83	0.15	217.4	236.2	0.92
CTCHP	3.35	0.23	198.2	227.5	0.87
RRTCHP	0.71	0.59	163.2	190.5	0.86

At this strain the steel and timber were still within their elastic ranges – timber's axial strength was adopted in accordance with AS 1720.1 [153] as

18 MPa for strength parallel to the grain – so the stress was calculated using the Young's moduli, 216 GPa and 10 GPa for the steel and timber respectively. Table 5-3 presents A_c / A_t, wherein A_c and A_t are areas of concrete and timber infills in the cross section of the composite elements respectively. I_t gives timber's percentage as an infill relative to the concrete. P_{exp} for each specimen shows the average *IPL* obtained from nominally identical specimens (replicas), while P_{exp} / P_{theory} gives the ratio of the experimental to theoretical axial strengths.

According to the ratio P_{exp} / P_{theory} and considering simplifications, reasonable consistency is seen comparing the experimental results of this study with the theoretical predictions, as in all cases the difference between the test results and the predictions is less than 20%. Except for the fully concrete filled specimens, theoretical results overestimate the experimental values. This is because the infill in FFCHP specimens was more uniform as it was made of a single material well confined from outside by steel. Given the aforementioned difference, it is believed that the lower transverse rigidity of the timber as the inner limit of the concrete in such composites should be further investigated to draw definitive conclusions on the composite functionality of the two materials. Notwithstanding, this does not universally indicate higher efficiency of FFCHP specimens over concrete-timber filled specimens in all contexts as there are several elements identifying the new composites as an efficient element, which will be discussed further in the coming sections. All in all, the theoretical prediction presents a good agreement with the experimental results obtained in this research.

5.2.5 Weight versus capacity and other advantages of the current composite

It is quite evident that both concrete and timber effectively contributed to the axial capacity of the current structures. A few salient points are noted in this section to further legitimise the use of the current composite: (i) the weight gain has to be considered alongside the capacity gain which defines the *structural efficiency*. Thus, comparing timber with equivalent concrete and steel, the presence of timber is deemed to improve the performance of the composite element, given that timber has a great *structural efficiency* particularly in compression. (ii) Comparing the current composite specimens with the double skin concrete filled tubes the timber core helps facilitate casting the concrete in a more efficient way. The timber is cheaper than the tubes utilised as the inner skin of the mentioned tubes, and more importantly, a solid timber, as an infill, can more effectively prevent the inward failure of the concrete. Above all, the compressive capacity of the timber – given that timber is an inherently compression bearing material – is employed in this composite leading to the capacity enhancement. (iii) Although the cost (both financial and environmental) of the timber relative to concrete and equivalent steel differs in various countries based on the availability of the resources, timber is considered by and large less expensive than the two other materials. As an instance, timber is less costly and has substantially less environmental impact than concrete and steel in Australia, and the usage of timber is more extensively seen especially in low-rise buildings in this country.

The capacity ratios together with the weight ratios of different specimens are presented in Figure 5-9. For the specimens with the timber as the dominant material (RRTCHP), the capacity was enhanced by about two times with a significant reduction in the total weight of the composite element relative to the fully concrete-filled specimens. For the other specimens, the capacity improved proportional to the weight increase. Nonetheless, due to pros and cons of utilising different materials in terms of availability, durability, fire resistance, cost, total weight and capacity, the significance of the weight versus capacity must be carefully assessed respectively for any particular project. It further appears that the new composite can significantly improve the fire resistance of timber structures. As such, the new composite can be employed to enhance the axial capacity of different timber columns and, where required, the fire resistance of timber elements in the future.

5.2.6 Comparison of the present specimens with fully timber filled tubes

A comparison is drawn between the results of this section with the results of fully timber filled CHS tubes – TIMC.4 and TIMC.5 are discussed later in this chapter, also available in [151]. TIMC.4 is timber filled tube, confined with 3 layers of CFRP, and TIMC.5 is timber filled tube with no CFRP. The same materials of steel and timber as well as the same loading and boundary conditions were used. The fully timber filled specimen (TIMC.5 without CFRP confinement) reached the capacity of around 213 kN. This indicates that although various materials (i.e. concrete and timber) may have different strengths, for these particular materials the axial capacity increase is only about 35% when the concrete infill is substituted with its timber counterpart. Therefore, in terms of the *structural efficiency*, and given the significant weight difference between the two materials, such specimens outperform the fully concrete filled specimens. Furthermore, the same capacity was obtained for a fully timber filled specimen confined with CFRP (TIMC.4 discussed later in this chapter, also available in [151]) and the FFCHP specimens. TIMC.4 clearly possessed a much lighter weight, but almost the same strength, relative to FFCHP, demonstrating that the fully timber filled specimen TIMC.4 had a greater *structural efficiency.* All in all, it appears that the employment of timber can be quite comparable to the concrete infill under axial compression. Nevertheless, as mentioned earlier the cost of each material (e.g. CFRP utilised in TIMC.4) has to be considered to make meaningful comparisons in practice for any particular projects. Yet, given that a number of geometrical (e.g. *D/t* ratio of the tubes, etc.), and material parameters may affect the structural response of such a composite, further research into the topic is still required to reach more definitive conclusions.

5.2.7 The effect of timber infill on energy absorption

Although the crushing response of the current specimens is not of the central focus of this study, two parameters, *average crushing load* (*ACL)* and *specific absorbed energy* (*SAE*), are presented in Figure 5-10 to discuss the behaviour of the specimens in the plastic region. These two quantities are mentioned in the literature, and it is noted that *SAE* is determined as absorbed energy per unit mass of a crushed specimen [155], where the absorbed energy is the area under the load-displacement curve for the crushed region, considering the *average crushing load*. The *average crushing load* is the average load in the load-displacement curves for each specimen after the initial peak load (as the lower limit) is reached. The upper limit to calculate the *average crushing load* was considered the maximum displacement of 70 mm for the present specimens. It is found that *ACL* values of RTCHP and CTCHP specimens are quite comparable with the values of the fully concrete filled specimens such that *ACL* value of RTCHP.2 even exceeds the corresponding value of FFCHP.1.

(a)

(b)

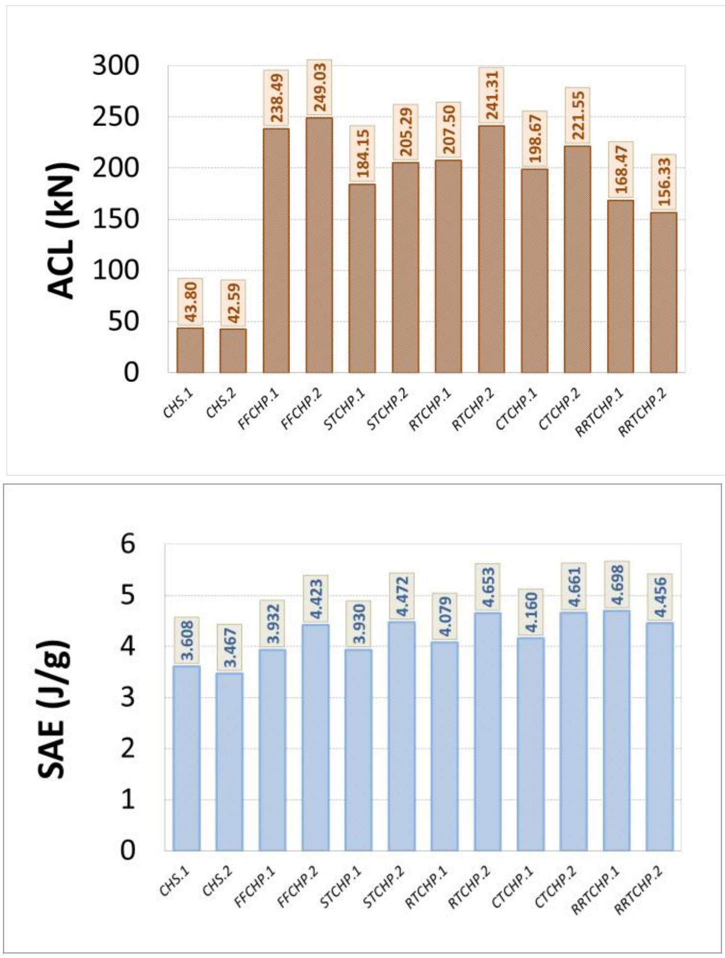

Figure 5-10: (a) Average crushing load for different specimens, and (b) specific absorbed energy for different specimens.

This suggests that, while maintaining a lighter weight, a timber core in some specimens also maintained the average crushing load relative to the fully concrete filled specimens. More importantly, the *SAE* values indicate that the *specific absorbed energy* values of the fully concrete filled tubes are by and large lower than the equivalent values for the timber and concrete filled specimens. The higher value of *SAE* in the specimens with timber cores is indicative of a higher ratio of energy absorption to the mass of the specimens which is desirable in practice for the projects in which the energy absorption is regarded a significant element. The proposed composite would be very suited to such applications because of its extreme ductility, as discussed earlier. It has been shown that values close to the peak capacity are maintained even with average overall shortening of around 33%.

In a nutshell, the advantage of considerable energy absorption can make the new composite quite useful for many applications such as different types of crash barriers or members under impact loading where a member has to undergo a substantial deformation without failure.

5.2.8 Conclusions

This section aimed to discuss the structural behaviour of a new composite comprising CHS tubes and concrete-timber infills under axial compression. Salient concluding remarks of this research are presented as follows:

In fully concrete filled tubes, the post-yielding behaviour of the specimens on average achieved a load lower than the initial peak, whereas the concrete-timber-filled specimens generally experienced higher loads after the first peak was obtained. This suggests the significant effect of the timber infill in providing a considerable ductility for such composite elements.

The two fully concrete filled tubes accounted for the greatest *IPL* with the axial capacity exceeding three times that of the reference specimens. For the concrete filled specimen with a rectangular timber core slightly less than three times increase was obtained. The concrete filled tubes with a circular and square timber infill exhibited the capacity increase of about 2.4 and 2.3 times respectively.

Both concrete and timber effectively contributed to the axial capacity of the current specimens. However, the weight gain needs be considered alongside the capacity gain. The presence of timber is deemed to improve the *structural efficiency* of the current composite element. The timber helps facilitate casting the concrete with a lower cost compared with the double skin tubes. A solid timber, as an infill, can more effectively prevent the inward failure of the concrete. Above all, the compressive capacity of the timber is employed leading to the capacity enhancement.

While having a much lighter weight, a timber core also maintained the average crushing load relative to the fully concrete filled specimens. The *SAE* values of the fully concrete filled tubes are by and large lower than the equivalent values for the timber and concrete filled specimens. The higher value of *SAE* in the specimens with timber cores is indicative of a higher ratio of energy absorption to the mass which is quite desirable in many practical scenarios.

5.3 CFRP confined circular steel tubes under axial compression

5.3.1 Introduction

Widespread usage of CHS tubes has greatly stimulated many researchers to investigate the structural behaviour of these elements. Furthermore, the applications of Carbon Fibre Reinforced Polymer (CFRP) are increasing in the areas of rectifying structural weaknesses in steel elements or to generally strengthen it against buckling. As other distinctive features, CFRP is light-weight yet strong, insusceptible to corrosion and a conveniently constructible material. Thus, the combination of steel and carbon fibre with a proper design mostly yields a reasonably strong and reliable structural element.

FRP is extensively and effectively utilised in concrete columns to confine the material and prevent spalling. As some instances, Xiao [156], Xiao et al. [157], Bisby and Stratford [158], Rousakis and Karabinis [159] and Bisby and Ranger [160] all investigated different aspects of FRP bonded concrete columns.

As well as concrete columns, steel elements reinforced by FRP have been examined through a great many studies. Axially compressed thin cylindrical shells were thoroughly looked into by Rotter [161]. A simple design rule was developed in this paper to determine the strengths of such cylinders. Hollaway and Cadei reported advances of upgrading metallic structures with advanced polymer composites [162]. Teng and Hu studied suppression of the local buckling in steel tubes reinforced by FRP confinement [163]. They found more ductility of the tubes as a result of the reinforcement, which generally always leads to retrofit of tubular structures subject to seismic loads. The usage of FRP in strengthening steel structures was thoroughly reviewed by Zhao and Zhang [164]. Along with the literature survey in this reference several future research topics were identified for investigation. Rehabilitation of tubular members with carbon reinforced polymers was studied by Seica et al. [165]. Steel beams strengthened through modern composite materials and CFRP were discussed by Miller et al. [166], and Ghanbari Ghazijahani et al. [167] and fatigue durability of the CFRP steel bond and failure modes were investigated. Haedir et al. reported and discussed the strength of CHS tubular beams reinforced by FRP sheets in pure bending [168]. It was found that the capacity of composite beams was largely affected by the amount of fiber reinforcement and the orientation of FRP as well.

Notwithstanding the abovementioned studies, limited research is published on confined steel CHS members. Among these are three studies pertaining to FRP jacketed steel tubes under compression. Teng and Hu conducted four tests including bare specimens with the diameter to thickness ratio around 40 and these circular steel tubes were confined with GFRP [141]. Different plies of GFRP were applied to various specimens. Although the capacity enhancement was insignificant for the reinforced specimens, the ductility was dramatically augmented which was believed to enhance the seismic resistance of such stub columns. Haedir and Zhao tested six CFRP jacketed high strength steel tubes with different *D/t* ratios [140]. For each specimen both longitudinal and hoop confinement with different layers was adopted. Unlike the GFRP tubes reported in Ref. [141], the capacity increased considerably for the specimens with more layers of CFRP confinement. Strength and deformation capacities of steel CHS members strengthened with carbon fibre was evaluated by Nishino and Furukawa through several experiments [169], in which two end plates were welded to both ends of the specimens.

It should be noted that, apart from the three references cited in the previous paragraph, there is no research into further development of FRP confined CHS members. Above all, given the fact that each mentioned study examined a particular aspect of externally bonded CHS members, further researches into developing the work seem still required. To this end, this section aims to investigate this subject to examine the structural behaviour of such elements.

5.3.2 Experimental program

Details of stub columns and CFRP

Figure 5-11 and Figure 5-12 show two types of confinement for the present specimens as well as different specimens used in this section. Tube specimens were all made of mild steel, which were supplied as high quality cold formed fabricated tubes with a seam area along the length. The seam area was not geometrically projected nor depressed so that no significant geometrical difference was found between the seam zone and the perfect body of the tubes. The material properties of the steel specimens are listed in Table 5-2. In total 7 specimens were tested, in which the first two, CCTU.1 and CCTU.2, were bare specimens and the remainder were confined with CFRP. Details of these specimens are given in Table 5-4.

The carbon fibre sheets used to wrap the specimens were SikaWrap Hex-230C supplied in a roll by Sika Australia Pty. Ltd. For preparation and subsequently confinement they were precisely cut into predetermined lengths. Sikadur®-330 twin solvent free, thixotropic epoxy adhesive was utilised for bonding the carbon fibre sheets. It is fitting to mention that both ends of the columns were carefully machined in a lathe in order that the load was capable of being applied uniformly.

Table 5-4: Specimens' geometry and confinement.

CHS tubes	**L_{tube} (mm)**	**D_{tube} (mm)**	**t (mm)**
	200, 300 and 400	76.2	1.6
Specimen	**Confinement**	**Wrapping direction**	**Length**
CCTU.1	Bare tube	N/A	200
CCTU.2	Bare tube	N/A	300
CCTU.3	3 plies, full	Longitudinal	200
CCTU.4	3 plies , full	Circumferential	200
CCTU.5	3 plies , full	Circumferential	300
CCTU.6	2 plies , full	Circumferential	300
CCTU.7	3 plies partial	Circumferential	400

Note: Partial confinement was applied to each end with the length of 80 mm.

Confinement process

Prior to applying the carbon sheets, the tube specimens were degreased and cleaned with proper chemicals, uniformly ground afterwards and finally meticulously cleaned with acetone to ensure that any additional particles were removed. The two part epoxy resin was thoroughly mixed as instructed in the ratio of 4:1 for parts A and B respectively. The epoxy resin was afterwards applied to the tubes. Then, a carefully controlled movement and compression was applied to the epoxy-smeared sheets so that they were gradually wrapped around the tubes in the desired patterns. The manual of the resin adhesive was followed so as to allow the epoxy to properly cure. Both ends of the tubes were kept epoxy free so that the load was applied smoothly to the whole end sections of the tubes.

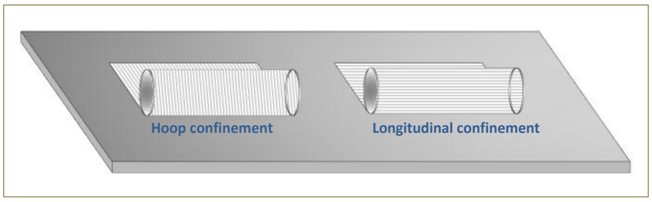

Figure 5-11: Two types of confinement, i.e. circumferential and longitudinal.

Test rig and procedure

As detailed before, the same Avery hydraulic testing machine with the ultimate capacity of 1000 kN was used to apply the load. A digital LVTD was employed to record the axial shortening of the tubes throughout the experiments.

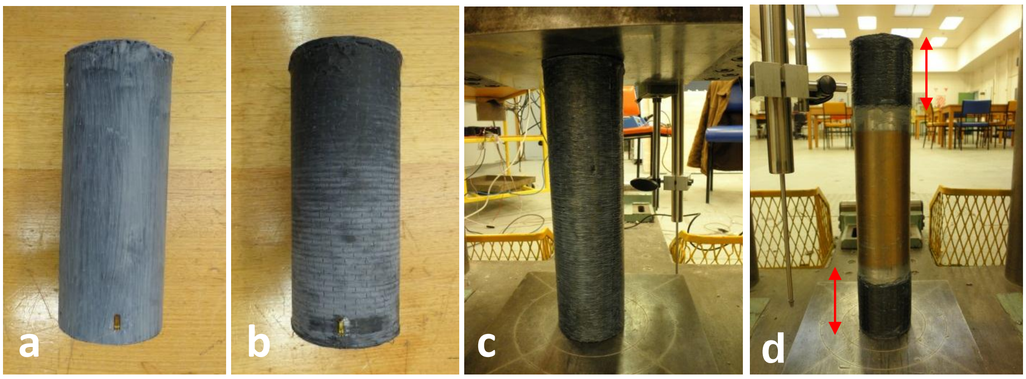

Figure 5-12: (a) and (b): CCTU.3 and CCTU.4, (c) CCTU.5, (d) CCTU.7, partially reinforced specimen.

A number of micro strain gauges were utilised for recording the strain values. Data were recorded through a HBM, R01857 (Quantum-X, 2014) data logger and proprietary software. For the first specimen a very small load was applied, then unloaded, in order to condition the testing apparatus to ensure that every component was working properly. The load was applied quite slowly during each test so as to apply a quasi-static loading and to record the deformations at each stage of loading.

5.3.3 Test results

Failure modes

Bare specimens

The specimens without any confinement, as expected, experienced plastic buckling in the form of a bulge wave mainly near one end of the columns. Figure 5-13 shows the plastic buckling of the unreinforced specimens. It was observed that upon the onset of buckling at one end, the deformational energy was accumulated at the buckled areas and as a result, the other regions of the tubes remained unbuckled. However, a closer review of the specimens revealed that the other end was deformed similarly, yet far less – in terms of severity of the deformations – than the predominantly buckled end. Specimen CCTU.2, being longer, exhibited characteristics of column buckling, producing an additional bulge near mid-length but on the opposite side of the specimen as the end bulge (Figure 5-13).

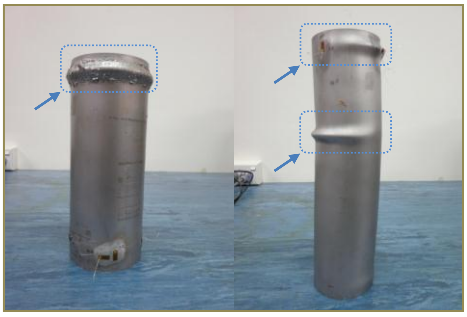

Figure 5-13: Bare specimens: CCTU.1 (left) and CCTU.2 (right).

Fully confined specimens

Specimens CCTU.3 and CCTU.4 after failure are shown in Figure 5-14 (a) and (b). These specimens were confined with different orientations of carbon fibre sheets. The direction of the fibres was longitudinal in CCTU.3, whereas for its counterpart specimen CCTU.4, this direction was circumferential. As can be observed, the failures in CCTU.3 and CCTU.1 were more or less alike, as outward buckling governed the deformations in both specimens. A similar bulge took place for CCTU.3 as did for the bare specimen. This led to a local tension in the CFRP, which ultimately caused the CFRP to break at the location of the local bulge.

Failure occurred at approximately the same cross section for CCTU.4 as for CCTU.3, though no outward deformation was observed in this specimen. Unlike CCTU.1 and CCTU.3, inward plastic buckling dominated the deformations in CCTU.4. As another salient observation, apart from the inward buckling at the section in the proximity to the top end, a few deformational waves were formed in the form of inward diagonal dents for CCTU.4, which is somewhat reminiscent of the Yoshimura buckling pattern (see Figure 5-14 (c) and (d)).

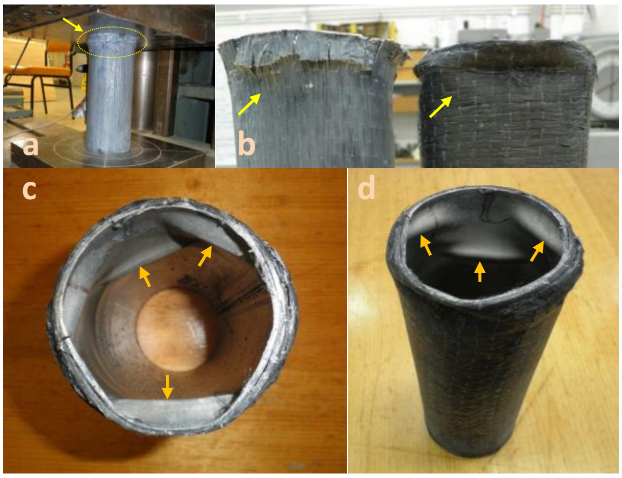

Figure 5-14: (a) formation of the plastic buckling in CCTU.3 and (b) CCTU.3 and CCTU.4, outward and inward buckling waves, (c) and (d) inward deformations in CCTU.4 specimen.

The difference in the failure mode is believed, in essence, to be attributed to different patterns of confinements in different specimens. For CCTU.3 the longitudinal CFRP fibres were insufficient to prevent the *elephant foot* buckling of the steel. Thus, the steel bulged outward and debonding took place between the CFRP and the steel at the location of buckling. On the other hand, outward deformation was fully prevented by the CFRP in CCTU.4 as it was applied in circumferential direction. As a consequence, the CFRP very well restrained the most vulnerable areas of the tubes, both ends near the edges, against buckling. To draw an analogy with the circumferential confinement provided by the CFRP, one may liken it to a strong belt covering the circumference such that once the tube is about to buckle outward, this circumferential belt – as it works in tension – prevents hoop expansion of the tubes.

As for CCTU.5, local buckling commenced in two tiers as inward deformations, and developed further in triangular shapes (see Figure 5-15 (a)). The failure for CCTU.6 was in large amplitude wrinkles close to the ends, while a local inward buckling was situated at the mid-length of the tube (see Figure 5-15 (b)).

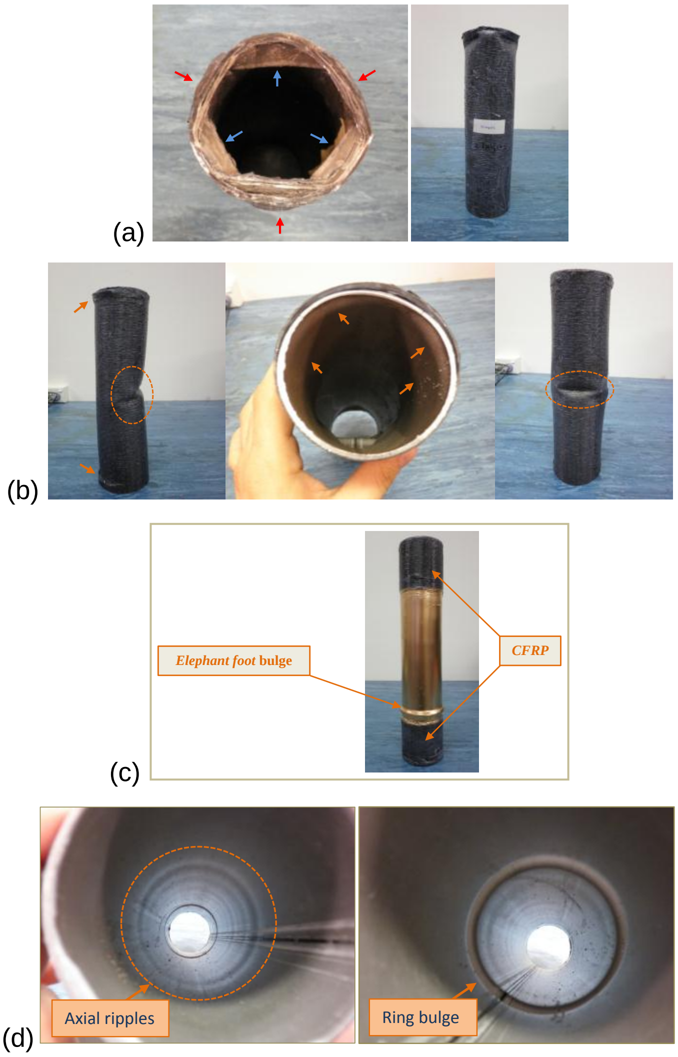

Figure 5-15: (a) Two tiers deformational waves in CCTU.5 (inward triangular shape) – first tier marked with red arrows and second tier marked with blue arrows, (b) failure mode of the specimen CCTU.6, (c) failure mode of CCTU.7 specimen (bulge wave), (d) axial ripples of CCTU.7 (left) and ring bulge (right).

Partial confinement

As pointed out earlier, CCTU.7 was reinforced partially at both ends, each covering 80 mm of the length. The buckling bulge for CCTU.7 transitioned into the unreinforced/bare steel 15 mm from the CFRP's termination (Figure 5-15 (c)). Note that one end was affected by the plastic buckling, whereas the other end appeared unbuckled. Nonetheless, observing the internal surface of the unreinforced steel, small amplitude ripples were plainly manifested to the naked eye (see Figure 5-15 (d)).

Load displacement and strain behaviour

Figure 5-16 shows the end shortening of different bare and confined specimens versus the axial compression. As can be seen, the confined specimens generally showed a more ductile response in the post buckling regime. By the same token, Teng and Hu showed a similar response for their GFRP jacketed steel columns [141, 163]. It is remembered that the ductility is particularly significant in seismic design since a sound seismic performance depends, in part, upon ductility of structural elements.

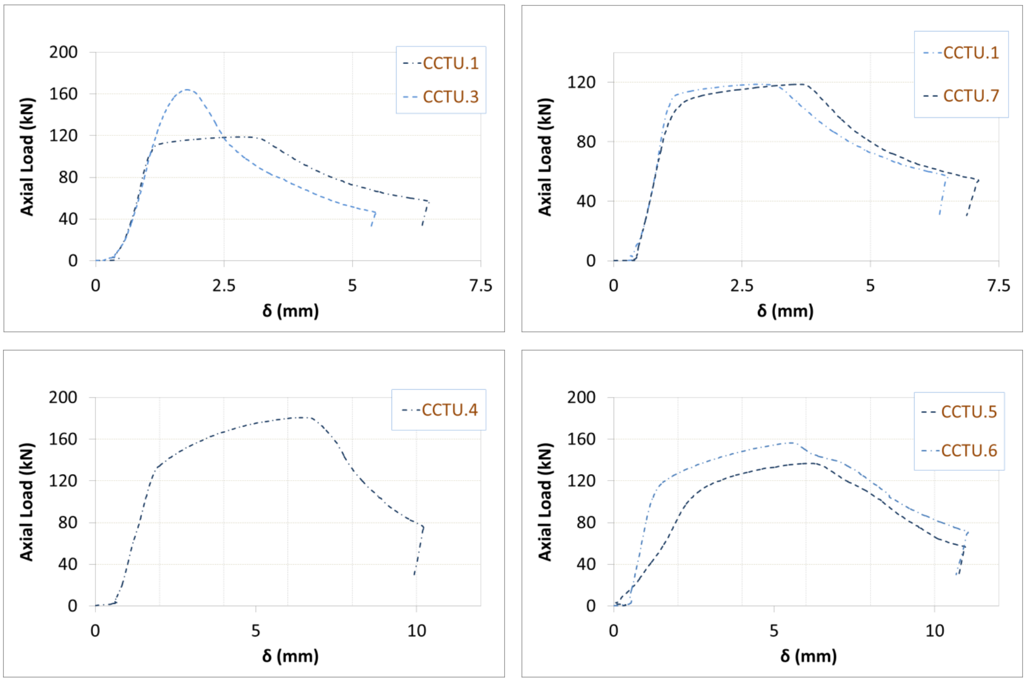

Figure 5-16: Load end-shortening response of different specimens.

It is quite obvious that CCTU.4 with hoop confinement possessed a greater ductility than CCTU.3 with longitudinal CFRP coverage, which suggests the usage of hoop confinement in these steel tubes is preferred. CCTU.5 and CCTU.6, however, largely showed a similar end shortening trend in terms of ductility, although the number of CFRP plies was different in these two specimens. A very similar trend is seen for the bare specimen of CCTU.1 and partially confined specimen CCTU.7. It was clear that CFRP significantly restricted locally confined areas of the CCTU.7 specimen such that the unreinforced part acted as a bare specimen. It is noteworthy that this response was only seen in the current short columns in which the global buckling was not dominant. For longer columns, however, a partial CFRP confinement is supposed to significantly decrease the free length of long columns. Consequently, the global (column) buckling mode would effectively be prevented or delayed in such columns.

Figure 5-17 shows the strain values of the bare specimen CCTU.1, in which SG.1 and SG.2 were longitudinally attached, each on a quarter of the circumference at 15 mm from the end. SG.3 was attached additionally circumferentially to the same place also at 15 mm from the end. It is plainly seen that SG.3, which was recording the circumferential strains, showed positive values, while SG.1 and SG.2 showed negative magnitudes indicating axial compressive strains. Positive values are believed to be attributed to the geometrical hoop expansion of the *elephant foot* buckling zone as SG.3 was applied exactly to the buckling area. Furthermore, a typical load strain response is seen through the curves demonstrating the plastic buckling of the current bare tubes.

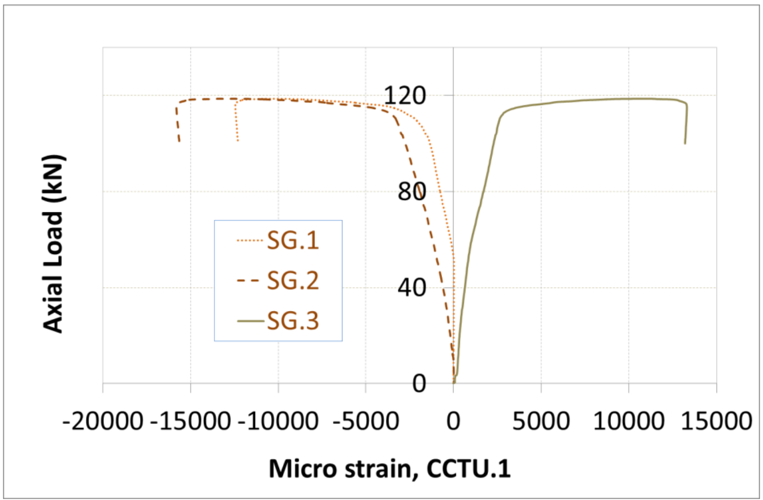

Figure 5-17: Strain magnitudes for the specimen CCTU.1.

5.3.4 Axial capacity and discussions

Axial capacity of the bare specimens

As presented earlier, a dimensionless buckling parameter (α) and a slenderness parameter (λ_e) are defined as α = *(E/f_y) (t/D_{tube})* and λ_e = *E/250α*. Also, section strength is defined herein as $P_{section}$. Note that f_y is the yield stress, E is the

Young's modulus, D_{tube} and t are outer nominal diameter and the wall thickness of the tubes respectively. The plastic buckling of the bare specimens are evaluated against the present theoretical equations which are found in Australian/New Zealand Standard AS/NZS4600 [96], and/or AISI Specification for the Design of Cold-formed Steel Structural Members [170]. As can be seen in Figure 5-18 (see Refs. [57, 59, 171]), P_{Ult} is quite close to $P_{section}$ for both bare specimens of CCTU.1 and CCTU.2 indicating that ultimate capacity was attained once the whole buckled section reached its full plastic capacity. Besides, it is evident that the points corresponding to CCTU.1 and CCTU.2 on Figure 5-18 lie within the results of the other studies [57, 59, 171], indicating the consistency of the present experiments.

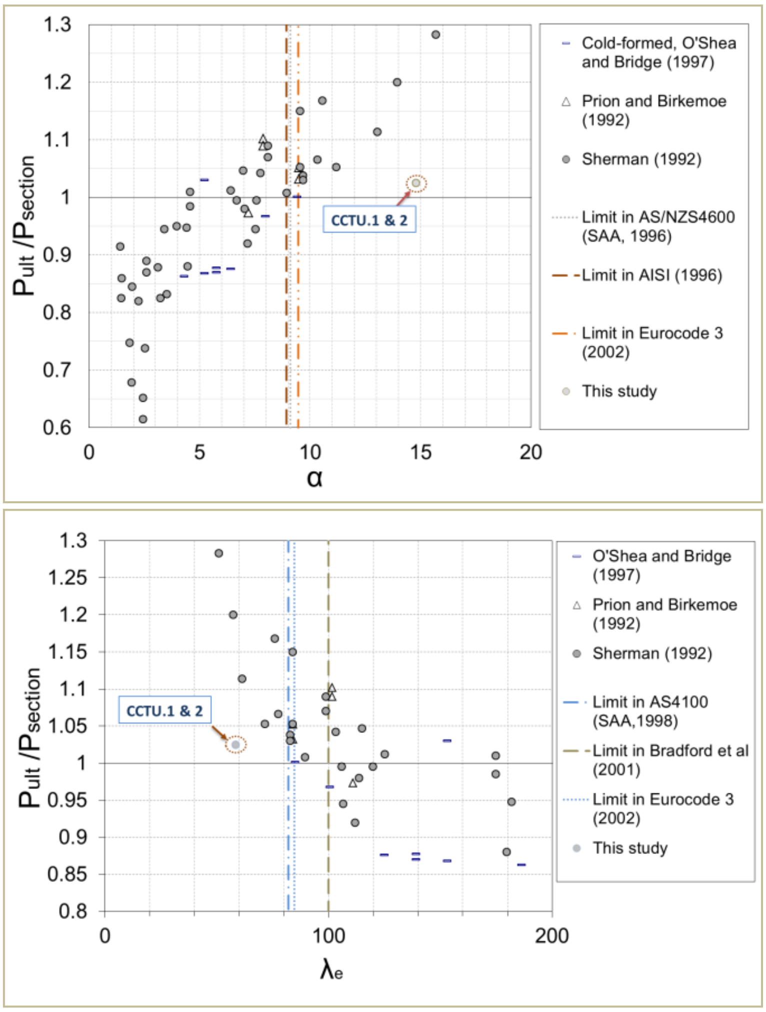

Figure 5-18: Comparison of the results with other studies and standards [57, 59, 171].

Previous experimental studies

This section evaluates the present experimental data against reported studies in the literature. Three experimental studies, as mentioned earlier, investigated confined CHS tubes, a summary of which are presented through Table 5-5 along with the features of the current specimens.

Haedir and Zhao tested six CFRP confined specimens [140], Teng and Hu three GFRP jacketed tubes [141, 163] and Nishino and Furukawa conducted experiments on three specimens with different layers of carbon fibre sheets [169]. Note that different methods of confinement as well as various *D/t* ratios were used in these different studies, as summarised in Table 5-5.

Table 5-5: Specimens used in this study and previous studies.

This study							
Specimen	CCTU.1	CCTU.2	CCTU.3	CCTU.4	CCTU.5	CCTU.6	CCTU.7
D/t	47.6	47.6	47.6	47.6	47.6	47.6	47.6
Confinement	N/A	N/A	3 Long.	3 Cir.	3 Cir.	2 Cir.	3 Cir. & partial
Haedir & Zhao (2011) [140]							
Specimen	CF-1A	CF-1B	CF-2A	CF-2B	CF-3A	CF-4A	
D/t	38	38	45	44	54	78	
Confinement	1 Cir. & 1 Long.	2 Cir. & 2 Long.	1 Long. & 1 Cir.	1 Long. & 1 Cir.	1 Cir. & 1 Long.	1 Cir. & 1 Long.	
Teng & Hu (2007) [141]							
Specimen	ST-F0	ST-F1	ST-F2	ST-F3			
D/t	39	40	39	39			
Confinement	N/A	1 Cir.	2 Cir.	3 Cir.			
Nishino & Furukawa (2004) [169]							
Specimen	NF2	NF3	NF4				
D/t	45	45	45				
Confinement	3 Cir.	5 Cir.	7 Cir.				

The capacity of different specimens is presented through Figure 5-19. Table 5-6 also lists the ultimate capacity and the percentage of the increase for various specimens if compared with the bare specimens. As tabulated, the axial capacity of the confined specimens was considerably different to the bare specimens. For the confined specimens with 300 mm length, the capacity enhancement was by and large similar to the results reported by Haedir and Zhao; bearing in mind that they used a combination of hoop and longitudinal confinement [140]. What's more, the capacity increased by around 32% for the specimen CCTU.6 indicating that two layers of circumferential confinement brought about approximately the same increase as specimens reported by

Haedir and Zhao, which comprised a combination of confinements and more layers. However, Teng and Hu found no significant increase in the capacity for their GFRP jacketed specimens [141, 163].

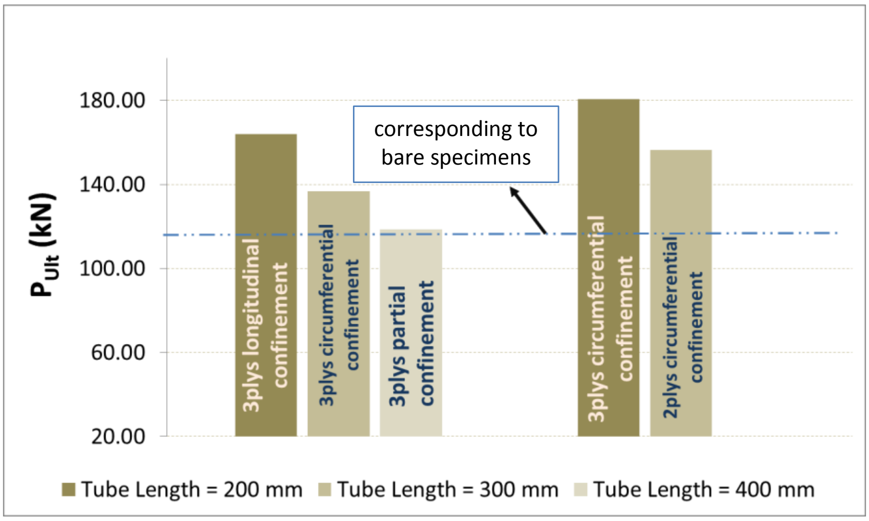

Figure 5-19: Ultimate capacity of the tubes with different confinements.

It is of interest that, a higher capacity rise was obtained for the specimens with 200 mm length in this study. The capacity grew by 52.6% for CCTU.4, which was fully confined with three plies of carbon fibre sheets in the circumferential direction. This rate of growth has not been reported by the other researches yet, as the greatest enhancement was reported for *CF-1B* in Ref. [140], where η was 1.34. The ratio η is defined as $\eta = P_{Ult}/P_{bare}$, where P_{Ult} is the ultimate load of specimens and P_{bare} is the ultimate capacity of unreinforced specimens (see Figure 5-20).

Table 5-6: Ultimate strength of bare and confined specimens.

Specimen	Ultimate load (kN)	Increase (percentage of average bare tube)
CCTU.1	118.7	–
CCTU.2	118.0	–
CCTU.3	164.0	38.6
CCTU.4	180.6	52.6
CCTU.5	136.6	15.5
CCTU.6	156.3	32.1
CCTU.7	118.6	0.25

Although it was believed that longitudinal confinement did not fully prevent the *elephant foot* buckling of the steel tube in CCTU.3, the capacity increase for this specimen was 38% in comparison with the bare specimen which is deemed rather a significant capacity rise. This increase took place due to the effect of length as it was obtained only for shorter specimens in this study.

Partial confinement

The increase in the axial capacity for the partially confined specimen (CCTU.7) was insignificant (0.25%). Thus, the partial confinement can only help reduce the unsupported effective free length in long columns and thereby the global buckling can be prevented. However, if plastic buckling governs the failure, i.e. the columns are not long enough for the global buckling, local CFRP can merely transition the failure position into the immediate unsupported location next to the confined area. As future work, it would be of interest to investigate the effect of varying the length of CFRP reinforcements on global buckling of partially confined long tubes.

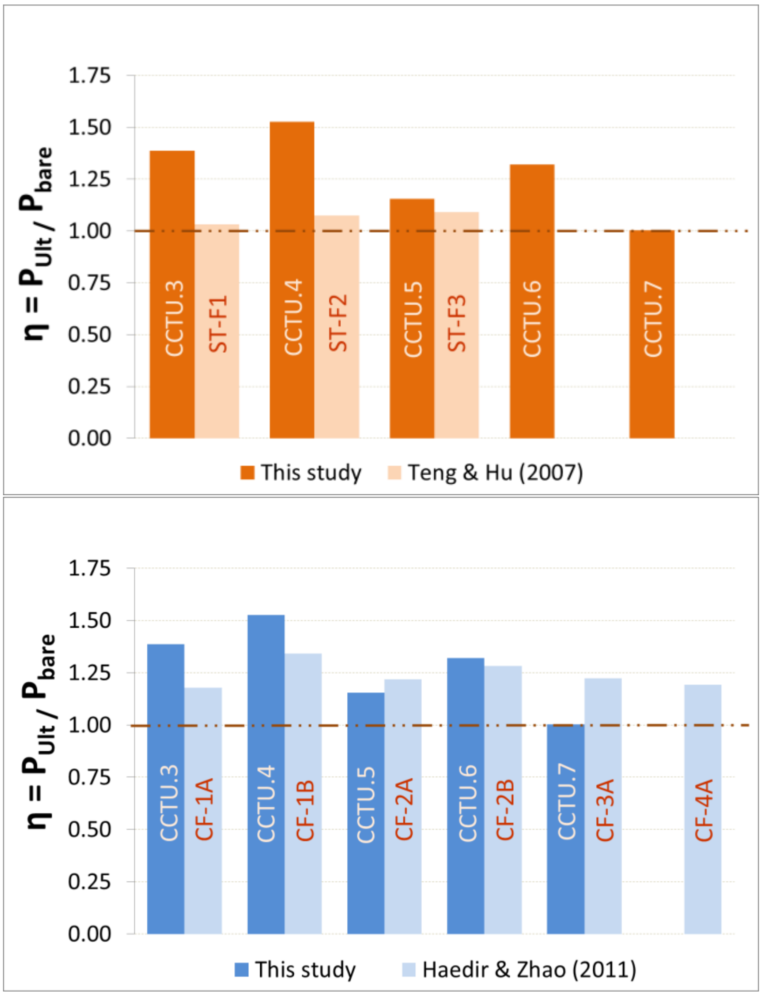

Figure 5-20: Comparison of the results by other studies [140, 141].

5.3.5 Summary and conclusions

This set of tests discusses CFRP confined circular tubes exposed to axial compression through an experimental study. In total 7 specimens were tested, wherein the first two were bare specimens and the remainder were confined with CFRP.

The specimens without any confinement experienced plastic buckling in the form of a bulge mainly near one end. The difference in the failure mode was attributed to different patterns of confinements in different confined specimens. The failure in CCTU.3 was outward buckling and the longitudinal CFRP fibre arrangement was insufficient to prevent the *elephant foot* buckling of the steel. Unlike CCTU.3 with longitudinal reinforcement, inward plastic buckling dominated the deformations in CCTU.4 with circumferential reinforcement. The failure for CCTU.6 was in large amplitude wrinkles close to the ends, while a local inward buckling was situated at the mid-length of the tube. The buckling bulge for the partially reinforced CCTU.7 specimen transitioned into unreinforced steel. It was clear that CFRP significantly restricted locally confined areas of this specimen.

Confined specimens generally showed a more ductile response in the post buckling regime. CCTU.4 with hoop confinement exhibited a greater ductility than CCTU.3 with longitudinal CFRP coverage, which suggests the preferred usage of hoop confinement in these steel tubes.

Axial capacity of the confined specimens was considerably affected. It is of interest that a higher capacity rise was obtained for the specimens with 200 mm length in this study. The capacity grew by 52.6% for CCTU.4, which was fully confined with three plies of carbon fibre sheets in the circumferential direction. Although longitudinal confinement did not fully prevent the *elephant foot* buckling of the steel tube in CCTU.3, the capacity increase for this specimen was 38%. This increase took place due to the effect of length as higher capacity growths were only obtained for shorter specimens in this study.

For the specimens with 300 mm length, the capacity enhancement was by and large similar to the results reported by Haedir and Zhao [140]. The capacity increased by around 32% for the specimen CCTU.6 indicating that two layers of circumferential confinement brought about approximately the same increase as specimens reported by Haedir and Zhao, which comprised a combination of confinements and more layers. Increase in the axial capacity was only 0.25%

for partially confined specimen (CCTU.7), which was insignificant. However, the partial confinement can reduce the unsupported effective free length in long columns and the global buckling can be prevented.

5.4 Timber filled CFRP jacketed circular steel tubes under axial compression

5.4.1 Introduction

With the advent of composite materials, growing industrial and research demands have been effectively stimulating researchers to come up with further innovative ideas on composite elements. Steel generally appears in composites as the basic material as its characteristic features – such as being light weight yet strong – allow engineers to have efficient designs. Notwithstanding, to minimise the weaknesses of the steel, e.g. buckling, designers often need recourse to different types of stiffeners and/or composite materials.

In the literature, various types of FRP are utilised to rectify and improve the load bearing capacity of the steel structures. Composite materials to rehabilitate metallic structures were thoroughly discussed by Hollaway and Cadei [162]. The benefits of employing FRP composites in comparison with steel plate bonding were discussed in this reference. Buckling behaviour of steel tubes confined by FRP composites were examined by Teng and Hu [163]. Further ductility as a consequence of the mentioned confinement was obtained in this research. A state of art review on FRP reinforced steel structures was carried out by Zhao and Zhang [164]. A few major aspects of the work, such as reinforcing steel hollow section, bonding between FRP and steel, and fatigue crack development in composite members, were exhaustively discussed in this paper.

Miller et al. examined steel girders with CFRP reinforcement [166]. It was found that based on several experimental programs referred to in this reference, CFRP plates can be effectively used to strengthen steel girders. Furthermore, Haedir and Zhao [140] and Teng and Y. Hu [141] investigated the effect of CFRP and GFRP confinement of steel CHS members under compression. The former research – wherein *CFRP* was used to make a composite element – demonstrated a considerable increase of the ultimate capacity, while the latter in which the *GFRP* was used, demonstrated a remarkable enhance of the ductility with insignificant capacity increases.

Over the past decade on the other hand, widespread usage of concrete filled tubes are found playing a leading role to make modern composite elements. Recent advances, as a few instances, were made by Teng et al. [33], Yang and Han [29, 30], Tao et al. [32], Dundu [28], Chitawadagi et al. [31]. Significant increase in the capacity was obtained for concrete filled tubes relative to the bare steel tubes, which was attributable to load carrying capacity of the concrete and steel respectively and, in turn, the interaction of the two materials was also of importance. Moreover, the other types of fillers for CHS tubes have been utilised as well in different researches such as polyethylene, different foams e.g. aluminium foam, mortar and so forth [172-174].

A CHS tube element with a moderate *D/t* ratio – where *D* is the diameter and *t* is the thickness – generally buckles in an *elephant foot* mode of buckling. In previous researches where tubes were confined with sufficient plies of different types of FRP outward buckling (*elephant foot* buckling) was fully arrested; as a result inward plastic buckling governed the failure. In this section of the thesis, an idea is presented in which both inward and outward buckling are prevented and/or delayed so that the ultimate capacity increases. To this end, the current composite element was designed comprising a CHS member, which was restricted inside by filling with timber and reinforced outside by confining with CFRP. Thus, the maximum capacity of the timber as well as the steel CHS member was fully employed through the composite action to gain further capacity. Different specimens with various geometric features and material combinations were examined. In this section, the failure of the present specimens, the capacity rise and load-displacement and load-strain responses were thoroughly discussed. Furthermore, this section compares the proposed composite with previous studies and equivalent steel sections and includes a summary of practical benefits of the new composite.

5.4.2 Experiments and instrumentation

Test rig

The testing apparatus was the Avery Universal Hydraulic Testing machine as described earlier and illustrated in Figure 5-1. As is seen, the machine consisted of two strong columns with many adjustment holes, along with two vertical shafts in order for adjustment of the top plate. The bottom plate, however, was installed to a vertically moving deck which was constructed on a rigid floor. A Linear Variable Differential Transformer (LVDT) was used to record the axial shortening of the specimens. A number of strain gauges were attached to the critical spots on the specimens, the layout of which will be presented in the coming sections. All data were recorded via stand-alone measurement data acquisition, Quantum X MX1615, HBM digital data recorder. A professional tool for measurement engineers "Catman" software was utilised to process and record the data.

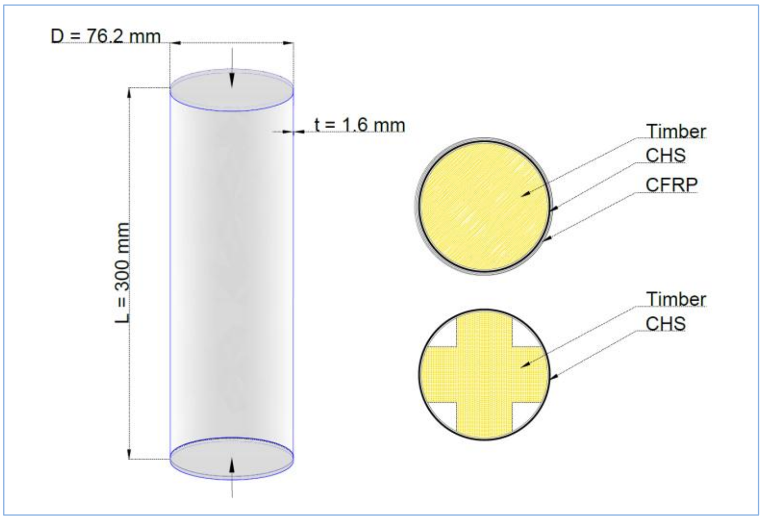

Figure 5-21: Details of the timber filled specimens and geometry of the tubes.

Specimens and preparation

(i) Materials: CHS tubes were provided as commercially available cold formed mild steel sections, the geometrical features of which are presented in Figure 5-21 and Table 5-7 and Table 5-8. Material properties, i.e. yield and ultimate stresses, and Young's modulus of the steel used for making the specimens were obtained using tensile tests (see Table 5-2). Carbon fibre sheets were SikaWrap Hex-230C supplied in a roll by Sika Australia Pty. Ltd and Sikadur®-330 thixotropic adhesive was used as epoxy resin. The employed timber was machine graded structural Radiata Pine with the stress grade of *MGP10*. Properties can be obtained based on the information provided by AS 1720.1 [153], and are listed in Table 5-2.

(ii) Specimen preparation: in order for the confinement of the specimens the surface of the CHS tubes were thoroughly cleaned, sandpapered and degreased with the recommended chemical solvents so that the steel surface was cleared of any particles or chemicals contaminating the external body of the tubes. Carbon fibre sheets were cut into desirable lengths. The two parts of the epoxy resin were mixed in accordance with its instruction manual in a ratio of one to four (1:4).

Table 5-7: Geometry of CHS specimens.

t (mm)	R (mm)	r (mm)	L (mm)
1.6	38.1	36.5	300

The steel surface was uniformly and smoothly smeared with the adhesive using an appropriate brush and the carbon fibre sheets were wrapped around the tubes, which were already placed on a very clean disposable plastic sheet so as to perform the confinement. Whilst confining, meticulous attention was paid to reach a uniform and reliable bond between the steel and CFRP and between different layers of CFRP as well. The curing process was followed thereafter, as instructed by the manufacturer. Different specimens are shown in Figure 5-22.

Figure 5-22: Different specimens, left to right: CFRP confined timber filled specimen, cruciform and fully timber filled CHSs and cruciform, and machined cruciform and solid timbers before insertion.

For the preparation of cylindrical timber blocks, a lathe was used to precisely machine the timber such that the external diameter tightly fit into the inside of the CHS. A cruciform timber as an alternative infill was in turn made in two parts, as is seen in Figure 5-22 and Figure 5-23. The two timber elements (items 1 and 2 in Figure 5-23) were fabricated such that two identical slots were accurately cut at the mid-width of the timbers by a proper timber cutting machine, up to the mid-length of each timber. Afterwards, the two parts were inserted and fit into each other so that a complete cruciform section was achieved. Since machining of both circular and cruciform timbers was quite accurate, insertion of the timbers into the CHS was carried out by placing the timber on one edge of CHS and inserting the timber applying a moderate impact with a hammer.

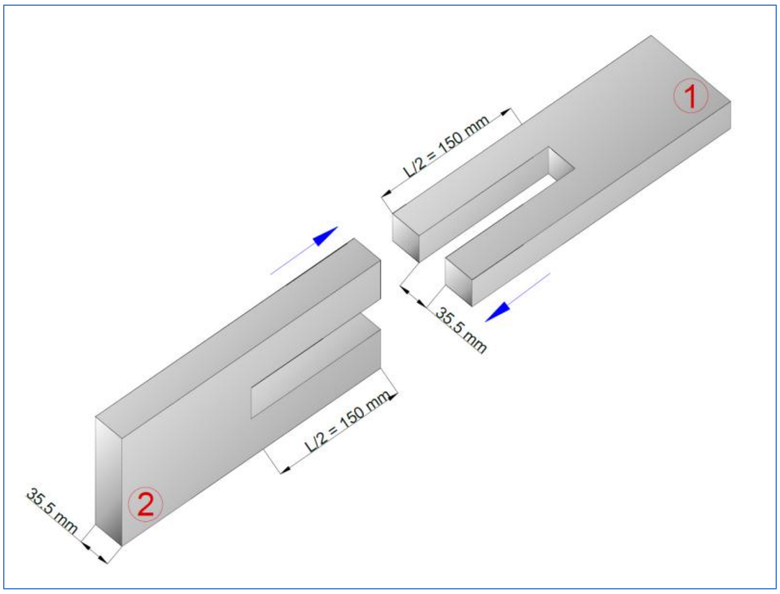

Figure 5-23: Schematic illustration of fabrication of cruciform timber.

Table 5-8: Specifications of specimens.

Specimen	Specimen features
TIMC.1	Bare Timber
TIMC.2	Bare Steel
TIMC.3	Steel confined with 3 layers of CFRP
TIMC.4	Timber filled steel confined with 3 layers of CFRP
TIMC.5	Timber filled steel with NO CFRP
TIMC.6	Cruciform timber filled steel with NO CFRP

5.4.3 Test observations and failure mechanisms

Bare and confined specimens

Figure 5-24 shows the failure of the bare timber specimen (TIMC.1). Failure occurred in the form of a diagonal shear crack at about 1/4 of the height at 45° to the specimen axis. Failure of the CHS specimen confined by 3 layers of CFRP, i.e. TIMC.3, is seen in Figure 5-25, in which inward buckling at the end was dominant. Deformation was detected in two tiers such that inward deformation in the form of a circumferential wave was seen at the top tier, while a few dent shape depressions were observed at the lower tier. It was clear that the CFRP worked in tension to restrain outward buckling, resulting in the

CFRP's rupture and failure. It should be mentioned that failure for TIMC.2 (bare steel) was in an *elephant foot* mode typical of plastic buckling, as expected given its D/t ratio. As such, it is clear that three plies of CFRP fully reinforced the CHS tube against the *elephant foot* buckling so that the inward deformations governed the failure.

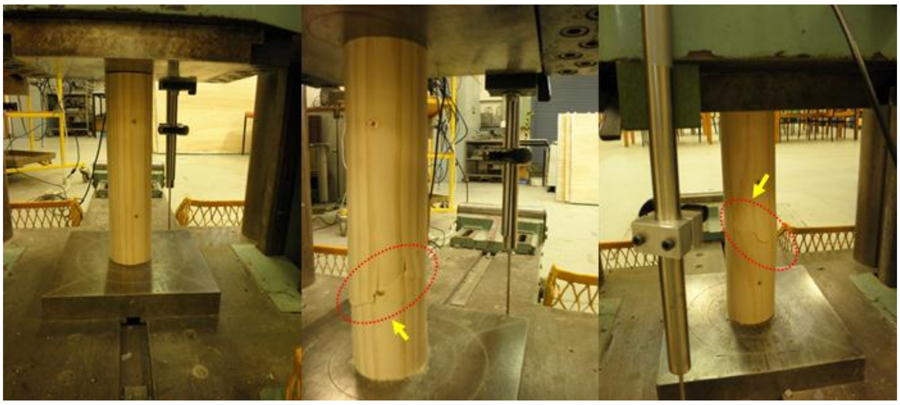

Figure 5-24: Bare timber specimen before and after failure (TIMC.1).

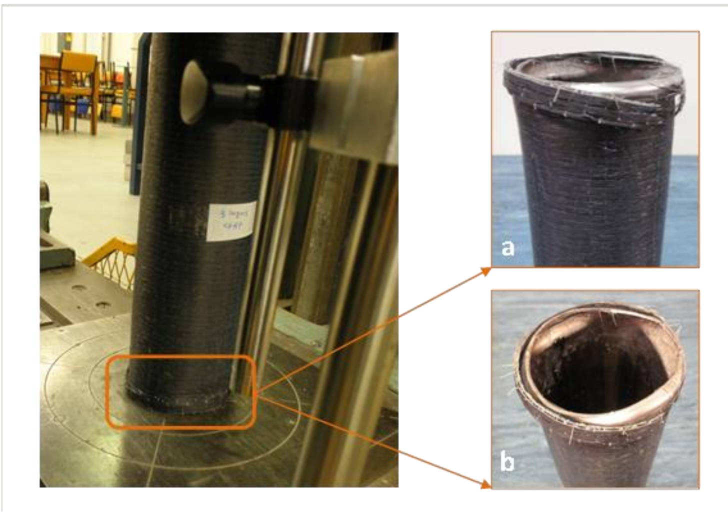

Figure 5-25: Failure of a CHS specimen confined by 3 layers of CFRP (TIMC.3): (a) failure of CFRP and (b) inward buckling of the tube.

Timber filled specimens

TIMC.4 and its failure mode are seen in Figure 5-26. It was quite obvious that failure is by column buckling, accompanied by local buckling at the hinge points located at around 1/3 height of the specimen, and to a lesser extent at the ends. At these hinges inward plastic deformations dominated the failure coupled with crushing of the timber inside the CHS member.

TIMC.5 failed with the steel buckling outwards, manifest as two semi *elephant foot* buckling waves, one close to the end and the other on the opposite side of the tube at about a third of the length of the specimen (see Figure 5-27). In this respect it has features of the column buckling observed in specimen TIMC.4, but the local buckling is more obvious and probably governs the load. Note that the area at and/or in between the two buckling waves is believed to be the failure location of the timber as well. TIMC.6, however, buckled exactly like the bare specimen with a bulge close to the one end of the specimen (Figure 5-28).

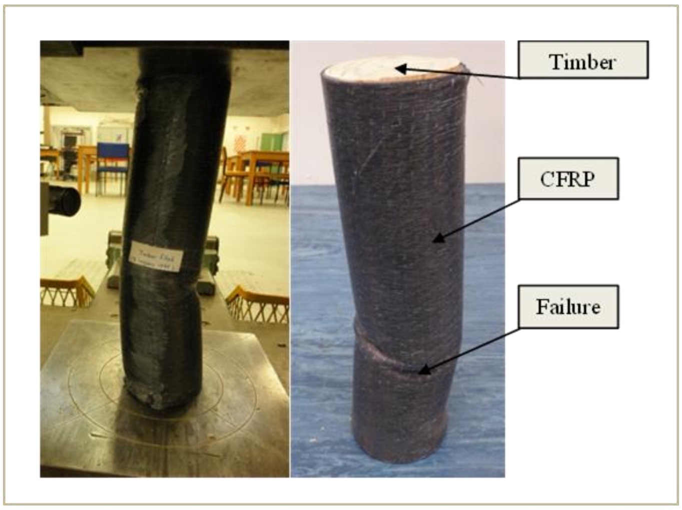

Figure 5-26: Timber filled CFRP confined specimen (TIMC.4) after failure.

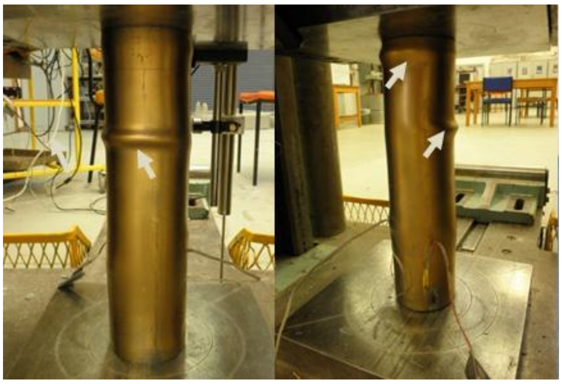

Figure 5-27: Timber filled specimen (TIMC.5) after failure.

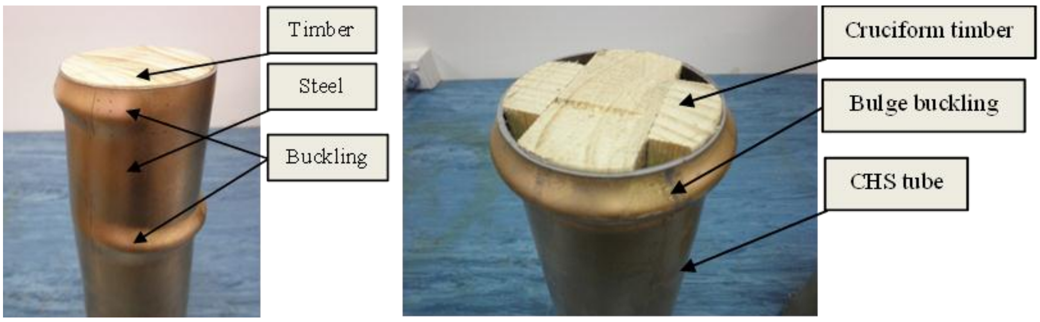

Figure 5-28: Fully timber filled specimen TIMC.5 (left), and cruciform timber filled specimen TIMC.6 (right) after failure.

5.4.4 Displacement and strain response

End shortening behaviour

End shortening curves for the bare timber specimen, bare steel and timber filled steel without CFRP confinement are shown in Figure 5-29. In addition, the axial load displacement trend for different timber filled specimens is presented through Figure 5-30. It can be seen that TIMC.3 showed more ductile behaviour compared with TIMC.2 indicating that the effect of CFRP confinement was to extend or delay the onset of buckling. This behaviour was also reported by Teng and Hu [141], wherein glass fibre reinforced tubes showed greater ductility than their bare counterparts. It should be pointed out that the requirement for ductility is quite critical especially when seismic design is undertaken.

Plastic response of TIMC.1 and TIMC.5, i.e. bare timber and timber filled CHS steel member, can be compared in Figure 5-29 (right). It appears that TIMC.5 experienced greater plastic elongation compared to TIMC.1. Although the curve had a slight slope during elongation, the curve essentially displayed a plateau after attaining the peak load. For TIMC.1, however, the load decreased after the maximum load was obtained. It is believed that the mentioned plastic elongation in TIMC.5 is attributed to the structural interaction between the timber and steel in this composite element. This is because both TIMC.1 and TIMC.2 experienced a very small elongation at the peak load and the load gradually dropped afterwards. However, when both materials were combined, i.e. timber was filled inside the CHS, a considerable plastic elongation took place in comparison with the bare specimens.

The same phenomenon is verified considering the end shortening behaviour of TIMC.6 (see Figure 5-30). TIMC.6, albeit slightly different, behaved similarly in terms of plastic response to TIMC.5. The small difference was due to the reduction of material that a cruciform timber has in comparison with the cylindrical solid timber. Figure 5-30 also compares axial displacement of TIMC.4 and TIMC.5, the latter of which has no CFRP. The effect of CFRP confinement is highlighted by these two graphs. TIMC.4 showed a much more ductile response than its equivalent specimen without CFRP. In the linear region both curves behaved exactly the same implying that CFRP had no stiffening effect when loading was applied in the elastic region. However, with the onset of the slight nonlinear stress-strain behaviour in sample TIMC.5 a difference appeared between the curves. In general, though, TIMC.4 showed a more ductile response. It is noteworthy that for concrete filled CHS tubes, in contrast to the present combinations, the ductility of the composite tubes was either the same or less than the bare steel counterparts, as reported in Ref. [175] for instance.

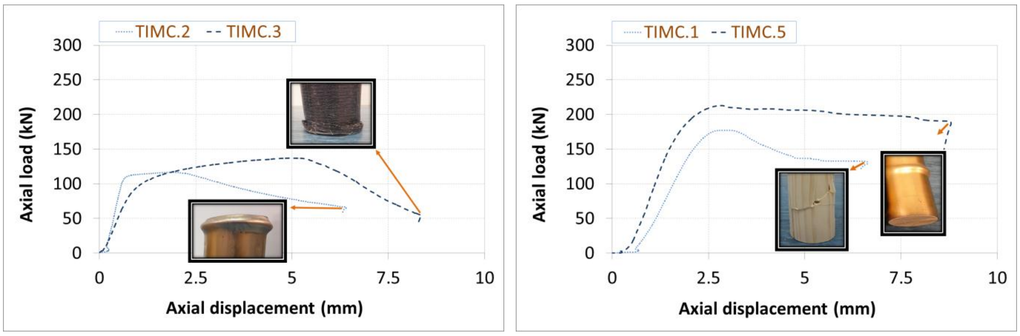

Figure 5-29: End shortening curves for specimens TIMC.1, TIMC.2, TIMC.3 and TIMC.5.

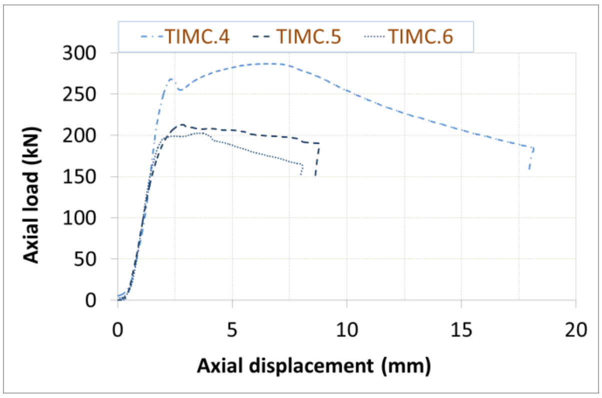

Figure 5-30: Axial load displacement for different timber filled specimens.

Strain response

Layout of the strain gauges SG1 through SG.3 is shown in Figure 5-31, in which SG3 recorded the circumferential strains, whereas the other two reported the axial strains. Three points 15 mm from the end were adopted for strain gauges since this area was the most vulnerable to the bulge shape *elephant foot* buckling. Figure 5-32 gives the strain versus the axial compression load for three of the specimens. For TIMC.5 and TIMC.6, a typical load-strain behaviour was obtained in which plastic elongation took place and reached a plateau once the peak load was attained. The magnitudes of the strains in TIMC.5 and TIMC.6 both approaching the peak load followed by a plastic plateau were similar, indicating a consistent load strain response in cylindrical and cruciform filled tubes. In TIMC.2, however, the magnitude of axial strains was lower than TIMC.5 and TIMC.6. Positive values were obtained for the circumferential strain gauge (SG3) attached to TIMC.2 signifying the hoop enlargement of the circumference at the location of the bulge buckling, i.e. *elephant foot*.

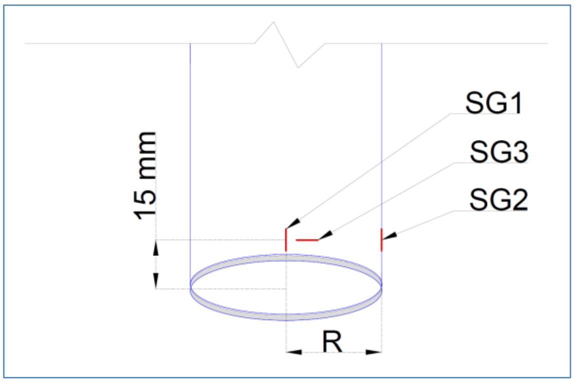

Figure 5-31: Layout of the utilised strain gauges.

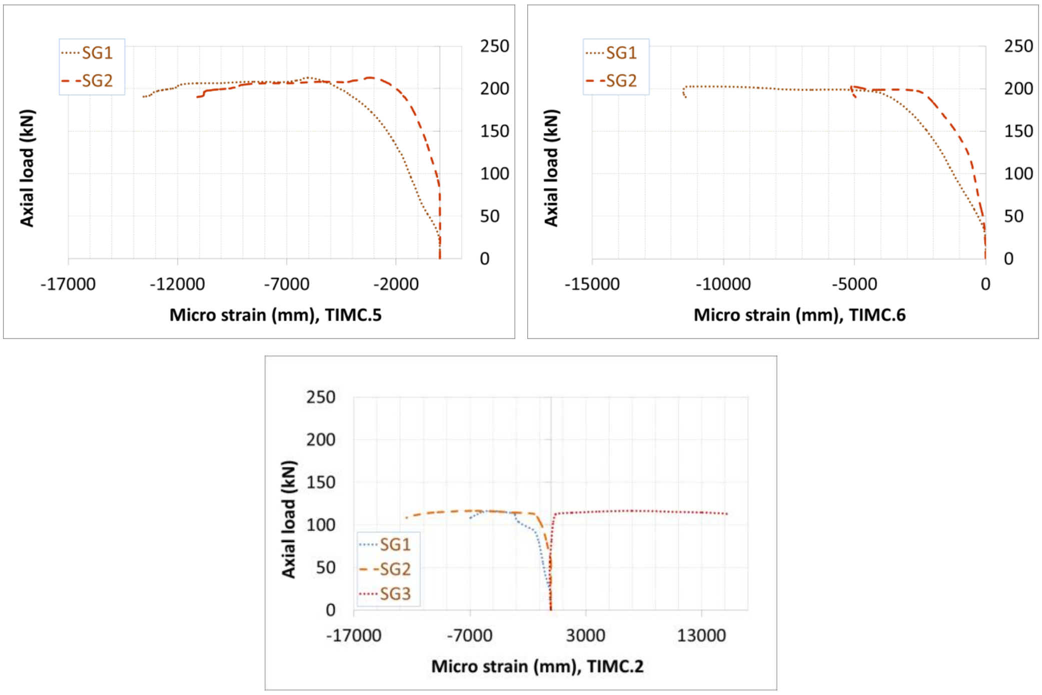

Figure 5-32: Strain values for three different unconfined specimens.

5.4.5 Ultimate capacity

Timber-filled and CFRP-jacketed specimens

Load carrying capacity of the present specimens with different specifications is given in Figure 5-33. It is quite evident that TIMC.4, which included a timber filled core and is confined with three layers of CFRP, had the greatest ultimate axial load of around 287 kN. Thus, the composite materials (timber and CFRP) increased the capacity relative to the bare specimen by around 146%, which was remarkable. TIMC.5 and TIMC.6, the timber filled specimens (without CFRP confinement) had the second highest axial capacity with approximately 213 kN and 203 kN, or around 83% and 74% increase (Figure 5-34). The difference between the capacity of TIMC.5 and TIMC.6 was insignificantly at around 5%, implying that the cruciform timber-filled section brought about approximately the same increase as the cylindrical timber filled specimen.

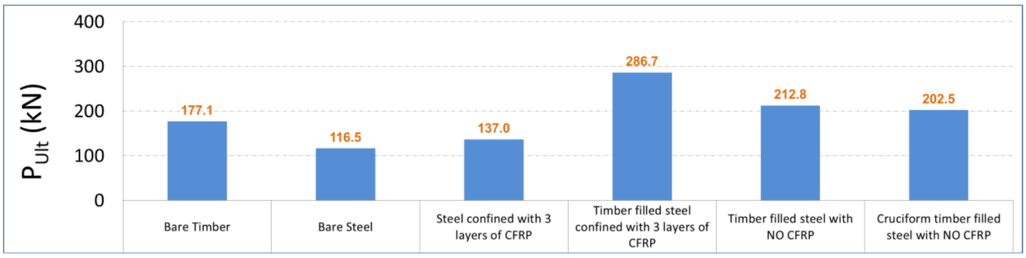

Figure 5-33: Ultimate capacity of different specimens with various specifications.

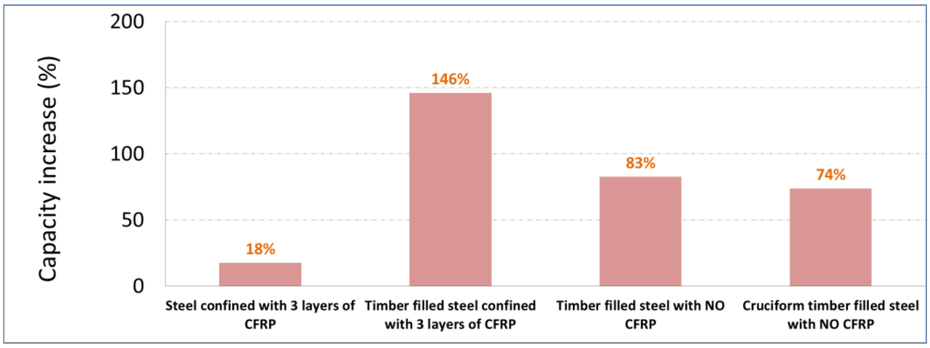

Figure 5-34: Capacity increase for different timber filled and/or confined specimens relative to the bare steel specimen.

The CHS tube confined with three plies of CFRP experienced a capacity enhancement of around 18% if compared with TIMC.2, the bare steel specimen. This increase is attributed to the fact that the bulge buckling at the end of the CHS specimen was fully prevented by the CFRP so that the steel had to buckle inward. This phenomenon was also reported by the previously mentioned study conducted by Haedir and Zhao [140], who reported an increase of 34% in the ultimate load.

5.4.6 Other studies and further evaluations

5.4.6.1 *Weight versus capacity: current and concrete filled specimens*

It is worth mentioning that both timber filled and concrete filled tubes may be used in different applications. Nevertheless, timber filled tubes increased the load carrying capacity while maintaining a light weight. Figure 5-35 shows the total weight of different specimens (W_{co}) measured after specimen preparation and before testing. As can be seen and expected, the timber filled CFRP confined specimen (TIMC.4) accounted for the highest weight. TIMC.5 was slightly lighter than TIMC.4, due to the mass of the three layers of confining CFRP in TIMC.4, whilst TIMC.4 was approximately 18% heavier than the specimen filled with the cruciform timber. Figure 5-35 also gives W_{co}/W_{tu} wherein W_{tu} denotes the weight of the bare steel specimen. This ratio was 1.86 for the strongest specimen, i.e. TIMC.4, while the magnitude of W_{co}/W_{tu} was around 1.78 and 1.58 for the other timber filled specimens (TIMC.5 and TIMC.6) respectively.

It is fitting to mention that although different types of concrete can possess various weight values, the equivalent values for a *typical concrete* filled CHS member can be calculated, which helps provide a significant insight if compared with the current timber infill. The internal volume of the current CHS tubes is 0.0013 m^3, so for a concrete with a normal density of 2400 kg/m^3, the equivalent weight to fill the current CHS is 3013.4 g, which is around five times more than the weight of an equivalent timber 634 g.

On the other hand, although different types of concretes have different strengths, an illustration can help draw a meaningful comparison. Ren et al. defined a parameter as Eq. (5.2), viz. strength index (*SI*), in which N_{ue} was the measured strength of the specimens at the peak load and N_{ur} was the strength of a *reference specimen* [175]. It was pointed out that use of a concrete infill increased *SI* from 169% to 286% for different shapes of tube specimens. In particular the *SI* was enhanced by 226.8% for a CHS tube. In the present experiments the capacity was increased by 146% for the TIMC.4 by the addition of the timber infill and CFRP, but with substantially less increase in weight than a concrete infill.

$$SI = \frac{N_{ue}}{N_{ur}} \tag{5.2}$$

To say the least, the use of timber-filled specimens deserves to be of interest to researchers and designers if proper equipment is proposed and developed for fabrication of such elements, as it exhibits very good capacity to weight ratios.

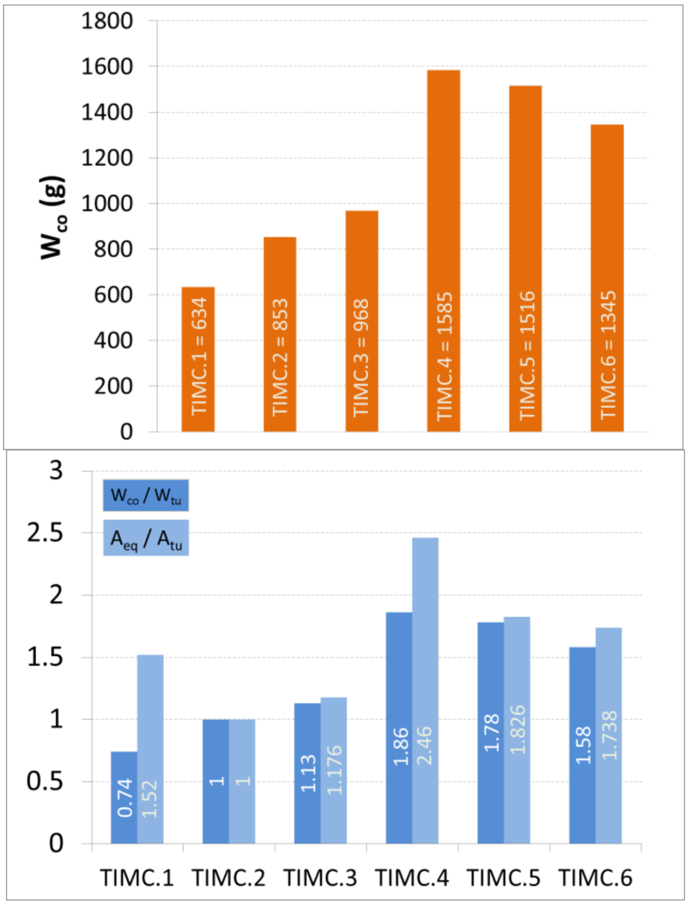

Figure 5-35: Comparative quantifying the parameters: W_{co}, W_{co}/W_{tu} and A_{eq}/A_{tu}.

5.4.6.2 *Equivalent steel sections*

The ratio A_{eq}/A_{tu} was also plotted in Figure 5-35 alongside the weight ratio, in which A_{eq} stands for the equivalent cross section area of a CHS tube and A_{tu} is the cross section area of the current CHS specimens (with $t = 1.6$ mm). In order to calculate A_{eq}, it is assumed that the same strength is obtained for each specimen, but *merely steel* is used to make an equivalent specimen. To this end, the outer diameter of the current steel tubes is assumed constant and the thickness of the tube only changes, in which the tube is supposed thicker.

Based on the mentioned assumptions, the equivalent sections were calculated – using $\sigma=P/A$ in which P is the axial load and A is the area of the cross section – for all specimens and the results are presented in Figure 5-35. It is quite clear that TIMC.4 had the highest capacity, with A_{eq}/A_{tu} of 2.46 indicating that the steel section of equivalent strength possessed a weight of almost 2.5 times the bare specimen TIMC.2, compared with an actual weight ratio of only 1.86 due to the addition of the CFRP and timber.

The same comparisons can be drawn for the other specimens through Figure 5-35, whereby one may conclude that timber infill and a sufficient confinement for the current CHS members are significantly effective and hence, undoubtedly worthwhile of further consideration.

5.4.6.3 *Practical benefits of the new composite*

It is believed that the benefits of the current composite element considerably outweigh the challenges of the fabrication, especially if a proper fabrication process is proposed and subsequently developed. The most important advantages of the present timber filled elements can be summarised as: (i) a lightweight element yet strong, relative to equivalent steel to provide the same strength, (ii) low cost of timber in comparison with the equivalent materials such as steel or concrete, (iii) connection possibility of different elements through welding due to the existence of steel, whereas for wood constructions there is no such capability, (iv) protecting the timber from decay as timber is fully covered by the steel material, (v) providing better resistance in fire as this combination of materials can protect the structures from collapse based on timber's ability to maintain its strength at high temperatures due to the protection provided by a thin charred surface layer, compared with pure steel constructions, which are quite vulnerable to the fire collapse in a relatively short time, and (vi) optimal usage of space as for the pure steel elements the internal space of the tubes remains inaccessible and accordingly useless, while using the present composite element brings about a significant increase in capacity with no more space occupation as the timber is placed inside the tubes.

5.4.7 Summary and conclusions

In this study, new composite elements comprising steel cylindrical hollow sections, solid timber infill and CFRP confinements were tested under pure axial compression. The summary of the key findings are as follows:

For the bare timber specimen, failure occurred in the form of a diagonal crack at about 1/4 of the height on a plane inclined at 45˚. For bare steel and cruciform timber filled specimens (TIMC.2 and TIMC.5), failure was by *elephant foot* mode of plastic buckling. Inward plastic buckling was dominant for the CHS specimen confined by 3 layers of CFRP and TIMC.4 as well.

TIMC.3 showed more ductile behaviour if compared with TIMC.2. Moreover, TIMC.4 showed a much higher ductile response compared with its equivalent specimen without CFRP, all indicating the effect of CFRP confinement which caused more ductility for the current specimens.

The CHS tube confined with three plies of CFRP experienced a capacity enhancement of around 18% compared with the bare steel. The specimen TIMC.4 including a timber filled core and confined with three layers of CFRP comprised the greatest ultimate axial load increased up to around 287 kN. Thus, the composite materials (timber and CFRP) improved the capacity of the bare specimen by around 146%, which was remarkable. TIMC.5 and TIMC.6, the timber filled specimens but without CFRP confinement, accounted for the second highest axial capacity with approximately 213 kN and 203 kN, or around 83% and 74% increase respectively.

The ratio W_{co}/W_{tu} was 1.86 for the strongest specimen (TIMC.4), while this ratio was around 1.78 and 1.58 for the other timber filled specimens (TIMC.5 and TIMC.6) respectively. The weight of concrete with the density of 2400 kg/m^3 to fill the current CHS equals 3013 g, which is far greater than the weight of an equivalent timber 634 g (around five times more).

Strength index for a concrete filled CHS tubes is reported in Ref. [175] to enhance by 227%, while for TIMC.4 specimen in this study the capacity grew around 146%. For TIMC.4 with the highest capacity, A_{eq}/A_{tu} was 2.46 indicating that the equivalent plain tube section possessed the weight of almost 2.5 times that of the bare specimen TIMC.2. When CFRP and timber take part alongside the steel, the weight of the composite element only increases 86%, yet they bring about the same capacity increase as the equivalent specimen.

In a nutshell, the use of timber-filled specimens can potentially gain the attentions of the researchers and designers if proper equipment is proposed and developed for fabrication of such elements. This is, in fact, concluded in the light of a higher weight increase of the equivalent concrete filled tubes in comparison with the present specimens and also the rate of the capacity enhancement for each case.

5.5 Rectangular steel tubes with timber infill and CFRP confinement under compression

5.5.1 Introduction

RHS sections as structural elements are extensively seen in the most fields of various industries particularly different types of structural applications. As an example, these elements take part as columns and beams in the building industry, in particular when these members are required to carry loads in multiple directions. Notwithstanding, the axial load capacity as a basic loading has, for the most part, gained great interest of investigators stimulating them to examine the structural response of these elements.

A vast volume of research exists in the literatures on tubular elements with different materials as an infill. Kavi et al. investigated foam filled aluminium tubes under axial loading [176]. It was found that foam filling resulted in higher energy absorption of the filled tubes relative to the sum of energy absorption for the sole foam and the tube individually. Aktay et al. studied quasi-static axial crushing of extruded polystyrene foam-filled thin-walled aluminium tubes through experimental and numerical analyses and the energy absorption of empty and filled specimens were discussed [177]. Mantena and Mann studied circular steel tubes filled with high-density structural foams and the effect of density was investigated on the structural behaviour of such structures [178].

Over the past two decades, on the other hand, the usage of different types of fibre reinforced polymer (FRP) as a reinforcing composite has been developed. As some instances, Teng and Hu [163], Seica et al. [165], Zhao and Zhang [164], Miller et al, Ghanbari Ghazijahani et al. [166, 179], Haedir et al. [168], Rotter [161], Hollaway and Cadei [162] evaluated various steel structures using different FRP reinforcements. It is noted that the enhancement of the capacity was observed to different extents through the mentioned researches for various structural elements. Ellobody studied the buckling behaviour of stiffened and unstiffened slender square and rectangular sections under axial compression by a finite element analysis [180]. The column strengths as well as failure modes were thoroughly discussed in this study. Furthermore, the predicted column strengths using a parametric study were evaluated against the strengths presented in design codes. For the unstiffened tubes the codes were found to be conservative.

Structural behaviour of axially compressed concrete filled RHS tubes were investigate by Liu and Gho [181]. A fibre model was proposed and developed in this study in order to examine the behaviour of the test specimens under compression. RHS tubes with concrete infill as stub columns were investigated by Han, where the effect of constraining factor and width ratio were evaluated. Axial and bending behaviour of high strength square concrete-filled steel tubes were studied by Varma et at. [182]. The inelastic response of steel tubes with a concrete infill as well as the local buckling of such steel tubes along with crushing of the concrete were discussed. In addition to the mentioned papers, Tao et al. [32], Yang and Han [29, 30], Dundu [28], Teng et al. [33] and Chitawadagi et al. [31] made different contributions through different papers as regards the concrete filled tubes and different aspects of such concrete filled structures were investigated through these references.

Unlike the mentioned studies and based on the conducted literature review, the structural response of a composite consisting of timber, steel and CFRP has not been reported yet. As such, this study focuses on this subject, in which several experimental models with varying materials – including plain specimens, timber filled specimens, and CFRP confined tubes – were tested to the failure. The plastic response, failure modes as well as the axial capacity of the specimens were studied and comprehensive discussions were conducted through which the effect of each material in the new composite element was described.

5.5.2 Experimental program

Test set up

All tests were conducted using the Avery machine as shown in Figure 5-1. A digital LVDT was installed perpendicular to the bottom plate to measure the axial shortening of the specimens throughout the tests. Strain gauges were employed to obtain the strain data of the specimens. The Avery machine was connected to a data acquisition system, whereby all required data was processed and filed so that the required data was subsequently readily accessible.

Table 5-9: Different specimens and specifications.

Specimen	Description
RTYU.1	Reference specimen 1
RTYU.2	Reference specimen 2
RTYU.3	Reference specimen 3
RTYU.4	Timber filled RHS
RTYU.5	Timber filled RHS, 2 layers CFRP
RTYU.6	Timber filled RHS, 3 layers CFRP
RTYU.7	Timber filled RHS, 2 layers full and a layer partial CFRP
RTYU.8	Solid timber

Specimens

In this set of the tests different materials – steel, CFRP sheets, epoxy and timber – were all readily commercially available to be used in this study. The RHS sections with the geometry as given in Figure 5-36 and Table 5-9 were cut into the desired length such that the end edges of the RHS section were precisely parallel to ensure that the axial load was applied uniformly. The timbers to be inserted into the RHS sections were accurately cut in length. All four side surfaces of the timber infills were machined by a *Planer Thicknesser* in order that the timbers were capable of being fit inside the RHS sections with a modest impact of a rubber hammer.

The utilised CFRP sheets were *SikaWrap Hex-230C* supplied in rolls by *Sika Australia Pty. Ltd*, which were subsequently cut into suitable lengths to be used in different specimens. Twin solvent free *Sikadur®-330*, thixotropic epoxy adhesive was employed in order to make the CFRP layers over the RHS members.

Prior to attaching the CFRP the steel's surface was scrupulously sandpapered and degreased such that the contaminating particles were fully removed. The aforementioned epoxy was prepared in accordance with the instructed ratio, mixed and applied to the first surface of the steel by means of a proper brush. The carbon fibre sheets were thereafter placed on the epoxy and rolled over the body of the steel by sufficient pressing of the hand over the member in a way that the flat surface of the workbench made the epoxy and the carbon fibre a reliable composite. The epoxy was fully absorbed into the gaps inherently existing between the carbon fibres.

(a)
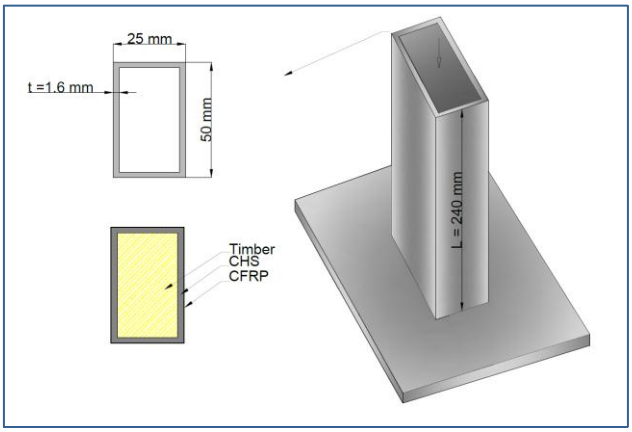

(b)


Figure 5-36: (a) Geometric specification of the specimens, (b) different specimens: bare, timber filled and CFRP confined.

Upon completion of the first layer, the epoxy was applied on the CFRP of the first layer to replicate the process so that the second layer was generated. The same steps were continued up until the designated numbers of layers of CFRP were attained. The curing of CFRP was performed according to the instructions provided by the supplier. In the end, a very reliable bonding between steel and carbon fibres and also between the multiple fibres was obtained.

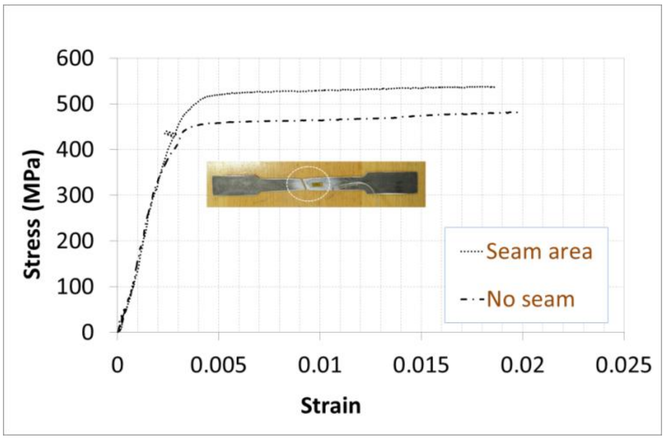

Figure 5-37: Stress strain behaviour of the material.

Material properties

Material properties of the steel used in making the RHS tubes were tested through two coupon tests, one of which was taken out of the seam area where a small longitudinal seam was apparent along the tubes, while the other coupon specimen was cut out of the plain area, i.e. without any seam. Stress strain curves are plotted in Figure 5-37. As is seen, the seam area experienced approximately 15% higher tensile capacity than the plain segment, which can be attributable to the effect of the welding.

Table 5-10: Calculations, stresses and the corresponding ratio.

A (mm^2)	f_y (MPa)	P_{ult} (kN), Ave.	$P_{exp}=P_{ult}/A$ (MPa)	Ratio (P_{exp}/f_y)
229.76	460.00	101.9	443.7	0.96

The linear parts of the two specimens were very similar, verifying that the elastic modulus was not noticeably affected by the seam, whilst with the onset of the nonlinear behaviours a small divergence was seen between the curves above 380 MPa. For the plain specimen, the yield stress was obtained as 460 MPa, the ultimate tensile stress was 495.3 MPa and the Young's modulus was 200 GPa. Material properties of the timber used in this research are listed in Table 5-2.

5.5.3 Observations and findings

Failure modes of different specimens

Reference specimen

Figure 5-38 (a) shows the failure mode of the bare steel specimens. The reference specimens were designated as RTYU.1–3, and were tested with the same loading and boundary conditions under compression. As can be seen, local buckling near the top and bottom dominated, accompanied in one specimen by an inward buckling near the mid-length which indicates column buckling. As a general trend, the buckling in these elements commenced very slowly and was manifest as small amplitude buckling waves near the end areas, which – as the load progressed – was followed by the deepening and developing of the buckling towards the sides.

(a)
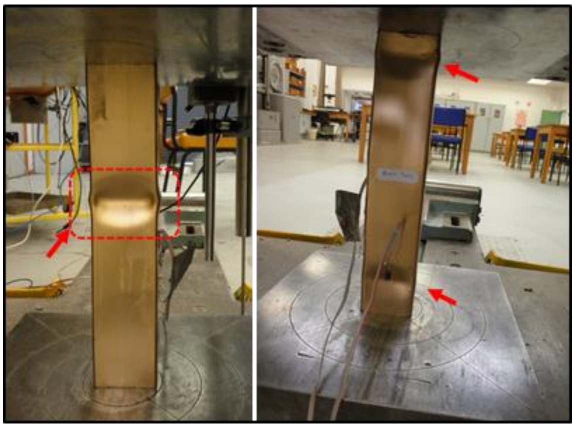

(b)
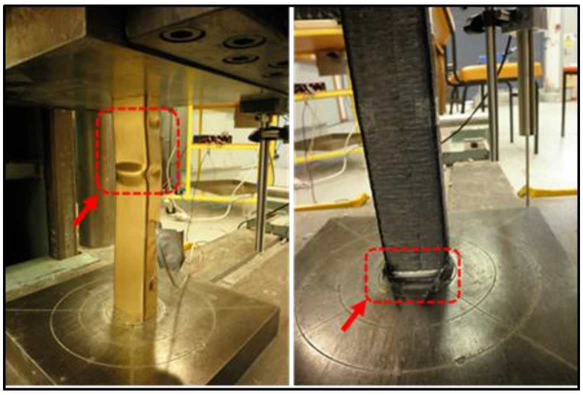

Figure 5-38: (a) Failure for bare RHS specimen (plastic buckling at both sides), (b) failure of the timber filled specimens: bare timber filled (left), CFRP confined timber filled (right).

(a)
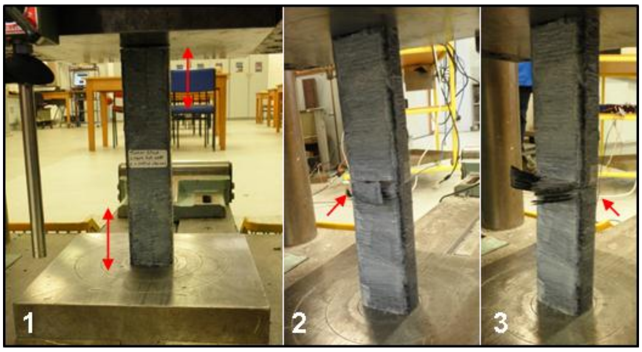

(b)
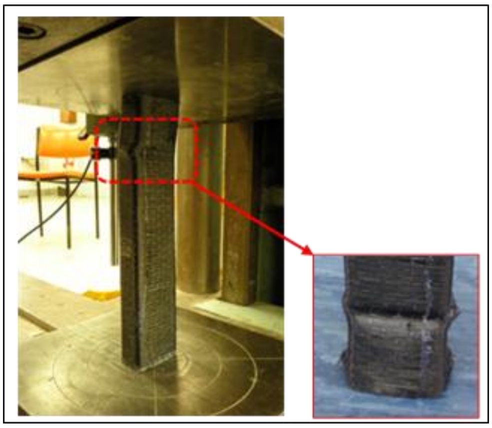

Figure 5-39: (a) RTYU.7, two layers full and a layer partial confinement, before testing (1), failure progress for this specimen (2,3), (b) timber filled specimen with three layers confinement of CFRP.

Timber filled and CFRP confined specimens

The bare timber filled specimen without CFRP (RTYU.4) is shown in Figure 5-38 (b, left), wherein local plastic buckling appeared at several zones in the top half of this specimen. Figure 5-38 (b, right) also shows the failure of the timber filled specimen confined by 2 layers of CFRP (RTYU.5). Outward bulging in the vicinity of the lower end edge was predominantly manifested in which the CFRP ruptured in that area, indicating that two layers of CFRP were not sufficient to fully restrain the outward buckling. The same failure mode (rupture of the CFRP) was seen in Figure 5-39 (a) for the RTYU.7 with two layers of CFRP for the whole length and third layer only confining 80 mm of each end, although in this case the CFRP failed near the mid-length where there were two layers.

(a) (b)

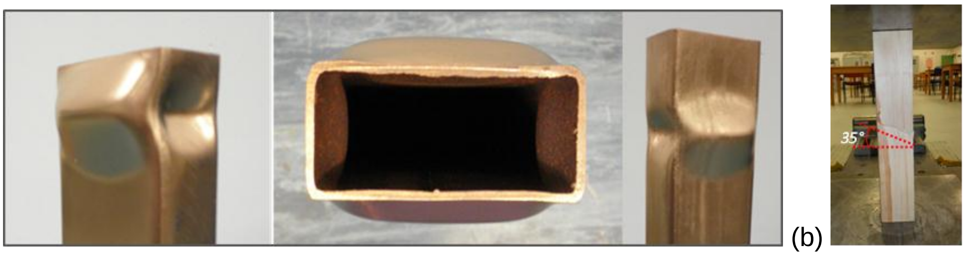

Figure 5-40: (a) Plastic buckling of the bare steel specimens, (b) failure of the bare timber specimen.

It appeared that three layers of CFRP sufficiently reinforced the both ends of the specimens and the buckling was arrested in these zones. It is of interest that the outward buckling was not dominant for the timber filled specimen fully confined by three layers of CFRP (see Figure 5-39 (b)). For this specimen, no rupture was detected for CFRP during the failure. Figure 5-40 shows the plastic buckling of the steel bare specimens and the failure of the bare timber. The failure in the plain timber took place at the middle of the length in the form of an inclined crack passing through at a 35˚ angle.

5.5.4 Axial displacement and strain response

Axial shortening

Figure 5-41 plots the axial shortening of different specimens. The three reference specimens are plotted in the top-left, and show a negligible difference in the load displacement response. One may bear in mind that the inherent differences of all specimens such as geometrical and fabrication non-uniformities can make slight differences, even though the specimens are nominally similar.

RTYU.4 and RTYU.5 are plotted alongside each other (top-right in Figure 5-41) in order to highlight the difference between these specimens and to determine the effect of CFRP. As can be seen, the general trend was similar for these two specimens throughout the linear region of the curves, while with the onset of the nonlinear response a difference is detected between the curves. It further appeared that the specimen confined with CFRP (RTYU.5) behaved with more ductility than its counterpart bare timber-filled specimen.

RTYU.6 and RTYU.7 are compared in Figure 5-41 (bottom-left), which – regardless of the impact on the capacity – showed an insignificant difference when it comes to the load displacement response. The bottom-right segment in Figure 5-41, on the other hand, compares the hollow RHS steel specimen (RTYU.3) and the solid timber specimen (RTYU.8), which obviously shows the difference between the response of the two materials (steel and timber). As expected, RTYU.3 clearly shows higher stiffness compared to RTYU.8.

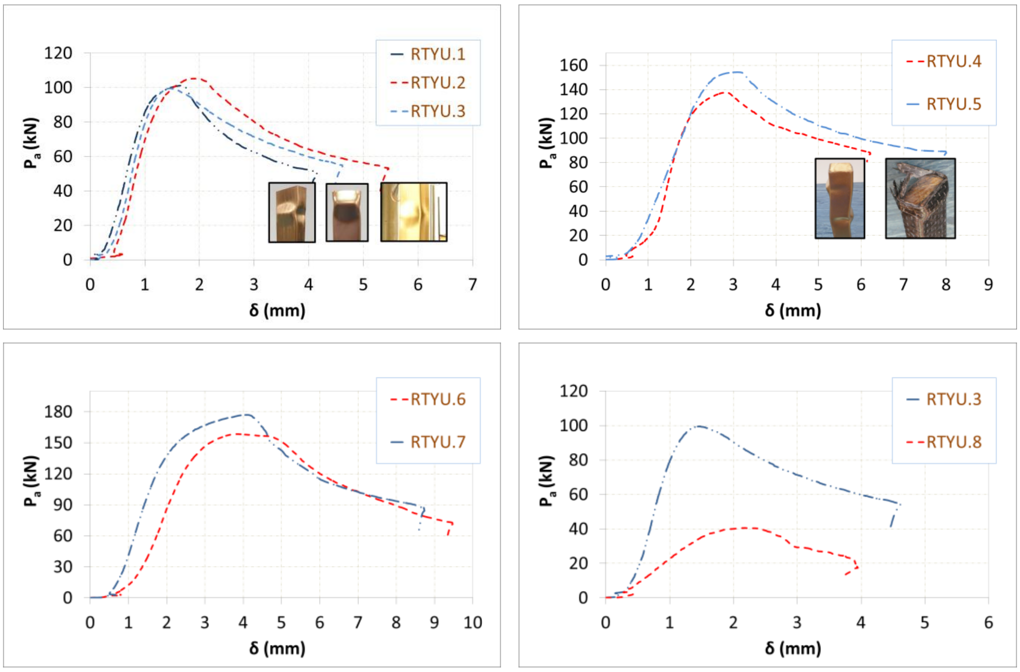

Figure 5-41: Axial shortening versus compression for different specimens.

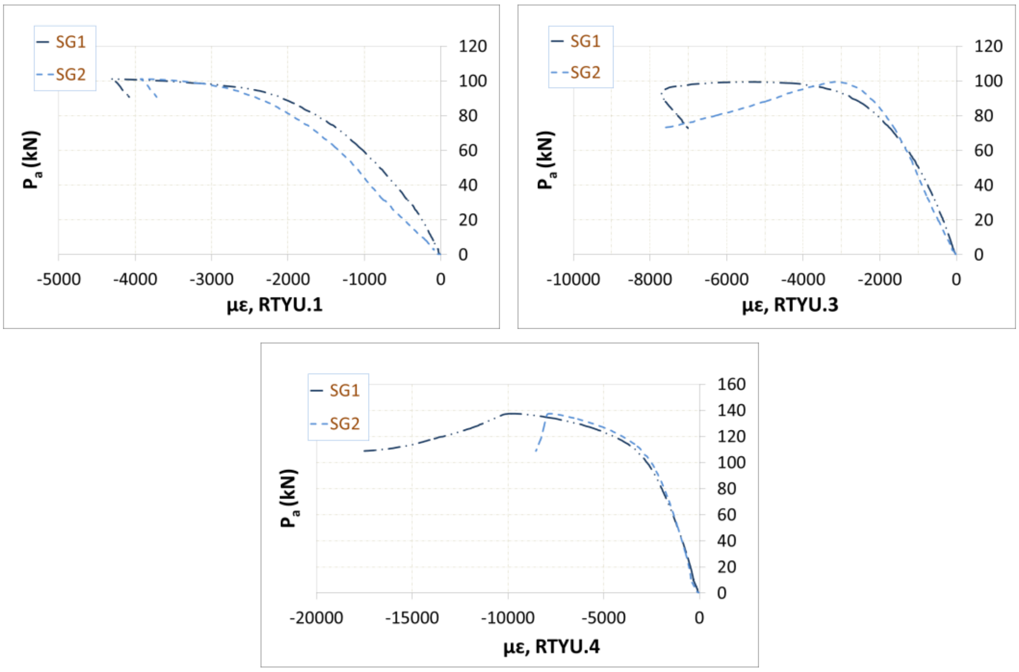

Figure 5-42: Micro strain values versus axial load for three different specimens.

Strain magnitudes

Strain values are plotted for three different specimens in Figure 5-42. Two strain gauges were attached to the body of the specimens: SG1 was attached on the long side of the cross-section 40 mm from one end, while SG2 was applied to the short side at the same distance as SG1. For RTYU.1 and RTYU.3 a typical elastic response is detected initially through the curves, followed by the plastic response reaching the ultimate capacity. In fact, the strains in these two nominally identical specimens differed only with respect to whether buckling occurred at the gauged end or at the end remote from the gauges. Strain values versus the axial load are also plotted for the unconfined timber-filled specimen. Comparing this specimen with RTYU.1 and RTYU.3, a great enhancement in the maximum strain is obtained, which is obviously attributed to the load increase caused by the timber infill.

5.5.5 Ultimate axial capacity

Figure 5-43 shows the ultimate axial capacity for the different plain and composite RHS specimens with different materials involved in their fabrication. The reference specimens showed a very similar ultimate load, in which the difference between RTYU.1 and RTYU.3 was around 1.5% while these specimens had a difference of around 5% with RTYU.2. As can be seen in Figure 5-43, RTYU.4, RTYU.5, RTYU.6 and RTYU.7 experienced higher capacities relative to the reference specimens.

Among these specimens RTYU.7 – fully confined with two layers of CFRP and one additional layer confining 80 mm of the both ends – accounted for the highest increase with a capacity of around 177 kN. By the same token, RTYU.5 and RTYU.6 with respectively two and three full layers of CFRP confinement comprised high capacity enhancements.

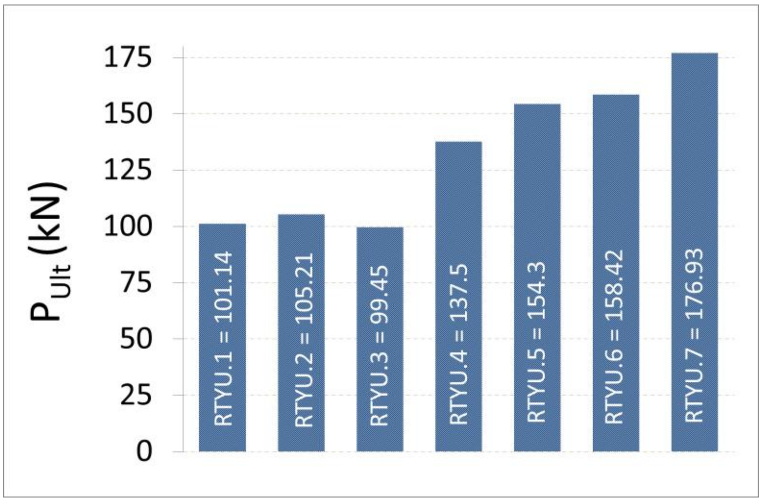

Figure 5-43: Axial capacity of different specimens.

It is believed that the axial capacity of the RHS steel tubes – in timber filled, CFRP confined specimens – took the highest part of the ultimate capacity for these composite specimens. In essence though, the confinement of the CFRP reinforced these specimens against the outward buckling as CFRP sufficiently restrained the surface of the steel.

Furthermore, the timber added a considerable axial resistance to the entire specimen, the effect of which was due to the additional material, and the prevention and/or delay of inward buckling of the steel. The capacity growth in specimen RTYU.4 was around 36%, which is deemed a considerable rise in the capacity, although the absence of CFRP confinement caused a lower increase in the axial capacity in comparison with its CFRP jacketed counterparts.

5.5.6 Comparison with other studies and discussions

Bare RHS

The bare RHS specimens were evaluated against the theoretical calculations. The Australian Standard for steel structures AS 4100 [183] specifies a nominal section capacity for axial compression as $N_s = k_f A_n f_y$, where A_n is the net area of the cross-section, f_y is the yield stress, and k_f is a form factor defined as the ratio of the effective area over the gross area. The effective area incorporates a reduction to account for the slenderness of each plate element and to calculate using the slenderness of each element defined through Eq. (5.3) and the yield slenderness limit applicable to the particular geometry. The present RHS sections have a form factor of 1, meaning that there is no reduction of the effective area due to plate element slenderness, therefore yield determines the nominal section capacity.

$$\lambda_e = \frac{b\sqrt{f_y/250}}{\mathrm{t}} \tag{5.3}$$

In practice, the stresses may significantly exceed the yield stress at ultimate loads, hence local buckling may still occur for a section that does not appear to be slender. So for a very thick walled section we might expect the experimentally determined ultimate load (assuming no member buckling) to significantly exceed the nominal section capacity defined in AS 4100, whereas for a section that only meets the slenderness criteria in AS 4100 we might expect the experimental section capacity to be very close to the nominal capacity defined in AS 4100. In the present experiments the reference specimens achieved on average 96% of the nominal section capacity as is seen in Table 5-10.

Strength Index for composite specimens

In order to compare the present results with those of Ren et al. [175] for concrete filled hollow sections we define a dimensionless *Strength Index* ξ (see Eq. (5.4)), wherein P_{ult} is the ultimate axial load of the composite elements under axial compression, A_s is the effective cross section of the plain steel tubes, f_y is the yield stress of the steel, A_i is the nominal cross section of the infill for the tubes – which can be calculated for concrete and timber filled tubes – and f_i is the compression strength of the infill element. For concrete filled tubes f_i equals f_c' (compressive strength at 28 days), while the compression stress of the timber infill is considered as f_i in the calculations. Note that as appears in Eq. (5.5), Eurocode 4 defined cross-sectional strength of the concrete filled stub columns as N_{uc} (see Refs. [175, 184]). As such Eq. (5.4) can be rearranged in the form of Eq. (5.6).

$$\xi = \frac{P_{ult}}{A_s f_y + A_i f_i} \tag{5.4}$$

$$N_{uc} = f_y A_s + f_c' A_c \tag{5.5}$$

$$\xi = \frac{P_{ult}}{N_{uc}} \tag{5.6}$$

It should be mentioned that Ren et al. tested different shapes, including *tc, cc, fc, dc, sc, and 1/4c,* of concrete filled hollow sections under axial compression [175]. A concrete mixture was employed with a nominal compressive strength of 60 MPa and the average value of the cube strength (f_{cu}) was 61.4 MPa after 28 days, which is considered a relatively high strength concrete. Figure 5-44 plots the *Strength Index* ξ as a dimensionless parameter for different concrete filled specimens presented in [175].

Moreover, the value of ξ = 0.94 for the timber filled specimen of this study was calculated as is seen in Figure 5-44. It is fitting to note that parameter ξ was defined such that the material properties as well as the cross sectional areas for the steel, timber and concrete are all included affecting the ultimate value of this parameter. Figure 5-44 shows that ξ is consistent for the concrete filled specimens (ranging 0.92–1.08), yet rather higher in general than the timber filled specimen. This suggests that considering this dimensionless parameter the timber filled specimens are by and large comparable with the concrete filled specimens. In other words – either for concrete or timber filled specimens – the summation of the strengths of the two materials approximately results in the ultimate capacity of the composite material as the *Strength Index* of ξ is obtained almost equal to the unity for the timber and concrete filled specimens.

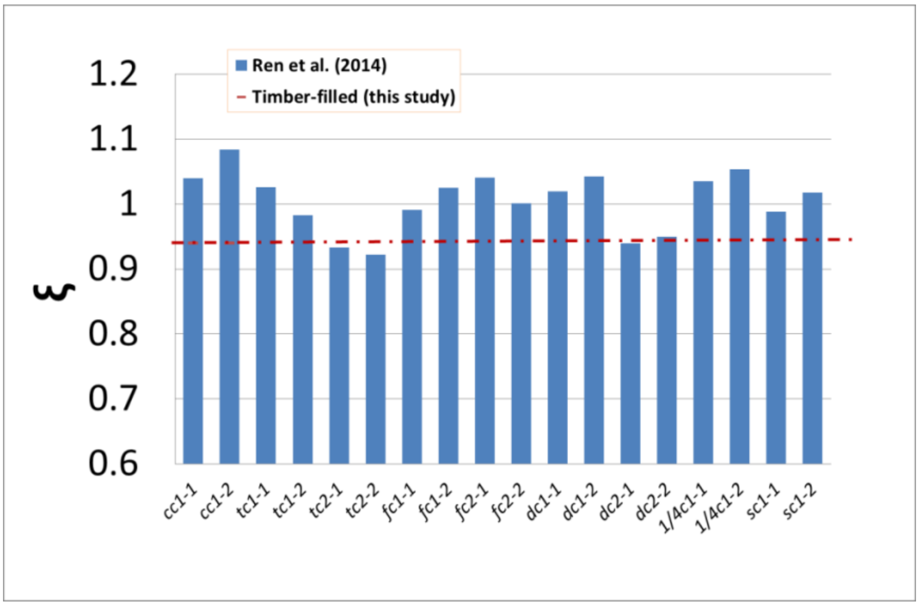

Figure 5-44: Dimensionless parameter ξ calculated for timber filled specimen (this study), and different shaped concrete filled specimens by Ren et al. [175].

Weight ratios and discussions

Figure 5-45 shows the weight ratio of the timber filled and CFRP confined specimens, in which W_{exp} denotes the total weight of the specimens measured before testing, while W_{re} is the weight of the reference specimen. Furthermore, the parameter ρ_a is defined in this study as the ratio of the ultimate capacity of each specimen to the *reference specimens*. This parameter (ρ_a) was also plotted as a bar chart in Figure 5-45. As can be seen, the usage of the timber in RTYU.4, as a sole composite material without any CFRP confinement, brought about the weight increase of 22% in comparison with the bare specimen, while 35% increase in the capacity was obtained. For the confined specimens of RTYU.5 and RTYU.6, however, the weight was increased on average by 39%, while the capacity growth was 53%. Finally for the specimen RTYU.7 the weight increased by 44% while the capacity rose by 74%, which indicates that the timber infill together with the CFRP confinement provided an additional capacity of around three-quarters of the bare specimen for the composite specimen of RTYU.7. In all cases, but particularly for RTYU.7, the strength gain significantly exceeded the weight gain.

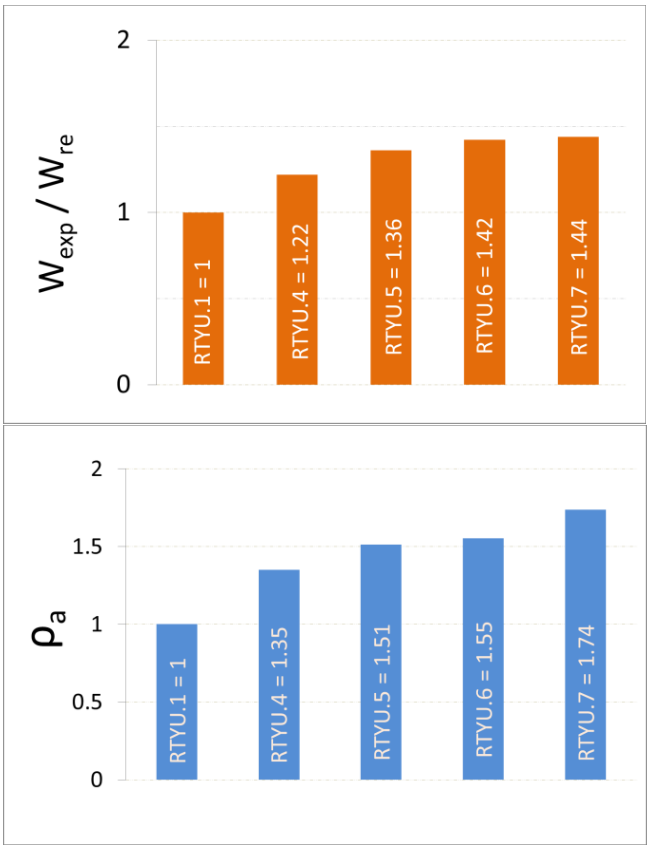

Figure 5-45: Weight ratio and capacity ratio of different specimens relative to the reference specimens.

5.5.7 Practicality and considerations

As pointed out earlier, some of the advantages of the current timber filled composite are: (i) wood (timber) is a cheaper material, yet relatively strong against compressive stresses, (ii) the timber is considerably lighter than alternative infills such as concrete, (iii) the connection possibilities compared with plain timber structures are enhanced through welding and/or bolting when timber is confined with steel, and (iv) this composite provides an optimal use of space since the timber is placed inside the tube and, at the same time, greatly increases the capacity.

It is noteworthy that all the comparisons drawn in the previous sections and the abovementioned advantages suggest that the usage of the two additional materials alongside the steel, i.e. timber and CFRP brings about a considerable enhancement in the capacity-to-weight ratio for the new composite member. In this light, timber as an infill for the hollow sections can certainly stimulate further considerations for the research on this subject, possibly leading to significant developments of this idea. Although proper equipment may be still required to fabricate this composite if mass production is intended, the combination of the timber with steel in compressive members may yield a cost effective lightweight composite member.

5.5.8 Summary and conclusions

A new composite element comprising rectangular steel tubular sections filled with timber and confined with CFRP was undertaken in this section. Several tests were conducted on different specimens with varying geometrical conditions and the impact of each material was studied on the structural behaviour of these structures. The summary of the findings are as follows:

Local buckling around the end areas coupled with an inward buckling near the mid-length were dominant in reference specimens. Plastic buckling appeared in several zones in the top half of the bare timber filled specimen. Three layers of CFRP sufficiently reinforced these specimens and the buckling was arrested for the timber filled CFRP confined (3 layers) specimen.

It appeared that the specimen confined with CFRP (RTYU.5) behaved with more ductility than its counterpart bare specimen. As expected, RTYU.3 clearly showed higher stiffness compared to RTYU.8. Comparing the bare timber-filled specimen with RTYU.1 and RTYU.2, a great enhancement in the maximum strain was obtained, which is obviously attributed to the load increase caused by the timber infill.

RTYU.4–RTYU.7 experienced higher axial capacities relative to the reference specimens, among which RTYU.7 accounted for the highest increase. The capacity of the timber added a considerable axial resistance to the timber filled specimens, the effect of which was additionally accompanied by preventing and/or delaying of the inward buckling of the steel by the timber infill. The confinement of the CFRP reinforced these specimens against the outward buckling as CFRP sufficiently restrained the surface of the steel; therefore, the capacity increased.

The bare RHS specimen was evaluated against the theoretical calculations of the Australian Standard, AS 4100 [183]. The ratio of the calculated axial stress to the experimental axial stress is very consistently close to unity. Considering the dimensionless *Strength Index* parameter (ξ) the timber filled specimens are by and large comparable with the concrete filled specimens. Either for concrete or timber filled specimens the summation of the strengths of the two materials approximately results in the ultimate capacity of the composite material as ξ is obtained almost equal to the unity for the timber and concrete filled specimens.

The usage of timber and CFRP brings about a considerable enhancement in the capacity-to-weight ratio for the new composite member. For RTYU.4, the usage of the timber as a sole composite material brought about the weight increase of 22% in comparison with the bare specimen, while 35% increase in the capacity was obtained for this specimen. Finally for the specimen RTYU.7 the weight increased by 44% while the capacity rose by 74%. Thus, the timber infill together with the CFRP confinement provided an additional capacity of around three-quarters of the bare specimen for this composite specimen. In all cases, but particularly for RTYU.7, the strength gain significantly exceeded the weight gain. In this view, timber as an infill for the hollow sections can certainly stimulate further research considerations, leading to significant developments of this innovative idea.

5.6 Composite timber beams strengthened by steel and CFRP

5.6.1 Introduction

Timber beams have extensively been used in building construction. In some countries timber structures are overwhelmingly dominant in the building industry due to some significant advantages such as cost effectiveness relative to steel and concrete. Numerous papers are found in the literature investigating the structural behaviour of timber beams. Many studies can be found examining timber beams strengthened by various materials to enhance the structural properties of the timber material, e.g. in tensile strength. As a few examples of pioneering studies, research conducted by Wangaard [185], Biblis [186], and Theakston [187] show a history of strengthening timber beams with fiberglass materials. Composite reinforcement of timber beams using carbon and glass fibre was carried out by Johns and Lacroix [188]. The capacity increase of the beams was partly attributed to confining and local bridging feature of the composite action of the timber beams. It should be noted that over the past twenty years, the *Advanced Structures and Composites Center* at *The University of Maine* has significantly contributed to the field of reinforced timber elements with composite materials. A few instances of the research performed by this leading institution of this area are Stevens and Criner [142], Battles [143], Dagher et al. [144], Lopez-Anido et al. [145], Dagher and Lindyberg [146], and Botting [147]. Dempsey and Scott [189] employed fastened FRP strips in order to reinforce wood members through an experimental study. The increase in the stiffness and ductility ratio were evaluated for the strengthened timber members.

Duarte et al. [190] studied the flexural capacity of timber beams reinforced with epoxy mortar plates. The reinforcement showed a significant improvement in the ultimate strength of the tested beams. Timber beams with glued-in GFRP rods under static and cyclic bending were discussed by Madhoushi and Ansell [191]. Glued-in joints provided significant ductility and energy absorbing capabilities for such structures.

O'Loinsigh et al. [192] experimentally and numerically investigated multi-layered wooden beams with varying numbers of wood dowels. Results indicated that a sizable bending stiffness was obtained when an optimum material combination was employed in such multi-layered beams. Structural behaviour of timber beams strengthened with CFRP strips was studied by Khelifa and Celzard [193]. It was found that the proposed theoretical approach can reasonably predict the behaviour of such structures. Flexural response of timber beams rehabilitated with CFRP was investigated experimentally by D'Ambrisi et al. [194]. The method of strengthening was found to be efficient, particularly in repairing old beams with initial defects.

Triantafillou and Deskovic [195] studied wood beams with FRP sheets as external strengthening elements. The results indicated considerable potential of the proposed reinforcing technique. Raftery and Harte [196] experimentally examined low-grade glued timber beams with FRP plates. A modest improvement in global and local stiffness was obtained for the specimens with FRP plate reinforcements.

Steel cords were utilised by Borri and Corradi [197] to rehabilitate timber structures. A higher stiffness and capacity were achieved for such composite beams. Furthermore, existing knots or fracture due to grain deviation or wood shrinkage was covered by the steel reinforcements, and crack openings due to the defects were prevented. The effect of GFRP reinforcement in shear strengthening of the timber beams was discussed by Hay et al. [198]. Diagonal GFRP sheets appeared to be more effective compared to vertical sheets in reinforcing timber stringers. Solid timber beams strengthened by steel plates in different positions were investigated by Jasieńko and Nowak [199]. It was pointed out that the increase in stiffness using FRP was larger than when steel reinforcement was employed. De Luca and Marano [200] investigated glulam timbers strengthened by steel bars with and without pre-tensioning. For such reinforced beams without pre-stressing, stiffness, ultimate load and ductility were enhanced by about 25.9%, 48.1% and 43.8% respectively relative to the plain specimen.

Alhayek and Svecova [201] discussed the bending strength and stiffness of GFRP strengthened timber beams. Half-scale and full-scale GFRP strengthened timber beams were studied by Gentile et al. [202]. Unlike the typical brittle failure of the unreinforced timber specimens, a ductile failure in the reinforced specimens was found in this study. The possibility to use CFRP rods as glued-in strengthening in glulam beams was evaluated by Micelli et al. [203]. The results were compared with the corresponding steel bolts and plates used in previous studies.

This study presents an innovative approach in reinforcing the structural timber elements, *Machine Graded Pine (MGP10)*, with both U-shape steel elements and *Carbon Fibre Reinforced Plastic (CFRP)* under a three-point flexural loading. The main innovation of this work is the employment of U-shape steel sections to fully strengthen both the tension and compression side of the timber. Previous studies predominantly used only *plates*, and only in the zone of maximum tensile stresses. It is hypothesised that the U-section reduces debonding compared to flat plates because of shear effects between the flanges and the timber. This study considers timber beams strengthened with steel only, CFRP only and a combination of the two, with a view to determining the behaviour of each case to reach the optimum arrangement. It may be mentioned that the proposed strengthening schemes can be employed to rehabilitate or repair bridge stringers as the geometry of the present timber specimens, e.g. span length to sections' height, can be found within the applicability range of the real stringers.

5.6.2 Experimental program

Test rig

The hydraulic testing machine (Avery) – employed for the previous tests as discussed earlier – with modified supports was used to apply the bending load (Figure 5-46). Three-point flexural testing was conducted with a simply supported condition and loading element. Digital *LVDTs* were used to record the mid-span displacement. Strain gauges were applied on predefined points on the beams. Five strain gauges, labelled SG.1–SG.5, were attached to the areas with maximum tension and compression stresses in the current beam specimens. A *Quantum X MX1615*, *HBM* data acquisition system with *Catman* software were used to record, process and analyse the data throughout the experimentation.

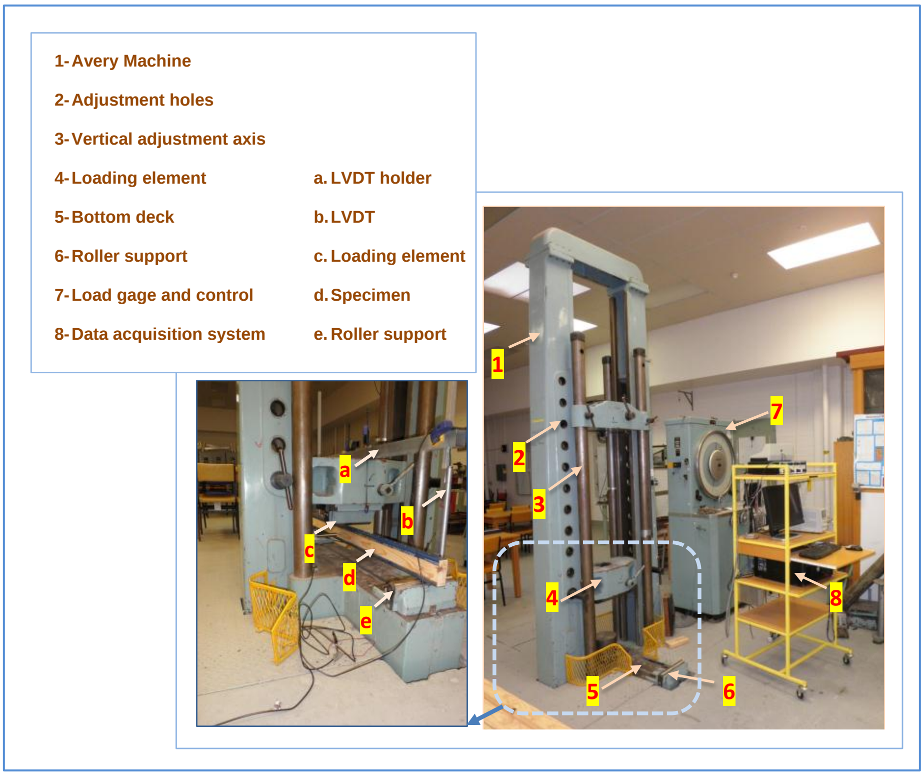

Figure 5-46: Test setup and detailed components.

Test specimens and preparation

Figure 5-47 and Figure 5-48 give detailed specifications of different specimens, where *F* is a concentrated load applied over a small area through a loading block (loading element or LB) to distribute the stress. In Figure 5-47, *h* and *b* are the height and the width of the timber sections respectively, and S-S, T-T, U-U and V-V are typical sections for the different specimens.

Table 5-11: Material properties of the timber and steel.

Structural timber, MGP10			
Stress grade in AS 1720.1	Bearing parallel to grain (MPa)	Ave. modulus of rigidity (MPa)	Ave. modulus of elasticity, parallel to grain (MPa)
Radiata Pine, MGP10	30	670	10000
Mild steel			
Yield stress (MPa)	Ultimate stress (MPa)	Young's modulus (GPa)	Poisson's ratio
433	466	197	0.3

CFRP, *MGP10* and U-shape steel are different materials, which are described later in this section. The loading element was introduced to prevent localised failure. Its length, being 15% of the clear span, does not substantially change the moment distribution within the beam.

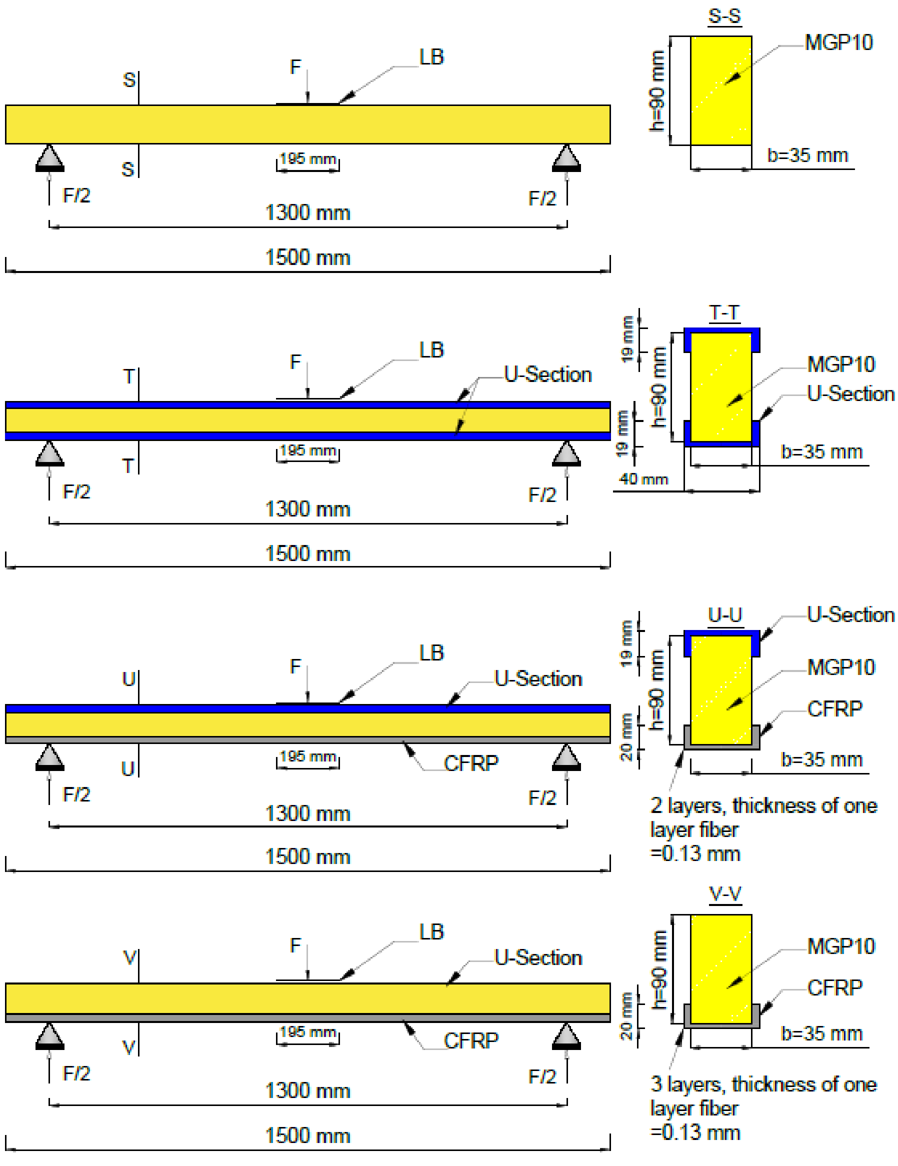

Figure 5-47: Schematic illustration of the beams and reinforcements along with geometrical details.

(a) *Materials:* The employed timber was machine-graded structural *Radiata Pine* with the stress grade of *MGP10*. Design material properties for *MGP10* are shown in Table 5-11, which were obtained from AS 1720.1 [153]. The moisture content of the timber was 10.9%, obtained by oven drying specimens according to Australian Standard AS 1080.1 [204]. The stress-strain response of the steel used for reinforcement, obtained through a tensile coupon test according to AS 1391 [91] is given in Figure 5-49, from which the Young's modulus is 197 GPa and the yield and ultimate stresses are 433 and 466 MPa respectively.

Specimen label: *ST-ST-Sc*	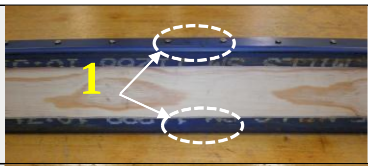
(1): Connection: *42 screws @ 80 mm, at mid-width of the section*	
Reinforcement: *Top and bottom steel*	
Specimen label: *ST-ST-E*	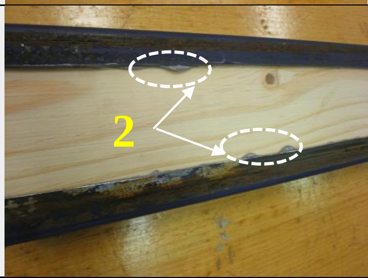
(2): Connection: *epoxy*	
Reinforcement: *Top and bottom steel*	
Specimen label: *NA-St-E* and *R-NA-St-E*	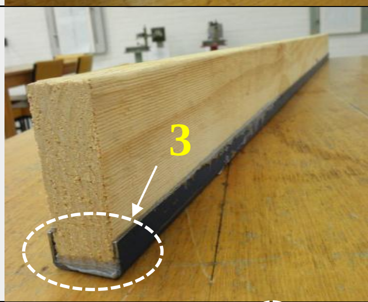
(3): Connection: *epoxy*	
Reinforcement: *bottom steel*	
Specimen label: *St-St-E* and *R-St-St-E*	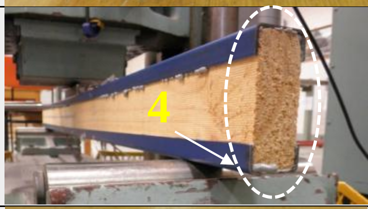
Connection: *epoxy*, **(4):** composite section	
Reinforcement: *Top and bottom steel*	
Specimen label: *St-FR-E* and *R-St-FR-E*	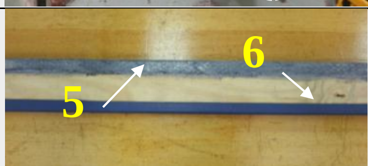
(5,6): Connection: *epoxy*	
Reinforcement: *Top steel, bottom CFRP (2 layers)*	
Specimen label: *NA-FR-E* and *R-NA-FR-E*	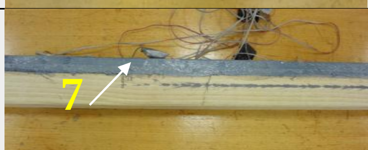
Connection: *epoxy*	
(7): Reinforcement: *bottom CFRP (3 layers)*	
Specimen label: *Plain-1, Plain-2, Plain-3, Plain-4 and Plain-5*	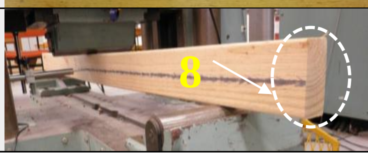
(8): *Pure timber section*	
Reinforcement: *N/A*	

Figure 5-48: Details of different specimens.

For the CFRP reinforcements, carbon fibre *SikaWrap Hex-230C* by *Sika Australia Pty. Ltd* and thixotropic adhesive *Sikadur*®*-330* as epoxy resin were employed. *SikaWrap Hex-230C* is a unidirectional carbon fibre sheet available as a 46 m long rolled sheet of width 610 mm. According to the information provided by the manufacturer, each layer has equivalent carbon thickness of 0.13 mm, based on an areal density of 230 g/m^2 and fibre volumetric density of 1800 kg/m^3. The fibres had Young's modulus of 230 GPa, ultimate strain of 1.5% and a unidirectional tensile strength of 3450 MPa. After 7 days at a temperature of +23°C, the tensile strength of the epoxy adhesive was 30 MPa, and the flexural and tensile moduli of elasticity were 3800 MPa and 4500 MPa respectively. Note that the thixotropic adhesive was also used for attaching both the steel reinforcement and CFRP to the timber. Based on the above material properties, CFRP is far stronger than steel in tension while steel is used in compression since the fibres are too flexible to sustain a significant compressive load; thus, the combination of the CFRP (in tension) and steel (in compression) provides optimal reinforcement of the timber.

Table 5-12: Description for different letters and numbers in the specimens' labels indicating various reinforcement schemes.

Letters in specimens' labels	**Description**
ST	Steel reinforcement with a thickness of 2.5 mm
St	Steel reinforcement with a thickness of 2 mm
FR	CFRP reinforcement
NA	No reinforcement
Sc	Screwed connection
E	Epoxy connection
R	Repeated specimens

Note: All names have the format of *A-B-C* or *R-A-B-C*, in which *A* and *B* indicate the material used for the top and bottom reinforcement respectively and can take values *ST*, *St, FR* or *NA*; and *C* indicates the method of connecting the reinforcement to the timber and can be either *Sc* or *E*. *R* only applies to repeated specimens (note that these are in addition to the original sample for a given configuration).

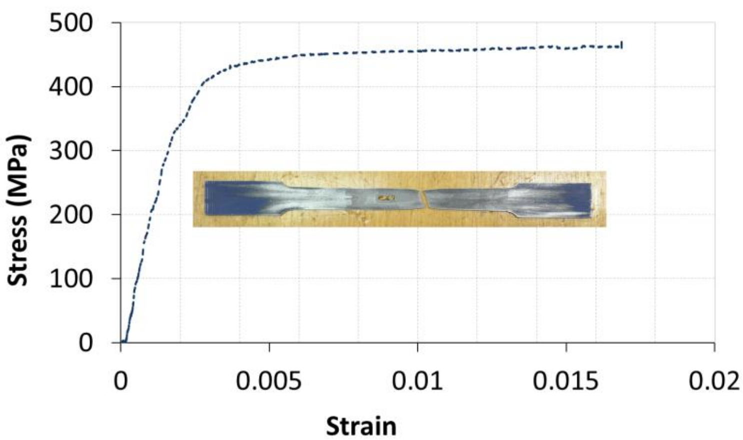

Figure 5-49: Tensile coupon test and stress-strain curve.

(b) *Preparation of the specimens:* The specimens were labelled with a self-explanatory scheme with different geometric and material conditions as shown in Figure 5-47 and Figure 5-48 (t is the thickness of the steel sections in Figure 5-48). Table 5-12 lists different letters and numbers used in the specimens' labels indicating various reinforcement schemes. The steel U-sections were made by cutting 40 × 2.5 mm or 40 × 2.0 mm SHS sections in half lengthwise. As is shown in Figure 5-48, in order to provide an indication of the accuracy and consistency of the test results, specimens *R-NA-St-E*, *R-St-St-E*, *R-St-FR-E* and *R-NA-FR-E* were duplicate specimens for *NA-St-E*, *St-St-E*, *St-FR-E* and *NA-FR-E* respectively. Five replicates, *Plain-1* to *Plain-5*, were provided for the plain specimen. The height and the width of the timbers were nominally 35 × 90 mm, which is a standard commercially available size. In order to prepare the timber beams, the timbers and their steel reinforcements were cut into the desired lengths. The corners of the timber beams were slightly curved to fit the curved corners of the SHS sections without any crushing of the timber. The carbon fibre sheets were cut into the designated lengths. The epoxy was applied to the surface and the carbon fibre sheets were placed in layers with the fibres aligned with the beam axis, with an adequate pressure so that the epoxy was properly smeared into the layers.

The epoxy, which consisted of two parts, was also used to connect the U-shape steel sections to the timbers. These parts were mixed in the ratio of 1:4 according to the instructions of the supplier. The contact surface of the steel was carefully sandpapered and any additional particles were removed by acetone. For specimens reinforced with steel on both top and bottom several clamps were employed during curing of the epoxy to keep the steel in its desired position and to provide reliable bonding. For specimens with steel on one side only, weights were used on the steel rather than clamps to avoid damage to the timber. Connection of the steel to the timber using screws rather than epoxy was used only in *ST-ST-Sc*, in which the screws were located at mid-width of the section ($b/2$). Note that 21 screws were located both on the top side of the beam and on the bottom at a longitudinal spacing of 80 mm. Screws on the top were staggered relative to those on the bottom. This method was abandoned in subsequent tests for reasons explained below.

5.6.3 Results and discussions

Tests observations and failure

Plain specimens

The failure in the plain timber specimens, i.e. specimens without reinforcement, was quite abrupt with a sudden tensile rupture in the timber. The failure was initiated in different areas in various plain specimens, which is believed to be generally due to the existence of knots and non-uniformities of the timber.

Steel reinforced specimens

As mentioned earlier, the specimen *ST-ST-Sc* was reinforced by steel sections on both the top and the bottom and screws were used to create the connection between the steel and the timber. A crack commenced in the tension side of the timber approximately opposite the load point and developed in an inclined manner at around 45˚, all the way through the neutral axis. Figure 5-50 presents the failure stages of *ST-ST-Sc*. Although a significant rise in the flexural capacity was gained after strengthening the timber beam with the steel sections, the existence of the screws (or possibly a knot) presumably initiated the onset of tensile cracks, which propagated as a shear failure. In light of this, the steel reinforcements were connected to the timber using epoxy for the subsequent specimens. The epoxy provided a very reliable connection for *ST-ST-E*; hence failure occurred in the timber with no debonding of the interface between steel and timber.

Figure 5-50: Failure progress of the specimen *ST-ST-Sc*: (1) crack initiation, (2) width of the crack while loading, and (3) progress of the width of the crack, and the approximate angle of the crack propagation.

NA-St-E and *R-NA-St-E* were reinforced along the bottom (tension) side of the timber beam only, using a steel U-section connected to the timber by epoxy. The progress of the flexural deflection for *NA-St-E*, leading to the crack initiation and its development, is seen in four stages in Figure 5-51. This figure indicates that the crack appeared in the tension side of the timber and developed upwards such that the neutral axis shifted towards the compression side. This indicated that the steel had reached its yield plateau, while the timber was still able to sustain increasing compressive stress.

For *St-St-E* and *R-St-St-E*, the top and bottom of the timber beam were reinforced with steel using epoxy in the interface between the two materials. This specimen underwent a failure in the mid-span with a crack starting from a single point developing towards the sides (see Figure 5-52). It is noteworthy that the typical brittle failure of the plain timber specimens was largely prevented and/or delayed in the specimens reinforced with steel, in which higher deflections were observed throughout the loading in comparison with the plain specimens.

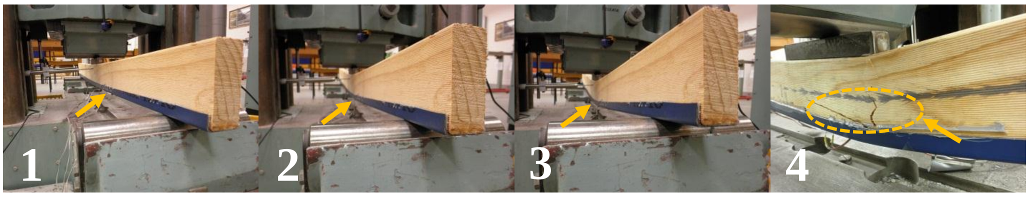

Figure 5-51: *NA-St-E* and its bending and fracture stages: (1–3) mid-span deflection of each stage, (4) crack initiation.

Specimens reinforced with CFRP and steel

Specimens *St-FR-E* and *R-St-FR-E* were reinforced by the steel on top (compression side), whilst CFRP was utilised on the tension side. It was believed that the compressive strength of the timber in combination with the steel reinforcement in the top half, coupled with a significant tensile strength provided by the CFRP on the bottom would yield a reliable composite section against bending. Failure occurred with a severe and abrupt destruction simultaneously in the CFPR fibres and grains of the timber as can be seen in Figure 5-53. After reviewing a video recorded from the experiment it was observed that longitudinal cracks took place along the specimen propagating upwards, all the way through the top, which stopped at the steel reinforcement. Brittle behaviour overwhelmingly dominated the failure in *St-FR-E* and *R-St-FR-E* relative to the specimens fully strengthened by the U-shape steel(s).

__Specimens reinforced with CFRP alone__

Comparing with the specimens *St-FR-E* and *R-St-FR-E*, a similar catastrophic failure was observed for the specimens *NA-FR-E* and *R-NA-FR-E* such that a destructive crack took place with a very loud sound, following absorption of a considerable amount of the flexural energy in the specimen. These specimens were reinforced on the tension side only with CFRP, and no steel on the compression side.

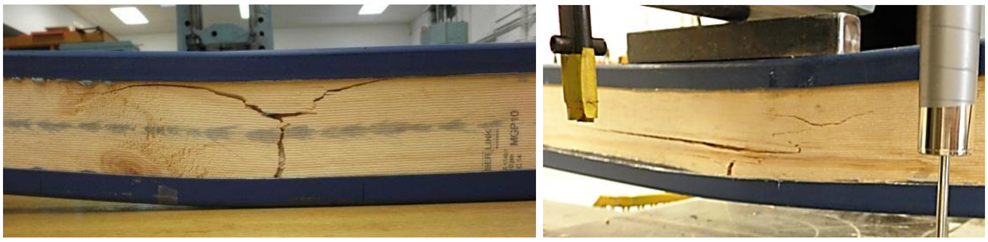

Figure 5-52: *St-St-E* (left), and *R-St-St-E* (right) after failure.

Figure 5-53: Loading and failure stages of the specimen *St-FR-E*: (1) pre-failure deflection of the beam, (2) deflection of the beam at failure, and (3) closer view of the development of cracks and destructive failure.

Load displacement response and ductility

Figure 5-54 presents the moment-displacement response at the mid-span for the reinforced timber specimens, where M is the bending moment and δ is the displacement. For the strengthened specimens, more deflections and in some cases ductility were obtained relative to the plain timber beams, which are presented later in this section. In *ST-ST-E*, the *LB element* was not employed which is why a considerable post-yielding regime was observed, since the deformations were localised at the load point. For *NA-St-E*, *R-NA-St-E*, *St-FR-E* and *R-St-FR-E*, the responses were similar, as no significant nonlinearity was seen when the specimens were under relatively lower loads. The nonlinearity was mostly due to the existence of the reinforcements in such composite beams, providing significant deflection, with 2–3 times the displacement relative to the plain specimens.

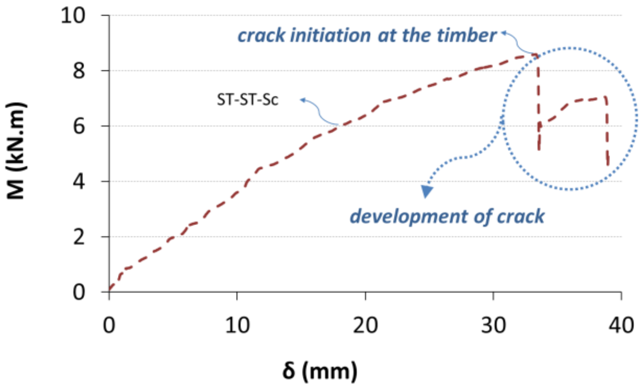

(a)

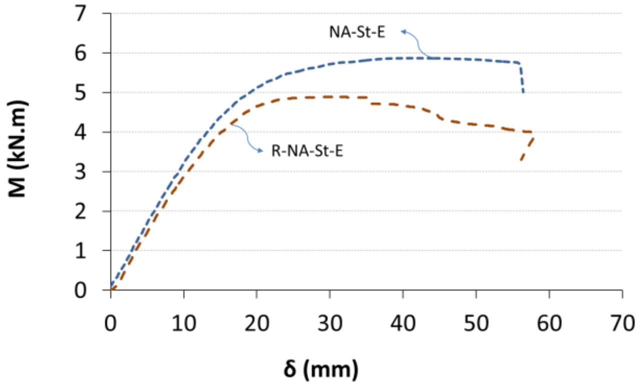

(b)

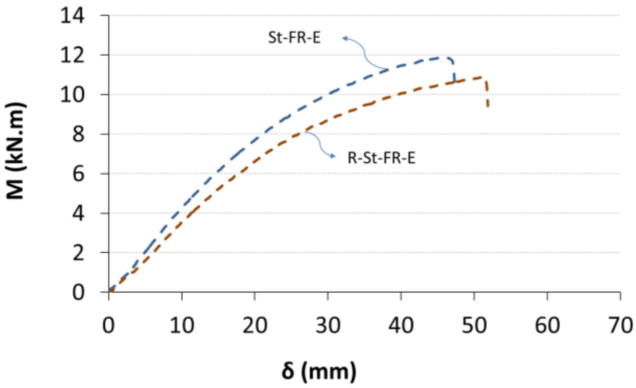

(c)

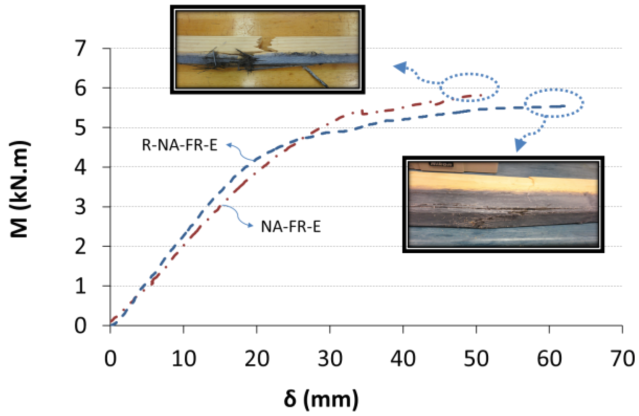

(d)

Figure 5-54: Displacement of the mid-span for different reinforced specimens: (a) *ST-ST-Sc*, (b) *NA-St-E* and *R-NA-St-E,* (c) *St-FR-E* and *R-St-FR-E,* (d) *NA-FR-E* and *R-NA-FR-E*.

Moreover, a significant yield plateau as an indication of the ductility increase was clearly observed for the specimens with bottom reinforcement only. The CFRP at the bottom also provided more ductility for *NA-FR-E* and *R-NA-FR-E* compared with the plain timber, although a catastrophic failure was eventually observed during the tests (see Figure 5-54).

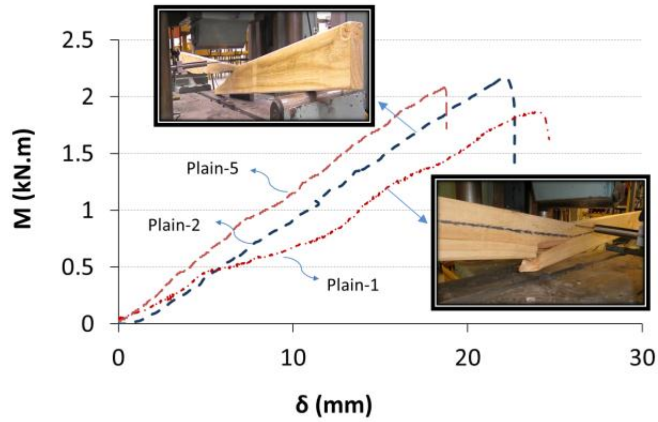

(a)

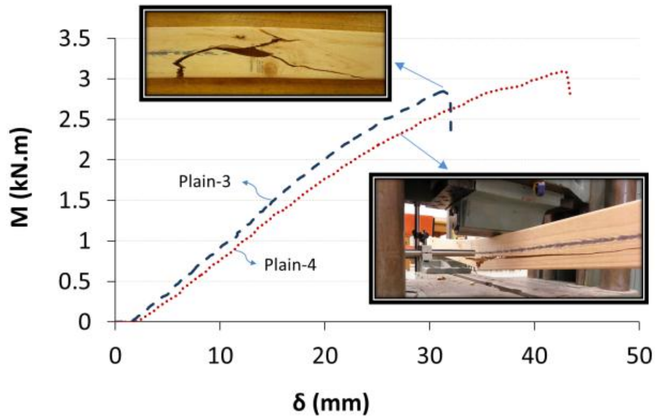

(b)

Figure 5-55: Displacement of the mid-span for the bare timber specimens: (a) *Plain-1*, *Plain-2* and *Plain-5,* (b) *Plain-3* and *Plain-4*.

Figure 5-55 presents the moment-displacement behaviour for the plain timber specimens *Plain-1* to *Plain-5*. A relatively linear response was observed for the specimens *Plain-1*, *Plain-2* and *Plain-5*. Likewise, a linear moment-displacement response, with a moderate non-linearity as the specimens approached a slightly higher ultimate moment, was obtained for *Plain-3* and *Plain-4*. As is typically observed for bare timber beams, all five specimens showed a brittle fracture in this set of tests.

Overall, regardless of the capacity increase, which will be discussed later, the ductility of the reinforced beams especially for the specimens with bottom reinforcement only was clearly improved compared with the bare timber specimens. The additional ductility came from the reinforcement, but may have been enhanced by the partial confinement of the timber by the steel or CFRP.

Strain values of the reinforced specimens

The location of the strain gauges is shown in Figure 5-56. The strains for the tension gauges (SG.3–5) are plotted in Figure 5-57 ($\mu\varepsilon$ indicates micro strain values). It is obvious from Figure 5-57 that the maximum strains for SG.4 in *ST-ST-E* were significantly higher than the other two strain gauges, even though the moment reduced for large displacements, signifying yield at mid-span in the steel, while for SG.3 and SG.5 the moment-strain curve returned approximately along the loading path, indicating the steel remained nearly within the elastic range at these locations. However, this phenomenon was not seen for *NA-FR-E*, which was strengthened by CFRP, due to the brittle response of *NA-FR-E* in comparison with *ST-ST-E*.

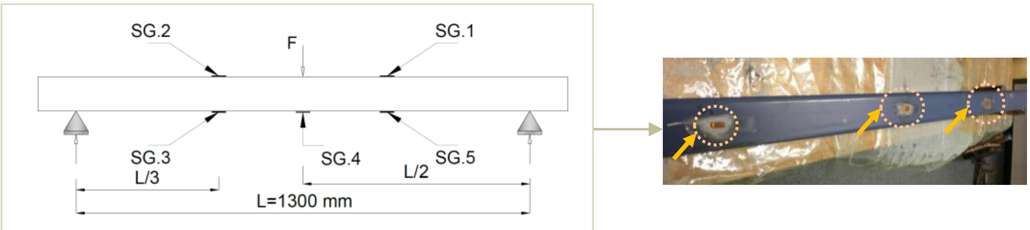

Figure 5-56: Layout of strain gauges in different specimens.

In *NA-St-E*, *St-St-E* and *St-FR-E* the responses recorded by the three strain gauges (SG.3–SG.5) were similar. Specimen *NA-St-E* experienced greater nonlinearity, which is attributable to a single steel reinforcement, whilst *St-FR-E* showed an extended linear range due to the existence of the CFRP. The additional U-shape steel section in the compression zone of the specimen *St-St-E* reduced the magnitude of the strains in comparison to its counterpart specimen *NA-St-E* where single steel reinforcement was applied.

Compressive strain values versus bending moment are plotted in Figure 5-58 for three different specimens, in which *St-FR-E* shows higher strain magnitudes, which suggests that the combination of steel and CFRP provided a higher strain capacity to the composite timber specimen than the specimens reinforced with only steel or CFRP. The same comparison can be made for *ST-*

ST-E and *St-St-E* where the difference in the steel sections for these specimens caused the difference in the strain magnitudes, although moment-strain graphs were mostly linear for the two specimens. Comparing the strain values of SG.1 and SG.2 – which were placed on the points with nominally the same compressive stresses – suggests that SG.1 showed closer values to SG.2 in *St-St-E* and *ST-ST-E* relative to the specimen *St-FR-E* in which CFRP took part in the tension part. This observation can be attributed to more uniformity of the material of the steel than CFRP, given that CFRP was prepared and applied to reinforce the timber beams in the laboratory.

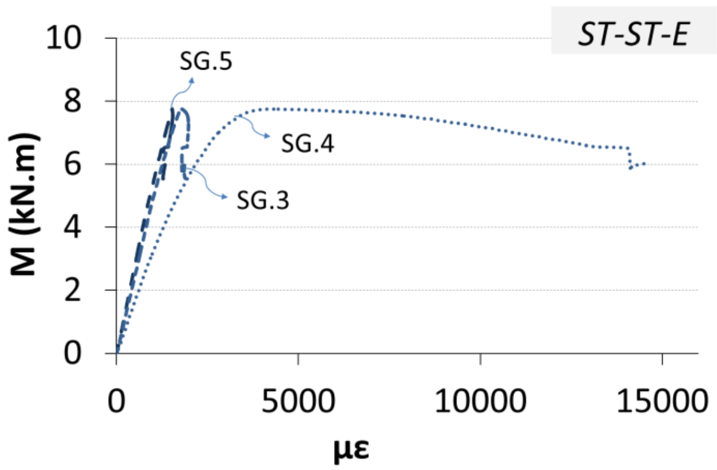

(a)

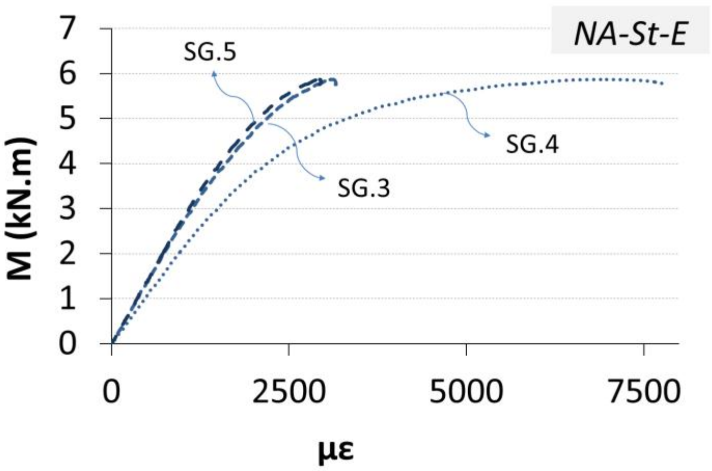

(b)

Continued in the next page.

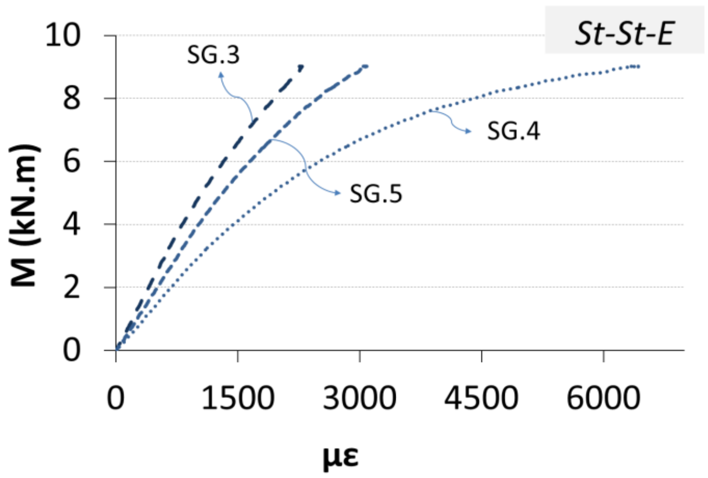

(c)

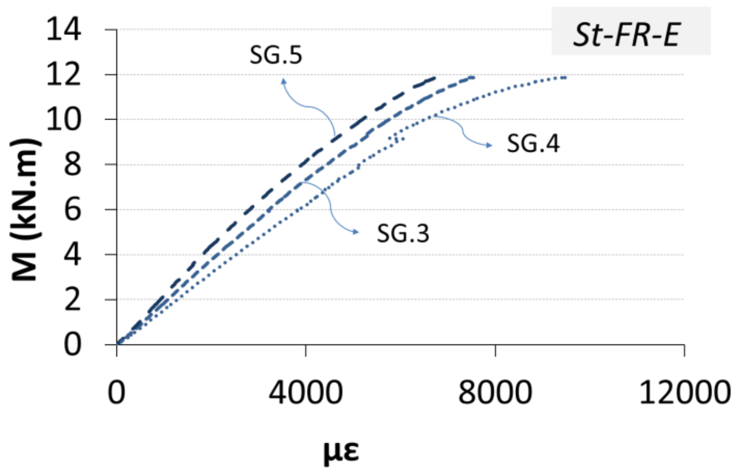

(d)

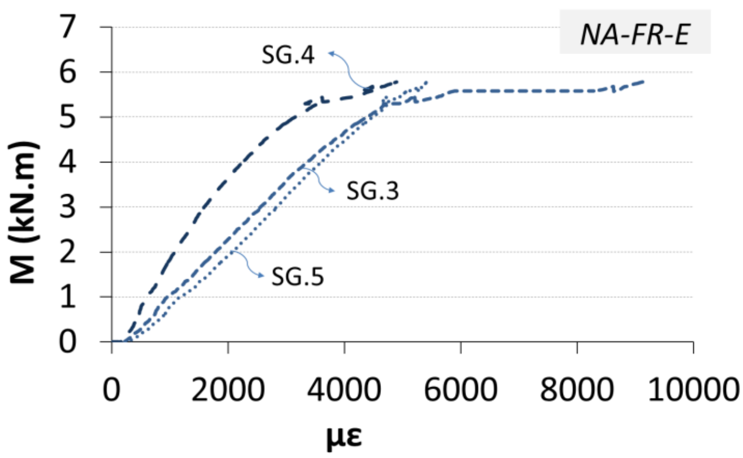

(e)

Figure 5-57: Strain values of the tension part (SG.3–5) in different specimens: (a) *ST-ST-E,* (b) *NA-St-E,* (c) *St-St-E,* (d) *St-FR-E,* (e) *NA-FR-E*.

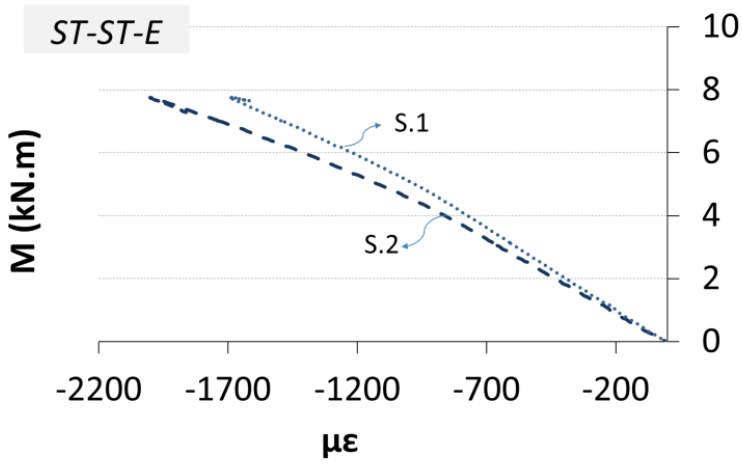

(a)

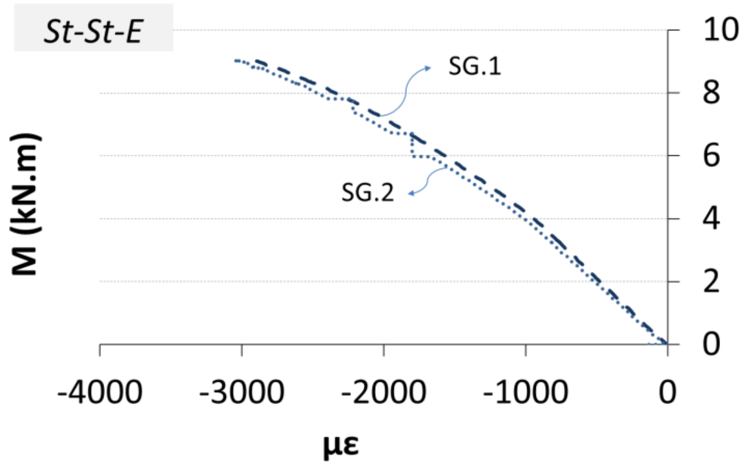

(b)

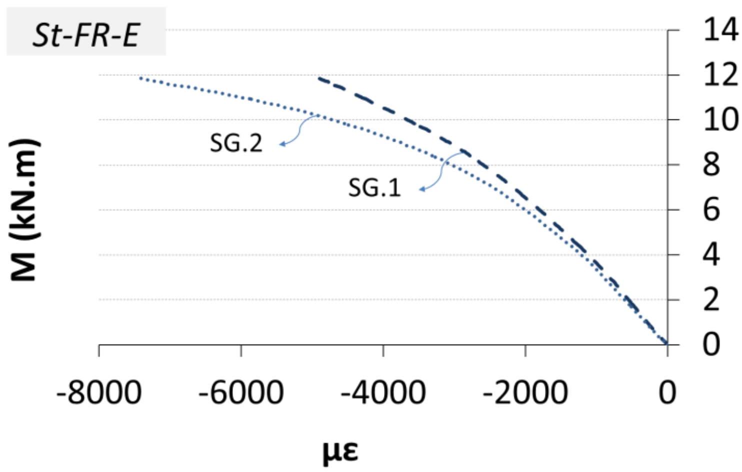

(c)

Figure 5-58: Compressive strain values (SG.1 and SG.2) in different specimens: (a) *ST-ST-E*, (b) *St-St-E*, (c) *St-FR-E*.

5.6.4 Flexural capacity and rigidity of different specimens

Flexural capacity of the plain and reinforced specimens along with the ratio ξ are presented in Table 5-13 and Figure 5-59, where ξ is the ratio of ultimate bending capacity (M_{ult}) to the average capacity of the five plain specimens *Plain-1* to *Plain-5* (M_{plain}). As can be seen, *St-FR-E* and *R-St-FR-E* accounted for the highest bending resistance among all specimens, indicating that the combination of steel and CFRP produced a significant additional capacity. The ratio ξ showed that the capacity of these specimens rose by approximately 4.7±0.2 times the average capacity of the plain specimens. Following that *St-St-E* and *R-St-St-E* with double side steel reinforcements comprised the second highest capacity increase, with a ratio of 4.1±0.4. For *ST-ST-Sc*, in which a double side screwed steel reinforcement was applied, ξ was about 3.6, which was significantly lower than *St-St-E* and *R-St-St-E* with glued steel reinforcement in spite of an additional 0.5 mm steel wall thickness. It is believed that the cracks were initiated by the screws on the tension side, which resulted in *ST-ST-Sc* not reaching the full potential capacity increase achievable with the same steel reinforcement but using epoxy to connect to the timber.

Table 5-13: Ultimate strength (M_{Ult}) and rigidity (K) of the specimens, average values and standard deviation.

Specimen	M_{Ult} (kN.m)	[c]$M_{Ult, Ave}$ (kN.m)	[a]Difference (%)	K (N.mm^2) $\times 10^{10}$	[c]K_{Ave} (N.mm^2) $\times 10^{10}$	[b]Difference (%)
ST-ST-Sc	8.59	-	256	4.71	-	221
ST-ST-E	7.75		221	10.00		581
NA-St-E	5.87	5.38±0.69	143	4.54	4.44±0.14	209
R-NA-St-E	4.89		103	4.34		196
St-St-E	9.02	9.95±1.32	274	9.30	9.06±0.35	534
R-St-St-E	10.89		351	8.81		500
St-FR-E	11.86	11.39±0.67	392	6.13	5.79±0.48	318
R-St-FR-E	10.91		353	5.45		271
NA-FR-E	5.82	5.68±0.19	141	2.83	3.10±0.37	93
R-NA-FR-E	5.55		130	3.36		129
Plain-1	1.87	2.41±0.53	-	1.31	1.47±0.10	-
Plain-2	2.17		-	1.48		-
Plain-3	2.85		-	1.56		-
Plain-4	3.10		-	1.43		-
Plain-5	2.08		-	1.56		-

Note: [a] Capacity difference (ultimate bending moment) of reinforced specimens from average capacity of the plain specimens. [b] Rigidity difference of reinforced specimens from the average rigidity of the plain specimens. [c] ± gives the values of standard deviation.

The capacity increase for the specimens with single side steel reinforcement (*NA-St-E* and *R-NA-St-E*) was considerably less than the double sided ones at ξ = 2.2±0.2. One may therefore conclude that the U-shape steel sections not only enhanced the tensile stress carrying capacity of the timber beams, but also brought about a significant capacity increase via other mechanisms through synergy between the steel and timber. For example it is evident that the distance between the two U-shape steel sections of the present composite beams – created by the height of the timber – considerably increased the *second moment of inertia* of the steel sections, and hence the bending capacity. The bending capacity was further amplified by the composite action between the steel and timber. Most significantly though buckling (lateral/torsional and local buckling) of the steel sections in the compression zone was prevented when the steel was connected to the timber, compared to the case that steel would be employed individually with no timber.

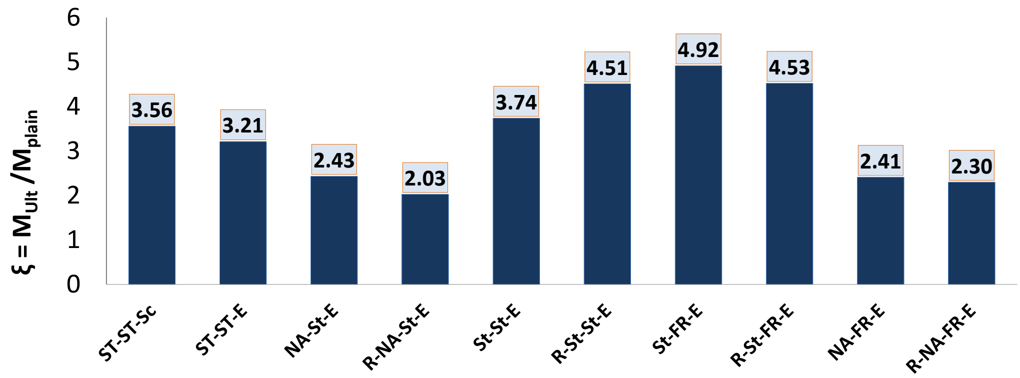

Figure 5-59: Capacity ratio of different reinforced specimens to the average value of the plain specimens.

It was also found that the capacity of the specimen *NA-FR-E* was clearly very close to *NA-St-E*, which demonstrates a similar effect of single reinforcements in the tension side whether it is a U-shape steel section or CFRP. However, *NA-St-E* showed more ductile behaviour than its counterpart, *NA-FR-E*.

Table 5-13 shows the rigidity values of the present specimens where K is the rigidity of each specimen and K_{Ave} is the average rigidity of the repeated specimens. Rigidity values were obtained from the initial elastic part of the load-displacement graphs for each specimen, using Eq. (5.7):

$$EI = \frac{\Delta P L^3}{48 \Delta \delta} \tag{5.7}$$

where ΔP is a given range of loading, $\Delta\delta$ is the corresponding displacement, L is the free span length, and E and I are Young's modulus and second moment of inertia. As listed in Table 5-13, the rigidity values of the reinforced specimens drastically increased relative to the plain timber beams. The enhancement of the rigidity was higher for the specimens *ST-ST-E, St-St-E* and *R-St-St-E*, which were reinforced by U-shape steel on the top and bottom of the timber elements. Unlike the capacity increase, which was higher for the specimens reinforced with steel and CFRP, the rigidity increase in the specimens with double steel reinforcements was considerably higher than the specimens with steel and CFRP reinforcements.

It is quite clear that for timber products the flexural capacity of different unreinforced specimens may differ from one another. This is obviously due to the fact that timber is a natural material including non-uniformities such as knots, etc. As a result, these imperfections in the material may undoubtedly trigger the failure in one plain specimen slightly differently from other nominally similar specimens. The combination of timber with materials such as steel and CFRP not only provides a considerable strength but also improves the predictability of the section capacity for such composite beams rather than plain timber beams.

5.6.5 Preference of U-shape sections over flat plate

The second moment of inertia of the present U-shape sections around the main axis against bending is far greater than beams strengthened with flat plates. This is basically due to the fact that the flanges of the U-shape sections provide a great additional second moment of inertia; as a result the flexural capacity of the entire member increases.

On the other hand due to natural defects of the timber material, initiation of the failure in the form of creation and development of cracks is very common in an unreinforced timber. It is quite obvious that U-shape sections cover and support – i.e. prevent easy development of cracks – a greater area of the timber than timber beams reinforced by flat plates. More importantly, the covered areas are located in the regions of maximum tensile and compressive stresses. Therefore, owing to the larger areas covered and supported by U-shape sections, the capacity increases more for the current composite element than for timber beams strengthened with flat plates. This is because the areas of the timber covered by U-shape steel and/or CFRP (uniform materials) are less vulnerable to creation and development of cracks created by natural defects of the timber material.

5.6.6 Comparisons, *structural efficiency* and further discussions

The natural imperfections of the timber material cause a lot of uncertainties in estimating a safe value to design these structures so that design codes must treat this very conservatively to comply with the safety requirements. Thus, the weakest sample among many tested specimens in a certain stress grade is always considered the reference specimen for the design purposes. The Australian Standard AS 1720.1 [153], specifies design bending stress for *Machine Graded Pine* with various stress grades, in which the bending capacity of *MGP10* is 17 MPa (a characteristic value for structural design). The lowest flexural strength of the five plain timber specimen tested was higher at 39.5 MPa, which is attributed primarily to two factors: first, that the present testing considers complete failure of the specimen, which obviously represents loading well beyond the “design” conditions, and second, the fact that the parts of the supplied timber with no severe defects were tested in this experimental program. For the reinforced specimens, the capacity increases were quite consistent considering the amount of the material used in different specimens. Nominally identical specimens (replicated reinforced specimens) showed reasonable agreements with each other, where the capacity difference between *St-St-E* and *R-St-St-E* was 21%, for *NA-St-E* and *R-NA-St-E* it was 20%, while for *NA-FR-E* and *R-NA-FR-E*, and *St-FR-E* and *R-St*-FR-*E* the difference was even lower at 5% and 9% respectively. This is in contrast to the maximum plain specimen having 66% higher capacity than the minimum, meaning that not only did the reinforcement produce a significant capacity increase, but there was also much greater certainty in the capacity, suggesting substantially higher design values may be used.

Structural efficiency (λ) is defined as the ratio of the ultimate strength to the weight of a structural element. *Structural efficiency* is a critical parameter in many projects, particularly where the weight of a structural member is an important factor. Figure 5-60 gives the ratio of ultimate bending capacity (M_{ult}) to the total weight (W_{total}) for different plain and reinforced specimens. As can be seen, *St-FR-E* and *R-St-FR-E* with a combination of steel and CFRP reinforcements gave the highest *structural efficiency*.

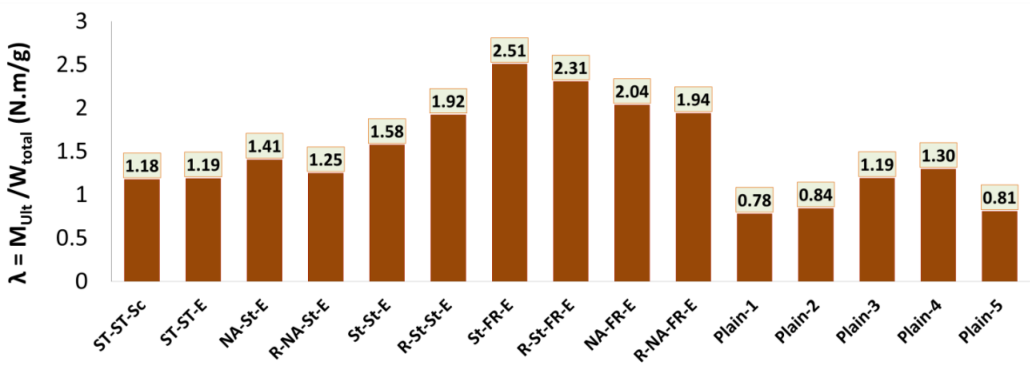

Figure 5-60: The ratio of ultimate capacity to the total weight.

Among these specimens, the average value of *St-FR-E* and *R-St-FR-E* is higher than the average value of *NA-FR-E* and *R-NA-FR-E*. This indicates that although steel (as a relatively heavier element) was used in the compression side of *St-FR-E* and *R-St-FR-E* to strengthen the timber, the capacity gain of the composite beam was higher than the weight gain. It is of interest that the comparison of the *structural efficiency* of the plain timber specimens with the other strengthened specimens shows that the reinforcements in all cases dramatically enhanced the *structural efficiency*. In light of this, the present reinforcements of steel and CFRP provided a very good light-weight structural element against bending.

5.6.7 Summary and concluding remarks

This section aimed to experimentally investigate U-shape steel and CFRP reinforced timber beams under three point bending. Different specimens were tested with various geometric and material specifications. The salient findings are:

The failure in the plain timber specimens was quite abrupt with a sudden rupture in the timber. Although a dramatic rise in the flexural capacity was gained for *ST-ST-Sc*, the existence of the screws presumably initiated the onset of the cracks. However, epoxy provided a reliable steel to timber connection for other specimens as the failure took place with no debonding. Typical brittle failure of the plain timber specimens was largely prevented and/or delayed in the specimens reinforced with the steel sections. Nonetheless, brittle behaviour overwhelmingly governed the failure in *St-FR-E* relative to the specimens fully strengthened by the U-shape steel(s).

The compressive stress of the timber in combination with the steel in the top half, coupled with a significant tensile stress provided by the CFRP on the bottom yielded an appropriate composite beam element. On this basis, *St-FR-E* achieved the greatest bending resistance – gaining a capacity of nearly 5 times the average capacity of the plain specimens. *St-St-E* with double side steel reinforcements comprised the second highest capacity increase.

U-shape steel sections not only enhanced the timber beams in tension, but also brought about a significant capacity increase. The similar flexural capacity of *NA-FR-E* and *NA-St-E* demonstrated a similar effect of single reinforcements in the tension side of the present specimens whether it is a U-shape steel section or CFRP.

In spite of having only a few replicates of each configuration, the differences in the mean values for the various configurations are clearly considerable indicating that the reinforcement produced substantial benefits for each configuration. Further testing may be required to quantify the statistical significance of results.

Considering the *structural efficiency* of the plain specimens, the reinforcements dramatically enhanced the *structural efficiency*. In view of this, the present reinforcements of steel and CFRP provided a promising light-weight structural element against bending.

5.7 Conclusions of Chapter 5

This chapter examines the sectional non-uniformity of steel tubular elements through their composite functionality. Aligned with the topic of the thesis, it was hypothesised that sectional non-uniformity developed through composite materials may help decrease the sensitivity of thin-walled steel tubular elements to normal fabrication-related geometrical non-uniformities. The composite materials of timber, CFRP and concrete were employed so as to synergise with the base element (steel) to reach a great capacity whilst maintaining the light weight for the current composites.

Four sets of tests were conducted to reach different composites for steel thin walled hollow sections under axial compression. CFRP confined circular tubes were studied. It was clear that CFRP significantly restricted locally confined areas of this specimen and accordingly considerably enhanced the capacity. Confined specimens generally showed a more ductile response in the post buckling regime. Hoop confinement exhibited a greater ductility than longitudinal CFRP coverage, suggesting the preferable usage of hoop confinement in these steel tubes. It is believed that the partial confinement reduced the unsupported effective free length in long columns and the global buckling was prevented. A new composite comprising CHS tubes and concrete-timber infills was introduced. Both concrete and timber effectively contributed to the axial capacity. The presence of timber improved the *structural efficiency* of the composite. The timber helped facilitate casting the concrete with a lower cost compared with the double skin tubes. The results suggested the significant effect of the timber infill in providing a considerable ductility for such composite elements. While having a much lighter weight, a timber core also maintained the average crushing load relative to the fully concrete filled specimens. The other composite comprised CHS tubes, a solid timber infill and CFRP confinements. The timber filled specimen confined with three layers of CFRP comprised the greatest ultimate axial load increase of around 146% relative to the bare and empty CHS tube. The same composite configuration was also applied to rectangular steel tubes. Three layers of CFRP sufficiently reinforced these specimens and the buckling was arrested for the timber filled CFRP confined (3 layers) specimen so that the axial capacity was increased. The usage of timber and CFRP brought about a considerable enhancement in the capacity-to-weight ratio for the new composite members. In all cases of timber filled tubes the strength gain significantly exceeded the weight gain. In brief, all tests of this chapter in which timber acted as an infill suggests that the use of timber-filled tubes can potentially gain the attentions of researchers and designers if the existing knowledge is extended and proper equipment is proposed and developed for fabrication of such elements.

The last section of this chapter aimed to investigate U-shape steel and CFRP reinforced timber beams under bending. The U-shape sections were two parts of a SHS tubular section. Typical brittle failure of the plain timber specimens was largely prevented and/or delayed in the specimens reinforced with the steel sections. The compressive strength of the timber in combination with the steel in the top half, coupled with a significant tensile stress provided by the CFRP on the bottom yielded an appropriate composite beam element. U-shape steel sections not only enhanced the timber beams in tension, but also brought about a significant capacity increase. The reinforcements dramatically enhanced the *structural efficiency* compared with the plain specimens.

All tests of this chapter demonstrate that the combination of timber and CFRP with thin-walled steel sections provides promising light-weight structural elements with enhanced capacity and ductility. The last section of the chapter indicates that this combination not only yields reliable results for structural members under axial compression but also flexural members may greatly benefit from the present composite functionality. The significant insight provided by the experimental results of this chapter necessitates further investigation of similar elements to broaden the knowledge and penetrate the knowledge into the practice.

Chapter 6

Conclusions

This thesis focused on an experimental investigation on thin walled steel members with geometric and sectional non-uniformities. Large imperfections were introduced as dents and cutouts on tubular steel structures, the effects of which were examined on the structural response of the tested elements. Remediation of the capacity loss of structures with non-uniformities was also proposed, including applying stiffeners, thickeners, corrugation, and usage of composite functionality. On the one hand composite elements were utilised to reinforce locally imperfect regions. On the other hand composite elements, also regarded as sectional non-uniformity, not only provided lightweight yet strong elements, but also reduced the sensitivity of thin steel sections to the normal fabrication related imperfections through composite functionality. Salient findings of the thesis are summarised as follows.

Thin shells with large geometric non-uniformities

Clearly the dent depth or cutout's geometry and the location were the most important variables in determining the load capacity reduction. Under different loading conditions, dented shells behaved differently in terms of buckling mode and ultimate capacity. The capacity decrease was proportional to the depth of the dent, while the orientation of the dent seemed to have different effects under different loads. Elephant foot and diamond mode buckling were generally dominant for all intact and dented specimens under axial compression, while lobar buckling was obtained for the pressurised shells. For all samples under axial compression the dent – albeit depending upon the depth and location – affected the stability of the structure as evident in the load displacement curves. A bifurcation type of load-displacement was observed for intact and dented thinner shells under axial loading, whilst a limit load type of failure was obtained for the thicker shells. Tested specimens, regardless of loading conditions, geometric non-uniformities and cross sections, even with the large dents or cutouts, were capable of carrying a considerable proportion of the peak axial load after initiation of buckling so that a significant post-buckling strength was maintained for the present specimens.

There seems to be an interrelation between the geometrical irregularity (surface undulation) and the material properties of the dented zone. The former may result in an adverse effect (due to non-uniformity) and an strengthening effect (due to undulation and increase of second moment of inertia) on the capacity whereas the latter appeared to have a positive effect, which is why the areas adjacent to the dented zones were more sensitive to the buckling. The reason is that the dented area is believed to have reached a hardened material in comparison to the intact areas, whilst the area adjacent to the dent was affected by the geometric non-uniformity of the large imperfection, the material of which not as hardened the dented zone.

For all types of dented shells under different loading conditions the decreasing trend was generalised through a regression equation which provides an insight into future numerical and experimental studies on the basis of the presented extensive experimental data. Based on the results of this section though, designers of similar tubular members may gain general insight to decide whether they have to change a dented element, strengthen or keep it, if they encounter similar damages in structures with the same slenderness. This decision, indeed, may be made considering the rate and the type of service loads, the position and the depth of the damage and the significance of the damaged member in different structures.

Perhaps, it would be advisable to categorise the geometrical imperfections in design codes into normal imperfections and large imperfections, e.g. dent or gouges caused by physical contacts. Future studies are still required to thoroughly clarify the effect of different shapes and amplitude of local imperfections on the shell structures with different geometric, loading and boundary conditions.

Reinforcement of thin shells with geometric non-uniformities

The effect of reinforcement on pressurised thin cylindrical shells with normal fabrication-related non-uniformities was studied. Partial and full length stiffeners (stringers) and also full length thickeners with varying number of strengtheners were applied (reinforcement with additional material). The main contributions of this set of experiments were the usage of partial reinforcement as well as the connection method by which the reinforcing elements were applied. This was followed by investigation of longitudinal corrugations in order to enhance the structural stability such structures (reinforcement without additional material). Reinforcement with additional material clearly led to more capacity rise in comparison to the specimens reinforced without additional material. However, the optimum number of corrugations resulted in a considerable capacity increase. As well, total cost of the shells reinforced with corrugation seems far less than reinforcement of the shells through additional material. On this basis, if and when appropriate equipment is provided, the corrugation idea seems to be generally preferable, although special consideration of each project must be taken into account before any decision is made regarding different methods of reinforcement.

Large geometric non-uniformities and cyclic bending

Fatigue response of moderately thin steel tubes was examined and the effect of dents as well as cutouts, as two major geometric non-uniformities was investigated. Following that the effect of CFRP reinforcement on the cyclic behaviour of tubes with cutouts was discussed.

It was found that the failure mode was highly dependent upon the size of the large imperfections. For shells with relatively small dents or cutouts as well as the intact specimens, the BTS mode was seen, which occurred beside and along the welding. The DWF mode occurred both in the dented zone and near the welding for the specimens with medium sized dents. The DCF mode occurred in the trough zone of the dent for the most severe case of the dented specimens, while there was no crack seen in the tension side of the specimens. The CCF mode was detected in medium and larger holes of the tested models such that failure occurred in the central cross-section of the cutout area and extended to the nominal neutral axis of an equivalent intact cross-section. Failure for all CFRP reinforced specimens was in the CCF mode except for the specimen with smallest cutout, which failed in the BTS mode.

The fatigue lives of dented specimens, and CFRP reinforced and unreinforced specimens with cutouts were highly dependent upon the size of non-uniformities. For dented tubes, the more the depth of the dent was, the shorter the fatigue life. For the specimens with cutouts, although a very small hole was not ultimately affected by the fatigue crack, a significant amount of stress concentration was developed near the hole. As a result, the stress concentration near the welding was significantly relieved. With an optimal diameter of a cutout, the stress concentration at the end of the tube was significantly relieved and hence the fatigue life of the specimen dramatically increased. For very large holes the influence of the cutout on the fatigue life was quite negative, which can be attributed to a relatively high loss of the material in the area of the cutout. Nonetheless, CFRP reinforcement dramatically enhanced the fatigue life of the specimens with cutouts such that in two specimens the number of cycles exceeded by 10 and even 14 times the ultimate number of cycles of the intact specimen with no CFRP. In other words, the tubes with cutouts strengthened with a small amount of CFRP significantly outperformed a tube with neither cutout nor strengthening (intact and bare specimen).

Steel elements and sectional non-uniformities (composite functionality)

Sectional non-uniformity of steel tubular elements was examined through their composite functionality. Aligned with the topic of the thesis, it was hypothesised that sectional non-uniformity, developed through composite materials, may help decrease the sensitivity of thin walled steel tubular elements to normal fabrication-related geometrical non-uniformities. The composite materials of timber, CFRP and concrete were employed so as to synergise with the base element (steel) to reach a great capacity whilst maintaining the light weight for the current composites.

CFRP confined circular tubes were studied. It was clear that CFRP significantly restricted locally confined areas of this specimen and accordingly considerably enhanced the capacity. Confined specimens generally showed a more ductile response in the post buckling regime. Hoop confinement exhibited a greater ductility than longitudinal CFRP coverage, suggesting the preferable usage of hoop confinement in these steel tubes. It is believed that the partial confinement reduced the unsupported effective free length in long columns and the global buckling was prevented. A new composite comprising CHS tubes and concrete-timber infills was introduced. Both concrete and timber effectively contributed to the axial capacity. The presence of timber improved the *structural efficiency* of the composite. The timber helped facilitate casting the concrete with a lower cost compared with the double skin tubes. The results suggested the significant effect of the timber infill in providing a considerable ductility for such composite elements. While having a much lighter weight, a timber core also maintained the average crushing load relative to the fully concrete filled specimens. The other composite comprised CHS tubes, a solid timber infill and CFRP confinements. The timber filled specimen confined with three layers of CFRP comprised the greatest ultimate axial load increase relative to the bare and empty CHS tube. The same composite configuration was also applied to rectangular steel tubes. Three layers of CFRP sufficiently reinforced these specimens and the buckling was arrested for the timber filled CFRP confined (3 layers) specimen so that the axial capacity was increased. The usage of timber and CFRP brought about a considerable enhancement in the capacity-to-weight ratio for the new composite members. In all cases of timber filled tubes the strength gain significantly exceeded the weight gain. In brief, all tests in which timber acted as an infill suggests that the use of timber-filled tubes can potentially gain the attentions of researchers and designers if the existing knowledge is extended and proper equipment is proposed and developed for fabrication of such elements.

U-shape steel sections, as two parts of a SHS tubular section, were combined with a timber core to act as a lightweight composite beam. Typical brittle failure of the plain timber specimens was largely prevented and/or delayed in the specimens reinforced with the steel sections. The compressive strength of the timber in combination with the steel in the top half, coupled with a significant tensile stress provided by the CFRP on the bottom yielded an appropriate composite beam element. U-shape steel sections not only enhanced the timber beams in tension, but also brought about a significant capacity increase. The reinforcements dramatically enhanced the *structural efficiency* compared with the plain specimens.

The combination of timber and CFRP with thin-walled steel sections provides promising light-weight structural elements with enhanced capacity and ductility. It appeared that this combination not only yields reliable results for structural members under axial compression but also flexural members may greatly benefit from the present composite functionality. As another advantage, the composite elements were deemed to be less sensitive to imperfections, since the transverse strength of the thin body of the steel members increased when combined with other materials.

Non-uniformities and final remarks

Overall, having observed the geometrical and sectional non-uniformity discussed throughout the entire thesis, brief remarks are presented as:

Non-uniformities appeared as imperfections (dent and cutout) generally had adverse effects on the capacity of the structural members under different loading schemes. In fact, one of the objectives of the thesis was to quantify the capacity change as a result of large imperfections. Having the thesis complete, great benchmark experimental data as well as the general trend of the capacity change are provided through different sections, which may be a proper point of departure for the future analytical and numerical research. Other types of the geometrical non-uniformities – e.g. stiffeners, corrugation, usage of composite functionality (referred to as sectional non-uniformities) – discussed in various sections of the thesis, generally significantly improved the capacity of the current thin-walled steel elements. As well as the capacity though, a major connection point between different non-uniformities is that the sensitivity to the first type of non-uniformity (imperfections) is greatly reduced if and when the other types of non-uniformities are applied to reinforce the present elements.

In short, the capacity of structural members, which are similar to the thin specimens studied in the thesis, is essentially affected by different types of geometric and sectional non-uniformities. Depending on the type of non-uniformity, the capacity may increase or decrease. We initially believed that investigating the current structural elements under an umbrella term of the non-uniformity would provide a general picture towards diverse response of thin-walled structures. This aim was achieved to a large extent, alongside which further insight was provided into different aspects of structural behaviour of these members.

Future work

This thesis endeavoured to study steel thin elements with local and sectional non-uniformities such that different variety of loading and geometric conditions was undertaken for structural elements under the umbrella topic of the thesis. Although quite extensive results were gained through this PhD thesis, further tests as well as numerical and analytical research into the topic may further broaden the knowledge and hence transform it from the laboratory scale to the real structures in full scale. Analytical studies and formulations are required to generalise the effect of the large imperfections. The cyclic response of CHS tubes with imperfections can be further examined through FE analyses. The propounded idea on stress concentration relief is believed to worth further evaluation, since it may generally reduce the risk of failure in many structures. This idea also requires further testing as well as theoretical investigation in terms of size of the cutout, which can be formulated for different D/t ratios, and also different distances of the cutout from the base. Four point bending tests can be considered for the composite beams including timber, steel and CFRP so that the results can be compared to the results of three point bending of this study. Future work should cover extensive testing with sufficient replicates when a natural material (here timber) with a lower uniformity takes part as a structural element in a composite. Finally, the optimal usage of timber as a composite member to lighten the total weight of structural elements, yet to enhance the capacity, and to reduce the total cost of composite members may be considered in future investigations.

BIBLIOGRAPHY

[1] H. Jiao and X.-L. Zhao, "Imperfection, residual stress and yield slenderness limit of very high strength (VHS) circular steel tubes," *Journal of Constructional Steel Research,* vol. 59, pp. 233-249, 2003.

[2] A. Sofiyev, "Influence of the initial imperfection on the non-linear buckling response of FGM truncated conical shells," *International Journal of Mechanical Sciences,* vol. 53, pp. 753-761, 2011.

[3] J.-G. Teng and J. M. Rotter, *Buckling of thin metal shells*: CRC Press, 2006.

[4] T. Hong and J. Teng, "Imperfection sensitivity and postbuckling analysis of elastic shells of revolution," *Thin-Walled Structures,* vol. 46, pp. 1338-1350, 2008.

[5] J. Teng and T. Hong, "Postbuckling analysis of elastic shells of revolution considering mode switching and interaction," *International journal of solids and structures,* vol. 43, pp. 551-568, 2006.

[6] A. G. Karasev, "Initial imperfection influence on the buckling load of closed elastic isotropic shallow conical shells," *Mathematics and Mechanics of Solids,* vol. 21, pp. 444-453, 2016.

[7] U. Hornung and H. Saal, "Buckling loads of tank shells with imperfections," *International Journal of Non-Linear Mechanics,* vol. 37, pp. 605-621, 2002.

[8] S. E. Firouzsalari and H. Showkati, "Thorough investigation of continuously supported pipelines under combined pre-compression and denting loads," *International Journal of Pressure Vessels and Piping,* vol. 104, pp. 83-95, 2013.

[9] C. Karroum, S. Reid, and S. Li, "Indentation of ring-stiffened cylinders by wedge-shaped indenters—Part 1: An experimental and finite element investigation," *International journal of mechanical sciences,* vol. 49, pp. 13-38, 2007.

[10] J. Paik, "Dented structures and residual strength," *Condition Assessment of Aged Structures,* p. 231, 2014.

[11] T.-D. Park and S. Kyriakides, "On the collapse of dented cylinders under external pressure," *International Journal of Mechanical Sciences,* vol. 38, pp. 557-578, 1996.

[12] Prabu, Bujjibabu, Saravanan, and Venkatraman, "Effect of a dent of different sizes and angles of inclination on buckling strength of a short stainless steel cylindrical shell subjected to uniform axial compression," *Advances in Structural Engineering,* vol. 10, pp. 581-591, 2007.

[13] B. Prabu, A. Raviprakash, and A. Venkatraman, "Parametric study on buckling behaviour of dented short carbon steel cylindrical shell

subjected to uniform axial compression," *Thin-Walled Structures,* vol. 48, pp. 639-649, 2010.

[14] N. Rathinam and B. Prabu, "Static buckling analysis of thin cylindrical shell with centrally located dent under uniform lateral pressure," *International Journal of Steel Structures,* vol. 13, pp. 509-518, 2013.

[15] N. Rathinam and B. Prabu, "Strength of dented thin cylindrical shells under external pressure," *Shell Structures: Theory and Application,* p. 433, 2013.

[16] A. Raviprakash, B. Prabu, and N. Alagumurthi, "Effect of size and orientation of a centrally located dent on the ultimate strength of a thin square steel plate under axial compression," *International Journal of Steel Structures,* vol. 12, pp. 47-58, 2012.

[17] A. Limam, L.-H. Lee, E. Corona, and S. Kyriakides, "Inelastic wrinkling and collapse of tubes under combined bending and internal pressure," *International Journal of Mechanical Sciences,* vol. 52, pp. 637-647, 2010.

[18] E. Corona, L.-H. Lee, and S. Kyriakides, "Yield anisotropy effects on buckling of circular tubes under bending," *International Journal of Solids and Structures,* vol. 43, pp. 7099-7118, 2006.

[19] P. Song and Y. Shieh, "Stop drilling procedure for fatigue life improvement," *International journal of fatigue,* vol. 26, pp. 1333-1339, 2004.

[20] C. Shin, C. Wang, and P. Song, "Fatigue damage repair: a comparison of some possible methods," *International journal of fatigue,* vol. 18, pp. 535-546, 1996.

[21] A. Murdani, C. Makabe, A. Saimoto, and R. Kondou, "A crack-growth arresting technique in aluminum alloy," *Engineering Failure Analysis,* vol. 15, pp. 302-310, 2008.

[22] H. Showkati and R. Shahandeh, "Experiments on the buckling behavior of ring-stiffened pipelines under hydrostatic pressure," *Journal of engineering mechanics,* vol. 136, pp. 464-471, 2009.

[23] K. Imani, H. Showkati, and T. Ghanbari Ghazijahani, "Bending experiments on reinforced circular thin plates under uniform pressure," *Journal of Constructional Steel Research,* vol. 80, pp. 308-316, 2013.

[24] J. Chen and J. Rotter, "Effective cross sections of asymmetric rings on cylindrical shells," *Journal of Structural Engineering,* vol. 124, pp. 1074-1080, 1998.

[25] M. Barkey, M. Turgeon, and T. V. Nare, "Buckling of stiffened thin-walled truncated cones subjected to external pressure," *Experimental Mechanics,* vol. 48, pp. 281-291, 2008.

[26] Y. B. Kwon, S. J. Seo, and D. W. Kang, "Prediction of the squash loads of concrete-filled tubular section columns with local buckling," *Thin-Walled Structures,* vol. 49, pp. 85-93, 2011.

[27] Y. B. Kwon and I. K. Jeong, "Resistance of rectangular concrete-filled tubular (CFT) sections to the axial load and combined axial compression and bending," *Thin-Walled Structures,* vol. 79, pp. 178-186, 2014.
[28] M. Dundu, "Compressive strength of circular concrete filled steel tube columns," *Thin-Walled Structures,* vol. 56, pp. 62-70, 2012.
[29] Y. Yang and L. Han, "Concrete filled steel tube (CFST) columns subjected to concentrically partial compression," *Thin-Walled Structures,* vol. 50, pp. 147-156, 2012.
[30] Y.-F. Yang and L.-H. Han, "Behaviour of concrete filled steel tubular (CFST) stub columns under eccentric partial compression," *Thin-Walled Structures,* vol. 49, pp. 379-395, 2011.
[31] M. V. Chitawadagi, M. C. Narasimhan, and S. Kulkarni, "Axial strength of circular concrete-filled steel tube columns—DOE approach," *Journal of Constructional Steel Research,* vol. 66, pp. 1248-1260, 2010.
[32] Z. Tao, B. Uy, F.-Y. Liao, and L.-H. Han, "Nonlinear analysis of concrete-filled square stainless steel stub columns under axial compression," *Journal of Constructional Steel Research,* vol. 67, pp. 1719-1732, 2011.
[33] J. Teng, T. Yu, Y. Wong, and S. Dong, "Hybrid FRP–concrete–steel tubular columns: concept and behavior," *Construction and Building Materials,* vol. 21, pp. 846-854, 2007.
[34] S. Aghajari, K. Abedi, and H. Showkati, "Buckling and post-buckling behavior of thin-walled cylindrical steel shells with varying thickness subjected to uniform external pressure," *Thin-walled structures,* vol. 44, pp. 904-909, 2006.
[35] B. Golzan and H. Showkati, "Buckling of thin-walled conical shells under uniform external pressure," *Thin-Walled Structures,* vol. 46, pp. 516-529, 2008.
[36] H. Showkati and P. Ansourian, "Influence of primary boundary conditions on the buckling of shallow cylindrical shells," *Journal of Constructional Steel Research,* vol. 36, pp. 53-75, 1996.
[37] J. Bennett, R. Dove, and T. Butler, "An investigation of buckling of steel cylinders with circular reinforced cutouts," *Nuclear Engineering and Design,* vol. 69, pp. 229-239, 1982.
[38] C. Dimopoulos and C. Gantes, "Comparison of stiffening types of the cutout in tubular wind turbine towers," *Journal of Constructional Steel Research,* vol. 83, pp. 62-74, 2013.
[39] H. Han, J. Cheng, F. Taheri, and N. Pegg, "Numerical and experimental investigations of the response of aluminum cylinders with a cutout subject to axial compression," *Thin-Walled Structures,* vol. 44, pp. 254-270, 2006.

[40] M. Shariati and M. M. Rokhi, "Numerical and experimental investigations on buckling of steel cylindrical shells with elliptical cutout subject to axial compression," *Thin-Walled Structures,* vol. 46, pp. 1251-1261, 2008.

[41] M. Shariati and M. M. Rokhi, "Buckling of steel cylindrical shells with an elliptical cutout," *International journal of steel structures*, vol. 10, pp. 193-205, 2010.

[42] R. Tennyson, "The effects of unreinforced circular cutouts on the buckling of circular cylindrical shells under axial compression," *Journal of Engineering for Industry,* vol. 90, pp. 541-546, 1968.

[43] S. Eggwertz and L. Å. Samuelson, "Design of shell structures with openings subjected to buckling," *Journal of Constructional Steel Research,* vol. 18, pp. 155-163, 1991.

[44] J. Jullien and A. Limam, "Effects of openings of the buckling of cylindrical shells subjected to axial compression," *Thin-Walled Structures,* vol. 31, pp. 187-202, 1998.

[45] T. Ghanbari Ghazijahani and H. Showkati, "Experiments on cylindrical shells under pure bending and external pressure," *Journal of Constructional Steel Research,* vol. 88, pp. 109-122, 2013.

[46] T. G. Ghazijahani and H. Showkati, "Bending experiments on thin cylindrical shells," in *Materials with Complex Behaviour II*, ed: Springer, 2012, pp. 119-139.

[47] S. Hauch and Y. Bai, "Bending moment capacity of groove corroded pipes," in *The Tenth International Offshore and Polar Engineering Conference*, 2000.

[48] C. Thinvongpituk, S. Poonaya, S. Choksawadee, and M. Lee, "The Ovalisation of Thin-walled Circular Tubes Subjected to Bending," in *Proceedings of the World Congress on Engineering*, 2008.

[49] T. Ghanbari Ghazijahani, H. Jiao, and D. Holloway, "Experimental study on damaged cylindrical shells under compression," *Thin-Walled Structures,* vol. 80, pp. 13-21, 2014.

[50] T. Ghanbari Ghazijahani, H. Jiao, and D. Holloway, "Experiments on dented cylindrical shells under peripheral pressure," *Thin-Walled Structures,* vol. 84, pp. 50-58, 2014.

[51] T. Ghanbari Ghazijahani, H. Jiao, and D. Holloway, "Experiments on Dented Steel Tubes under Bending," *Journal of Advances in Structural Engineering,* vol. 18, pp. 1807-1818, 2015.

[52] T. Ghanbari Ghazijahani, H. Jiao, and D. Holloway, "Fatigue Tests of Damaged Tubes under Flexural Loading," *Steel and Composite Structures, An International Journal*, vol. 19, pp. 223-236, 2015.

[53] S. Eyvazinejad Firouzsalari and H. Showkati, "Behavior of pre-compressed tubes subjected to local loads," *Ocean Engineering,* vol. 65, pp. 19-31, 2013.

[54] S. A. Karamanos and C. Eleftheriadis, "Collapse of pressurized elastoplastic tubular members under lateral loads," *International Journal of Mechanical Sciences,* vol. 46, pp. 35-56, 2004.

[55] T. Ghanbari Ghazijahani, H. Jiao, and D. Holloway, "Influence of a cutout on circular steel hollow sections under cyclic loading," *Journal of Constructional Steel Research,* vol. 100, pp. 12-20, 2014.

[56] T. Ghanbari Ghazijahani, H. Jiao, and D. Holloway, "Structural behavior of shells with different cutouts under compression: an experimental study," *Journal of Constructional Steel Research,* vol. 105, pp. 129-137, 2015.

[57] M. D. O'Shea and R. Q. Bridge, "Local buckling of thin-walled circular steel sections with or without internal restraint," *Journal of Constructional Steel Research*, vol. 41, pp. 137-157, 1997.

[58] D. R. Sherman, *Tubular members, in constructional steel design: an international guide. Dowling PJ, Harding JE, Bjorhovde R (editors), London: Elsevier Applied Science; 1992. p. 91-104.*

[59] H. Prion and P. Birkemoe, "Beam-column behavior of fabricated steel tubular members," *Journal of Structural Engineering,* vol. 118, pp. 1213-1232, 1992.

[60] Eu.3, "1-1-Eurocode 3: Design of steel structures-Part 1-1: General rules and rules for buildings," *European Committee for Standardization,* 2005.

[61] M. Bradford, H. Loh, and B. Uy, "Slenderness limits for CHS sections," in *Ninth international symposium on tubular structures,* 2001, pp. 377-381.

[62] T. G. Ghazijahani and H. Showkati, "Experiments on conical shell reducers under uniform external pressure," *Journal of Constructional Steel Research*, vol. 67, pp. 1506-1515, 2011.

[63] T. Ghanbari Ghazijahani and H. Showkati, "An experimental investigation on interactive behavior of thin walled cylindrical shells," *Materialwissenschaft und Werkstofftechnik,* vol. 44, pp. 386-394, 2013.

[64] T. Ghanbari Ghazijahani and H. Showkati, "Locally imperfect conical shells under uniform external pressure," *Strength of Materials,* vol. 45, pp. 369-377, 2013.

[65] T. Ghanbari Ghazijahani and T. Zirakian, "Determination of buckling loads of conical shells using extrapolation techniques," *Thin-Walled Structures,* vol. 74, pp. 292-299, 2014.

[66] J. Wang and A. Koizumi, "Buckling of cylindrical shells with longitudinal joints under external pressure," *Thin-Walled Structures,* vol. 48, pp. 897-904, 2010.

[67] C. De Paor, D. Kelliher, K. Cronin, W. Wright, and S. McSweeney, "Prediction of vacuum-induced buckling pressures of thin-walled cylinders," *Thin-Walled Structures,* vol. 55, pp. 1-10, 2012.

[68] M. Maali, H. Showkati, and S. Mahdi Fatemi, "Investigation of the buckling behavior of conical shells under weld-induced imperfections," *Thin-Walled Structures,* vol. 57, pp. 13-24, 2012.
[69] S. M. Fatemi, H. Showkati, and M. Maali, "Experiments on imperfect cylindrical shells under uniform external pressure," *Thin-Walled Structures,* vol. 65, pp. 14-25, 2013.
[70] A. Niloufari, H. Showkati, M. Maali, and S. Mahdi Fatemi, "Experimental investigation on the effect of geometric imperfections on the buckling and post-buckling behavior of steel tanks under hydrostatic pressure," *Thin-Walled Structures,* vol. 74, pp. 59-69, 2014.
[71] T. G. Ghazijahani and H. Showkati, "Locally imperfect conical shells under uniform external pressure," *Strength of Materials,* vol. 45, pp. 369-377, 2013.
[72] J. Singer, J. Arbocz, and T. Weller, *Buckling experiments: experimental methods in buckling of thin-walled structures* vol. 2: Wiley New York, 2002.
[73] M. H. Jawad, *Theory and design of plate and shell structures*: Chapman & Hall, 1994.
[74] C. T. Ross, "A proposed design chart to predict the inelastic buckling pressures for conical shells under uniform external pressure," *Marine Technology,* vol. 44, pp. 77-81, 2007.
[75] *British Standards Institution, Specification for unfired fusion welded pressure vessels: BSI, 2000.*
[76] *European Convention for Constructional Steelwork (ECCS). Buckling of steel shells-European recommendations ECCS-CECM-EKS, Belgium, 1988.*
[77] *EN1993-1-6: Eurocode 3Design of steel structures, Part 1.6: General rules-Strength and stability of shell structures. Eurocode 3 Part 1.6, CEN, Brussels. 2007.*
[78] *DIN 18800. Stahlbauten.Teil 4: Stabilitätsfalle, Schalenbeulen 1990.*
[79] *ECCS EDR5. European recommendations for steel construction. Buckling of shells, 5th ed. Rotter JM, Schmidt H, editors. European convention for constructional steelwork, Brussels; 2008. 384 p.*
[80] H. El-Sobky and A. Singace, "An experiment on elastically compressed frusta," *Thin-walled structures,* vol. 33, pp. 231-244, 1999.
[81] N. Gupta, N. M. Sheriff, and R. Velmurugan, "A study on buckling of thin conical frusta under axial loads," *Thin-walled structures,* vol. 44, pp. 986-996, 2006.
[82] N. Gupta and H. Abbas, "Axisymmetric axial crushing of thin frusta," *Thin-walled structures,* vol. 36, pp. 169-179, 2000.
[83] G. Prasad and N. Gupta, "An experimental study of deformation modes of domes and large-angled frusta at different rates of compression," *International journal of impact engineering,* vol. 32, pp. 400-415, 2005.

[84] O. F. Ifayefunmi, "Combined stability of conical shells," University of Liverpool, 2011.
[85] J. Błachut, "Interactive plastic buckling of cones subjected to axial compression and external pressure," *Ocean Engineering,* vol. 48, pp. 10-16, 2012.
[86] J. Błachut, "On elastic–plastic buckling of cones," *Thin-Walled Structures,* vol. 49, pp. 45-52, 2011.
[87] X. Zhao and K. M. Liew, "An element-free analysis of mechanical and thermal buckling of functionally graded conical shell panels," *International Journal for Numerical Methods in Engineering,* vol. 86, pp. 269-285, 2011.
[88] J. Błachut, A. Muc, and J. Ryś, "Plastic Buckling of Cones Subjected to Axial Compression and External Pressure," *Journal of Pressure Vessel Technology,* vol. 135, p. 011205, 2013.
[89] P. Gupta, "A study on mode of collapse of varying wall thickness metallic frusta subjected to axial compression," *Thin-Walled Structures,* vol. 46, pp. 561-571, 2008.
[90] T. G. Ghazijahani, H. Jiao, and D. Holloway, "Plastic buckling of dented steel circular tubes under axial compression: An experimental study," *Thin-Walled Structures,* vol. 92, pp. 48-54, 2015.
[91] *AS 1391, Australian Standard, Metallic Materials, Tensile Testing at Ambient Temperature, 2007.*
[92] T. G. Ghazijahani, H. Jiao, and D. Holloway, "Longitudinally stiffened corrugated cylindrical shells under uniform external pressure," *Journal of Constructional Steel Research,* vol. 110, pp. 191-199, 2015.
[93] P. Seide, "Axisymmetric Buckling of Circular Cones under Axial Compression," *J. Appl. Mech.,* vol. 23, no 4, pp. 625-628, 1956.
[94] L. Lackman and J. Penzien, "Buckling of circular cones under axial compression," *Journal of Applied Mechanics,* vol. 27, pp. 458-460, 1960.
[95] T. G. Ghazijahani, H. Jiao, and D. Holloway, "Influence of a cutout on circular steel hollow sections under cyclic loading," *Journal of Constructional Steel Research,* vol. 100, pp. 12-20, 2014.
[96] *SAA. Cold-formed steel structures. Sydney: Australian/New Zealand Standard AS/NZS4600, Standards, Australia, 1996*.
[97] I. F. Ozkan and M. Mohareb, "Moment resistance of steel pipes subjected to combined loads," *International Journal of Pressure Vessels and Piping,* vol. 86, pp. 252-264, 2009.
[98] J. Taby, T. Moan, and S. Rashed, "Theoretical and experimental study of the behaviour of damaged tubular members in offshore structures," *Norwegian Maritime Research,* vol. 9, pp. 26-33, 1981.
[99] C. P. Ellinas, "Ultimate strength of damaged tubular bracing members," *Journal of Structural Engineering,* vol. 110, pp. 245-259, 1984.

[100] C. Smith, W. Kirkwood, and J. Swan, "Buckling strength and post-collapse behaviour of tubular bracing members including damage effects," in *Proceedings of the Second International Conference on the Behaviour of Off-Shore Structures, held at Imperial College, London, England*, 1979.

[101] C. Smith, W. Somerville, and J. Swan, "Residual strength and stiffness of damaged steel bracing members," in *Offshore Technology Conference*, 1981.

[102] S. Kyriakides, C. Babcock, and D. Elyada, "Initiation of propagating buckles from local pipeline damages," *Journal of energy resources technology*, vol. 106, pp. 79-87, 1984.

[103] *Robert Bea, Tao Xu, Ram Pipe Requal (Pipeline Requalification Guidelines Project) Marine Technology and Management Group, University of California at Berkeley, Report 4. Risk Assessment and Management (RAM) based guidelines for requalification of marine pipelines, 2000.*

[104] T. Ghanbari Ghazijahani and H. Showkati, "Experiments on conical shell reducers under uniform external pressure," *Journal of Constructional Steel Research*, vol. 67, pp. 1506-1515, 2011.

[105] T. G. Ghazijahani, H. Jiao, and D. Holloway, "Experiments on dented cylindrical shells under peripheral pressure," *Thin-Walled Structures*, vol. 84, pp. 50-58, 2014.

[106] T. G. Ghazijahani, H. Jiao, and D. Holloway, "An experimental study on externally pressurized stiffened and thickened cylindrical shells," *Thin-Walled Structures*, vol. 85, pp. 359-366, 2014.

[107] C. Ross, "A redesign of the corrugated tin can," *Thin-walled structures*, vol. 26, pp. 179-193, 1996.

[108] C. T. Ross, "Collapse of corrugated circular cylinders under uniform external pressure," *International Journal of Structural Stability and Dynamics*, vol. 5, pp. 241-257, 2005.

[109] C. T. Ross and G. A. Waterman, "Inelastic instability of circular corrugated cylinders under external hydrostatic pressure," *Ocean engineering*, vol. 27, pp. 331-343, 2000.

[110] C. Ross and M. Humphries, "The buckling of corrugated circular cylinders under uniform external pressure," *Thin-walled structures*, vol. 17, pp. 259-271, 1993.

[111] C. Ross, A. Terry, and A. Little, "A design chart for the plastic collapse of corrugated cylinders under external pressure," *Ocean engineering*, vol. 28, pp. 263-277, 2001.

[112] C. T. Ross, *Pressure vessels: external pressure technology*: Elsevier, 2011.

[113] C. T. Ross and T. Heigl, "Buckling of corrugated axisymmetric shells under uniform external pressure," in *Proc ASME Conf on Structural Dynamics and vibrations, PD*, 1995, pp. 199-205.

[114] K. Wang, L.-W. Tong, J. Zhu, X.-L. Zhao, and F. R. Mashiri, "Fatigue Behavior of Welded T-Joints with a CHS Brace and CFCHS Chord under Axial Loading in the Brace," *Journal of Bridge Engineering,* vol. 18, pp. 142-152, 2011.

[115] T. Chen, Z.-G. Xiao, X.-L. Zhao, and X.-L. Gu, "A boundary element analysis of fatigue crack growth for welded connections under bending," *Engineering Fracture Mechanics,* 2012.

[116] K. Chang, C. Hsu, S. Sheu, and W.-F. Pan, "Viscoplastic response and collapse of 316L stainless steel tubes under cyclic bending," *Steel and Composite Structures, An Int'l Journal* vol. 5, pp. 359-374, 2005.

[117] K.-H. Chang, K.-L. Lee, and W.-F. Pan, "Buckling failure of 310 stainless steel tubes with different diameter-to-thickness ratios under cyclic bending," *Steel and Composite Structures, An Int'l Journal* vol. 10 No. 3, 2010.

[118] J. L. a. J. K. Junhee Park, "Cyclic test of buckling restrained braces composed of square steel rods and steel tube," *Steel and Composite Structures, An Int'l Journal,* vol. 13 No. 5, 2012.

[119] T. Ghanbari Ghazijahani, H. Jiao, and D. Holloway, "Experiments on Dented Steel Tubes under Bending," *Journal of Advances in Structural Engineering,* vol. 18, pp. 1807-1818, 2015.

[120] A. Limam, L.-H. Lee, and S. Kyriakides, "On the collapse of dented tubes under combined bending and internal pressure," *International Journal of Mechanical Sciences,* vol. 55, pp. 1-12, 2012.

[121] H. Jiao, F. Mashiri, and X.-L. Zhao, "Fatigue behavior of very high strength (VHS) circular steel tube to plate T-joints under in-plane bending," *Thin-Walled Structures,* vol. 68, pp. 106-112, 2013.

[122] F. Mashiri and X. Zhao, "Fatigue tests and design of thin CHS-plate T-joints under cyclic in-plane bending," *Thin-walled structures,* vol. 45, pp. 463-472, 2007.

[123] R. Alashti, G. Rahimi, and E. Poursaeidi, "Plastic limit load of cylindrical shells with cutouts subject to pure bending moment," *International Journal of Pressure Vessels and Piping,* vol. 85, pp. 498-506, 2008.

[124] M.-K. Yeh, M.-C. Lin, and W.-T. Wu, "Bending buckling of an elastoplastic cylindrical shell with a cutout," *Engineering structures,* vol. 21, pp. 996-1005, 1999.

[125] M. Shariati, "Buckling Load Analysis of oblique Loaded Stainless Steel 316ti Cylindrical Shells with Elliptical Cutout," *Research Journal of Recent Sciences,* vol. 8, 2012.

[126] I. Lavassas, G. Nikolaidis, P. Zervas, E. Efthimiou, I. Doudoumis, and C. Baniotopoulos, "Analysis and design of the prototype of a steel 1-MW wind turbine tower," *Engineering structures,* vol. 25, pp. 1097-1106, 2003.

[127] E. Poursaeidi, G. Rahimi, and A. Vafai, "Plastic buckling of cylindrical shells with cutouts," *Asian Journal of civil engineering (Building and housing)*, vol. 5, pp. 191-207, 2004.
[128] M. Bijak-Zochowski, A. M. Waas, W. Anderson, and C. Miniatt, "Reduction of contact stress by use of relief notches," *Experimental mechanics*, vol. 31, pp. 271-275, 1991.
[129] H. Han, F. Taheri, and N. Pegg, "Quasi-static and dynamic crushing behaviors of aluminum and steel tubes with a cutout," *Thin-walled structures*, vol. 45, pp. 283-300, 2007.
[130] M. W. Hilburger and J. H. Starnes Jr, "Buckling behavior of compression-loaded composite cylindrical shells with reinforced cutouts," *International Journal of Non-Linear Mechanics*, vol. 40, pp. 1005-1021, 2005.
[131] T. Ghanbari Ghazijahani, H. Jiao, and D. Holloway, "Fatigue Tests of Damaged Tubes under Flexural Loading," *Journal of Steel and Composite Structure* vol. 19, No. 1, pp. 223-236, 2015.
[132] F. R. Mashiri and X.-L. Zhao, "Thin circular hollow section-to-plate T-joints: Stress concentration factors and fatigue failure under in-plane bending," *Thin-walled structures*, vol. 44, pp. 159-169, 2006.
[133] F. Mashiri, X.-L. Zhao, P. Grundy, and L. Tong, "Fatigue design of welded very thin-walled SHS-to-plate joints under in-plane bending," *Thin-walled structures*, vol. 40, pp. 125-151, 2002.
[134] L.-W. Tong, X. Zhao, F. Mashiri, P. Grundy, and H. Z. Zheng, "Fatigue behaviour of welded thin-walled joints between circular and square hollow sections," *International Journal of Steel Structures*, vol. 6, pp. 37-44, 2006.
[135] W. Li, L.-H. Han, and X.-L. Zhao, "Axial strength of concrete-filled double skin steel tubular (CFDST) columns with preload on steel tubes," *Thin-Walled Structures*, vol. 56, pp. 9-20, 2012.
[136] H. Huang, L.-H. Han, Z. Tao, and X.-L. Zhao, "Analytical behaviour of concrete-filled double skin steel tubular (CFDST) stub columns," *Journal of Constructional Steel Research*, vol. 66, pp. 542-555, 2010.
[137] K. Uenaka, H. Kitoh, and K. Sonoda, "Concrete filled double skin circular stub columns under compression," *Thin-walled structures*, vol. 48, pp. 19-24, 2010.
[138] W. Li, Q.-X. Ren, L.-H. Han, and X.-L. Zhao, "Behaviour of tapered concrete-filled double skin steel tubular (CFDST) stub columns," *Thin-walled structures*, vol. 57, pp. 37-48, 2012.
[139] Y.-F. Yang, L.-H. Han, and B.-H. Sun, "Experimental behaviour of partially loaded concrete filled double-skin steel tube (CFDST) sections," *Journal of Constructional Steel Research*, vol. 71, pp. 63-73, 2012.

[140] J. Haedir and X.-L. Zhao, "Design of short CFRP-reinforced steel tubular columns," *Journal of Constructional Steel Research,* vol. 67, pp. 497-509, 2011.
[141] J. Teng and Y. Hu, "Behaviour of FRP-jacketed circular steel tubes and cylindrical shells under axial compression," *Construction and Building Materials,* vol. 21, pp. 827-838, 2007.
[142] N. D. Stevens and G. K. Criner, "B848: Economic Analysis of Fiber-Reinforced Polymer Wood Beams," 2000.
[143] E. Battles, H. Dagher, and B. Abdel-Magid, "Durability of composite reinforcement for timber bridges," *Transportation Research Record: Journal of the Transportation Research Board,* pp. 131-135, 2000.
[144] H. Dagher, M. Bragdon, and R. Lindyberg, "Advanced fiber-reinforced polymer-wood composites in transportation applications," *Transportation Research Record: Journal of the Transportation Research Board,* pp. 237-242, 2002.
[145] R. Lopez-Anido, A. P. Michael, and T. C. Sandford, "Experimental characterization of FRP composite-wood pile structural response by bending tests," *Marine Structures,* vol. 16, pp. 257-274, 2003.
[146] H. Dagher and R. Lindyberg, "Development of the AASHTO specifications for FRP-reinforced glulam beams," in *82nd Annual Meeting of the Transportation Research Board,* 2003, pp. 2-1.
[147] J. K. Botting, "Development of an FRP Reinforced Hardwood Glulam Guardrail," 2003.
[148] L.-H. Han, Q.-X. Ren, and W. Li, "Tests on stub stainless steel–concrete–carbon steel double-skin tubular (DST) columns," *Journal of Constructional Steel Research,* vol. 67, pp. 437-452, 2011.
[149] L.-H. Han, Y.-J. Li, and F.-Y. Liao, "Concrete-filled double skin steel tubular (CFDST) columns subjected to long-term sustained loading," *Thin-walled structures,* vol. 49, pp. 1534-1543, 2011.
[150] T. Ghanbari Ghazijahani, H. Jiao, and D. Holloway, "Rectangular steel tubes with timber infill and CFRP confinement under compression: Experiments," *Journal of Constructional Steel Research,* vol. 114, pp. 196-203, 2015.
[151] T. G. Ghazijahani, H. Jiao, and D. Holloway, "Timber filled CFRP jacketed circular steel tubes under axial compression," *Construction and Building Materials,* vol. 94, pp. 791-799, 2015.
[152] *AS 1012, Australian Standard, Methods of Testing Concrete, 1993.*
[153] *AS 1720.1, Australian Standard, Timber Structures-Part 1: Design Methods, 2010.*
[154] *AS 3600, Australian Standard, Concrete Structures, 2009.*
[155] L. Yan and N. Chouw, "Crashworthiness characteristics of flax fibre reinforced epoxy tubes for energy absorption application," *Materials & Design,* vol. 51, pp. 629-640, 2013.

[156] Y. Xiao, "Applications of FRP composites in concrete columns," *Advances in Structural Engineering,* vol. 7, pp. 335-343, 2004.
[157] Y. Xiao, W. He, and K.-k. Choi, "Confined concrete-filled tubular columns," *Journal of structural engineering,* vol. 131, pp. 488-497, 2005.
[158] L. A. Bisby and T. J. Stratford, "The ultimate condition of FRP confined concrete columns: New experimental observations and insights," in *Advances in FRP Composites in Civil Engineering*, ed: Springer, 2011, pp. 599-602.
[159] T. C. Rousakis and A. I. Karabinis, "Adequately FRP confined reinforced concrete columns under axial compressive monotonic or cyclic loading," *Materials and structures,* vol. 45, pp. 957-975, 2012.
[160] L. Bisby and M. Ranger, "Axial–flexural interaction in circular FRP-confined reinforced concrete columns," *Construction and Building Materials,* vol. 24, pp. 1672-1681, 2010.
[161] J. M. Rotter, "Local collapse of axially compressed pressurized thin steel cylinders," *Journal of Structural Engineering,* vol. 116, pp. 1955-1970, 1990.
[162] L. Hollaway and J. Cadei, "Progress in the technique of upgrading metallic structures with advanced polymer composites," *Progress in Structural Engineering and Materials,* vol. 4, pp. 131-148, 2002.
[163] J. Teng and Y. Hu, "Suppression of local buckling in steel tubes by FRP jacketing," in *Proceedings, 2nd international conference on FRP composites in civil engineering, Adelaide, Australia*, 2004, pp. 8-10.
[164] X.-L. Zhao and L. Zhang, "State-of-the-art review on FRP strengthened steel structures," *Engineering Structures,* vol. 29, pp. 1808-1823, 2007.
[165] M. Seica, J. Packer, P. Ramirez, S. Bell, and X. Zhao, "Rehabilitation of tubular members with carbon reinforced polymers," 2006.
[166] T. C. Miller, M. J. Chajes, D. R. Mertz, and J. N. Hastings, "Strengthening of a steel bridge girder using CFRP plates," *Journal of Bridge Engineering,* vol. 6, pp. 514-522, 2001.
[167] T. Ghanbari Ghazijahani, H. Jiao, and D. Holloway, " Fatigue Experiments on Circular Hollow Sections with CFRP Reinforced Cutouts," *Journal of Constructional Steel Research (accepted in press).* 2015.
[168] J. Haedir, M. Bambach, X.-L. Zhao, and R. Grzebieta, "Strength of circular hollow sections (CHS) tubular beams externally reinforced by carbon FRP sheets in pure bending," *Thin-walled structures,* vol. 47, pp. 1136-1147, 2009.
[169] T. Nishino and T. Furukawa, "Strength and deformation capacities of circular hollow section steel member reinforced with carbon fiber," in *Proceedings of 7th Pacific structural steel conference, American Institute of Steel Construction*, 2004.

[170] *AISI. Specification for the design of cold-formed steel structural members. Washington, DC: American Iron and Steel Institute; 1996.*
[171] MA Bradford, HY Loh, and B Uy, *In: H Puthli, editor. Slenderness limits for CHS sections: tubular structures IX. Rotterdam: Balkema*, pp. 377-81, 2001.
[172] G. Campana, G. Bertuzzi, G. Tani, L. Bonaccorsi, and E. Proverbio, "Experimental investigation into laser welding of aluminum foam filled steel tubes," in *Proceedings of the 5th International Conference on Porous Metals and Metallic Foams, MetFoam*, 2008, pp. 453-456.
[173] I. Hall, O. Ebil, M. Guden, and C.-J. Yu, "Quasi-static and dynamic crushing of empty and foam-filled tubes," *Journal of materials science,* vol. 36, pp. 5853-5860, 2001.
[174] M. Iwata and M. Murai, "Buckling-restrained brace using steel mortar planks; performance evaluation as a hysteretic damper," *Earthquake engineering & structural dynamics,* vol. 35, pp. 1807-1826, 2006.
[175] Q.-X. Ren, L.-H. Han, D. Lam, and C. Hou, "Experiments on special-shaped CFST stub columns under axial compression," *Journal of Constructional Steel Research,* vol. 98, pp. 123-133, 2014.
[176] H. Kavi, A. K. Toksoy, and M. Guden, "Predicting energy absorption in a foam-filled thin-walled aluminum tube based on experimentally determined strengthening coefficient," *Materials & design,* vol. 27, pp. 263-269, 2006.
[177] L. Aktay, A. Toksoy, and M. Güden, "Quasi-static axial crushing of extruded polystyrene foam-filled thin-walled aluminum tubes: experimental and numerical analysis," *Materials & design,* vol. 27, pp. 556-565, 2006.
[178] P. R. Mantena and R. Mann, "Impact and dynamic response of high-density structural foams used as filler inside circular steel tube," *Composite structures,* vol. 61, pp. 291-302, 2003.
[179] T. Ghanbari Ghazijahani, H. Jiao, and D. Holloway, "Fatigue Experiments on Circular Hollow Sections with CFRP Reinforced Cutouts," *Journal of Constructional Steel Research,* vol. 106, pp. 322-328, 2015.
[180] E. Ellobody, "Buckling analysis of high strength stainless steel stiffened and unstiffened slender hollow section columns," *Journal of Constructional Steel Research,* vol. 63, pp. 145-155, 2007.
[181] D. Liu and W.-M. Gho, "Axial load behaviour of high-strength rectangular concrete-filled steel tubular stub columns," *Thin-Walled Structures,* vol. 43, pp. 1131-1142, 2005.
[182] A. H. Varma, J. M. Ricles, R. Sause, and L.-W. Lu, "Experimental behavior of high strength square concrete-filled steel tube beam-columns," *Journal of Structural Engineering,* vol. 128, pp. 309-318, 2002.
[183] *AS 4100, Australian Standard, Steel Structures, 1998.*

[184] *EN 1994-1-1, Eurocode 4: Design of Composite Steel and Concrete Structures - Part 1-1: General Rules and Rules for Buildings, 2004.*

[185] F. Wangaard, "Elastic deflection of wood-fiberglass composite beams," *Forest Products Journal,* vol. 14, pp. 256-260, 1964.

[186] E. Biblis, "Analysis of wood-fiberglass composite beams within and beyond the elastic region," *Forest Products Journal,* vol. 15, pp. 81-88, 1965.

[187] F. Theakston, "A feasibility study for strengthening timber beams with fiberglass," *Canadian Agricultural Engineering,* vol. 7, pp. 17-19, 1965.

[188] K. C. Johns and S. Lacroix, "Composite reinforcement of timber in bending," *Canadian Journal of Civil Engineering,* vol. 27, pp. 899-906, 2000.

[189] D. D. Dempsey and D. W. Scott, "Wood members strengthened with mechanically fastened FRP strips," *Journal of Composites for Construction,* vol. 10, pp. 392-398, 2006.

[190] A. C. Duarte, J. H. Negrão, H. M. Cruz, and A. M. Balseiro, "Bending strength of timber beams rehabilitated with reinforced epoxy mortar plates," *Journal of structural engineering,* vol. 134, pp. 792-800, 2008.

[191] M. Madhoushi and M. P. Ansell, "Behaviour of timber connections using glued-in GFRP rods under fatigue loading. Part I: In-line beam to beam connections," *Composites Part B: Engineering,* vol. 39, pp. 243-248, 2008.

[192] C. O'Loinsigh, M. Oudjene, E. Shotton, A. Pizzi, and P. Fanning, "Mechanical behaviour and 3D stress analysis of multi-layered wooden beams made with welded-through wood dowels," *Composite Structures,* vol. 94, pp. 313-321, 2012.

[193] M. Khelifa and A. Celzard, "Numerical analysis of flexural strengthening of timber beams reinforced with CFRP strips," *Composite Structures,* vol. 111, pp. 393-400, 2014.

[194] A. D'Ambrisi, F. Focacci, and R. Luciano, "Experimental investigation on flexural behavior of timber beams repaired with CFRP plates," *Composite Structures,* vol. 108, pp. 720-728, 2014.

[195] T. C. Triantafillou and N. Deskovic, "Prestressed FRP sheets as external reinforcement of wood members," *Journal of Structural Engineering,* vol. 118, pp. 1270-1284, 1992.

[196] G. M. Raftery and A. M. Harte, "Low-grade glued laminated timber reinforced with FRP plate," *Composites Part B: Engineering,* vol. 42, pp. 724-735, 2011.

[197] A. Borri and M. Corradi, "Strengthening of timber beams with high strength steel cords," *Composites Part B: Engineering,* vol. 42, pp. 1480-1491, 2011.

[198] S. Hay, K. Thiessen, D. Svecova, and B. Bakht, "Effectiveness of GFRP sheets for shear strengthening of timber," *Journal of Composites for Construction,* vol. 10, pp. 483-491, 2006.

[199] J. Jasieńko and T. P. Nowak, "Solid timber beams strengthened with steel plates–Experimental studies," *Construction and Building Materials,* vol. 63, pp. 81-88, 2014.

[200] V. De Luca and C. Marano, "Prestressed glulam timbers reinforced with steel bars," *Construction and Building Materials,* vol. 30, pp. 206-217, 2012.

[201] H. Alhayek and D. Svecova, "Flexural stiffness and strength of GFRP-reinforced timber beams," *Journal of Composites for Construction,* vol. 16, pp. 245-252, 2012.

[202] C. Gentile, D. Svecova, and S. H. Rizkalla, "Timber beams strengthened with GFRP bars: development and applications," *Journal of Composites for Construction,* vol. 6, pp. 11-20, 2002.

[203] F. Micelli, V. Scialpi, and A. La Tegola, "Flexural reinforcement of glulam timber beams and joints with carbon fiber-reinforced polymer rods," *Journal of Composites for Construction,* vol. 9, pp. 337-347, 2005.

[204] *AS 1080.1, Australian Standard, Timber, Methods of Test, Moisture Content, 2012.*